Summer 2010

A theory of calcium dynamics in generating force and low-frequency fatigue in paralyzed human soleus

Matthew James Conaway
University of Iowa

A THEORY OF CALCIUM DYNAMICS IN GENERATING FORCE AND LOW-FREQUENCY FATIGUE IN PARALYZED HUMAN SOLEUS

by

Matthew James Conaway

An Abstract

Of a thesis submitted in partial fulfillment of the requirements for the Doctor of Philosophy degree in Biomedical Engineering in the Graduate College of The University of Iowa

July, 2010

Thesis Supervisors: Associate Professor Edwin L. Dove
Professor Richard K. Shields

ABSTRACT

Paralyzed muscle fatigues more quickly than intact muscle. The reason for this difference is currently unknown. This work will bridge this gap in knowledge by evaluating the predictive abilities of higher-resolution closed-form mathematical models of muscle force and fatigue. Knowledge garnered from this effort will suggest possible mechanisms for the differences in fatiguability of muscle in different states of health.

The hypothesis to be tested is that the concept missing from present models, and thus the present understanding of the physiology, is the dynamic behavior of divalent calcium (Ca^{2+}) during induced muscle contraction. If the behavior of Ca^{2+} can be understood as a Riccati-Bass diffusion process, muscle force and low-frequency fatigue in paralyzed muscle can be more accurately predicted over the time course of response to neuromuscular electrical stimulation. The abilities of existing mathematical models to predict force and low-frequency fatigue are compared to the predictive abilities of new models that include the Riccati-Bass equation.

There are several major findings of this study. First, it was found that the structure of the Conaway models better predicts force and low-frequency fatigue than do the Ding models. Second, the cross-bridge friction is the dominant process in generating force in fresh muscle at frequencies greater than 5 pps. Finally, the calcium leak current is dominant in low-frequency fatigue in paralyzed muscle. It is concluded that the process of muscle fatigue occurs as

calcium channel remodeling and inactivation of excitation-contraction coupling from ionic crowding accelerate with every additional contraction.

Abstract Approved: _____
Thesis Supervisor

_____
Title and Department

_____
Date

_____
Thesis Supervisor

_____
Title and Department

_____
Date

A THEORY OF CALCIUM DYNAMICS IN GENERATING FORCE AND LOW-FREQUENCY FATIGUE IN PARALYZED HUMAN SOLEUS

by

Matthew James Conaway

A thesis submitted in partial fulfillment of the requirements for the Doctor of Philosophy degree in Biomedical Engineering in the Graduate College of The University of Iowa

July, 2010

Thesis Supervisors: Associate Professor Edwin L. Dove
Professor Richard K. Shields

Graduate College
The University of Iowa
Iowa City, Iowa

CERTIFICATE OF APPROVAL

_____

PH.D. THESIS

_____

This is to certify that the Ph. D. thesis of

Matthew James Conaway

has been approved by the Examining Committee for the thesis requirement for the Doctor of Philosophy degree in Biomedical Engineering at the July, 2010 graduation.

Thesis Committee: _____
Edwin L. Dove, Thesis Supervisor

_____
Richard K. Shields, Thesis Supervisor

_____
Laura A. Frey-Law

_____
Nicole M. Grosland

_____
Michael A. Mackey

_____
Er-Wei Bai

To my Family

I will not presume to treat the whole of such a vast subject, but will limit myself to a few well-known truths.

Pierre Louis Moreau de Maupertuis, Accord between different laws of Nature that seemed incompatible

ACKNOWLEDGEMENTS

There are many to thank in the process of thesis preparation. First, I would like to thank my thesis advisor, Professor Edwin Dove in Biomedical Engineering, for agreeing to supervise me. He was very patient even as I belatedly figured out from Professor Martin Cassell and others that a Ph.D. is not about coursework. All credit for the actual MATLAB coding goes to him. Without such programming assistance, this thesis might not have been possible.

I also wish to thank the other members of my committee for their service. In particular, I thank Professor Richard Shields and Laura Frey Law in Physical Therapy for the initial guidance in formulating the project. The data used in this thesis came directly from Professor Shields, who later helped me obtain funding from the National Institutes of Health.

One who deserves special mention is Professor Evans Harrell at the Georgia Institute of Technology. It was at Tech in 1989 when I first learned about the Riccati/logistic equation as a harried and confused engineering undergraduate in his introductory ordinary differential equations course. Little did I know at that time how that course, and that one differential equation, would affect my career! At a critical point in my life, after my graduation from Tech, it was Professor Harrell who said that I needed to get going and do something. Even now, I still get valuable advice and support from him.

For the translation of the 1724 Riccati and the 1733 Euler papers, all credit and thanks are due to Dr. Ian Bruce at the University of Adelaide. Dr. Bruce is a

mathematician and historian of science who has a website on treatises from the 17th and 18th century, www.17centurymaths.com. He has translated the original manuscripts from Latin into English.

This work was supported by Award Number R01NR010285 from the National Institute of Nursing Research. The content is solely the responsibility of the author and does not necessarily represent the official views of the National Institute of Nursing Research or the National Institutes of Health. Additional support was provided by The University of Iowa Graduate College through a Summer Fellowship, the Strategic Initiative Fund, and other resources.

Finally, I thank my family. Their love and support have been immeasurable. As we are now scattered across the country, I am the one who returned to Iowa to renew the family connection with this great University. I came on a long, strenuous, and wandering journey to do this Ph.D. in Iowa City. Hopefully, I have done the family proud.

Of course, nothing is ever possible without the Cherisher and Sustainer of All the Worlds. I am grateful to the Most High for this experience and hope that I can use it in my humble quest to be of selfless service to Mankind. Be it so!

TABLE OF CONTENTS

LIST OF TABLES xi

LIST OF FIGURES xvi

1. INTRODUCTION 1

1.1. Rationale 1
1.2. Long-term goal 2
1.3. Specific aims 3
1.3.1. Developing a theory of force–fatigue in stimulated paralyzed muscle 3
1.3.2. Comparing models of muscle force and fatigue to experimental data 3
1.4. General approach 4
1.4.1. Modification of Ding models of muscle force and fatigue 4
1.4.2. Validation of models with trained/ untrained muscle as approximation for nonparalyzed/paralyzed muscle 6

2. MUSCLE BIOLOGY 7

2.1. Action potentials and muscle physiology 7
2.2. Calcium channels and motor unit physiology 23
2.3. Skeletal muscle contraction 29
2.4. Muscle fatigue: truth and fiction 31
2.5. The human soleus 36

3. CLINICAL ISSUES IN MUSCLE ELECTROSTIMULATION 41

3.1. Physiology of paralyzed muscle 41
3.1.1. Biological changes 41
3.1.2. Clinical sequelae 45
3.2. Engineering issues and therapeutic protocols 46
3.2.1. Physiologic constraints 46
3.2.2. Therapeutic inputs 49
3.3. Electrical stimulation of muscle 53
3.3.1. Intact muscle 53
3.3.2. Denervated muscle 58

4. MODELS OF MUSCLE FORCE AND FATIGUE 62

4.1. Introduction 62

4.2. Hill model 65
4.3. Huxley model 69
4.4. Zahalak models 77
4.5. Ding models 85
4.5.1. Force model 85
4.5.2. Fatigue model 98
4.5.3. The nature of the problem with the Ding models 107
4.5.4. Criticism of statistical methods 112

5. A THEORY OF CALCIUM CURRENT IN PARALYZED MUSCLE 113

5.1. A mathematical construct of growth, diffusion, and decay in muscle 113
5.1.1. A theory of diffusion 113
5.1.2. Riccati-Bass diffusion function 123
5.2. The role of calcium in force and fatigue in paralyzed muscle 126
5.2.1. An early model of calcium current in skeletal muscle 126
5.2.2. The relationship of calcium-troponin binding, calcium channel activation, and voltage sensitivity to force generation in paralyzed muscle 128
5.2.3. The roles of inactivation of excitation-contraction coupling and voltage sensitivity in decreased force-generating ability, and increased fatigability, in paralyzed muscle 135

6. METHODS 141

6.1. Human subjects 141
6.2. Experimental setup, instrumentation, recording procedures, and data collection 142
6.2.1. Experimental setup 143
6.2.2. Instrumentation 144
6.2.3. Recording procedures 145
6.2.4. Data collection 146
6.3. Validation protocols 147
6.3.1. Introduction 147
6.3.2. Determining differences in force-fatigue model structure 149
6.3.2.1. Physiological rationale 150
6.3.2.2. Closed-form parameterized model of muscle force 152
6.3.2.3. Data analysis 161

6.3.3. Muscle force protocol 162
6.3.3.1. Physiological rationale 163
6.3.3.2. Closed-form parameterized model of muscle force 164
6.3.3.3. Data analysis 170
6.3.4. Muscle fatigue protocol 171
6.3.4.1. Physiological rationale 171
6.3.4.2. Closed-form parameterized model of muscle fatigue 174
6.3.4.3. Data analysis 180
6.4. Solution techniques, parameterization approach, error calculation, and statistical methods 181
6.4.1. Solution techniques 181
6.4.2. Parameterization 184
6.4.3. Error calculation 185
6.4.4. Statistical methods 186

7. RESULTS 188

7.1. Introduction 188
7.2. Validation and testing of the Conaway models 188
7.2.1. Conaway force model 188
7.2.2. Conaway fatigue model 191
7.3. Determining differences in force and fatigue model structures 194
7.3.1. Global comparison between Ding and Conaway model structures 194
7.3.2. Comparison between Ding and Conaway force models 196
7.3.3. Comparison between Ding and Conaway fatigue models 199
7.4. The role of τ_2 in the Conaway force model 201
7.4.1. 10 CT 202
7.4.2. Doublet ramp 205
7.4.3. 20 DDT 207
7.4.4. Parametric behavior in modeled trained and untrained muscle 209
7.4.5. Analyses of variance for k_m, τ_1, and τ_2 218
7.5. The role of τ_{leak} in the Conaway fatigue model 219
7.5.1. Parametric plots for modeled trained muscle 220
7.5.2. Parametric plots for modeled untrained muscle 222
7.5.3. Analyses of variance for τ_{leak}, $\alpha_{\tau 1}$, and τ_{fat} 225

8. CONCLUSION 228

8.1. Evaluating the specific aims 228
8.1.1. Major findings 228
8.1.2. Interpretations, discoveries, and insights 229
8.1.3. Problems and weaknesses in the study 242
8.2. Future work to address long-term goals 242
8.2.1. Directions in modeling 243
8.2.2. Suggested experiments in vitro 244
8.2.3. Clinical applications 245
8.3. Summary 246

APPENDIX A: THE RICCATI EQUATION 248

A.1. The Riccati equation and its extensions 248
A.1.1. Introduction 248
A.1.2. The Bernoulli equation 249
A.1.3. The general Riccati equation 249
A.1.4. Solution of the general Riccati equation 252
A.1.5. Growth and diffusion models 253
A.2. Applications of the general Riccati equation 267
A.2.1. Biomedical applications of the general Riccati equation 267
A.2.1.1. The dose-response relationship 267
A.2.1.2. Epidemiologic models 270
A.2.1.3. Biochemistry, physiology, and psychophysics 274
A.2.2. Applications of the general Riccati equation in engineering and physical science 282
A.2.2.1. Autocatalysis 282
A.2.2.2. The Kalman filter and recursive Bayesian estimation 286
A.2.2.3. Optimal control 288
A.2.3. Socioeconomic applications of the general Riccati equation 293
A.2.3.1. Models of population growth 293
A.2.3.2. Other economic and social behavior 295
A.3. Implications 296
A.3.1. Towards a paradigm based on fundamental laws 297
A.3.2. A cursory argument to the sublime 301

APPENDIX B: SPINAL CORD INJURY 303

APPENDIX C: HISTORY OF ELECTRICITY IN MEDICINE 306

APPENDIX D: BIOCHEMISTRY OF LACTIC ACIDOSIS AND GLYCOLYSIS 311

APPENDIX E: PHYSICOCHEMICAL PRINCIPLES UNDERLYING CALCIUM-TROPONIN BINDING 319

E.1. Periodic reactions 319
E.2. Concepts of equilibrium 322
E.3. The Principle of Le Chatelier 325
E.4. Michaelis-Menten kinetics 327
E.5. Hysteresis 335

APPENDIX F: MISCELLANEOUS FREE PARAMETER DATA 341

APPENDIX G: A FATIGUING BOUT IN TRAINED MUSCLE 346

APPENDIX H: A FATIGUING BOUT IN UNTRAINED MUSCLE 354

REFERENCES 358

LIST OF TABLES

Table 4-1. List of parameters for Ding muscle force model. 97

Table 4-2. List of parameters for Ding muscle fatigue model for nonparalyzed muscle. 103

Table 6-1. Initial optimal parameter sets for Ding and Conaway force-fatigue models. 153

Table 6-2. List of parameters for the Conaway muscle force model. 160

Table 6-3. List of parameters for Conaway muscle fatigue model. 161

Table 7-1. Parameter values for Conaway fatigue model validation in trained limb in Subject 18. 192

Table 7-2. Parameter values for Conaway fatigue model validation in untrained limb in Subject 18. 193

Table 7-3. Comparison of error statistics in Conaway fatigue model validation for trained and untrained limb. The Conaway fatigue model has very low error, in all metrics, for both trained and untrained muscle. 194

Table 7-4. Prediction measures across various inputs, training status, and fatigue states from both models in unconstrained optimization. 194

Table 7-5. Comparison of average mean square error and average correlation coefficient in Ding and Conaway model structures under unconstrained optimization. 195

Table 7-6. Prediction measures from the Ding and Conaway force models for inputs with frequencies greater than 5 pps in unconstrained optimization in trained muscle from Subject 18. 196

Table 7-7. Prediction measures from the Ding and Conaway force models for inputs with frequencies greater the 5 pps in unconstrained optimzation in untrained muscle from Subject 18. 197

Table 7-8. Single factor analysis of variance for mean squared error Between Ding and Conaway force models. 198

Table 7-9. Parameter values for Conaway fatigue model validation in trained limb in Subject 18. 199

Table 7-10. Comparison of error statistics between Ding and unconstrained Conaway fatigue models in trained and untrained limbs in Subject 18. 200

Table 7-11. Single factor analysis of variance for mean squared error between Ding and Conaway fatigue models. The difference in model predictive ability is highly significant. 201

Table 7-12. Optimized parameter values for Conaway force model using $\{k_m, \tau_1, \tau_2\}$ with 10 CT input. 202

Table 7-13. Optimized parameter values for Conaway force model using $\{k_m, \tau_1\}$ with 10 CT input. 203

Table 7-14. Optimized parameter values for Conaway force model using $\{k_m\}$ with 10 CT input. 204

Table 7-15. Loss functions and Akaike FPEs for the three optimized Conaway force models for 10 CT input. Note that $\{k_m, \tau_1, \tau_2\}$ generates the least prediction error. However, $\{k_m, \tau_1\}$ gives the most realistic values. 205

Table 7-16. Optimized parameter values for Conaway force model using $\{k_m, \tau_1, \tau_2\}$ with double ramp input. 205

Table 7-17. Optimized parameter values for Conaway force model using $\{k_m, \tau_1\}$ with double ramp input. 206

Table 7-18. Optimized parameter values for Conaway force model using $\{k_m, \tau_1\}$ with 20 DDT input. 208

Table 7-19. Loss functions and Akaike FPEs for the two optimized Conaway force models for 20 DDT input. It is shown that for the 20 DDT input, the set $\{k_m, \tau_1, \tau_2\}$ generates the least prediction error while returning realistic physiologic values. 209

Table 7-20. Free parameters in Conaway force model found using Subject 18 trained fresh muscle. Note how they vary with the frequency-contraction index. There are no discernable trends for k_m and τ_1. 216

Table 7-21. Free parameters in Conaway force model found using Subject 18 untrained fresh muscle. Note how they vary with the frequency-contraction index. There are no discernable trends for k_m and τ_1. 217

Table 7-22. Two-way analysis of variance with replication for k_m. No factor is statistically significant. 218

Table 7-23. Two-way analysis of variance with replication for τ_1. No factor is statistically significant. 218

Table 7-24. Two-way analysis of variance with replication for τ_2. Neither the training status nor the interaction between frequency and training status has statistical significance. However, the factor of input frequency is significant statistically. 219

Table 7-25. Free parameters in Conaway fatigue model found using Subject 17 trained fatigued muscle. Note how they vary with the contraction index. The standard deviations for $\alpha_{\tau 1}$ and τ_{fat} increase with each contraction. Hence, those parameters have little influence in fatigue. The parameter τ_{leak} is dominant. 224

Table 7-26. Free parameters in Conaway fatigue model found using Subject 18 untrained muscle. Note how they vary with the contraction index.The standard deviations for $\alpha_{\tau 1}$ and τ_{fat} increase with each contraction. Hence, those parameters have little influence in fatigue. Again, the parameter τ_{leak} is dominant. 225

Table 7-27. Two-way analysis of variance with replication for τ_{leak}. The analysis shows that the interaction term between contraction index and training has the greatest contribution to the variance in τ_{leak}. All factors are statistically significant. 225

Table 7-28. Two-way analysis of variance with replication for $\alpha_{\tau 1}$. The two main factors are statistically significant. 226

Table 7-29. Two-way analysis of variance with replication for τ_{fat}. No factor is statistically significant. Hence, it has the least influence of the three free parameters in the Conaway fatigue model. 226

Table D-1. Summary of reactions in glycolysis. 312

Table F-1. Subject 17 trained warmup. 341

Table F-2. Subject 18 untrained warmup. 341

Table F-3. Behavior of free parameters from doublet ramp inputs in untrained muscle optimized on the set $\{k_m, \tau_1\}$. The parameters do not change much between first and second contractions for all Subjects. There are no discernable trends. 344

Table F-4. Behavior of free parameters from doublet ramp inputs in trained muscle optimized on the set $\{k_m, \tau_1\}$. The parameters do not change much between first and second contractions for all Subjects. There are no discernable trends. 345

Table G-1. Parameter values for contraction 1 in the trained limb of Subject 17. 346

Table G-2. Parameter values for contraction 2 in the trained limb of Subject 17. 347

Table G-3. Parameter values for contraction 3 in the trained limb of Subject 17. 348

Table G-4. Parameter values for contraction 4 in the trained limb of Subject 17. 349

Table G-5. Parameter values for contraction 5 in the trained limb of Subject 17. 350

Table G-6. Parameter values for contraction 6 in the trained limb of Subject 17. 351

Table G-7. Comparison of error statistics of the Conaway fatigue model for each contraction of the trained limb of Subject 17. The statistics are consistent throughout the fatiguing bout. 352

Table G-8. Loss functions and Akaike FPEs for each contraction of the trained limb of Subject 17. The functions are consistently low throughout the fatiguing bout. 352

Table H-1. Parameter values for contraction 1 in the untrained limb of Subject 18. 354

Table H-2. Parameter values for contraction 2 in the untrained limb of Subject 18. 355

Table H-3. Parameter values for contraction 3 in the untrained limb of Subject 18. 356

Table H-4. Comparison of error statistics of the Conaway fatigue model for each contraction in the untrained limb of Subject 18. The statistics are consistent throughout the fatiguing bout. 357

Table H-5. Loss functions and Akaike FPEs for each contraction of the untrained limb of Subject 18. The functions are consistently low throughout the fatiguing bout. 357

LIST OF FIGURES

Figure 1-1. General Riccati-Bass function. 5

Figure 2-1. Electric circuit model of an excitable membrane. 8

Figure 2-2. A. A schematic view of an idealized action potential illustrates its various phases as the action potential passes a point on a cell membrane. B. Figures A-D give current flow direction in the membrane for each phase. 9

Figure 2-3. Action potential, schematic and real. 10

Figure 2-4. Schematic overview of the cable theory view of a piece of neuronal fiber. When an electrical current is moving along the inside of a fiber the cytosol exerts a resistance (r_l). Simultaneously current will escape through the phospholipid bilayer (with resistance r_m) to the outside; and due to electrostatic forces a buildup of charge (c_m) will take place along the bilayer. 14

Figure 2-5. Continuous propagation of an action potential in an unmyelinated axon. 16

Figure 2-6. Model of saltatory conduction in a myelinated axon. 17

Figure 2-7. Schematic of motoneuron and neuromuscular junction. 20

Figure 2-8. Schematic of T-tubules with the SR and the contractile machinery. 22

Figure 2-9. Structure and feedback loop of Ca_{v1} channel. 24

Figure 2-10. Calcium cycle. 27

Figure 2-11. Depiction of the contraction of a muscle through the overlap of thick and thin filament fibers. 31

Figure 2-12. Chemical structures of lactic acid and sodium lactate. 34

Figure 2-13. Medial view of muscles of the left leg. 39

Figure 2-14. Axial section through the left leg approximately 10 cm below the knee joint. 40

Figure 3-1. Determining rheobase and chronaxie from an asymptotic strength-duration curve. 1) The *rheobase* is the minimum input amplitude that will elicit a response. In this example, this value is 0.35 V. 2) Twice the rheobase is 0.7 V. 3) The *chronaxie* is the input duration that elicits a response when the input amplitude is exactly twice the rheobase. In this example, the chronaxie is 0.22 ms. 48

Figure 3-2. Galvanic current. 49

Figure 3-3. Faradic current. 50

Figure 3-4. Pulsed current. 51

Figure 3-5. Example of train vs. burst. 52

Figure 3-6. Electron flow in a conductor. 54

Figure 3-7. Current flow through tissue. 54

Figure 3-8. Force summation as a function of stimulation frequency. 56

Figure 3-9. Example of on time and off time in a stimulation cycle. 57

Figure 4-1. Schematic of force-velocity relationship in skeletal muscle. 65

Figure 4-2. Schematic of the force-velocity relationship predicted by the Hill equation. 67

Figure 4-3. Schematic of Hill model with contractile element (CE) with series elastic element (SE). 68

Figure 4-4. Schematic of Hill models with contractile element (CE) with parallel elastic element (PE) and series elastic element (SE). 68

Figure 4-5. Schematic of Huxley 1957 cross-bridge model. 71

Figure 4-6. Schematic for rate functions of bonding, f, and unbonding, g. 72

Figure 4-7. Normalized comparison of Hill model (solid curve) and Huxley model (circles) for force-velocity relationship. 73

Figure 4-8. Schematic of T_1 and T_2. 74

Figure 4-9. T_1 and T_2 as a function of length step. 75

Figure 4-10. Schematic of event sequence in Huxley 1971 theory. 76

Figure 4-11. Schematic of excitation-contraction coupling. 78

Figure 4-12. Diagram of tight coupling (solid line) and loose coupling (solid plus dashed lines). Curved arrows indicate Ca^{2+}-Tr interactions. 79

Figure 4-13. Three-state kinetic model with ATP energetics. 82

Figure 4-14. Fast isometric transient curves. 84

Figure 4-15. Schematic of the isometric model of muscle force. 87

Figure 4-16. Duplication of force response and C_N from a doublet ramp using the Ding force model. This shows that the Ding force model does a reasonable job at calculating C_N even with a constant R_0. However,the peaks in the C_N curve are not uniform in magnitude and do not necessarily correspond as shown in the literature with each pulse of the doublet ramp stimulus. 109

Figure 4-17. Duplication of a fatiguing contraction from a 10 CT input using the Ding fatigue model. It is shown that in the Ding fatigue model, the force tetani remain unfused. Furthermore, the peaks in the C_N curve remain at relatively high magnitude. Nevertheless, the original parameters of Ding et al (56) were used in this simulation. This suggests that an adequate accounting of the calcium dynamics during fatigue is lacking in this model. 110

Figure 4-18. Behavior of A, R_0, and τ_c in the Ding fatigue model from a 10 CT input. All parameters remain constant throughout a contraction. 111

Figure 5-1. The modified exponential function. 115

Figure 5-2. Diffusion curves for different combinations of external and internal influence. 116

Figure 5-3. Trajectories of the “logistic” difference equation. 120

Figure 5-4. Variation of the relative rate, R, for different values of n. The Case n=1 corresponds to the Verhulst logistic growth law. 121

Figure 5-5. Logistic growth diagrams for different values of n. 121

Figure 5-6. Graph of total adopters for product cycle. 125

Figure 5-7. Graphs of innovators, imitators, and new adopters for product cycle. 126

Figure 5-8. State diagram of stop transducer. The limits of action are at x=h and x=-h. 126

Figure 5-9. Block diagram of calcium mediated activated force generation model. 128

Figure 5-10. Calcium current flow diagram in c.m.am. 130

Figure 5-11. Evidence of early depression in the cat soleus in response to subsequent pulses. Note that pulses C2-C4 have progressively longer times to peak force. 131

Figure 5-12. Averaged and superimposed twitches in cat soleus. The response of j-1stimuli was subtracted from j stimuli to document to nonlinear contribution of C_j. 133

Figure 5-13. Movement of charge in normal rat e.d.l. (squares) and soleus (circles) as a function of voltage. The dashed curve is the soleus curve scaled to maximum and demonstrates the voltage sensitivity differential in the two fiber types. 133

Figure 5-14. Average movement of charge in paraplegic rat soleus (circles) as a function of voltage. The dashed curve is the solid curve scaled to a maximum and demonstrates the change in charge movement in denervated soleus. 138

Figure 6-1. Torque measurement apparatus including adjustable axis of rotation, stabilization cuff, and femoral strap. 143

Figure 6-2. Schematic representation of the stimulation patterns, showing Only the 10 pps series and the doublet ramp used for parameter determination for each model. 146

Figure 6-3. Hypothetical C_N curve from a Riccati-Bass diffusion function for R_0 resulting from a doublet ramp input. It varies with time and Accounts for nonlinear summation of activation from each pulse. 148

Figure 6-4. Assumed structure of muscle in Conaway models. 149

Figure 6-5. Duplication of force response and C_N from a twitch using the Conaway force model for one contraction. Since R_0 was found to be constant for this input, no plot is given for that curve. 157

Figure 6-6. Duplication of force response and C_N from a 5 DDT input using the Conaway force model for two contractions. 158

Figure 6-7. Behavior of R_0 from a 5 DDT input using the Conaway force model for two contractions. Note its sharp decrease. 159

Figure 6-8. Duplication of force response and C_N from a 10 DDT using the Conaway force model for one contraction. 164

Figure 6-9. Behavior of R_0 from a 10 DDT input using the Conaway force model for one contraction. Note its increased lag. 165

Figure 6-10. Duplication of force response and C_N from a doublet ramp using the Conaway force model for one contraction. 166

Figure 6-11. Behavior of R_0 from a doublet ramp input using the Conaway force model for one contraction. Note the smoothness of the curve. 166

Figure 6-12. Duplication of force response and C_N from a 20 DDT input using the Conaway force model for one contraction. 167

Figure 6-13. Behavior of R_0 from a 20 DDT input using the Conaway force model for one contraction. Note its increased lag and earlier inflection. 167

Figure 6-14. Hypothetical Riccati-Bass voltage sensitivity with $\mu_2/\mu_1=1.001$. For small ratios of μ_2 to μ_1, the voltage sensitivity changes so rapidly that the muscle inactivates quickly. Hence, fatigue would onset very suddenly. 168

Figure 6-15. Hypothetical Riccati-Bass voltage sensitivity with $\mu_2/\mu_1=10.01$. For large ratios, the muscle inactivates at a slower pace. Fatigue would onset very slowly. If that were physiologic reality, however, muscles would easily be damaged due to overwork from the lack of a refractory period. 168

Figure 6-16. Power law analysis of Riccati-Bass functions for b=1.0, 1.5. Increases in b shift the curves rightward and accelerate inflection. 169

Figure 6-17. Duplication of a fatiguing contraction and C_N from a 10 CT input using the Conaway fatigue model for one contraction. It is shown that in the Conaway fatigue model, the force tetani fuse and decrease in magnitude. 175

Figure 6-18. Behavior of k_m in the Conaway fatigue model for one contraction. It is shown that, in the Conaway fatigue model, k_m decays over a period of contraction. However, in the Ding model, k_m is a fixed parameter constant throughout a contraction. 176

Figure 6-19. Effects of variations in τ_{leak} on the curves for force and C_N in the Conaway fatigue model for one contraction. The parameter τ_{leak} has the most effect on the shape of the curves by simulating fasciculations. 177

Figure 6-20. Effects of variations in $\alpha_{\tau 1}$ on the curves for force and C_N in the Conaway fatigue model for one contraction. When $\alpha_{\tau 1}$ is large, The concavity of the C_N curve changes. 178

Figure 6-21. Effects of variations in A on the curves for force and C_N in the Conaway fatigue model for one contraction. The parameter A has the least effect on the shape of the curves. 179

Figure 7-1. Validation of Conaway force model with 5 pps train with beginning doublet in trained muscle in Subject 18. The model had 77.4% agreement with the data. 189

Figure 7-2. Twitch in trained muscle in Subject 18. The model had 94.48% agreement with the data. 189

Figure 7-3. Doublet ramp in trained muscle in Subject 27. The model had 72.78% agreement with the data. 190

Figure 7-4. 10 DT stimulation in untrained muscle in Subject 18. The model had 80.92% agreement with the data. 190

Figure 7-5. 20 CT in untrained muscle in Subject 18. The model had 94.06% agreement with the data. 191

Figure 7-6. Fatigue in trained limb of Subject 18. The agreement of the Conaway model with the experimental data is 0.982282. 192

Figure 7-7. Fatigue in untrained limb of Subject 18. The agreement of the Conaway model with the experimental data is 0.9990524. 193

Figure 7-8. Comparison between Ding and unconstrained Conaway fatigue models in Subject 18 untrained limb. 200

Figure 7-9. 10 CT optimized on $\{k_m, \tau_1, \tau_2\}$. The fit of the optimized model is 95.17%. However, the value for τ_2 is out of the range reported in the literature. 202

Figure 7-10. 10 CT optimized on {k_m, τ_1}.The fit of the optimized model is 82.65%. However, the free parameter values are consistent with the literature. 203

Figure 7-11. 10 CT optimized on {k_m, τ_1, τ_2}. The fit is 82.67%. However, the parameter values do not make sense physiologically. The parameter k_m decreases dramatically in this optimization. 204

Figure 7-12. Doublet ramp optimized on {k_m, τ_1, τ_2}. The fit of the model is 82.99%. However, the optimized values for k_m and τ_2 are well outside of reported ranges. 206

Figure 7-13. Doublet ramp optimized on {k_m, τ_1}. The model fit is 70.41%. However, the optimized parameter values are within ranges reported in the literature. 207

Figure 7-14. 20 DDT optimized on {k_m, τ_1, τ_2}. The model fit is 94.77%. In addition, the optimized free parameter values are within reported ranges. 207

Figure 7-15. 20 DDT optimized on {k_m, τ_1}.The model fit decreases to 72.31%. In addition, the value for τ_1 does not fall within previously reported ranges. 208

Figure 7-16. Behavior of k_m as a function of frequency and contraction in trained muscle. 210

Figure 7-17. Behavior of τ_1 as a function of frequency and contraction in trained muscle. 211

Figure 7-18. Behavior of τ_2 as a function of frequency and contraction in trained muscle. 212

Figure 7-19. Behavior of k_m as a function of frequency and contraction in untrained muscle. 213

Figure 7-20. Behavior of τ_1 as a function of frequency and contraction in untrained muscle. 214

Figure 7-21. Behavior of τ_2 as a function of frequency and contraction in untrained muscle. 215

Figure 7-22. Behavior of τ_{leak} as a function of contraction index in trained muscle in Subject 17. 220

Figure 7-23. Behavior of $\alpha_{\tau 1}$ as a function of contraction index in trained muscle in Subject 17. 220

Figure 7-24. Behavior of τ_{fat} as a function of contraction index in trained muscle in Subject 17. 221

Figure 7-25. Behavior of τ_{leak} as a function of contraction index in trained muscle in Subject 18. 221

Figure 7-26. Behavior of $\alpha_{\tau 1}$ as a function of contraction index in trained musclein Subject 18. 221

Figure 7-27. Behavior of τ_{fat} as a function of contraction index in trained muscle in Subject 18. 222

Figure 7-28. Behavior of τ_{leak} as a function of contraction index in untrained muscle in Subject 17. 222

Figure 7-29. Behavior of $\alpha_{\tau 1}$ as a function of contraction index in untrained muscle in Subject 17. 222

Figure 7-30. Behavior of τ_{fat} as a function of contraction index in untrained Muscle in Subject 17. 223

Figure 7-31. Behavior of τ_{leak} as a function of contraction index in untrained muscle in Subject 18. 223

Figure 7-32. Behavior of $\alpha_{\tau 1}$ as a function of contraction index in untrained muscle in Subject 18. 223

Figure 7-33. Behavior of τ_{fat} as a function of contraction index in untrained muscle in Subject 18. 224

Figure A-1. General logistic curve with inflection point at (-ln c/a, b/2c). 254

Figure A-2. Sigmoid function. 255

Figure A-3. Hyperbolic tangent function with τ=1. 256

Figure A-4. Allometric metabolic (top) and growth curves (bottom). 258

Figure A-5. Comparative growth curves for fish, mouse, and man. 259

Figure A-6. Riccati-Bass diffusion function and associated power law with b=1. 260

Figure A-7. Riccati-Bass diffusion function and associated power law with b=1.5. 261

Figure A-8. Riccati-Bass diffusion function and associated power law with b=2. 261

Figure A-9. Riccati-Bass diffusion function and associated power law with b=2.5. 262

Figure A-10. Riccati-Bass diffusion function and associated power law with b=3. 262

Figure A-11. Riccati-Bass diffusion function and associated power law with b= π. 263

Figure A-12. Riccati-Bass diffusion function and associated power law with b=3.5. 263

Figure A-13. Riccati-Bass diffusion function and associated power law with b=4. 264

Figure A-14. Riccati-Bass diffusion function and associated power law with b=4.5. 264

Figure A-15. Riccati-Bass diffusion function and associated power law with b=5. 265

Figure A-16. Riccati-Bass diffusion function and associated power law with b=5.5. 265

Figure A-17. Riccati-Bass diffusion function and associated power law with b=50. 266

Figure A-18. Riccati-Bass diffusion function and associated power law with b=100. 266

Figure A-19. Dose-response curves for two different stressors. Note that the potency/efficacy point changes as the curve shifts in the abscissa. 268

Figure A-20. SIR epidemic model. The epidemic stops when the number of susceptibles drops. Blue=Susceptible, Green=Infected, and Red=Recovered. 270

Figure A-21. SIS epidemic model. Susceptibles and infected equilibrate. 272

Figure A-22. Heme group. 274

Figure A-23. Hemoglobin oxygen-dissociation curve. 276

Figure A-24. A schematic example of a response function. The dynamic range D, threshold response r_{min} and maximal discharge r_{max} are illustrated. The size of the corresponding "just noticeable difference" in the signal, Δs, depends on the slope of the response function. It is smallest where the slope is highest. 278

Figure A-25. Classical definitions of sensitization, hyperalgesia, and allodynia. 281

Figure A-26. Family of autocatalytic curves for different initial concentrations. An increase in reactant concentration accelerates the autocatalysis. 283

Figure A-27. Limit of stability for conversion of aggregate A to A' in an autocatalytic reaction. 284

Figure A-28. Variation of product concentration as a function of time in an autocatalytic reaction. 285

Figure A-29. Model underlying the Kalman filter. Circles are vectors, squares are matrices, and stars represent white noise. 286

Figure A-30. Markov process with **X** as visible measurements and **Z** as Hidden state. 287

Figure A-31. Heaviside step function. 291

Figure A-32. Smooth approximation to Heaviside step function. 292

Figure A-33. Set of trajectories in a costate vector in an optimal control scheme. 292

Figure A-34. General curve of population growth. 294

Figure A-35. Gompertz curves. 296

Figure A-36. A brachistochrone is the shortest distance along a curve. 297

Figure A-37. The cycloid (blue) and its generating circle (red). 298

Figure C-1. Duchenne stimulator. 307

Figure C-2. Leyden jar. 309

Figure C-3. Neuromuscular electrical stimulation device. 309

Figure D-1. Phosphagen reaction system. 311

Figure D-2. Hexokinase, phosphofructokinase, and G3P dehydrogenase reaction steps in glycolysis. 313

Figure D-3. Lactate dehydrogenase (LDH) reaction. 314

Figure D-4. ATP hydrolysis. 316

Figure D-5. Schematic representation of mitochondrial respiration and ATP regeneration. 318

Figure E-1. Periodic reactions with time-varying concentrations of reactants. The dynamics of [Y] lag the dynamics of [X]. 320

Figure E-2. Example of damped periodic reactions for x and y with y_0=1, M=0.8, φ=π/6, p=0.707, and q=0.707. The dynamics of y are damped and lag the dynamics of x. 321

Figure E-3. Dynamic equilibrium of a chemical system. Free energy is required to drive a reaction through the intermediate state and past the equilibrium point in either direction. 323

Figure E-4. An example of the Principle of Le Chatelier. Changing the concentration of A drives the reaction in its opposing direction towards equilibrium. 326

Figure E-5. Traditional Michaelis-Menten kinetics plot. The kinetics are asymptotically bound. 330

Figure E-6. Fractal rate law plots of reaction velocity as a function of the concentration of substrate: (a) Cartesian plot. Sigmoidal behavior increases with kinetic order (g). Traditional Michaelis-Menten rate law is top curve with g=1. (b) Hill plot. A slope (g_s/g_e) greater than 1 indicates non-hyperbolic cooperativity. The rate law is governed by asymptotic lines. The top asymptote is the traditional Michaelis-Menten law. 333

Figure E-7. A hypothetical depiction of macromolecular crowding. 334

Figure E-8. Idealized elastic hysteresis. The area in the center of the hysteresis loop is the energy dissipated. 336

Figure E-9. Hypothetical B vs. H magnetization hysteroid. 337

Figure E-10. Chemical system with bistability and oscillating states of concentration surge and depletion. 338

Figure E-11. State diagram of stop transducer. The limits of action are at x=h and x=-h. 339

Figure F-1. Behavior of k_m in trained limb of Subject 17 at warm-up. 341

Figure F-2. Behavior of τ_1 in trained limb of Subject 17 at warm-up. 342

Figure F-3. Behavior of τ_2 in trained limb of Subject 17 at warm-up. 342

Figure F-4. Behavior of k_m in untrained limb of Subject 18 at warm-up. 343

Figure F-5. Behavior of τ_1 in untrained limb of Subject 18 at warm-up. 343

Figure F-6. Behavior of τ_2 in untrained limb of Subject 18 at warm-up. 344

Figure G-1. Contraction 1 of fatiguing bout in the trained limb of Subject 17. The agreement of the Conaway model with the experimental data is 0.98436. 346

Figure G-2. Contraction 2 of fatiguing bout in the trained limb of Subject 17. The agreement of the Conaway model with the experimental data is 0.985999. 347

Figure G-3. Contraction 3 of fatiguing bout in the trained limb of Subject 17. The agreement of the Conaway model with the experimental data is 0.982276. 348

Figure G-4. Contraction 4 of fatiguing bout in the trained limb of Subject 17. The agreement of the Conaway model with the experimental data is 0.9870934. 349

Figure G-5. Contraction 5 of fatiguing bout in the trained limb of Subject 17. The agreement of the Conaway model with the experimental data is 0.989389. 350

Figure G-6. Contraction 6 of fatiguing bout in the trained limb of Subject 17. The agreement of the Conaway model with the experimental data is 0.987693. 351

Figure G-7. Peak forces for each contraction in a fatiguing bout n the trained limb of Subject 17. The peak forces generally decay with each contraction. This shows that potentiation occurs in fatiguing paralyzed muscle. 353

Figure H-1. Contraction 1 of fatiguing bout in the untrained limb of Subject 18. The agreement of the Conaway model with the experimental data is 0.975184. 354

Figure H-2. Contraction 2 of fatiguing bout in the untrained limb of Subject 18. The agreement of the Conaway model with the experimental data is 0.932472. 355

Figure H-3. Contraction 3 of fatiguing bout in the untrained limb of Subject 18. The agreement of the Conaway model with the experimental data is 0.912205. 356

CHAPTER 1: INTRODUCTION

1.1 Rationale

Chronic spinal cord injury (SCI) elicits deleterious musculoskeletal adaptations, such as muscle paralysis and spasticity that adversely affect health in those who are injured. Increasingly, desired rehabilitation outcomes will require limb preservation which may be done via electrical stimulation of paralyzed muscle. However, few models predict fatigue in paralyzed muscle. The soleus muscle provides an ideal *in vivo* model of the effects of SCI on muscle properties, as it transforms from predominantly slow fiber type to that of fast-fatigable (FF) or type IIb fibers (164), which prolongs relaxation in the fatigued state. Clinically, this is important since a close association between optimal stimulation frequency and contractility exists. (42, 164)

Ding and colleagues have tried several approaches to model fatigue in nonparalyzed and paralyzed muscle using their version of a Hill-Huxley model. (48-56) However, they demonstrated that the parameter relationships found for nonparalyzed muscle did not apply to paralyzed muscle. (51) Thus, it is not yet clear which permutation of parameters may optimally represent fatigue in paralyzed muscle. Further, it was hypothesized that more complex nonlinear models would provide the most accurate predictions of overall force as well as specific force properties such as peak force. (66) Furthermore, according to Bellinger (11), during exercise, defects in calcium release impair muscle function. It has been shown that during exercise in rodents and man, the primary calcium

channel required for excitation–contraction coupling in skeletal muscle, the ryanodine receptor (RyR1), is progressively PKA-hyperphosphorylated and undergoes other biochemical degradations. This destabilizes the RyR1 subunit calstabin1 (FKBP12) which yields leaky channels that cause decreased exercise tolerance in rodents. This suggests a possible mechanism by which calcium leak via RyR1 channels depleted of calstabin1 elicits defective signaling, muscle damage, and impaired exercise tolerance. Thus, this study would provide the first systematic evaluation of mathematical models of paralyzed muscle fatigue by modifying currently available models to incorporate calcium dynamics and leakage.

1.2 Long-term goal

The long-term goal of this study is to alter the delivery protocol of electrical pulses from stimulators to paralyzed limbs, such that muscle fatigue is minimized, thus benefiting many with spinal cord injury. The information which is to be garnered could be implemented in future designs of electrical muscle stimulators. This information could also be used as the basis of a quantitative index of muscle fatigue. Additionally, these modeling efforts will suggest *in vitro* experiments to verify the calcium dynamics in muscle. With this enhanced understanding of the physiology of paralyzed muscle, safer and more appropriate therapeutic stress protocols that employ electrical stimulation can be developed for persons with spinal cord injury. Safer protocols will lead to improved health care and quality of life for paralyzed people by reducing risk of injury from

inadvertent overstimulation of muscle. Reduced risk of injury will lead to decreased health care costs.

1.3 Specific aims

1.3.1 Developing a theory of force-fatigue in stimulated paralyzed muscle

The first specific aim of this work is to develop a theoretical model of force generation in stimulated trained and untrained chronically paralyzed human muscle. It is hypothesized that the calcium dynamics of stimulated paralyzed muscle behaves as a diffusion process during nonfatigue contraction. In addition, during fatigue, it is hypothesized that the process of sustained force decay is accelerated via leaky calcium channels. The model will be validated by comparing simulated force and fatigue profiles to experimental soleus data from paralyzed human trained and untrained limbs. The results of the model will be compared with published results.

1.3.2 Comparing models of muscle force and fatigue to experimental data

The second specific aim is to compare the predictions made by the model with data measured from trained and untrained paralyzed human soleus muscle. It is hypothesized that a dynamic conceptualization of the calcium flux in contracting paralyzed muscle will yield more accurate prediction of fatigue during a course of electrotherapeutic stimulation. It is further hypothesized that incorporating the dynamics of calcium leakage during extrinsically induced contraction will generate better understanding of paralyzed muscle physiology. The new models will be compared and contrasted to existing models by

evaluating the level of agreement of simulated force and fatigue profiles to experimental soleus data from chronically paralyzed human trained and untrained limbs.

1.4 General approach

Paralyzed muscle fatigues more quickly than nonparalyzed muscle. The reason for this difference is currently unknown. This work will bridge this gap in knowledge by evaluating the predictive abilities of higher-resolution closed-form mathematical models of muscle force and fatigue. Knowledge garnered from this effort will suggest possible mechanisms for the differences in fatigability of muscle in different states of health.

1.4.1. Modification of Ding models of muscle force and fatigue

The hypothesis to be tested is that the concept missing from present models, and thus the present understanding of the physiology, is the dynamic behavior of divalent calcium (Ca^{2+}) during induced muscle contraction. Current models assume that the calcium dynamics in electrically stimulated muscle is quasistatic if not constant, in spite of experimental evidence of calcium leakage from muscle during prolonged stimulation. In addition, it is hypothesized that the calcium dynamics in paralyzed muscle are different than the calcium dynamics in nonparalyzed muscle in fresh and fatigued states. If the behavior of Ca^{2+} can be understood as a dynamic process with leakage, muscle force and low-frequency fatigue can be more accurately predicted over the time course of response to neuromuscular electrical stimulation. Eventually, a transition between fresh and

fatigued states may be detected and a quantitative index of low-frequency fatigue may be developed with this enhanced physiological understanding.

The abilities of existing mathematical models to predict force and low-frequency fatigue will be compared to the predictive ability of new models. These new models will be existing models that are modified with a leakage term and the contractile dynamics of Ca^{2+} described by a time-varying nonlinear differential equation first articulated by Riccati. $y'=P(t)+Q(t)y+R(t)y^2$, and in particular formulated by Bass. (10, 158) The Riccati differential equation arises ubiquitously in diverse fields such as biology, chemistry, physics, engineering, medicine, finance, and the social sciences. (16, 99, 100) In its myriad variations, this equation describes processes of growth, diffusion, and decay on scales that are generally exponential. (9, 57) Hence, it is presumed to be an excellent candidate to model the calcium dynamics of muscle in response to doses of external electrical stimulation. The typical dose-response curves in medical science are generated from the logistic equation. The logistic equation is a special case of the Riccati equation when P(t)=0. (179, 180)

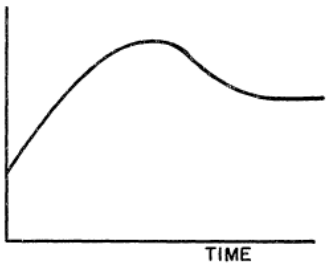

Figure 1-1. General Riccati-Bass function. (10)

1.4.1 Validation of models with trained/untrained muscle as approximation for nonparalyzed/paralyzed muscle

With the physiologic approximation of paralyzed trained muscle to nonparalyzed muscle, the improved models of force and low-frequency fatigue in muscle will enhance the understanding of underlying physiological mechanisms. Shields et al (165) found that these approximations are valid and yield reliable results in experimental studies of muscle force and fatigue.

CHAPTER 2: MUSCLE BIOLOGY

2.1 Action potentials and muscle physiology

Neuromuscular physiology is based on the action potential, which is a wave of electrical discharge that travels along the membrane of a cell. Action potentials are an essential feature of animal life. They rapidly transmit information within and between tissues, and are extensively used by the nervous system for communication between neurons and muscles as well as other organs. (1, 72-74, 78, 91-93, 95, 97)

At baseline, the resting potential is what would be maintained were there no action potentials, synaptic potentials, or other changes to the membrane potential. In neurons the resting potential is approximately -70 mV. The resting potential is mostly determined by the ion concentrations on both sides of the cell membrane and the ion transport proteins that are in the cell membrane. Active transport of potassium and sodium ions into and out of the cell, respectively, is accomplished by a number of sodium-potassium pumps embedded in the cell membrane. Each pump transports two ions of potassium into the cell for every three ions of sodium pumped out. In some cases, the electrogenic sodium-potassium pumps significantly contribute to the resting membrane potential. However, in most cells, the dominant modulator of the resting potential is the potassium leak channel. Yet, the resting cell membrane is approximately 75 times more permeable to potassium than to sodium because potassium leak channels are always open. As a result, the resting membrane potential is closer

to the equilibrium potential of potassium (E_K=−80 mV) than the equilibrium potential of sodium (E_{Na}=+70 mV). (1, 72-74, 78, 91-93, 95, 97, 111)

Like the resting potential, action potentials depend upon the permeability of the cell membrane to sodium and potassium ions. Transient changes in conductance for different ions alter the membrane voltage required to initiate, sustain, and terminate action potentials. At resting potential, some potassium leak channels are open but the voltage-gated sodium channels are closed. Even though zero net current flows, potassium moves across the membrane. This pulls the resting potential close to the equilibrium potential of potassium. A local membrane depolarization from an excitatory stimulus causes some sodium channels in the neuronal membrane to open. Sodium ions diffuse in through the channels along their electrochemical gradient, and, being positively charged, they begin to reverse the voltage inside the membrane from negative to positive. (1, 72-74, 78, 91-93, 95, 97)

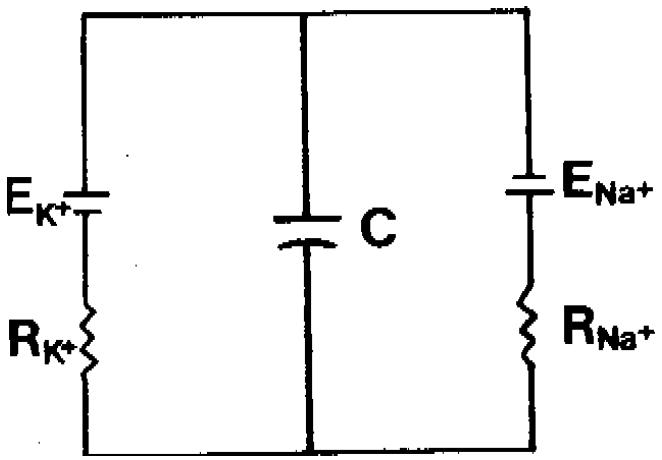

Figure 2-1. Electric circuit model of an excitable membrane. (107)

As sodium ions enter and the membrane voltage becomes less negative, more sodium channels open. This causes an even greater influx of sodium ions and, in turn, the sodium current overtakes the potassium leak current. Thus, the membrane voltage goes positive inside. When membrane voltage has peaked at around +30 mV, voltage-sensitive inactivation gates on the sodium channels have already begun closing. This prevents further influx of sodium ions. Simultaneously, voltage-sensitive activation gates on the potassium channels begin opening. (1, 67-69, 73, 86-88, 90, 92)

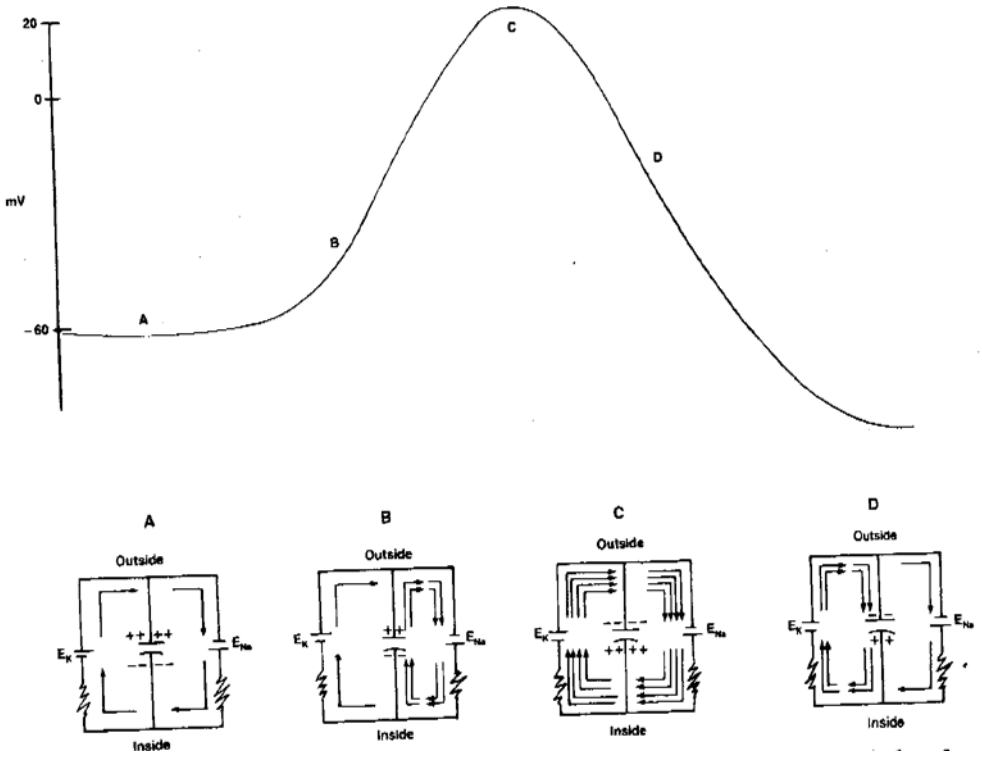

Figure 2-2. **A.** A schematic view of an idealized action potential illustrates its various phases as the action potential passes a point on a cell membrane. **B.** Figures A-D give current flow direction in the membrane for each phase. (107)

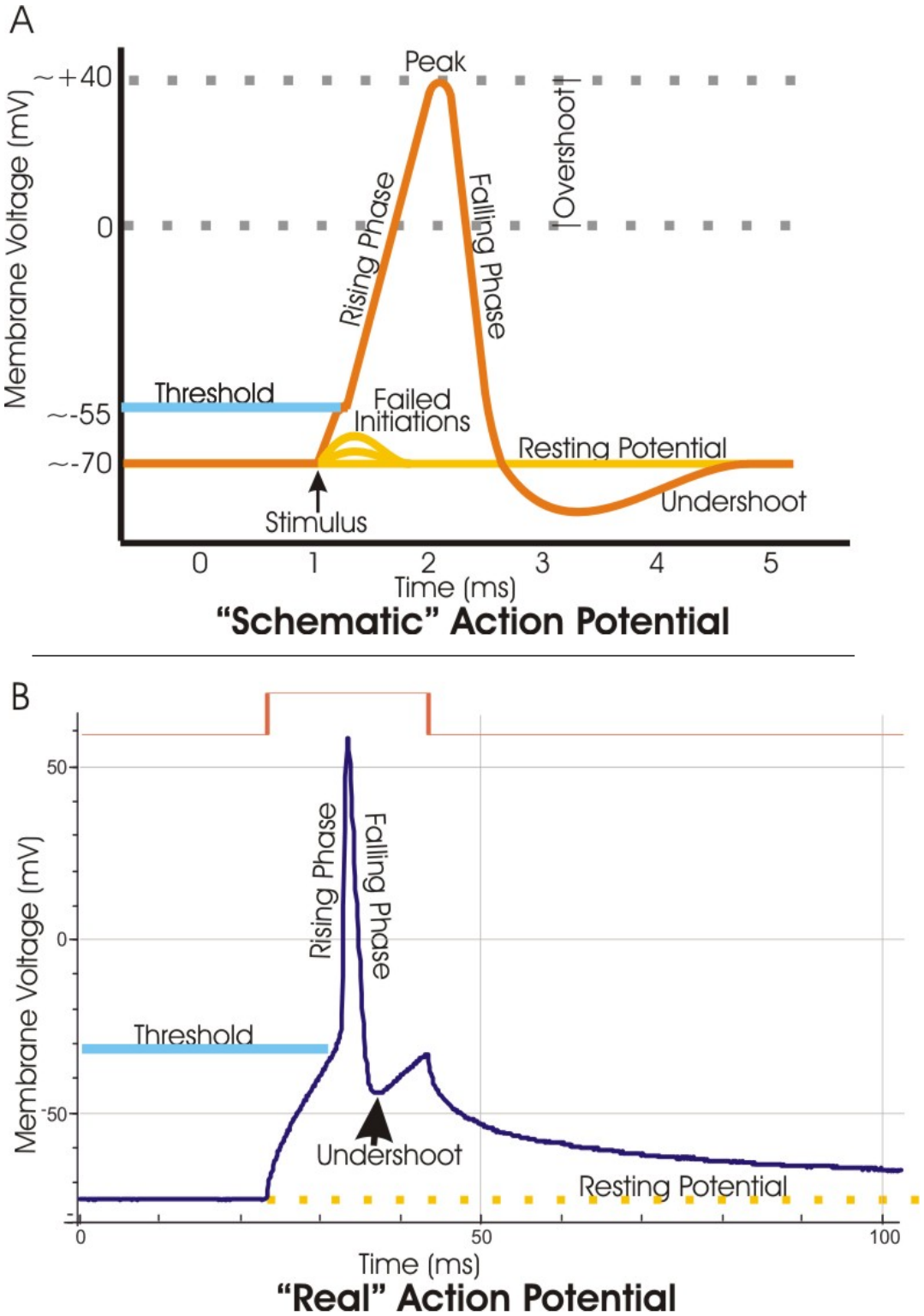

Figure 2-3. Action potential, schematic and real. (1, 73)

As the potassium channels open, a large amount of potassium ions are driven outward by the potassium concentration gradient. As potassium ions diffuse out, this reverses the membrane voltage to negative inside the membrane. Thus, the neuron is repolarized. Closure of the potassium channels is thus dependent on voltage as well as time. The resulting repolarization of the membrane elicits potassium channel closure. Yet, these channels do not instantaneously close due to membrane voltage. Instead, the delayed rectifier potassium channels have a lagging response. As a result, potassium ions continue flowing out of the cell even after repolarization. Hence, the membrane voltage falls below the normal baseline value for an instant. This is known as undershoot. (1, 72-74, 78, 91-93, 95, 97, 107)

Action potentials are triggered when an initial depolarization reaches the threshold voltage. This threshold is approximately 15 millivolts more positive than the resting membrane voltage of the cell. It is reached when the inward sodium current is greater than the outward potassium current. The net influx of positive charges depolarizes the membrane. This causes more sodium channels to open and greater inward current to flow in a positive-feedback loop that highly depolarizes the membrane. (1, 72-74, 78, 91-93, 95, 97, 107)

Threshold for action potential can be shifted by varying the balance between sodium and potassium currents. For example, if some of the sodium channels are inactivated, then a given level of depolarization, fewer sodium channels will open and larger depolarizations will be needed to elicit action potentials. This is known as the refractory period. (1, 72-74, 78, 91-93, 95, 97)

Nevertheless, the action potential threshold is often confused with the "threshold" of sodium channel opening. This is not correct. Since sodium channels have no threshold, they open stochastically upon depolarization, which does not actually open the channel. Rather, it increases the probability of a channel opening. Even in hyperpolarization, a sodium channel will still sometimes open. Moreover, the action potential threshold is not identical to the voltage at which sodium current has influence. The action potential threshold is the point where it exceeds the potassium current. (1, 72-74, 78, 91-93, 95, 97)

Cell membranes that contain ion channels can be modeled as passive RC circuits to better understand the propagation of action potentials in biological membranes. In such a circuit, the resistor represents membrane ion channels, while the capacitor models the insulating lipid membrane. Variable resistors are used for voltage-gated ion channels, as their resistance changes with voltage. A fixed resistor represents the potassium leak channels that maintain membrane resting potential. The sodium and potassium gradients across the membrane are modeled as voltage sources. (1, 95, 97, 107)

Current flow in an axon can be quantitatively represented by cable theory and, by extension, the compartmental model. In simple cable theory, the neuron is connoted as an electrically passive, coaxial cable. It is modeled with the following partial differential equation known as the cable equation. (1).

$$\mathrm{T}V_t = \lambda^2 V_{xx} - V \qquad (2\text{-}1)$$

where V(x, t) is the voltage across the membrane at a time t and a position x on the axonal longitude, and where λ and t are the characteristic scales of length and time on which the voltage decays in response to an input stimulus. Based on Figure 2-4, these scales can be calculated from the impedances per unit length.

$$T = r_m c_m \tag{2-2}$$

$$\lambda = \left(\frac{r_m}{r_l}\right)^{\frac{1}{2}} \tag{2-3}$$

These dimensional metrics explain the relationship between the conduction velocity and the diameter of the neuron in unmyelinated fibers. For example, the time-scale grows larger with both the membrane resistance r_m and capacitance c_m. By Q=CV, increase in capacitance requires additional charge be transferred to elicit a given voltage across the membrane. However, increase in resistance means that less charge is transferred per unit time. This retards equilibration. Moreover, if the lengthwise internal resistance r_l is less, because its radius is larger, in one axon than in another, the spatial decay length λ increases and the propagation velocity of an action potential should increase. If the resistance across the membrane r_m increases, that decreases the mean "leakage" transmembrane current. This, in turn, causes λ to lengthen and increases the action potential velocity of conduction. (1) Hence, propagating action potentials can be modeled by joining several RC circuits, each one representing a patch of membrane.

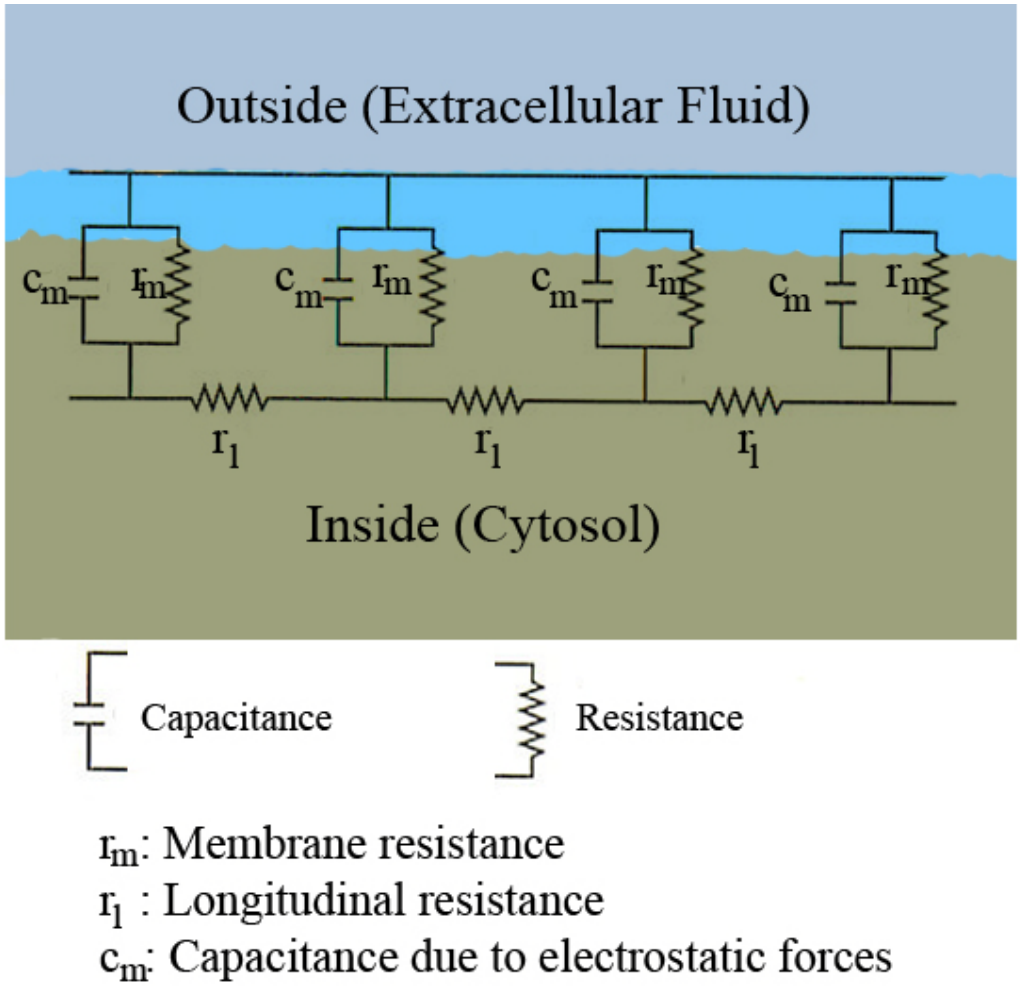

Figure 2-4. Schematic overview of the cable theory view of a piece of neuronal fiber. When an electrical current is moving along the inside of a fiber the cytosol exerts a resistance (r_l). Simultaneously current will escape through the phospholipid bilayer (with resistance r_m) to the outside; and due to electrostatic forces a buildup of charge (c_m) will take place along the bilayer. (1)

In unmyelinated axons, action potentials propagate as an interaction between passively spreading membrane depolarization and electrically active sodium channels. When one area of membrane is depolarized enough to open

its sodium channels, sodium ions go into the cell via facilitated diffusion. Positively-charged sodium ions then electrostatically repel adjacent ions down the axon and attract negative ions away from the apposing membrane. The process replicates with an action potential regenerated at each segment of axonal membrane. (1, 72-74, 78, 91-93, 95, 97)

Action potentials propagate faster in larger-diameter axons, with other things being equal, at speed of 10-100 m/s. The primary reason for this is that the axial resistance of the axon lumen is lower in larger diameters. This is due to an increase in the ratio of cross-sectional area to membrane surface area. As the membrane surface area is the main propagation impedance in an unmyelinated axon, increasing this ratio is an efficient way of increasing conduction speed. (1, 72-74, 78, 91-93)

In myelinated axons, saltatory conduction is how an action potential apparently jumps down the axon via the nodes of Ranvier. Saltatory conduction increases nerve conduction velocity while maintaining relatively constant axon diameter and has played an important role in the evolution of larger and more complex organisms. Examples are humans and other mammals, whose nervous systems must rapidly transmit information across relatively great distances. Without saltatory conduction, conduction velocity would require substantial axonal diameters. This would result in organisms that have nervous systems which are too large for their bodies. (1, 25, 78, 91-93, 95, 97)

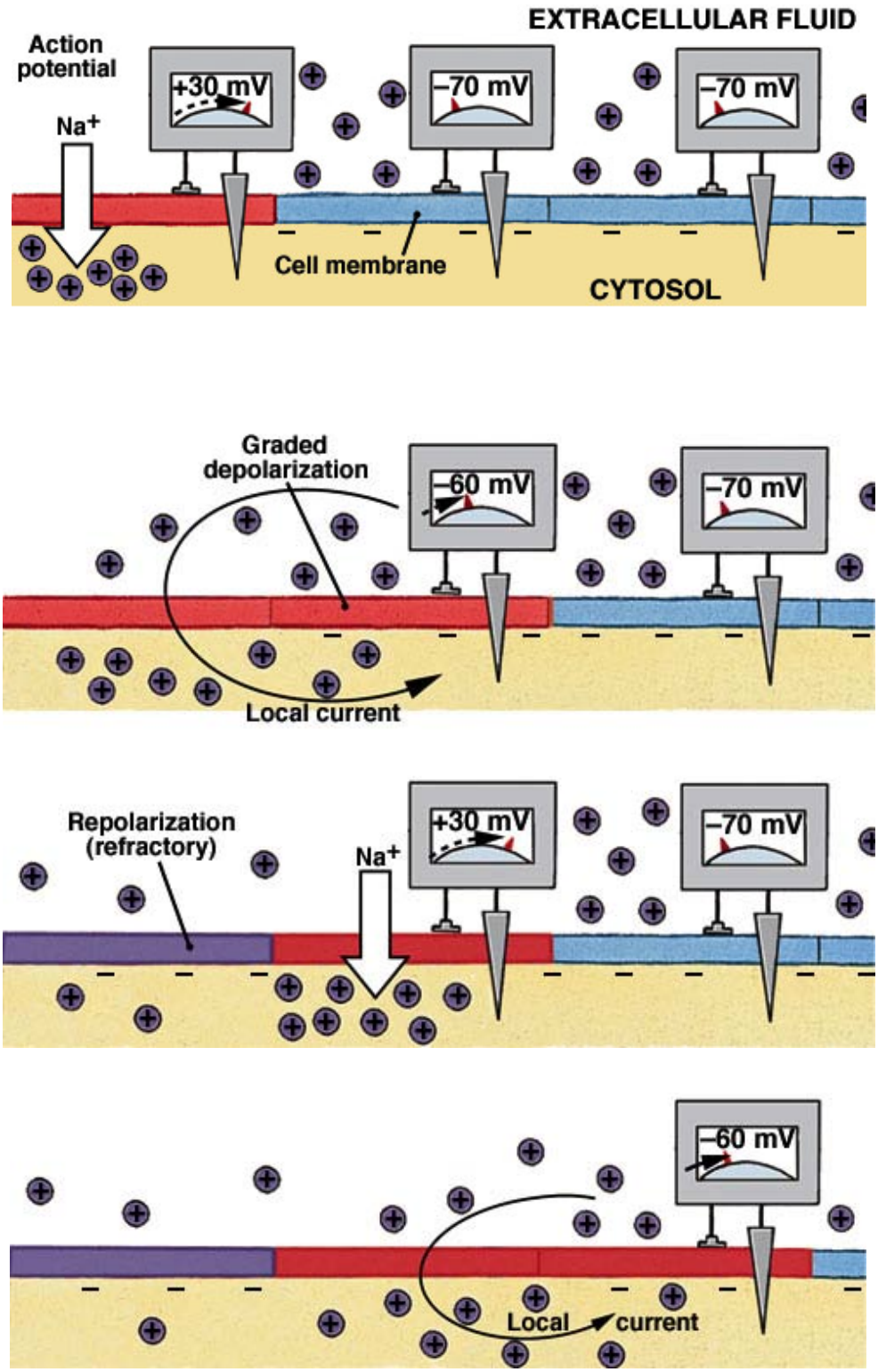

Figure 2-5. Continuous propagation of an action potential in an unmyelinated axon. (1, 97)

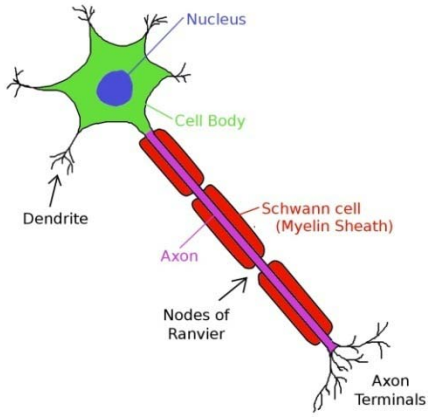

Figure 2-6. Model of saltatory conduction in a myelinated axon. (1, 97)

The main impedance in unmyelinated axons is membrane capacitance. In an electric circuit, the impedance of a capacitor can be decreased by decreasing the cross-sectional area of its plates, or by increasing the distance between plates. The nervous system primarily uses myelin to decrease membrane impedance. Myelin is an insulating sheath wrapped around axons by Schwann cells and oligodendrocytes. These wrap around the axon and decrease impedance by moving the intracellular compartmental fluids farther apart. (1, 25, 95, 97, 107)

The resulting insulation allows the essentially instantaneous conduction of ions through a myelinated segment of axon, but prevents the regeneration of action potentials through those segments. Action potentials are only regenerated at the unmyelinated nodes of Ranvier. Myriad sodium channels on these bare segments allow action potentials to be efficiently regenerated at those points. As a consequence of myelination, the insulated portion of the axon behaves like a

coaxial cable. The axon conducts action potentials rapidly because its membrane capacitance is low. This minimizes action potential degradation because of high membrane resistance. When this passively propagated signal reaches a node of Ranvier, it initiates an action potential and repeats the cycle. (1, 72-74, 78, 91-93, 95, 97)

The length of myelinated segments of axon is important to saltatory conduction. Axons should be as long as possible to maximize the passive conduction speed, but not so long that the decay of the passive signal is too great to reach threshold at the next node of Ranvier. In reality, myelinated segments are long enough for the passively propagated signal to travel for at least two nodes while retaining enough magnitude to fire an action potential at the second or third node. Thus, the safety factor of saltatory conduction is high by allowing transmission to bypass injured nodes. (1, 25, 73, 88)

When a membrane has undergone an action potential, a refractory period follows. Thus, although the passive transmission of action potentials across myelinated segments would suggest that action potentials propagate in either direction, most action potentials travel unidirectionally because the node behind the propagating action potential is refractory. This period arises primarily because of the voltage-dependent inactivation of sodium channels (73, 87-88). In addition to the voltage-dependent opening of sodium channels, these channels are also inactivated in a voltage-dependent manner. Immediately after an action potential, during the absolute refractory period, virtually all sodium channels are inactivated and thus it is impossible to fire another action potential in that

segment of membrane. With time, sodium channels are reactivated in a stochastic manner. As they become available, it becomes possible to fire an action potential, albeit one with a much higher threshold. This is the relative refractory period and together with the absolute refractory period, lasts approximately five milliseconds. (1, 78, 92, 93)

An action potential proceeding along a membrane is prevented from reversing its direction by the refractory period, and will eventually depolarize the entire cell. When the action potential reaches an area where all the cell membrane is already depolarized or still in the refractory period, the action potential can no longer propagate. Because an action potential propagates only along contiguous membrane, another mechanism is necessary to transmit action potentials between cells. Neurons communicate with each other at a chemical synapse. Other cell types, such as cardiac muscle cells, can communicate action potentials via electrical synapses. (1, 78)

The synapse is a very small gap between neurons that allows one-way communication. As the presynaptic neuron undergoes an action potential, voltage-sensitive calcium channels open and cause the release of neurotransmitters into the synapse. These chemical transmitters can initiate an action potential in the postsynaptic neuron, allowing communication between neurons. Some neurotransmitters inhibit action potentials, and the interaction of excitatory and inhibitory signals allows complex modulation of signals in the nervous system. (1, 72, 78)

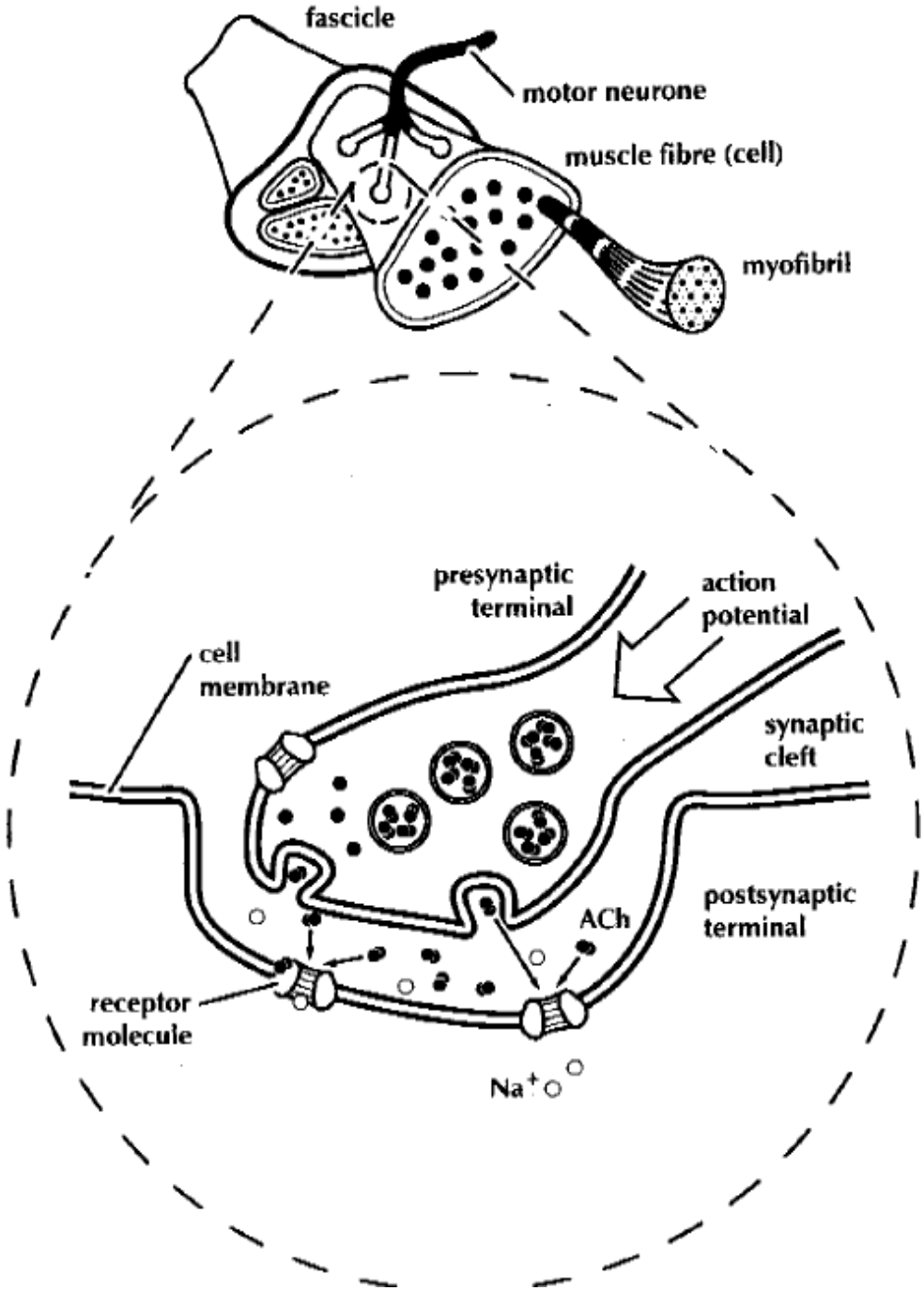

Figure 2-7. Schematic of motoneuron and neuromuscular junction. (64)

Three important concepts are derived from the description of the action potential. First, an ionic current always flows from a region of greater

concentration to a region of lesser concentration. These currents are always inward for Na and outward for K. Second, the membrane voltage only varies when there is a capacitive current. When the capacitive current is outward, the membrane depolarizes. When the capacitive current is inward, the membrane hyperpolarizes. Finally, extending Kirchhoff's current law says that all currents flow in complete circuits with the total current across the membrane at any given time is equal to zero. (1, 72, 107) In addition, a crucial implication of action potential generation lies on the fact that the membrane can only be excited when an outward capacitive current is elicited. Clinically, according to Kukulka, "the purpose of the electrical stimulus is to induce an outward capacitive current." (107)

As an electric current is given to a peripheral nerve, the initial depolarization occurs at the cathode. This is because an outward capacitive current is elicited at this site. If the excitation is of sufficient amplitude, a subsequent inward sodium current combined with the outward capacitive current generates the action potential. When an action potential arises in a peripheral nerve, it will propagate bidirectionally with respect to the spinal cord. (72, 78, 106) Ionic currents generated at a synapse produce a change in the electric potential of the postsynaptic nerve or muscle cell. If this change in potential is of large enough to make the resting voltage less negative, an action potential will be arise in the postsynaptic neuron or muscle fiber. (1, 72, 78, 92, 93, 102)

From a clinical point of view, nevertheless, the recruitment of motoneurons by electrical stimulation applied cutaneously cannot be predicted in terms of the

size of motoneurons and types of motor units excited. According to Kukulka (107), treatment goals can only be defined in general, qualitative terms based on observing the quality and quantity of the elicited muscle contraction rather than the selective excitation of one fiber type over another.

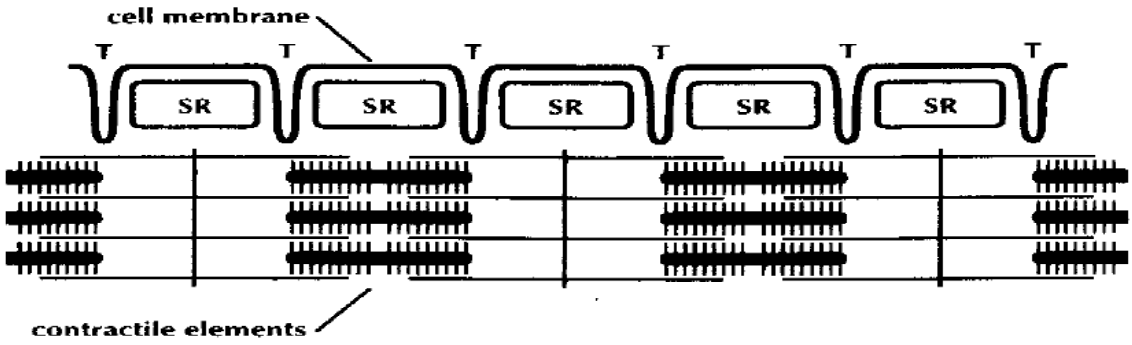

Figure 2-8. Schematic of T-tubules with the SR and the contractile machinery. (64)

In skeletal muscle, an action potential propagates down the T-tubule and causes a voltage-gated change in the dihydropyridine (DHP) receptor modulates the ryanodine (RYA) channel. This releases Ca^{2+} from the sarcoplasmic reticulum (SR). Soluble molecules such as ATP, Ca^{2+}, and reactive oxygen species, as well as calmodulin, modulate the SR calcium-releasing ryanodine channel as well as the phosphorylation reactions that occur post-translationally. Finally, the enzyme sarco(endo)plasmic calcium-ATPase (SERCA) pumps Ca^{2+} back into the sarcoplasmic reticulum to complete the chemical cycle. (72, 123, 165, 175)

It has been found that the frequency of the chemical cycle described above varies according to the size of the neuron from which an action potential is generated. Henneman and Olson (76) found that small motoneurons fire more readily than motoneurons that are large. Thus, small motoneurons have greater firing frequencies than do large cells. As a result, the small motor units with which they connect are more heavily activated with respect to larger units. This relationship is generally believed to vary inversely with size. In their 1965 paper, Henneman and Olson (76) discuss usage in the following manner.

> "Usage is the link which connects the apparently unrelated properties of size and speed in a meaningful way. Since units of small size are often used intensely and for prolonged periods, they must of necessity consist of muscle fibers which function economically and are not subject to fatigue. They must always be ready to respond despite a preceding period of prolonged activity. Rapidly contracting pale fibers cannot meet these requirements, as we have shown. Slowly contracting red fibers have the appropriate resistance to fatigue. Hence, the small size of a unit, which implies heavy usage, necessarily specifies red fibers and these, in turn, are slowly contracting."

2.2 Calcium channels and motor unit physiology

Voltage-gated Ca^{2+} channels modulate calcium diffusion into cells upon membrane depolarization. Electrophysiological studies have revealed different calcium currents, designated L-, N-, P-, Q-, R-, and T-type. The high-voltage-activated Ca^{2+} channels are complexes of a pore-forming S1 subunit of about 190–250 kDa; a transmembrane disulfide-linked complex of S2 and S3 subunits; an intracellular d subunit; and in some cases a transmembrane S4 subunit. The Cav_1 family of S1 subunits conducts L-type calcium currents. These currents initiate muscle contraction, endocrine secretion, and gene transcription. They are

controlled mainly by phosphorylation pathways that involve second messenger-activated proteins. Meanwhile, the Cav_2 family of subunits conducts N-type, P/Q-type, and R-type calcium currents. These initiate rapid synaptic transmission and are modulated mainly by direct interaction with membrane proteins. Finally, the Cav_3 family of subunits conducts T-type calcium currents. These currents are found in cardiac cells. They are transmitted more rapidly and at more negative membrane voltages than other calcium current types. (32)

All calcium channels share general structural characteristics. Each domain of the principal subunits is composed of six transmembrane helices (S1 through S6) and a membrane-bound loop between S5 and S6. The S4 segments function as the voltage sensors for activation. These move outward and rotate in the presence of the electric field and initiate a steric change that opens the pore. The S5 and S6 segments and the membrane-bound loop between them form the pore lining of the channels. The narrow outer pore is lined by the loop, which contains a pair of glutamate residues in each domain that are necessary for divalent calcium selectivity. The S6 segments line the inner pore. Especially for the L-type channels, these segments form the receptor sites for the pore-blocking Ca^{2+} antagonist drugs. (32)

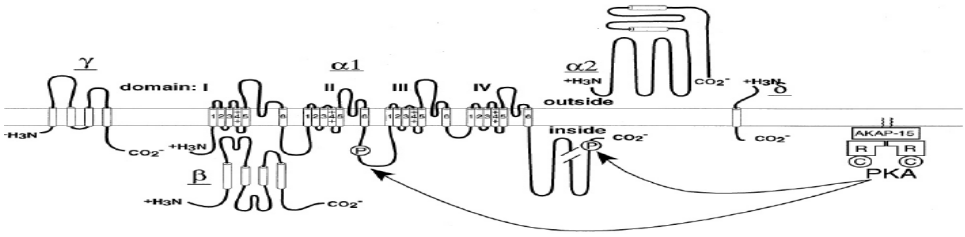

Figure 2-9. Structure and feedback loop of Ca_{v1} channel.

In skeletal muscle, single twitches do not need free calcium and excitation-contraction coupling is thought to occur directly by protein-protein interactions between the dihydropyridine-dependent voltage-gated Ca^{2+} channel in the transverse tubules and the ryanodine-dependent Ca^{2+} release channel (RyR) in the sarcoplasmic reticulum. Contractile force increases by high-frequency synaptic transmission from motor nerves as well as by adrenaline and calcitonin gene-related peptide (CGRP) via the cAMP signaling pathway. These effects do require extracellular calcium and thus are somewhat modulated by variations in Ca^{2+} influx. Phosphorylation by cAMP-dependent protein kinase enhances activation of the L-type currents. Repetitive depolarization dramatically enhances Ca^{2+} currents in the critical membrane voltage range near -20 millivolts and is strongly voltage-and kinase-dependent. This may be due to the interaction between voltage gating and phosphorylation of the calcium channel itself. It is suggested that this regulatory mechanism markedly elevates Ca^{2+} channel activity during tetanic or high-frequency stimulation of skeletal muscle cells. (32)

In excitation-contraction, conformational coupling is regulated by the intracellular loop joining domains II and III of the S1 subunit. Depolarization of the transverse tubules by the propagating action potential activates $Cav_{1.1}$ channels. These channels quickly turn on the ryanodine-sensitive calcium release channel via protein-protein interactions to commence Ca^{2+} release and muscle contraction. However, the channels slowly initiate their own calcium conductance activity which maintains calcium homeostasis by facilitating entry of the ion into the cytoplasm. Recent experiments have shown that the ryanodine-sensitive

calcium release channel must not only be present but also bind to domains II and III for the transverse tubule $Cav_{1.1}$ channel to function normally. (32, 123)

Ryanodine receptors in the SR of skeletal and cardiac muscle are vital in excitation-contraction coupling. However, the channels are also present in the endoplasmic reticulum of nervous and immune tissues. In all tissues, three highly homologous isoforms of ryanodine receptor have been identified as very large homotetrameric proteins of about 2 MDa. These isoforms contain large regulatory domains and are always associated with channel modulators such as calmodulin and immunophilins. It has been found that the type 1 isoform in skeletal muscle is electromechanically coupled to surface membrane voltage sensors. However, the other two isoforms have been found to be activated by other ligands, including divalent calcium itself, as well as endogenous second messengers. (172)

All muscle fibers use calcium for regulation and signaling. As a result, contractile characteristics of muscle fibers depend on the different proteins involved in that process. The diversity of the main proteins of the calcium cycle primarily determines these characteristics. The calcium signaling apparatus is comprised of the ryanodine receptor that is the SR calcium release channel, the troponin protein complex that modulates the effect of $Ca^{2=}$ to the contractile myofibrillar structures, the pump responsible for SR calcium reuptake, and calsequestrin, the protein that stores calcium in the SR. In addition, myriad Ca^{2+}-binding proteins is present in muscle tissue. Parvalbumin, calmodulin, S100 proteins, annexins, sorcin, myosin light chains, beta-actinin, calcineurin, and

calpain may play crucial roles in calcium-modulated muscle contraction under specific conditions. Or, they may control other activities such as protein metabolism and growth. (12)

Regulation of contraction and relaxation by divalent calcium in different muscle types occurs by three major mechanisms. The first discovered and best described mechanism is the troponin-tropomyosin system attributed to the actin filaments, which is restricted to skeletal and cardiac muscles. The second mechanism is found in vertebrate smooth muscle in which calcium, in conjunction with calmodulin (CaM), activates myosin light-chain kinase. In turn, the phosphorylation of the myosin initiates muscle contraction. The third mechanism is found in invertebrates and consists of direct calcium-myosin binding. This system is regulated by light-chain myosin. In each muscle type, nevertheless, velocity of contraction and other physiological parameters very much depend on the structure of its specific calcium handling system. (12)

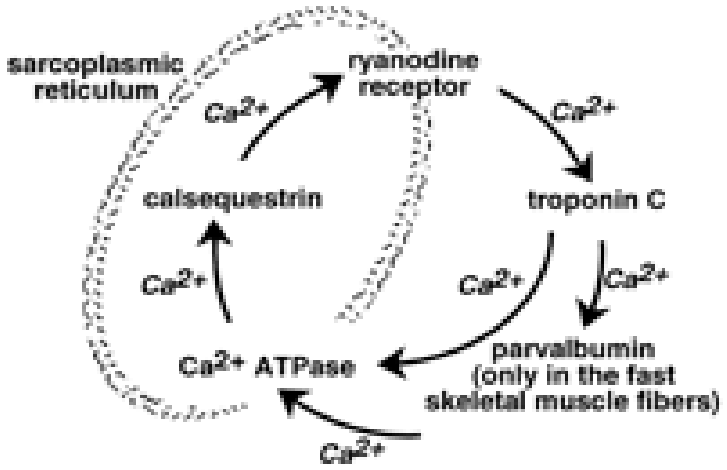

Figure 2-10. Calcium cycle. (12)

At rest, myofibrillar calcium concentrations in the cytosol are maintained at approximately 50 nM. The calcium cycle begins with a depolarization of the surface membrane and t-tubule. This releases Ca^{2+} from the SR via the RyR and elevates cytosolic Ca^{2+} locally about 100-fold. The electrochemical signal transduction at the t-tubule membrane occurs via structural changes of the dihydropyridine receptor (DHPR) that are charge-dependent. In turn, Ca^{2+} binds in a fast reaction to one of the troponins on the thin filament and activates muscle contraction. (12, 123)

It is known that when a muscle is activated and the generated force increases, the motor units that comprise the muscle activate in a set sequence. The mechanisms that facilitate this phenomenon include motoneuron size, the synaptic organization of inputs to the motoneuron, and the physical properties of the neuronal membrane. Orderly recruitment of motoneurons occurs in a sequence that progresses from low- to high-threshold units. (76, 77, 157)

Motor units can be described via a quadripartite classification scheme, based on fatigability and unfused tetanus. The four types of motoneurons are slow contracting (S), fast contracting and fatigue resistant (FR), fast contracting and intermediate fatigability, (F_{int}), and fast contracting and fatigable (FF). Any measurement of a motor unit property would show that parameter values would distribute along a continuum. However, when several parameters are considered aggregately, motor units cluster into four separate groups. From the "concept of orderly recruitment", S-type motor units are recruited first and FF-type motor

units are recruited last. However, in voluntary muscle activation, there is substantial overlap between motor unit types activated. (63, 76, 157)

When muscle is electrically stimulated, the recruitment of motor units is quite distinct from voluntary activation. Electrically activating a muscle with an nonparalyzed nerve supply stimulates the intramuscular branches of the nerve. It does not, however, result in direct activation of the muscle fibers. This is because nerve branches are more excitable than muscle fibers. When nerves are stimulated, the elicited action potentials propagate bidirectionally along the axon, transmit across neuromuscular junctions, and then propagate along the muscle fibers to activate the contractile mechanisms. Hence, electrical activation of a muscle does not bypass an nonparalyzed peripheral nerve supply. The order of motor unit recruitment via electrical stimulation depends on the motor axon diameter, the distance from axon to active electrode, and the cutaneous afferent inputs to the motoneuron that have been elicited from the artificial signal. These three factors induce an order of recruitment during electrical stimulation that is vastly different than natural activation of a muscle. (63, 76, 77, 157)

2.3 Skeletal muscle contraction

Cells of skeletal muscle are activated by acetylcholine, which is a neurotransmitter that is released at neuromuscular junctions by motoneurons. Upon activation, the sarcoplasmic reticulum release divalent calcium which induces muscular contraction by way of the sliding filament mechanism which is driven by adenosine triphosphate (ATP). The ATP is produced by metabolizing creatine phosphate and glucose within the muscle cells by mitochondria, as well

as by metabolizing humoral fatty acids. Each motoneuron regulates a group of muscle cells, and the grouping is known as a motor unit. Recruitment of additional units occurs when more strength is required than can be garnered from a single motor unit and superposes via spatial summation. No further increase in contraction strength occurs once all motor units are recruited. To increase the contraction strength, the frequency of neuronal firing must be increased. This yields tetanic contraction and superposes temporally. (1, 73)

All muscle cells are comprised of myosin and filaments in series. The fundamental unit of organization of these filaments in cardiac and skeletal muscle cells is the sarcomere. A sarcomere is composed of a central bidirectional myosin filament flanked on both sides by two actin filaments which are oriented in opposite directions. When each end of the myosin filament ratchets along the overlapping actin filament, the two thin filaments move closer together. Thus, the sarcomere has its ends drawn in shortens. Sarcomeres are connected to each other by 'Z lines'. These structures fix the ends of thin filaments such that the filaments point in opposite directions on each side of the Z line which permits sarcomeres to be in series. In muscle fiber contraction, all sarcomeres contract together so that summated force is transmitted to the ends of the fiber. (1, 73)

If movement continued indefinitely, all muscles would be in constant contraction. To prevent that, the body must modulate myosin-actin binding which is achieved through myoplasmic divalent calcium. When the muscle is at rest, the tropomyosin/troponin complex that is wrapped around the actin filaments sterically hinders the myosin from binding to actin. When calcium diffuses into the

myoplasm, the divalent ions bind to troponin ad induces a conformational change. The conformational change causes tropomyosin to move as well and exposes the binding sites on actin. Then, myosin binds to the exposed binding sites and the muscle contracts. (1, 73)

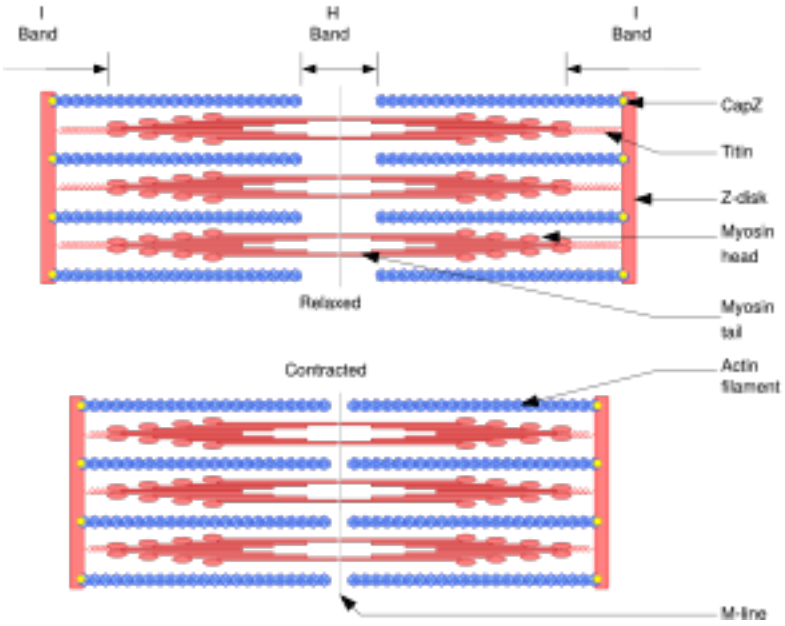

Figure 2-11. Depiction of the contraction of a muscle through the overlap of thick and thin filament fibers. (1, 73)

2.4 Muscle fatigue: truth and fiction

In common usage, the word “fatigue’’ is used to denote reduction in mental or physical performance. However, in biology, the word has a more specific physiologic meaning. *Muscle fatigue* is denoted as the “failure to maintain the required or expected force” (62). Central and peripheral motor elements may modulate muscle fatigue. The rate of fatigue depends on the

muscles employed and the duration of the contractions. Generally, about 50% of muscle force can be lost in the first sixty seconds of a maximal contraction. This definition of fatigue is adequate to distinguish fatigue from *weakness.* In weakness, there is lack of ability to generate an initial force appropriate to a situation. When needed, the denotation of muscle fatigue can broaden to include a lack of capacity to sustain rapidly executed movements such as tapping the fingers as fast as possible. In this kind of fatigue, it is possible that the crucial component is a decrease in the magnitude of the motor commands generated in the supraspinal system. (130)

The central nervous system components that may be varied in muscle fatigue include the psychoemotional factors that modulate the sense of *effort,* as well as the various descending motor pathways and connections in the medulla, pons, midbrain, and spinal cord. It has long been known that the descending motor pathways include the corticospinal, rubrospinal, tectospinal, vestibulospinal, and reticulospinal tracts. In addition, the topographic map of movements in M1 is worked out. However, virtually nothing is known about the identities of the neurons that generate the desire to move or assess effort. Yet, the peripheral elements of muscle fatigue include impulse conduction in the motoneurons and muscle fibers, neuromuscular transmission, excitation-contraction coupling, and the process of muscle contraction itself. In typical individuals, fatigue can arise from interplay between peripheral elements. (128-130)

Traditionally, muscle fatigue has been explained by production of lactic acid and the formation of the salt sodium lactate. It has been reasoned that if the rate of lactate production is high enough, the cellular protons are released in excess and decreases in cellular pH. This sequence of biochemical events has been termed lactic acidosis and has been a classic explanation of the biochemistry of muscle acidosis for almost a century. This has yielded the inference that lactate production causes acidosis and, in turn, muscle fatigue during intense stimulation. Yet, clear evidence shows no biochemical basis for lactate production causing acidosis. Instead, it has been shown that lactate production retards acidosis and, furthermore, ample evidence shows that acidosis is caused by other reactions. Each molecule of ATP hydrolyzes ADP and P_i and releases a proton. When the ATP demand of steady-state muscle contraction is filled by mitochondrial respiration, protons are used for oxidative phosphorylation and to maintain the proton gradient in the intermembranous space without accumulation. However, when the intensity of stimulation increases well beyond steady state, there is greater demand ATP regeneration from the glycolysis-phosphagen system which increases release of protons and causes acidosis. Under these conditions, lactate production is increased to prevent accumulation of pyruvate and supply the NAD^+ ion required for the second phase of glycolysis. Indeed, if lactate was not produced in muscle during stimulation, acidosis and fatigue would onset much more rapidly and performance would drastically decrease. (159)

One of the early pioneers of the “lactic acidosis” concept was A. V. Hill who in 1922 who shared a Nobel prize with Otto Meyerhoff for work on the energetics of carbohydrate metabolism in skeletal muscle. In particular, Meyerhoff described most of the glycolytic pathway and showed lactic acid to be produced as a side reaction to anaerobic glycolysis. Meanwhile, Hill worked out the quantitative measure of the energy release from conversion of glucose to lactic acid. From that, he proposed that glucose oxidation in times of limited oxygen availability or great energetic demands supply a large amount of energy to drive muscle contraction very quickly. (159)

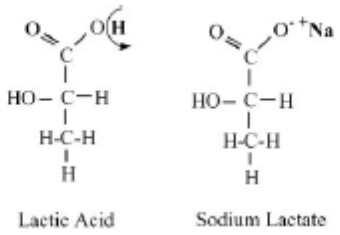

Figure 2-12. Chemical structures of lactic acid and sodium lactate. (112, 169)

According to Robargs (159), this pioneering work of Meyerhoff and Hill ingrained the idea relating lactic acid production and acidosis into the thinking of biochemists and physiologists. Hill elucidated the rationale for muscle to have a spontaneous and robust source for energy production to fuel high-frequency and high-magnitude muscle contractions. Meanwhile, Meyerhoff described the biochemical pathway that led to lactic acid production. There was immature contemporary understanding of acid-base chemistry to comprehend the

ionization of nontraditional acid molecules and there was also a lack of understanding of mitochondrial respiration to see its role in modulating proton balance in cells. At that time, the research in animals on the production of lactic acid from fermentation established the link between anaerobiosis, lactic acid production, and acidosis, which was assumed to be causal. More recent studies also accepted a cause-effect interpretation between decreases in blood or muscle pH with increases in lactate production. In order to bolster the argument for calcium current causing muscle fatigue, the lactic acid hypothesis as well as the biochemistry of glycolysis and acidosis must be understood. See Appendix D for the detailed biochemical mechanisms and pathways.

Instead of proton release, metabolic acidosis results from nonequilibration of the proton release rate and the proton buffering and removal rate. The biochemistry shows that H^+ release generates via the lysis of blood glucose and the hydrolysis ATP. However, there is no immediate increase in cellular acidity due to the capacity and structure of the proton buffering and removal system. The buffering system in the cell, including lactate production, binds protons to protect intracellular accumulation of H^+. Hydrogen ions are also removed from the cytoplasm via mitochondrial and sarcolemmal transport and a bicarbonate-dependent exchanger. Yet, in skeletal muscle, when the proton production rate is greater than the rate of proton buffering and removal, metabolic acidosis occurs. Remarkably, lactate production functions as a buffering system by consuming protons, as well as an H^+ remover by transporting protons across the sarcolemmal membrane, to shield the cell from metabolic acidosis. (112, 159)

In contrast, it has been found that, during repeated tetanic contraction, there was little or no pH decrease. However, failure of calcium release has been found to be a major contributor to muscle fatigue. Impaired calcium release from the SR has been identified as a factor in muscle fatigue in isolated fibers. Several possible mechanisms for impaired calcium release have been suggested. These include decreased action potential magnitude which could be caused by extracellular potassium accumulation. This may suppress voltage sensor activation. Also, decreased SR Ca^{2+} channel opening occurs due to the drop in cytoplasmic ATP and the elevated concentrations of divalent magnesium that arise during fatigue. It could be that decreased calcium available for release can occur if inorganic phosphate diffuses into the SR and precipitates with calcium into a salt. (2, 3, 4)

2.5 The human soleus

According to the 39th edition of Gray's Anatomy (173), the soleus is a broad flat muscle located immediately anterior to gastrocnemius. It originates from the posterior surface of the head and proximal quarter of the fibular shaft, the soleal line and the middle third of the medial tibial border, and from a band of fibers between the tibia and fibula that arches over neurovascular bundle. This is an aponeurotic origin. The origins of the vast majority of the muscle fibers arise from its posterior surface and pass obliquely to the tendon of insertion. Other muscle fibers take their origin from the anterior side of the aponeurosis. They are short, oblique and bipennate in arrangement. Convergence of these fibers occurs on a narrow tendon in the center of the muscle that merges distally with

the principal tendon. This principal tendon gradually thickens and narrows, joining the tendon of gastrocnemius. The result of the junction is the calcaneal tendon. The soleus is covered proximally by gastrocnemius. Yet, more distally the muscle is wider than the tendon of gastrocnemius and is accessible on both sides. Moreover, sometimes the soleus has an extra distal and medial part, with possible insertions into the calcaneal tendon, the calcaneus itself, or the fascial sheath that envelops the foot flexor muscles. Superficially, the soleal surface contacts with the gastrocnemius and the plantaris. Deeply, its surface contacts with flexor digitorum longus, flexor hallucis longus, tibialis posterior and the posterior tibial neurovascular bundle. The tibial nerves and vessels are separated from the muscle via deep transverse fascia of the leg. This is seen in Figures 2-13 and 2-14.

The soleus has two main arteries for its blood supply. The superior part branches from the popliteal artery approximately at the soleal arch. Meanwhile the inferior part branches from the proximal common peroneal artery or at times from the posterior tibial artery. Additionally, an auxiliary supply comes from the lateral sural, peroneal or posterior tibial arteries. Furthermore, an extensive venous plexus is located within the muscle belly. It has physiological importance as part of the muscle pump complex. From the aspect of pathology, it commonly is the site of origin for deep vein thromboses. Finally, the nerve supply of the soleus muscle comes from the two branches of the tibial nerve as well as S1 and S2. (174, 182)

Taken together, the gastrocnemius and soleus form a tripartite muscular

mass sharing the calcaneal tendon commonly called the triceps surae. These muscles are the primary plantarflexors of the foot. In addition, the gastrocnemius is also a knee flexor. The muscles of the triceps surae are typically large and powerful. However, each muscle has a distinct yet complementary function. The muscle that provides the force for propulsion in ambulation at all speeds is the gastrocnemius. Acting from its deep location, the soleus is more involved with steadying the leg and foot during standing. This role in posture is also implied by its high content of slow, fatigue-resistant muscle fibers. In many adult mammals, nevertheless, the soleus is almost exclusively composed of fibers of this type. However, such a rigid demarcation of the functions does not seem likely in the human. Nevertheless, in upright standing, the ankle joint is loose-packed. Since the weight of the body transmits along a vertical line that passes behind the ankle, a strong brace is required at that location to sustain joint stability. It has been shown by electromyography that these stabilizing forces are supplied primarily by the soleus. During bipedal human standing, soleus shows continuous activity. Meanwhile, gastrocnemius shows only occasional recruitment. (174, 182)

According to Henneman and Olson (76, 77), the soleus has all the properties which the gastrocnemius does not possess. Because the soleus has longer fibers arranged nearly parallel with the principal axis of the leg, more shortening of the muscle is possible. However, this increased range of shortening come at the expense of generated force. Furthermore the degree rubicund color of muscle fibers is associated with economy and fatigue resistance. These

properties are functionally essential in the soleus since the small diameter of its motoneurons results in heavy muscle usage.

The common assumption is that the segregation of different properties in soleus and gastrocnemius came about because of requirements which could not be accommodated by a single muscle. The power and speed vital for running and jumping demanded one muscle fiber arrangement. The capacity to shorten enough for the fullest possible range of ankle extension called for a very different arrangement. In response to the conflicting needs, separate heads designed for different purposes evolved as mutual mechanical complements. (76, 77)

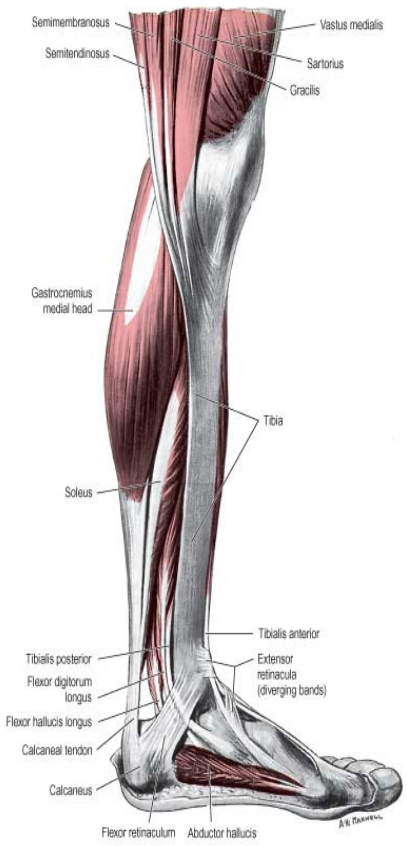

Figure 2-13. Medial view of muscles of the left leg. (174)

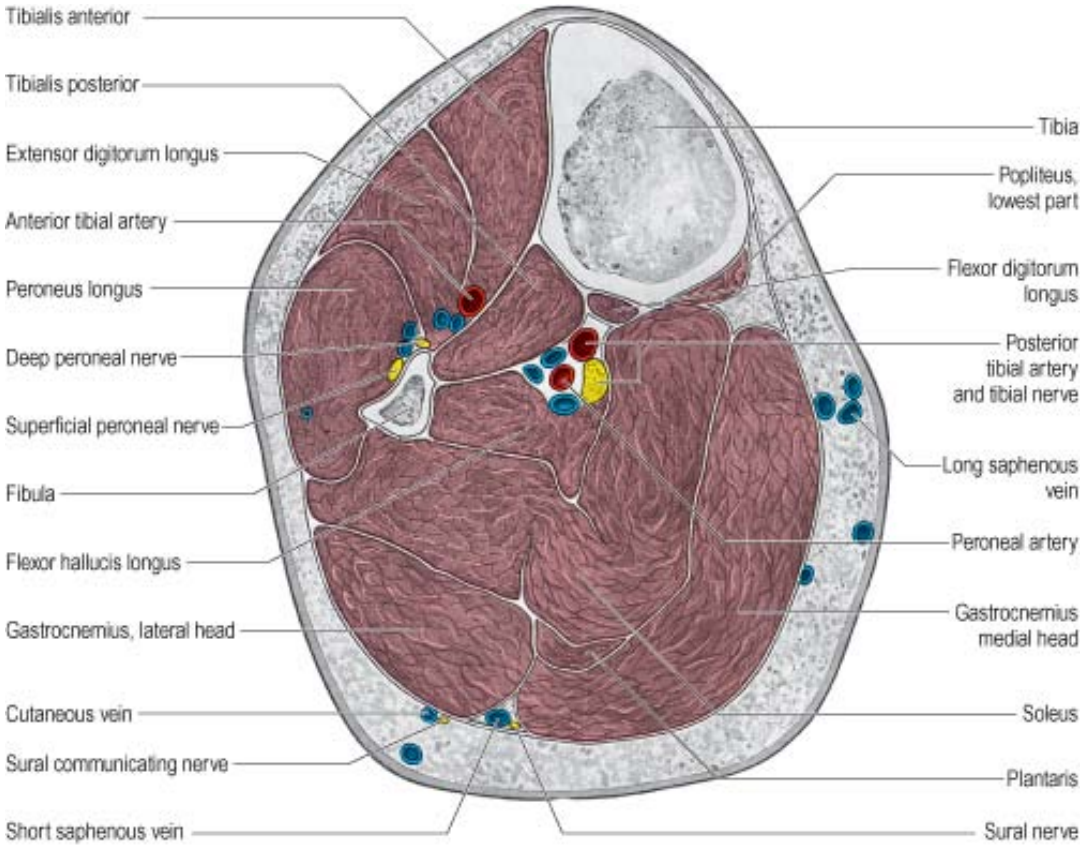

Figure 2-14. Axial section through the left leg approximately 10 cm below the knee joint. (174)

CHAPTER 3: CLINICAL ISSUES IN MUSCLE ELECTROSTIMULATION

3.1 Physiology of paralyzed muscle

Injury to the spine may result in a motor nerve being crushed or severed. Also, nerves may degenerate or inflame as part of a pathophysiological sequence. Whatever the etiology, nerve dysfunction has serious repercussions for both muscle fibers and motoneurons and their axons. After nerve transection or crush, the distal nerve stump continues to propagate action potentials for many hours. In rats, usually 24 hours elapse before electrical activity decrease and approximately 80 hours pass before all the axons lose excitability. In humans and other primates, impulse propagation may continue for up to 200 hours (128-130). When the axon starts to deteriorate, the process is denoted as Wallerian degeneration (128-130, 184). The nature of these degenerative changes has been confirmed with the electron microscope (189, 190).

3.1.1 Biological changes

Following spinal cord transection, according to Cummings (38), muscles undergo a number of physiologic, biochemical, and anatomic alterations. The muscle fibers atrophy, neuromuscular junctions degenerate, and membrane electrical properties are changed. Other pathologies include an increase in the subsarcolemmal nuclei and lysosomes, and a temporary increase in the synthesis of sarcoplasm and its reticulum. Also, contraction time is found to increase in paralyzed muscle, while the force generated by the contraction decreases. (167, 168)

Before injury occurs, the muscle has a constant supply of trophic substances from the motoneurons that ensure the physiologic integrity of its fibers. However, upper motor neuron lesion discontinues this trophic influence. Hence, the muscle fibers experience progressive deterioration until the fibers are reinnervated either by collateral axons from surviving motoneurons or by neurons regenerating over the lesion site (25, 123). It is widely believed that if reinnervation has not happened within two years post injury, then the contractile elements of the muscle will have transformed into fibrous connective tissue, thus making further recovery of function impossible. The most striking change observed following nerve lesion is the progressive muscular atrophy. Atrophy due to denervation is denoted by a decrease in the diameter of individual muscle fibers that leads to a decrease in muscle size. (25, 38)

Although profound muscular atrophy is the first visible change seen after spinal cord injury, according to Cummings (38) it is not the first change to occur. The first change reported following spinal cord injury is actually the partial gain in electric potential of the sarcolemma. As early as three hours following transection of a neuromuscular junction, the baseline resting potential of the sarcolemma (-80 mV) is found to be reduced by 1 to 2 mV. Following this, the resting potential decreases until approximately 24 hours after injury, it resets at about -65 mV. (38, 72)

The sarcolemmae of vertebrate skeletal muscle further change after spinal cord injury in other ways. One way is to develop sensitivity to acetylcholine (ACh) beyond the neuromuscular junction. Acetycholine sensitivity happens in

paralyzed muscle because the receptors for the neurotransmitter that normally present only in the motor endplate in intact muscle become incorporated into the whole of the sarcolemma after injury. It has been suggested that elevated acetylcholine sensitivity may in fact stimulate reinnervation. (1, 38, 76, 167)

According to Shields (171), with the typical homogeneity in fiber type and accessibility of its whole nerve to stimulation, the soleus muscle is “an ideal model” to increase understanding of the physiology that underlies force generation in paralyzed muscle. In the acute phase of injury, the paralyzed soleus muscle resists fatigue and maintains up to 80% of its pre-injury force generation after a series of fatigue-inducing contractions. However, in the chronic phase of injury (greater than 2 years), paralyzed soleus muscle an only generates about 25% of its pre-injury force after a fatigue series (168-171). These alterations in fatigability are thought to demonstrate, the measured conversion from a muscle with a predominance of slow Type I fibers (168) to a more fatigable muscle with primarily fast Type IIb fibers (30, 168). This transformation happens slowly during the first several years after a spinal cord injury. (168)

Recent evidence has shown that, at the microscopic levels, paralysis due to spinal cord injury yields muscle fiber hybrids that express heterogeneity of fast and slow properties (185). Previously, the common belief was that the soleus remains resistant to fatigue after upper motor neuron lesion, independent of other cellular conversions. This is because the cat soleus was shown to maintain a fatigue index of 0.93 one year after transection of the spinal cord. However,

more current longitudinal studies demonstrated that the spinally isolated cat soleus had indices of fatigue that range from 0.67 to 0.87 (190). In contrast, fatigue indices in the rat soleus have been respectively shown to be 0.66 and 0.50 at 3 and 6 months after transection of the spinal cord (184). These findings in other mammalian species were consistent with those in man (159-169). Yet, time after injury, fatigue-assessment method, techniques to transect the spinal cord, and species may play important roles in the dissimilarities that are observed in fatigue in paralyzed muscle. The discrepancies in post-paralysis management between wheelchair-using humans and caged quadrupeds use for experimentation may cause variations in overall muscle length, stiffness, and spasticity. All of these factors may affect plasticity in the neuromuscular system (47, 73, 77).

Post-injury changes in muscle fatigability and speed properties, neuromuscular transmission (33, 170), relationship between torque and frequency (170), low-frequency fatigue (33, 168, 170), effects of training (169, 170), and post-fatigue potentiation (171) support the opinion that chronically paralyzed soleus muscle in man has the physiology similar to that of a muscle composed of fast-fatigable Type IIb fibers.

Conversion of skeletal muscle from slow to fast leads to long duration muscle fatigue. Low-frequency fatigue (LFF), such as the chronically paralyzed fast soleus muscle has previously demonstrated (168, 170), occurs via a compromise in the excitation-contraction coupling mechanism. Commonly known as “uncoupling”, impaired release of calcium ions by the SR and a change

in the sensitivity of the calcium receptor have been suggested as contributors to LFF (115, 120, 191). In addition, myosin regulatory light chain (RLC) phosphorylation increases when fibers convert from slow to fast due to a reduction in use (20, 21). When activated continuously for a long period of time, fast skeletal muscle, becomes “uncoupled”. This is because fast skeletal muscle is specifically designed to act in a phasic manner. As the concentration of calcium ions decreases from repetitive activation, not as much free Ca^{2+} is available to phosphorylate myosin light chains. (2, 176)

3.1.2 Clinical sequelae

Chronic absence of upper motor neuron input in human muscle, usually due to spinal cord injury (SCI), elicits deleterious musculoskeletal adaptations, such as muscle paralysis and spasticity that adversely affect health in those who are injured. Increasingly, desired rehabilitation outcomes will require limb preservation which may be done via electrical stimulation of paralyzed muscle. However, few models predict fatigue in paralyzed muscle. The soleus muscle provides an ideal *in vivo* model of the effects of SCI on muscle properties, as it transforms from predominantly slow fiber type to that of fast-fatigable (FF) or type IIb fibers (72, 77, 164), which prolongs relaxation in the fatigued state. This is important since a close association between optimal frequency and contractility exists. (164)

Since spasticity is a major complication of spinal cord injury, giving a denotation of it would be prudent for this discussion. Lesions of premotor projections produce this specific form of increased muscle tone. In spasticity, the

leg extensor muscles and arm flexor muscles usually indicate this increase in muscle tone. It is associated with tendon jerks and hyperactivity of the stretch reflexes. Spasticity is commonly defined as measured resistance to the passive movement of the limb. Rapid movements elicit greater resistance than slow movements. Clonus may result from rapidly imposed movements. The reduced threshold of the monosynaptic stretch reflex comes from the increase in excitability of the reflex pathway. The weakness associated with spasticity in spinal cord injury results partially from the abnormal motor unit recruitment patterns. In patients with spasticity, measured resistance to passive limb movements may abruptly melt away. Known as the clasp knife phenomenon, the sudden decrease in force depends on muscle length and joint angle. This inhibitory process results from afferent nerve activation in the muscle itself, but not in the muscle spindle. (47, 73, 97)

In spastic gait, tension develops differently from that of normal gait and is seen to be independent of hyperactive monosynaptic stretch reflexes. Overactive stretch reflexes are correlated with an inhibition of polysynaptic reflexes that are essential to function. When supraspinal control of spinal reflexes is disrupted, the inhibition of monosynaptic reflexes is absent. Hence, in patients with spasticity, the overall muscle activity in the leg is decreased and less regulated. (47)

3.2 Engineering issues and therapeutic protocols

3.2.1 Physiologic constraints

According to Myklebust (145), constant current stimulators provide a current which flows at a constant amplitude, within a specified range of

impedance. As the impedance varies, the voltage varies to maintain the current at a constant level. Meanwhile, constant voltage stimulators provide a constant voltage source, within a specific impedance range. Thus, the current varies according to changes in impedance. In the majority of physiologic applications, therefore, a constant current source is favored over a constant voltage source. The impedance of the electrodes, of the biological material, and of the electrode-body interface may change during stimulation. However, with constant current stimulation, the changes in impedance do not change the current flowing through the biological tissues. It is the level of current which is responsible for the resultant physiologic effects. Hence, by using a constant current stimulator, the one can maintain better control of the physiologic response of the patient to electrical stimulation.

Furthermore, practical consequences may be deduced from the concepts of rheobase and chronaxie (1, 145). Rheobase is half the current that is required for the duration of chronaxie to elicit an action potential or muscle twitch. In mathematical neurophysiology, the chronaxie is the minimum time over which an electric current twice the strength of the rheobase needs to be applied, in order to stimulate a muscle fiber or neuron. (1, 42) Thus, a stimulus duration longer than the chronaxie is not desirable. This is because current consumption increases without decreasing the action potential threshold significantly. Also, smaller electrodes are more favorable because the pulse duration they require may be decreased without compromising patient safety. Hence, estimation of the safety

margin with decreasing output of the generator is possible if the chronaxie of a specific electrode is known. (94)

The inherent capacitance of living tissue is particularly relevant to the therapeutic administration of electricity. When a pulse of constant voltage is applied to the body, a large amount of current flows initially and charges the tissue capacitance. As the tissue charges, the current decreases to a steady state if the pulse duration is long enough. Because of the large initial current flow at the beginning of the pulse, the effective pulse duration may be smaller than the duration of the actual voltage pulse. However, when a pulse of constant current is given to the body, the transmitted current to the tissue does not change over time. Thus, the resulting voltage at the tissue rises rapidly because of current flow through the resistive portion of the electrode-tissue impedance. As the tissue capacitance increases, this results in a slow rise in voltage. (145)

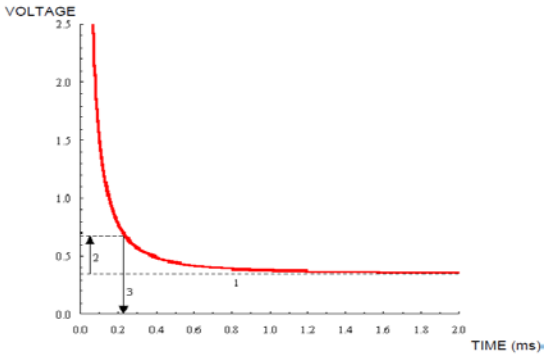

Figure 3-1. Determining rheobase and chronaxie from an asymptotic strength-duration curve. 1) The *rheobase* is the minimum input amplitude that will elicit a response. In this example, this value is 0.35 V. 2) Twice the rheobase is 0.7 V. 3) The *chronaxie* is the input duration that elicits a response when the input amplitude is exactly twice the rheobase. In this example, the chronaxie is 0.22 ms. (145)

3.2.2 Therapeutic inputs

Parameters of electrical stimulation for therapeutic applications are defined in terms of the stimulus waveform and its time-, frequency-, and amplitude-dependent characteristics. For therapeutic waveforms, clinicians frequently describe waveforms as either direct current, alternating current, or pulsed current. In this context, direct current is defined as the continuous unidirectional flow of charged particles in which the waveform properties remain constant over time. Historically, the term galvanic has been used in the literature to describe an uninterrupted DC stimulus. (145)

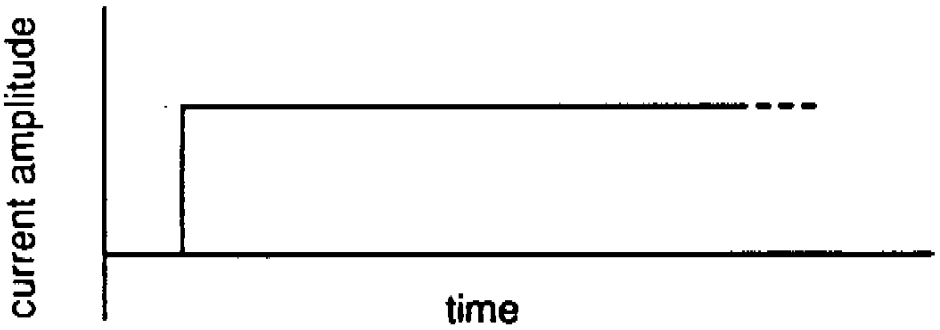

Figure 3-2. Galvanic current. (145)

Alternating current is the constant bidirectional flow of charged particles and may be symmetrical or asymmetrical with respect to the baseline. Traditionally, the term faradic has been employed to describe the unbalanced asymmetrical biphasic waveform. Meanwhile, pulsed current is the unidirectional or bidirectional flow of charged particles which periodically stops for a finite duration before the next event. Similarly, a pulse is defined as an isolated

electrical event separated by a finite duration from the next event. Finally, the interpulse interval is defined as the time between pulses. (145)

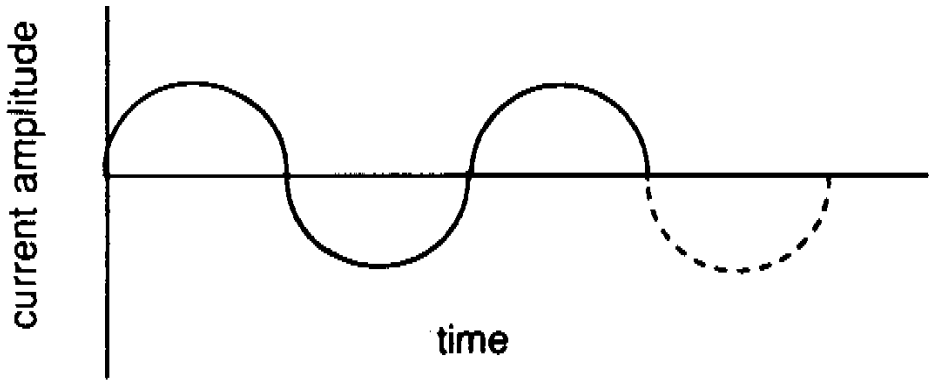

Figure 3-3. Faradic current. (145)

Pulsed current is described by special time-dependent characteristics of the individual pulse. The phase is the unidirectional current flow for a finite duration. A pulsed stimulus may be monophasic or biphasic. In the monophasic waveform, the pulse is the phase. This is because the waveform deviates in one direction from the baseline and returns to the baseline after a finite period of time. Meanwhile, the biphasic waveform deviates in one direction from the baseline and then deviates in the opposite direction from the baseline to make the pulse complete. A biphasic pulse may be symmetrical or asymmetrical. In the symmetrical biphasic pulse, the waveform characteristics such as amplitude, duration, rise time, and decay are the same with reference to the baseline. In the asymmetrical biphasic pulse, however, one or more of the waveform

characteristics is unequal with reference to the baseline. Asymmetrical biphasic pulses can either be balanced or unbalanced. In a balanced asymmetrical pulse, the phase changes are electrically identical. However, in an unbalanced asymmetrical pulse, the phase changes are not electrically identical. (145)

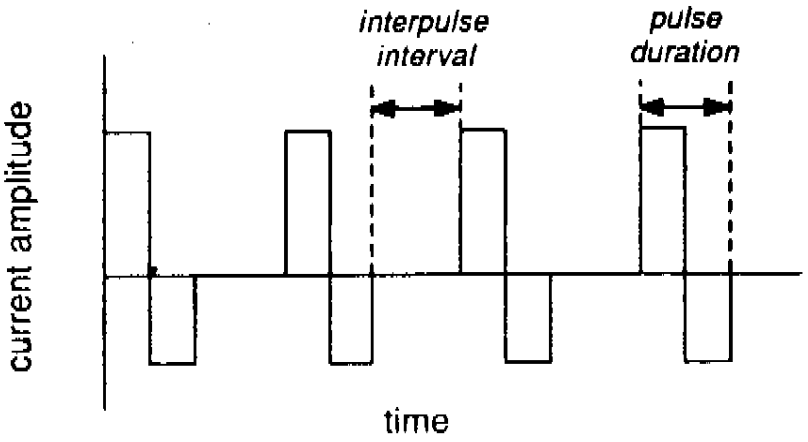

Figure 3-4. Pulsed current. (145)

In pulsed current, the phase duration is the time that has passed from the beginning to the end of a single phase. The interphase or intrapulse interval is the amount of time between two successive parts of a pulse when electrical activity is absent. Meanwhile, pulse duration or pulse width is the time that has passed from the beginning to the termination of all phases in a single pulse. Finally, the interpulse interval is the period of time that has passed between two consecutive pulses. (145)

Units of stimulus frequency are either in pulses per second (pps) or cycles per second (Hz). A period is the time from a reference point of a waveform to the identical point of the next waveform. In alternating currents, the duration of the waveform equals one period. In pulsed currents, the period is equal to the sum pulse duration and the interpulse interval. Pulsed and alternating currents can be varied within a specific period of time. This is known as modulation. Modulations may be used alone or in combinations. They may be consecutive or varied with reference to pulse per cycle or a series of pulses per cycle. Amplitude modulations (AM) are changes in the peak intensity in a series of waveforms. Phase duration, pulse duration, and frequency may additionally be varied. Ramp or surge modulations are increases or decreases in the phase changes over time. These may be accomplished by changing either the waveform duration or the amplitude of the waveform. The time period of the ramp gives a complete description of the input. (145)

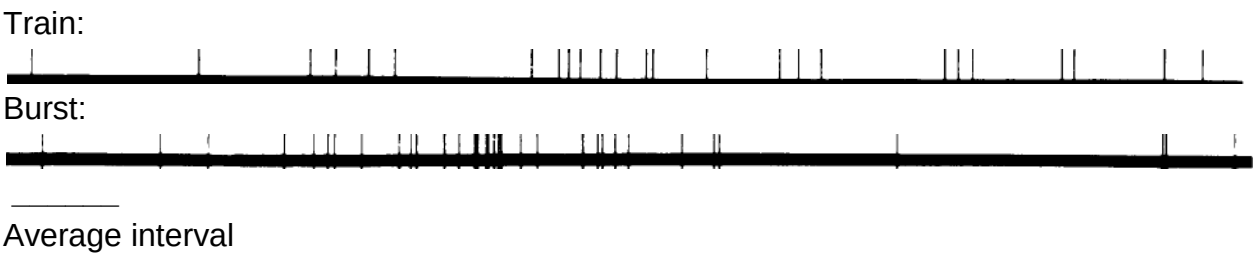

Figure 3-5. Example of train vs. burst.

The pattern of a series of pulses may be defined in terms of time-dependent parameters. A continuous repetitive sequence of pulses or cycles of pulsed current denotes a train. A finite series of pulses or an envelope of pulsed current, administered at a specific frequency, amplitude, or duration is a burst. Bursts are separated by an interburst interval. Meanwhile, burst duration is the amount of time that has passed between the beginning and the end of a burst. Finally, the duty cycle is the ratio of on-time to total-time of trains or bursts of pulses. The duty cycle is generally expressed as a percentage. The clinical ramifications of the duty cycle are paramount in the area of fatigue induced by neuromuscular electrical stimulation (NMES). (145)

3.3 Electrical stimulation of muscle

3.3.1 Intact muscle

According to DeVahl (42), Pflueger's law states that, under normal conditions, less current is required from a negative stimulus to elicit a muscle contraction of given strength than from a positive stimulus. Therefore, the negative electrode is often used to evoke the muscle contraction and is termed the active electrode. This is because depolarization of the physiologically excitable tissue is most easily accomplished at the cathode. Excitable tissue at the positive electrode is less able to depolarize. Thus, the positive electrode is often termed the inactive or reference electrode. Nevertheless, a current through either electrode is capable of eliciting a muscle contraction. However, the positive electrode is not that effective in doing so, unless the stimulus magnitude increases

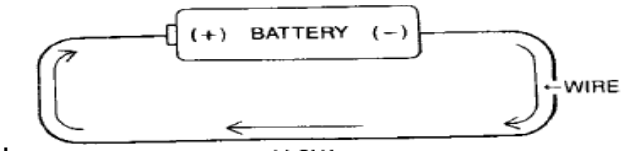

Figure 3-6. Electron flow in a conductor. (42)

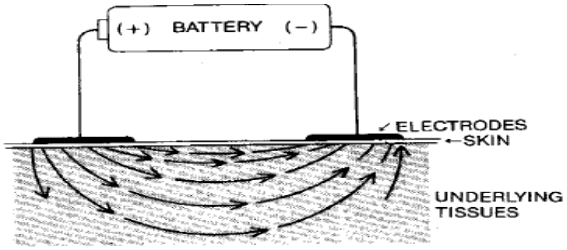

Figure 3-7. Current flow through tissue. (42)

Although numerous waveforms are available in electrotherapy devices, two waveforms have been used traditionally for NMES. They are the asymmetrical biphasic and the symmetrical biphasic quadrilateral waves. Both the square and rectangular waves allow an equal amount of current to flow in either phase. This circumvents undesirable electrochemical effects and possible irritation of the skin. The asymmetrical biphasic square wave permits selective recruitment of smaller muscles by allowing the clinician to differentiate between electrodes, and select the most effective direction of current flow for depolarization. When the current flows from the positive to the negative poles, depolarization occurs under the negative electrode. When current flows in the reverse direction, it flows at low magnitude so depolarization generally does not

happen at the positive electrode. The stimulating phase acts much as a monophasic current. The balancing phase merely reduces the probability of untoward polar effects. (42)

The nature of symmetric biphasic square wave requires that the current flows “hard and fast” (42) in both phases. This permits both electrodes to act as active electrodes. This particular waveform is favored for stimulating groups of large muscle such as the triceps surae. Several studies suggested that biphasic waveforms are preferred to sinusoidal wave forms when applied at intensities sufficient to evoke muscle contractions. When both biphasic waveforms were compared for comfort, the symmetric biphasic waveform was favored. Tissue irritants are known to accumulate under one of the electrodes for unbalanced biphasic waveforms without symmetry. A buildup of charge occurs and causes a burning or itching sensation at the electrode site. However, the application of a balanced, symmetric biphasic input circumvents this aggregation of charge and the associated noxious sensory effects. However, most devices have a maximum current of 100 milliamps. As current amplitude increased, the number of recruited motor units increases, which in turn, increases the muscle force generated. (42)

Many devices for NMES have fixed-phase duration of between 0.2 and 0.4 milliseconds. If the phase duration is set at 0.3 milliseconds, the generation of muscle force can be modulated from the point at which a muscle contraction just begins to near maximal force by increasing or decreasing current magnitude. During electrically induced muscle contractions, according to DeVahl (42), a

phase duration of 0.3 ms is favored for comfort over a narrower (0.05 ms) or wider (1.0 ms) one. However, a stimulus with a phase duration of 0.05 ms requires that a larger current be employed for a pulse charge sufficient to elicit a muscle contraction. The larger current is also sufficient to recruit small diameter afferent fibers that elicit a nociceptive event when excited. (42)

The rate at which the individual pulses are delivered to the nerve is denoted the frequency and is measured in pulses per second (pps) or Hz. Low frequencies (1 to 5 pps) generate twitch contractions and permit little sustained tension to develop in the muscle. Low frequency stimulation is employed to locate motor points since the twitching muscle may be readily ascertained and little fatigue or discomfort occurs. Higher frequencies (10 to 20 pps) cause a fasciculating contraction of the muscle termed incomplete tetany. In healthy muscle at frequencies of approximately 30 pps, the contractions generally fuse or tetanize. Thus, a smooth contraction is apparent. This type of contraction allows the most force to develop in the muscle. In paralyzed muscle, however, complete tetany may occur at 10 to 20 pps. (42)

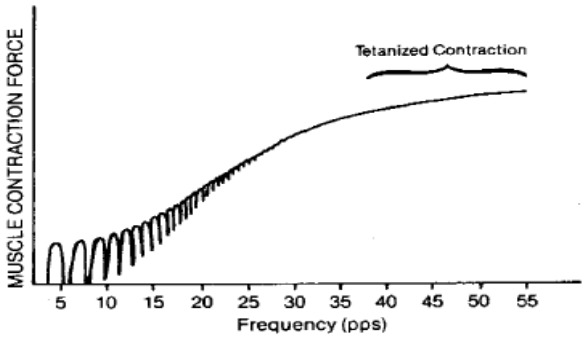

Figure 3-8. Force summation as a function of stimulation frequency. (42)

Clinically, according to DeVahl (42), it is often better to limit the tetanizing frequency, because fatigue at the neuromuscular junction can set in at 30 pps. To prevent excess fatigue and to effectively work the target muscle, the electrical input may be automatically turned on and off. This simulates the contraction and relaxation of the volitional exercise. In most NMES devices, contraction time is usually denoted as “on time” and is measured in seconds. Similarly, the relaxation time is denoted as “off time” and is also measured in seconds. The ratio of contraction to relaxation time is proportional to the duty cycle. The duty cycle is calculated as a percentage derived by the following equation:

$$\text{Duty cycle} = \frac{\text{Pulse-train duration} \times 100\%}{\text{Total cycle time}} \qquad (3\text{-}1)$$

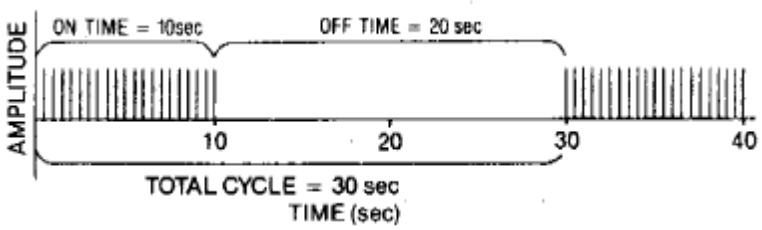

Figure 3-9. Example of on time and off time in a stimulation cycle. (42)

Fatigue can critically affect the benefits that may be gained from medium frequency (MF) NMES of 10-15 pps. Although it is widely agreed that MF NMES can generate stronger contractions than low voltage, low frequency NMES, it has been demonstrated that a 25-pps rectangular wave generated a 25 percent increase in torque. Meanwhile the medium frequency NMES generated only a 13 percent increase. (42)

3.3.2 Denervated muscle

According to Cummings (38), the microenvironment of denervated muscle and the peripheral nervous system has been thought to have characteristics that may either enable or inhibit neuromuscular regeneration and reinnervation. The reunion of the peripheral nerve stump and restoration of the terminal nervous structures, such as muscle, are the combined effect of three factors. These factors are the neurotrophic action of the Schwann cell sheaths and other terminal structures, the mechanical direction of the nerve sprouts along the old myelin sheaths, and, the overproduction of fibers to guarantee the arrival of some of them at the periphery. However, the most essential factor is the trophism of the peripheral nerve stump, motor plates and sensory structures.

An additional factor that may facilitate denervated muscle reinnervation and recovery is long-term electrical stimulation. Although the effects of long-term electrical stimulation of intact muscle are well documented, the effect of long-term stimulation of denervated muscle is not well understood. Chronic, low frequency, indirect electrical stimulation of innervated fast-twitch muscle, similar to that occurring in nerves of slow-twitch muscle, has been shown to transform

the functional properties of a fast-twitch muscle to resemble those of a slow-twitch muscle. (38, 77, 168)

After muscle denervation, the therapeutic activities to restore nerve continuity always include concerns for maintenance of the target tissues of nerve regeneration in the best possible homeostatic condition until the regeneration and reinnervation processes are finished. Those efforts are limited by the fact that there are no universally accepted therapeutic protocols to preserve denervated muscle in a functional condition. However, electrical stimulation is one therapeutic modality that has been advocated slow atrophy of denervated muscle. (38)

According to Cummings (38), there are several indications for electrostimulation of denervated muscle. First, appropriate electrical stimulation can cause contraction in denervated muscle. Regular contraction of denervated muscle may help limit edema and venous stasis, and therefore impede muscle fiber transformation. Furthermore, recovery time after muscle denervation has been shown to decrease with therapeutic electrical stimulation. However, there are also several indications against electrostimulation of denervated muscle. First, contraction of the muscle may disrupt regenerating neuromuscular junctions and subsequently slow reinnervation. Denervated muscle is more susceptible to trauma than innervated muscle. Hence, electrostimulation may further injure the denervated muscle. In addition, long-term electrical stimulation until reinnervation occurs, if at all, is not worth the money and time required. Nevertheless, the therapeutic effectiveness of electrostimulation of denervated

muscle depends upon numerous factors. These factors include the type of current and its magnitude, stimulus duration and frequency, type of contractions, length and frequency of therapy sessions, time between therapy sessions, and time that has passed between injury and start of electrotherapy.

Faradic or faradic-like current having a pulse duration of less than 1.0 millisecond has been reported as somewhat useful in delaying atrophy during the first two weeks following denervation. After that period, the excitability of the muscle becomes so that only interrupted, DC square waves that have a pulse duration of more than 10 milliseconds, or alternating current of less than 10 pps will cause single-twitch contractions. Furthermore, to ensure the optimal response when stimulating denervated muscle, the waveform of the input current should have a pulse duration at least equal to the chronaxie of the denervated muscle. Thus, ascertaining chronaxie is crucial in setting the stimulus duration. In addition, the current magnitude should be large enough to evoke a maximal contraction of the denervated muscle fibers, especially when a denervated muscle is stimulated transcutaneously. Fibers within the deeper regions of denervated muscles may not receive stimulation if the input magnitude is too small. Finally, the magnitude of the current together with the pulse width of the input must be large enough to excite a muscle having a prolonged chronaxie. (38)

Finally, Cummings (38) gives succinct instructions placing electrodes to achieve optimal stimulation in denervated muscle. An alternative is also enumerated.

"The transcutaneous electrical stimulation of denervated muscle is accomplished through surface electrodes. The electrode configuration is usually monopolar with the active or treatment electrode positioned over the part of the denervated muscle that is most electrically excitable. The inactive or dispersive electrode is placed over a distant body part. The size of the active electrode is very small (i.e., 1 to 2 cm^2), providing for a large current density and for a more specific localization at the most electrically excitable part of the muscle. The size of the inactive or dispersive electrode is large enough that current flow under the inactive electrode is not perceived by the patient."

"An alternate configuration would be bipolar stimulation with the active electrode on the most excitable part of the muscle and the dispersive electrode over the tendon. The optimal stimulation site is that point along the muscle which is most electrically excitable and is not the conventional motor point because the nerve is not functioning. This point is the site at which a minimal amount of current will elicit a minimally visible contraction of the muscle being stimulated. This site of greatest excitability should be determined for each denervated muscle at the beginning of each stimulating session. Since the muscle being stimulated is denervated, the response of the muscle to stimulation will be a sluggish and somewhat wormlike contraction instead of the brisk contraction observed when stimulating innervated muscle."

CHAPTER 4: MODELS OF MUSCLE FORCE AND FATIGUE

4.1 Introduction

There have been many studies and models of muscle force. Bobet and Stein (17) studied the properties of nonparalyzed human soleus muscle via systems analysis. Individual pulses and random pulse trains were used as input stimuli to a branch of the nerve to soleus. The resulting variations in muscle tension were recorded. With these data, the frequency-response function between input pulses and resulting muscle tension conformed to that of a second-order, low-pass filter. It was found that the natural frequency, low frequency gain, and damping ratio changed in a systematic way with the angle of the ankle joint. As the joint was flexed, the natural frequency decreased, the low frequency gain increased, and the damping ratio was unaffected or increased slightly. The importance of the work was stated in the following way.

> "The problems of load compensation and stability of posture are much greater in a bipedal animal such as man, but no studies are available to compare human soleus to that of the cat. The reasons are the obvious difficulties of isolating the soleus muscle in a living human being, but the human soleus differs in that a substantial portion of it lies superficially in the leg. This has enabled us to stimulate the human soleus muscle selectively to study its properties in the time and frequency domains and to compare an intact muscle in a normal human subject to a partially isolated cat muscle. The study was limited to muscle properties in relaxed, normal subjects."

However, the work serves as a benchmark for comparing the changes in muscle properties that result from volitional activation in nonparalyzed subjects

and facilitated analysis of changes that arise in various pathological states, such as spastic paresis. (74)

Hannaford developed a phasic excitation-activation (PEXA) model of motoneuron excitation and the resulting activation and force development of a motor unit. In the model, input is a dose of depolarizing current and the output is muscle force. The model includes dynamics and nonlinearities such as the response of motoneurons to doses of depolarizing current and the "catch-like" effect produced by overlapping motoneuron action potentials. The parameter values used in this model were derived from experimental data. (70)

According to Hannaford (70), motoneuron excitation is the mechanism in which injected current depolarizes the axon hillock and sends a depolarization wave down the axon. Activation dynamics describe how depolarization of the neuromuscular junction yields the “active state”. Meanwhile, muscle force generation denotes the transition from ‘‘active state’’ to generate muscle force. In building the model, Hannaford divided the motor unit system into three anatomic subsystems named as the motoneuron, muscle activation, and muscle unit. First, the motoneuron was modeled as a transresistance amplifier, a high-pass filter, and a spike generator implemented as a voltage-to-pulse rate converter. Its output was a series of impulses which decrease in firing rate with an input of constant current. In the “activation dynamics’’ block, the model consisted of a pulse rate-to-voltage converter that was piecewise linear, a nonlinear RC circuit, and a multiplier. This part produced multiplicative effects of the action potential impulses to simulate the nonlinearity. Finally, the muscle was modeled by a

second-order nonlinear model obtained by removing a single muscle from the sixth-order nonlinear full joint model. Hence, the modeled motoneuron was designed to approximately replicate responses from current-step to pulse-rate.

The Hannaford muscle model contained a block of first-order representation of activation-deactivation. As a low-pass version of the input, the output of was denoted as the hypothetical tension or “active state’’. This tension was termed hypothetical since the velocity-dependent force of the viscous subtracts from the tension before generating measurable force. Hence, the velocity necessary for the force is of the internal muscle node, which can be nonzero without change in muscle length. Thus, the viscous effect occurs even under isometric conditions. Similar to other studies, Hannaford found that the muscle model dynamics could be described by two state equations in which scale related the enhanced spike magnitude of the neural input signal to muscle force production. (70)

When modeling muscle force, two very different models which are commonly used were developed separately by Hill and Huxley. Hill models of skeletal muscle are based on the work of Archibald Vivian Hill. They are phenomenological and describe the force behavior of muscles for specific conditions of length and speed. Huxley cross-bridge models are based on the work of Andrew Fielding Huxley. They are structural models based on the supposed interaction of actin and myosin filaments via cross-bridges and the concept of force production in sarcomeres. (59)

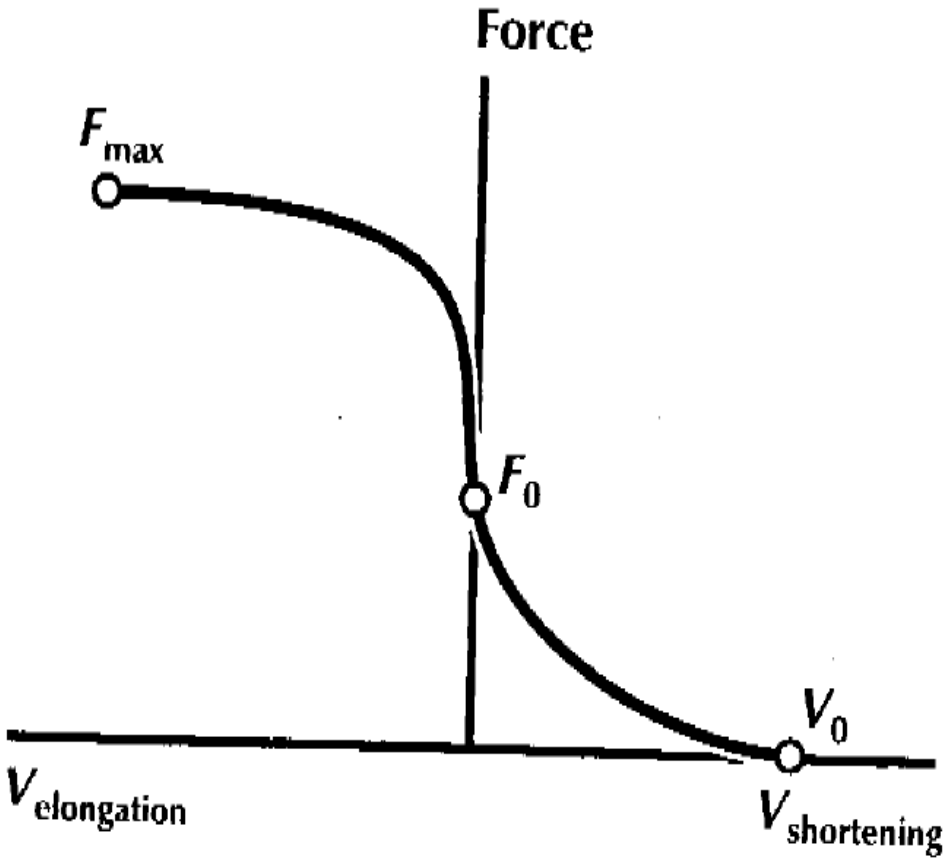

Figure 4-1. Schematic of force-velocity relationship in skeletal muscle. (59)

4.2 Hill model

In his famous experiments on the heat of shortening of skeletal muscle, Hill (75) showed that a muscle produced heat isometrically. When the contracting muscle was suddenly released under a load which allowed for shortening, there was an increase in the rate of heat production which was proportional to the shortening velocity and stopped at the end of a contraction. The total extra heat generated during shortening was proportional to the decrease in length. When the muscle size was considered and the stimulation was held supramaximal, the

shortening heat (H) could be expressed as H=ax, where x is the decrease in length during the contraction, and a represents a constant of proportionality in force. The value of a depends on the physiological cross-sectional area of the muscle as well as the level of activation. He showed that the value a/P_0, P_0 being the maximal isometric force, is fairly constant. This result can be understood by realizing that P_0 also depends on the physiological cross-sectional area and the level of activation of the muscle. During shortening, a muscle generates extra heat. Since the shortening heat is equal to ax and the work is equal to Px, the extra energy liberated during isometric contractions becomes (P**+**a)x. The rate of energy liberation becomes (P**±**a)dx/dt = (P**±**a)v where v is the shortening velocity. He also showed that the rate during shortening was inversely proportional to the afterload P applied to muscles. Thus, the rate of extra energy liberation is zero when $P = P_0$. Therefore, $(P+a)(v+b)=(P_0-P)$, where a defines the absolute rate of energy liberation.

Based on the experimental work available in 1938, Hill (75) deduced that active skeletal muscle has an undamped elastic element cascaded with a damped element. The original idea that viscosity underlies the damping characteristics of active skeletal muscles was quickly jettisoned for various reasons. First, viscosity was incongruous with the empirical observation on stretching muscle. Second, given the differences in active and passive muscle characteristics, viscosity would have had to vary markedly upon muscle activation. Third, it had been found that shortenings produced more energy than isometric contractions.

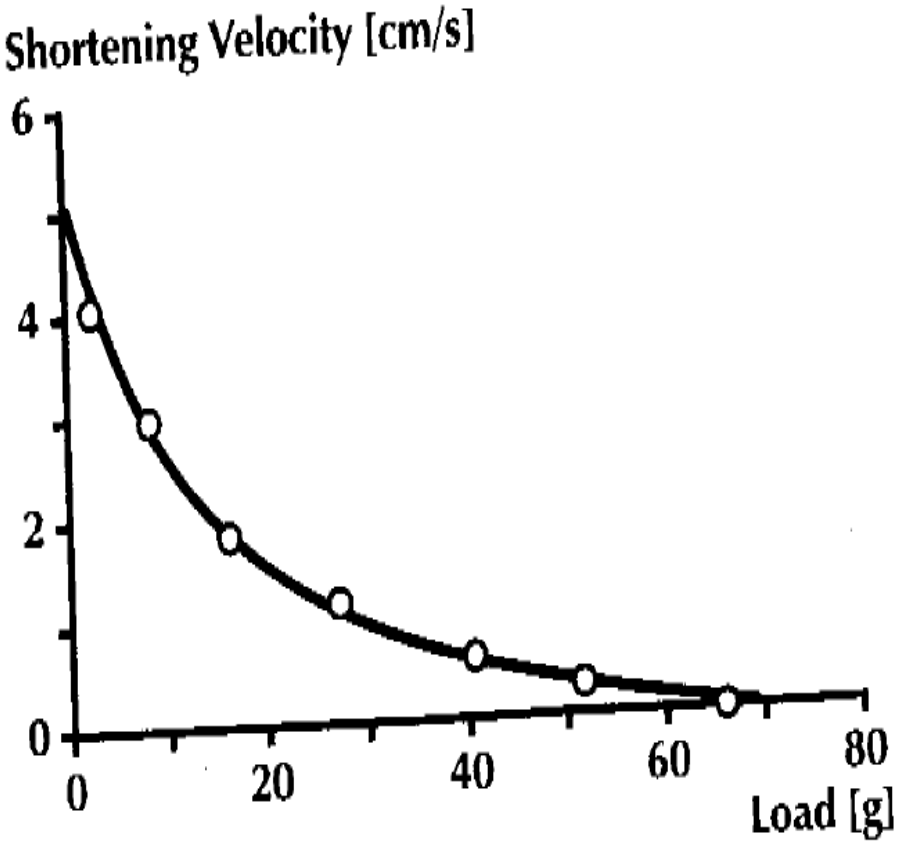

Figure 4-2. Schematic of the force-velocity relationship predicted by the Hill equation. (75)

From the contemporary experiments, it was also concluded that active skeletal muscle consists primarily of a contractile element cascaded with a purely elastic element. The contractile element characteristics were governed by equation which was derived by Hill (75) based on his empirical observations on the shortening heat in frog skeletal muscle.

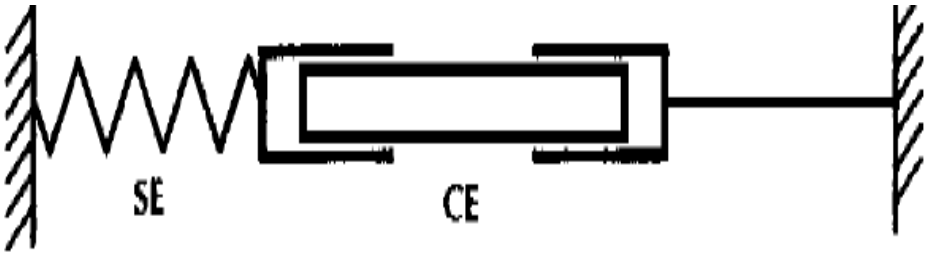

Figure 4-3. Schematic of Hill model with contractile element (CE) with series elastic element (SE). (59)

To factor in the passive forces observed in lengthened skeletal muscles, the basic Hill model is usually appended with an undamped elastic spring in parallel with the contractile and series elastic element. (59)

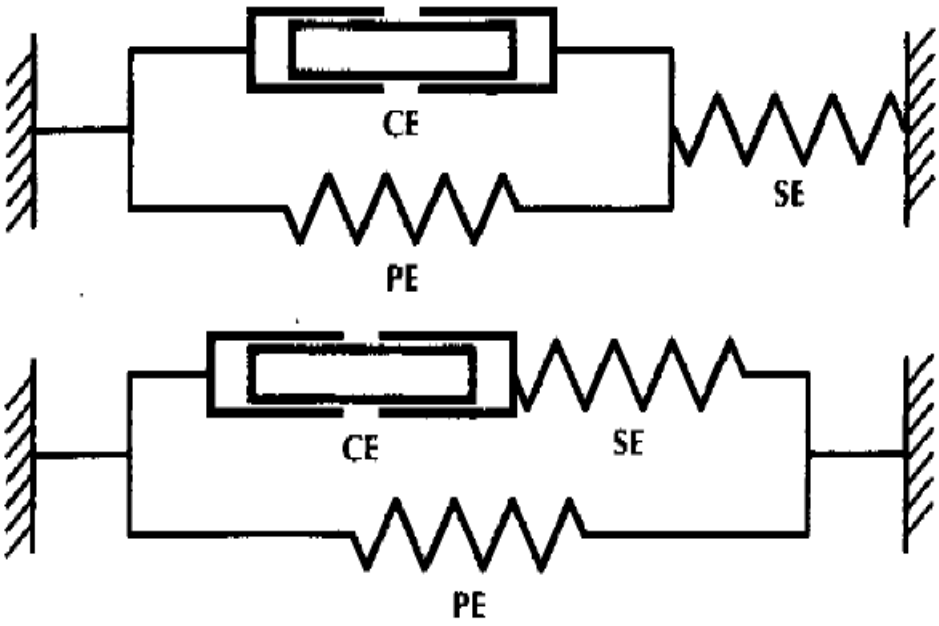

Figure 4-4. Schematic of Hill models with contractile element (CE) with parallel elastic element (PE) and series elastic element (SE). (59)

Although Hill type models may be considered purely phenomenological, when using these models, the properties of the contractile and elastic elements need to be known. A further limitation of Hill-type models based on the characteristic equation is that the equation is valid solely for constrained contractile conditions, such as maximal activation around optima! length. The force-velocity relationship of submaximally contracting muscle is not known in detail. In addition, the force-velocity relationship at nonoptimal lengths is not completely known. One conceptual limitation of Hill-type models is that the history of the natural force behavior of muscle cannot be predicted. In particular, the characteristic equation of Hill implies that a unique relationship exists between force, velocity, and length. Yet, that is not the case. Nevertheless, Hill models describe the approximate muscle dynamics for specific contractile conditions without providing insight into the mechanisms of force production. Despite these limitations, Hill models continue to be used more frequently in biomechanical models of musculoskeletal systems than any other muscle model. Such popularity comes from the accessible mathematics of the model as well as the qualitatively accurate predictions generated for various states of muscle contraction. (59)

4.3 Huxley model

With respect to the biophysics of force production in muscle as well as muscle energetics, the most preferred model for the past four decades has been the Huxley or cross bridge model. Cross-bridge models exclusively consider the

contractile machinery by synthesizing the known anatomical properties of skeletal muscle with the known energetic aspects of contraction. (59)

The cross-bridge model of muscle force generation was first articulated by Andrew Fielding Huxley (80). It is considered the first attempt at a unifying theory of muscle contraction. The reason for that is because it simultaneously considered the mechanical, thermal, chemical, and structural changes, which were known to happen in a contraction, No other muscle model has been so universally accepted. That is because no other model considered all phenomena as expansively as the cross-bridge theory did. Contemporaneously, the cross-bridge theory is the 'gold standard' of muscle force generation models. Although the model has been changed in numerous ways, the essential theory first articulated in 1957 is still used. However, in contrast to the phenomenological Hill type models, the cross-bridge model allows for the quantitative study of energetics during muscle contraction. Thus, using the molecular composition of skeletal muscle, the chemistry of contraction was modeled on the laws of Newtonian mechanics. Yet, even though the cross-bridge model is used almost universally in muscle biophysics, it is almost never employed in biomechanics. The primary reasons for not using the cross-bridge model in biomechanics arise from its erudite mathematics, and its consideration of the sarcomere as its fundamental unit rather than fiber or whole muscle. (59)

In its fundamental form, the cross-bridge model may be delineated in the following manner. There are cross-bridges originating from the myosin filaments which attach to specific locations on the actin filaments. During attachment, the

cross-bridges ratchet the actin past the myosin filaments. This produces force and muscle contraction. (64, 80-83)

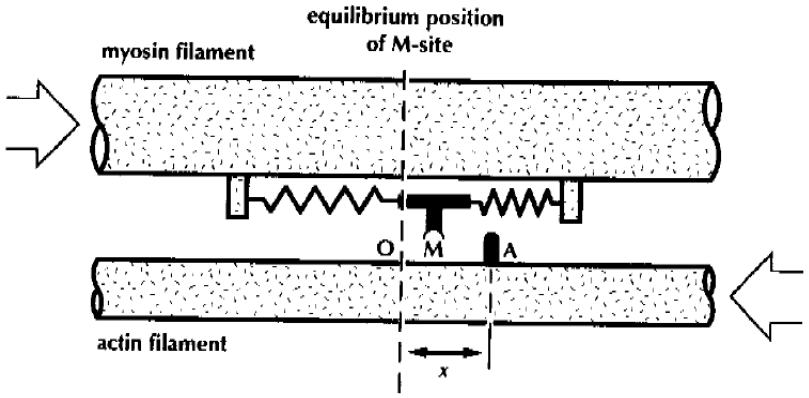

Figure 4-5. Schematic of Huxley 1957 cross-bridge model. (80)

In the cross-bridge theory (80) it is assumed that myosin filaments have projections which were connected by elastic springs. The projection with its connection point M is believed to oscillate about its equilibrium position (O) because of thermal agitation. M is thought to attach to specific binding sites (A) on the actin filament if M approaches A. The combination of M-sites with A-sites is believed to happen spontaneously and asymmetrically only on one side of O so that the superposition of the M- and A-sites would generate force and motion which shortens the sarcomere.

It is believed that attachment and detachment are regulated by rate functions f and g, respectively. These are modeled as linear functions of the distance from the active site on the actin filament, to the equilibrium position of

the side piece. Since the linking of an M- with an A-site is assumed to spontaneously occur, breaking the M-A linkage is assumed to require energy from an active process by splitting a high-energy phosphate compound. To generate force without noise, it is assumed that there are numerous binding sites for possible linkage of the myosin and actin filaments. These sites are believed to be staggered with respect to one another so that different linking sites can contact at different relative motions of both filaments. The linkage sites are also assumed to be so distal that events at one linkage do not affect events at another linkage. (80)

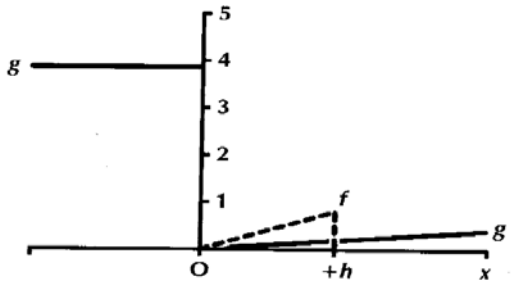

Figure 4.6. Schematic for rate functions of bonding, f, and unbonding, g. (80)

When comparing the theoretical predictions to the properties of forcibly stretched muscle, several observations were recorded. Katz (93) found that the slope of the force-velocity curve for slow lengthening was about six times that of the analogous slope for slow shortening. The Huxley (80) theory also predicted the asymmetry, by a factor of 4.33, in the force-velocity curve about the isometric point. Katz (93) also discovered the force during rapid lengthening of a stimulated muscle to be about 1.8 that of the isometnc force. From the rate

functions given by Huxley (80), the force for increasing speeds of lengthening was found to asymptotically converge to 5.33 times the isometric force. This is an overprediction. In addition, the cross-bridge theory of Huxley (80) poorly predicts the heat production of a forcibly stretched muscle. The theory predicts that the rate of heat liberation linearly increases with the lengthening velocity. This prediction grossly overestimates the heat production in lengthening muscle. (59)

In the 1957 theory (80), a cross-bridge can either be attached or detached. When a fully activated muscle rapidly shortens, many cross-bridges detach during shortening, and recovery of force depends on the cross-bridge attachment rate. However, the attachment rate function is not fast enough to account for quick recovery of force. However, models with substantially faster attachment rate functions cannot predict the Hill force-velocity relationship as well as the 1957 model of Huxley and cannot account for the thermal data observed experimentally during muscle shortening. (59)

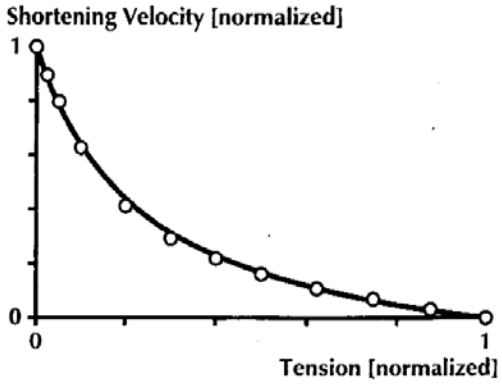

Figure 4-7. Normalized comparison of Hill model (solid curve) and Huxley model (circles) for force-velocity relationship. (80)

Another property of muscle contraction which cannot be predicted sufficiently with the Huxley (80) theory is the transient force resulting from a stepwise change in length. When a muscle rapidly shortens, the force decreases almost simultaneously with the displacement and then quickly recovers. Two parameters defined by Huxley and Simmons (81) for describing these fast force transients are known as T_1 and T_2. T_1 denotes the minimum force achieved during the rapid shortening. Meanwhile, T_2 denotes the force after the quick recovery phase. T_1 progressively decreases with increasing release distances. The T_1 versus length step curve is thought to depict the undamped elasticity in the contractile apparatus. Since T_2 is always larger than T_1, this denotes a force recovery of milliseconds after the displacement.

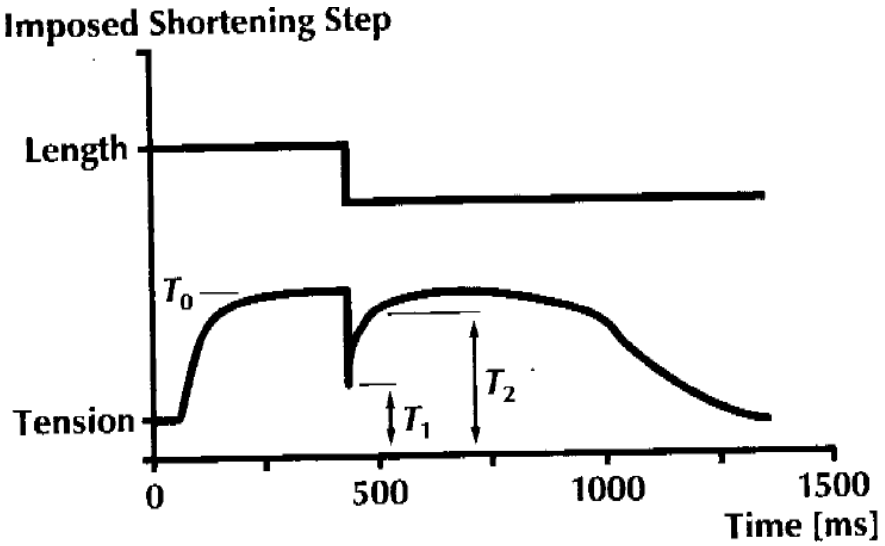

Figure 4-8. Schematic of T_1 and T_2. (59)

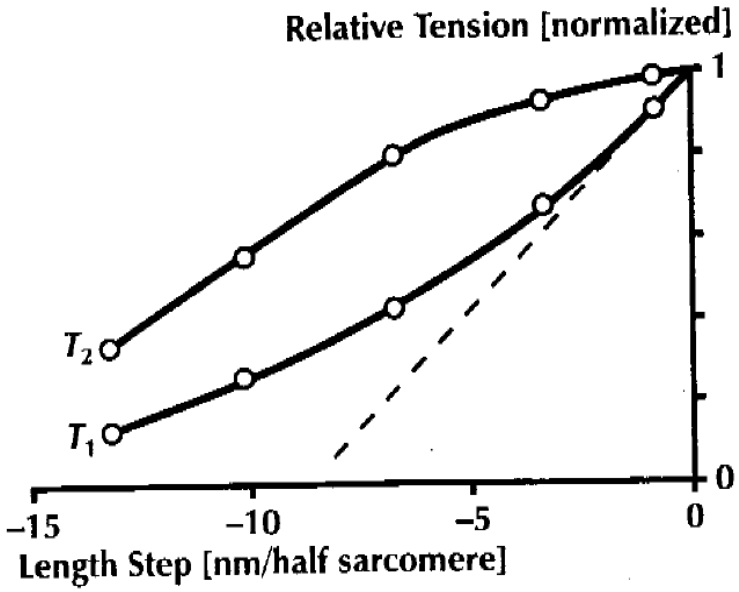

Figure 4-9. T_1 and T_2 as a function of length step. (81)

To account for the transient force after a stepwise change in length without losing the predictive power of the 1957 model, Huxley and Simmons (81) modified the model by introducing different attachment states for the cross-bridge. This allows the cross-bridge to perform external work in a finite number of steps during attachment. A change is stable state corresponds with a decreasing potential energy. Huxley and Simmons (81) also assumed that each cross-bridge contains an undamped elastic element which allows the linkage to change its stable state of attachment without relative motion of the myofibrils. Hence, the transient force generated from a rapid change in length can be explained as follows. If a muscle is released suddenly, the cross-bridge head will not rotate. Therefore, decreased force during the displacement (T,) corresponds with the force-elongation characteristic of the undamped elastic unit in the cross-bridge.

After the sudden displacement, quick force recovery is admissible since the cross-bridge head rotates in its linkage from high to low potential energy. This rotation stretches the elastic element in the cross-bridge and increases the cross-bridge force.

Huxley and Simmons (81) articulated a cross-bridge model that has three stable, attached states and derived differential equations for a stable two-state system. Many other extended models with a variety of stable states have been described. (64, 78, 79, 182, 183) However, the essentials of all of these models originate from the 1971 cross-bridge model.

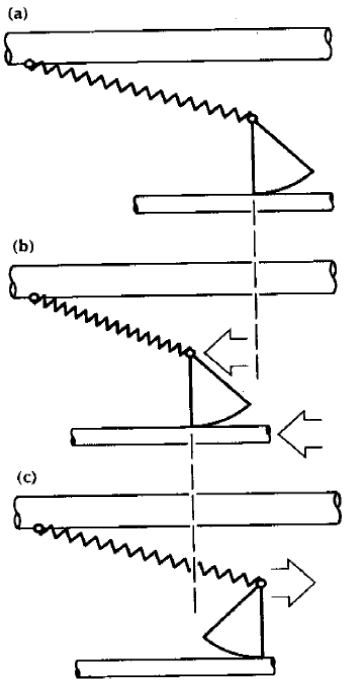

Figure 4-10. Schematic of event sequence in Huxley 1971 theory. (81)

4.4 Zahalak models

Zahalak and Ma (190) broadened the basic Huxley model to account for the role of calcium in activating the contractile mechanism. They sought a simplified model of calcium activation dynamics that would capture the fundamental physical nature of activation as the basic Huxley two-state model captures the essential physical nature of contraction.

They began by assuming that the total number of cross-bridges can be divided into two subgroups: aM, “participating” cross-bridges which can interact with activated actin, and (1-a)M, “nonparticipating” cross-bridges which cannot interact with actin. The amount of participating cross-bridges, a, is defined a function of contractile tissue length. The amount may be less than one at long muscle lengths because of decreased overlap between actin and myosin, and at short muscle lengths due to steric hindrance. It was further assumed that there is a range of muscle lengths where a=I, and that muscle in tetanic contraction produces maximal force at these lengths. Next, they assumed that there for all time a one-to-one-to-one correspondence between a myosin cross-bridge, its nearest actin binding site, and a troponin molecule modulating that site for myosin bonding. This allows for focusing on the behavior of the myosin-actin-troponin (MAT) complex. If (1-a)M cross-bridges are non-participating, then it is assumed that an equal number of troponin molecules. Each troponin molecule has four sites for calcium binding. Two are high-affinity and two are low-affinity. Only the low-affinity sites are significant in modulating muscle contraction. The high-affinity sites bind magnesium ions competitively with calcium. The dynamics

of these sites are assumed to be too slow to have a significant role in generating muscle force. The two calcium ions are assumed to bind in sequence to a troponin molecule. The troponin facilitates access to actin binding sites only upon binding two calciums. Two possible schemes for the kinetics of the myosin-actin-troponin complex, known as loose coupling and tight coupling, were initially proposed. In loose coupling, calcium binds and unbinds from troponin independently from the state of bonding between myofilament proteins. However, in tight coupling, troponin can release its bound calciums only after the cross-bridge it is modulating is free from actin. The four rate constants that vary with the concentration of free calcium are assumed to be equal. (190)

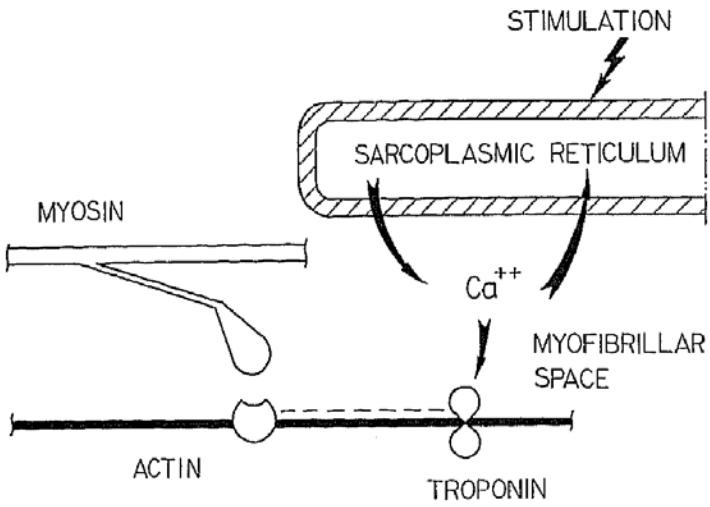

Figure 4-11. Schematic of excitation-contraction coupling. (190)

According to Zahalak and Ma (190), the four states characterizing MAT complexes for the subgroup of participating cross-bridges under tight coupling can be labeled as follows:

state 0 - unbonded actin site with its troponin free of calcium,

state 1 - unbonded actin site with one calcium ion attached to troponin

state 2 - unbonded actin site with two calcium ions attached to troponin,

state 3 - bonded actin site with two calcium ions attached to troponin.

Zahalak and Ma (190) also considered the alternative hypothesis of loose coupling between the dynamics of calcium/troponin and actin/myosin. It was assumed that troponin binds to two calcium ions in sequence, and that the binding and release of calcium by troponin occurs exclusive of actin/myosin interactions. Thus calcium kinetics may be described by the following states.

(A-M-T) + (AMI) = state 0,

(A-M-TC2) + (AMTCa) = state 1,

and (A-M-TCa2) + (AM-TCa2) = state 2 + state 3.

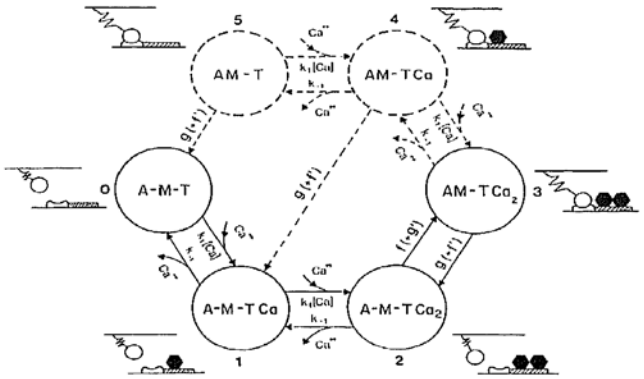

Figure 4-12. Diagram of tight coupling (solid line) and loose coupling (solid plus dashed lines). Curved arrows indicate Ca^{2+}-Tr interactions. (190)

With explicit expressions for the total concentration of calcium in the myofibrilar space, Zahalak and Ma (189) generated a calcium mass balance equation. A finite number of pumping sites in the SR implies that the calcium pump is saturable. Its performance was modeled as a classic Michaelis-Menten enzyme reaction. That gives [Ca]=V[Ca]/([Ca]+K) where V and K are the two Michaelis-Menten parameters for the reaction. They argued that representing that process by a Michaelis-Menten equation is congruent with the parallel representation of the contraction process by a Huxley model with two states.

Finally, Zahalak and Ma (190) modeled the rate of passive calcium injection from first principles. Calcium injection is thought to be the result of a gating mechanism which is driven by a calcium gradient across the sarcoplasmic reticulum. While the action potential modulates changes in membrane permeability, it has been suggested that the process machinery is unimportant for contraction dynamics. Because calcium injection resulting from muscle action potential usually happens within ten milliseconds, and calcium diffusion is also very rapid, it is believed that only the net flux of calcium ions released by an individual muscle action potential is the driving force for the subsequent contraction. Yet, that process is comparatively slow. Therefore, the basic assumption that could have been made about calcium injection is that the individual muscle action potential releases a specific quantum of calcium ions over a set time course. Hence, this gives $[Ca]_u=R_0x(t)$ where R_0 is the additional calcium concentration from one action potential and x(t)defines a sum of normalized impulses $x(t)=\Sigma x(t-t_l)$ satisfying $x(t)=0$ for $t < 0$ and $\int_0^\infty x(t)\,dt=1$. To

model the nonuniform addition of calcium ions after each muscle action potential, they allowed R_0 to vary inversely with the extrareticular concentration of free calcium. To maintain the injection gradient in the model, the parameter $[Ca]_t$ was required to have the same order of magnitude as the average calcium concentration in muscle.

For the modified two-state model, two independent kinetic paths between the attached and detached states were recognized. Zahalak and Ma (190) formulated the coupled activation-contraction equations as

$$\frac{d}{dt}[\mathrm{Ca}]_t = R_0(1-\frac{[\mathrm{Ca}]}{[\mathrm{Ca}]^*})x(t) - V_m\frac{[\mathrm{Ca}]}{[\mathrm{Ca}]+K_m} \qquad (4\text{-}1)$$

for calcium dynamics, and

$$\frac{\partial n}{\partial t} - v(t)\frac{\partial n}{\partial x} = (f+g')(r\alpha - n) - (f'+g)n \qquad (4\text{-}2)$$

for loose coupling, or

$$\frac{\partial n}{\partial t} - v(t)\frac{\partial n}{\partial x} = r(f+g')(\alpha - n) - (f'+g)n \qquad (4\text{-}3)$$

for tight coupling, where f, g, f', and g' are all functions of the length of the actin-myosin bond.

In their quest to derive solvable constitutive relationships to describe whole muscle energetics and mechanics, Zahalak and Ma (190) assert that is little value to use a complex model for calcium dynamics with many states without a congruent multistate model for contraction dynamics. Their analysis clarified many physiologic assumptions, such as those regarding tight versus loose coupling. Such clarifications were argued as necessary to generalize from a model of molecular contraction to macroscopic constitutive relationships for

whole muscle. In addition, they developed the model for calcium activation dynamics under alternating hypotheses of loose coupling or tight coupling between the respective dynamics of calcium-troponin and actin-myosin. Of the two assumptions, the tight coupling hypothesis was deemed to be more natural on the basis of the steric interaction theory of calcium regulation of actin via troponin and tropomyosin. However, the assumption of tight coupling greatly complicates analysis under the Huxley theory. However, it was found, with their approach, that tight coupling was no more difficult to model than loose coupling. They found the resulting generalization of the Huxley two-state model to be fourth-order.

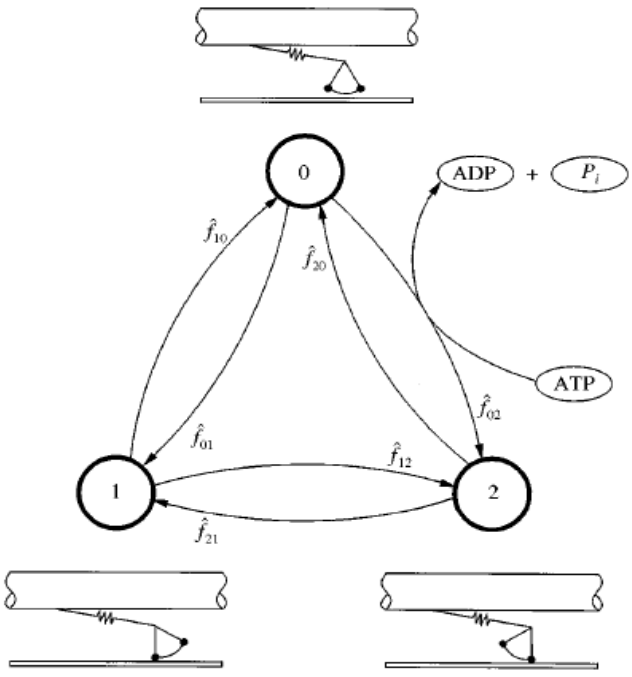

Figure 4-13. Three-state kinetic model with ATP energetics. (190)

However, according to Zahalak (191), contemporary muscle physiologists thought the two-state cross-bridge paradigm as outdated and unusable as models with as many as eighteen states had been proposed. Even Huxley eventually referred to it as a "skeleton theory" (83). Zahalak (191) asserted, however, that the two-state cross-bridge model is still valid for macroscopic dynamics of muscle contraction and analyzed in detail the Huxley-Simmons three-state model with matched asymptotic expansions. In this analysis, the Huxley two-state model was shown to be the "outer" solution of the cross-bridge state equations. Meanwhile, the Huxley-Simmons (81) reduced two-state model was shown to be the "inner" solution. From the asymptotic analyses, general conclusions were drawn by Zahalak, with respect to the role of the two-state model and how it relates to higher-order models with more than two states. (191)

According to Zahalak (191), the apparent cross-bridge force that is derived from the asymptotic analysis is a nonmonotonic function of cross-bridge length. The function has a region of negative stiffness where a single cross-bridge subjected to such a force would have mechanical instabilty. However, as they attach to common myosin filaments, single cross-bridges are forced to move together over short time spans. This effectively averages the cross-bridge force, F(x), over an interval of the order of h_0. If that interval corresponds to the negative stiffness interval, then the average cross-bridge force will smooth out. Hence, the force in each individual filament and the whole muscle will stabilize and be monotonic as the T_2 curve shows.

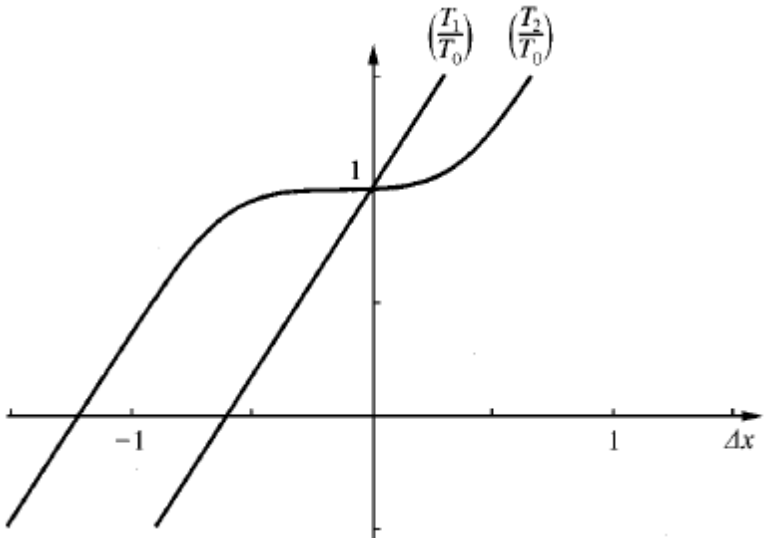

Figure 4-14. Fast isometric transient curves. (191)

Mathematically, the assumption of Huxley and Simmons (81) was equivalent to defining the cross-bridge distribution in steady state as a set of Dirac delta functions. Difficulties of physical interpretation arose nevertheless. This is because there is an asymptotically infinitesimal probability that a cross-bridge will possess at any instant an exact bond length for making attachment possible. In the asymptotic theory, Zahalak circumvents this difficulty because the bond lengths in steady state are not localized. Instead, they are uniformly distributed over an interval of length h_0. An empirically approximate function was found to be tanh {(m/2)(y + (1/2))}. As a result, the Huxley-Simmons equation was shown to be fairly close to the asymptotic theory if it is assumed that $x+x_0=1/2$. With that constraint, the total steady-state amount of attached cross-bridges in the first state predicted by the Zahalak theory was 0.5. (191) That result agreed with the assumption and analysis of Huxley and Simmons (81).

Hence, Zahalak (191) concluded that the two-state model is still a valid approximation of muscle dynamics, excluding fast displacements. However, asymptotic analysis demonstrated that the cross-bridge force must be defined as a nonlinear function of the cross-bridge length that saturates as stretch increases. The nonlinear cross-bridge force is modulated in part by the fast equilibrium between the two states of attachment. The typical assumption of constant cross-bridge stiffness in two-state models is at best a crude but useful approximation.

4.5 Ding models

Ding and colleagues have tried several approaches to model force and fatigue in able-bodied muscle using their version of a Hill-Huxley model. (48-55) The original Ding model is different from those previously reported because it has a simple structure and few parameters (48). At the molecular level, the process of muscular contraction is quite complex. Compared with models developed by Hannaford (70), Huxley (80), Zahalak and Ma (190), and Zahalak (191), Ding and colleagues (48) did not factor in the cross-bridge kinetics. Unlike previous models, which has three states of calcium transient, the Ding calcium kinetics only contains two simplified states The predicted Ca^{2+} transients and Ca^{2+}-troponin concentrations were similar to those found by Hannaford (70), and fell within physiological ranges.

4.5.1 Force model

The force model was developed by decomposing the contractile response into distinct physiological steps: calcium release and reabsorption by the

sarcoplasmic reticulum (SR), calcium binding and unbinding to troponin, and force mechanics including cross-bridge cycling along with the friction and elasticity of the muscle fibers. (48)

$$\frac{d[\mathrm{Ca}^{2+}]_{SP}}{dt} = 2(k_1[\mathrm{Ca}^{2+}]_{SP}^2 + k_2)[\mathrm{Ta}] - 2k_1[\mathrm{T}_0][\mathrm{Ca}^{2+}]_{ST}^2 + k[\mathrm{Ca}^{2+}]_{SR} - (k + k_0)[\mathrm{Ca}^{2+}]_{SP} \quad (4\text{-}4)$$

$$\frac{d[\mathrm{Ta}]}{dt} = k_1[\mathrm{T}_0][\mathrm{Ca}^{2+}]_{SP}^2 - (k_1[\mathrm{Ca}^{2+}]_{SP}^2 + k_2)[\mathrm{Ta}] \quad (4\text{-}5)$$

Although the binding process is usually considered to be a two-step reaction, Ding et al (48) only considered its overall effect of the forward and backward reaction rates. From basic chemical kinetics and membrane transport, the two differential equations that describe the calcium transient in the sarcoplasm and the calcium-troponin binding processes are in the muscle. In the first chemical equation, the first two terms represent the dissociation of Ta and binding of Ca to troponin, respectively. The third term is the rate of concentration increase due to diffusion from the SR and the fourth term corresponds to diffusion and reabsorption of calcium back into the SR. In the second equation, the first term represents the binding of calcium to troponin and the second term represents the dissociation of the calcium-troponin complex.

Finally, formation of calcium-troponin complex (Ta) causes conformational change of actin and consequently results in the exposure of the cross-bridge binding sites on actin. Then cross-bridges attach to actin and pull the thin filaments toward the center of the thick filaments. The macroscopic result of this process is the generation of force which is modeled by a linear spring, a damper, and a motor in series. The damper represents the viscous resistance of the

contractile and connective tissue. The force exerted by the damper is given by F=b(V-dx/dt).where b is the damping coefficient, x is the length of the spring, and V is the contractile velocity of the motor. (48)

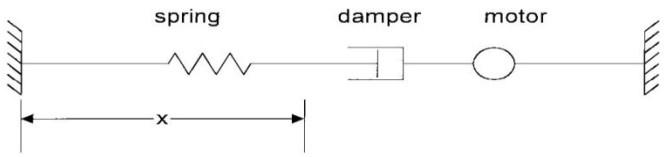

Figure 4-15. Schematic of the isometric model of muscle force. (48)

For simplicity, a linear spring was considered to represent the tendinous portion and the series elastic component of the muscle. (48) The force exerted by the spring is given by F=Kx, where K is the spring constant. Differentiating Hooke's law with respect to time and the subsequent algebra gives $dF/dt=KB[Ta](1-F/F_m)-F/b/K$.

The term b/K represents the time constant over which the force decays. The model (48) assumes that the friction between actin and myosin fibers is higher during cross-bridge recycling due to chemical bonds between the fibers so the term $b/K=\tau_1+\tau_2[Ta]/[T_0]$, where τ_1 is the value of the time constant in the absence of cross-bridges and is the additional frictional component due to the actin-myosin bonds. Making additional substitutions for KB and b/K gives $dF/dt=A[Ta](1-F/F_m)-F/(\tau_1+\tau_2[Ta]/[T_0])$.

Later, Ding and colleagues (49) decomposed the contractile response to account for the distinct physiological step of cross-bridge activation. To model cross-bridge activation, it was shown that the force-prediction ability of the model is relatively insensitive to the specific curvature and amplitude of the calcium and calcium-troponin complex transient. This implied that the first two steps in the 1997 model (48) could be combined into one by the unitless factor, C_N. From the following differential equation, the dynamics of C_N are modulated by the time constant, τ_c, which describes qualitative the rate-limiting step before the actin and myosin mechanically translate across each other and generate force. (49)

$$\frac{dC_N}{dt} = \frac{1}{\tau_c}\sum_{i=1}^{n}\exp\left(-\frac{t-t_1}{\tau_c}\right) - \frac{C_N}{\tau_c} \tag{4-6}$$

This solves analytically to:

$$C_N = \sum_{f=1}^{n} \frac{t-t_1}{\tau_c}\exp\left(-\frac{t-t_1}{\tau_c}\right) \tag{4-7}$$

The differential equation describing force-generation with C_N is

$$\frac{dF}{dt} = A\frac{C_N}{1+C_N} - \frac{F}{\tau_1 + \tau_2\frac{C_N}{1+C_N}} \tag{4-8}$$

The isometric force dynamics are governed by this equation which describe the transient behavior of the two state variables, C_N and F, subject to the four parameters τ_c, A, τ_1, and τ_2. C_N behaves as a Michaelis-Menten process. (49)

The model predicted isometric forces for rat gastrocnemius and human quadriceps femoris muscles with reasonable accuracy during brief subtetanic and tetanic isomeric contractions. It successfully predicted nonfatigued force

responses when muscles were held at long or short length and fatigued force responses at long length. Subjective and objective evaluations of the force response showed that the shape of the predicted force responses closely matched the responses that were measured. Comparisons between the predicted and measured force-time integrals also suggested excellent agreement between the predicted and measured forces. Although significant differences between the predicted and measured force-time integrals were observed with some stimulation patterns, most differences were small. (49)

The 1998 model was simpler than previously developed models and had fewer parameters. With just four free parameters, the model allowed robust parameter estimation from the force data due to the convergence to identical values from different initial estimates. Also, this model was the first to be tested on muscles in different physiological states. One advantage of this model was that it could predict muscle fatigue. The 1998 model was also successful with human muscles at varying lengths. Different from the initial model, the quality of the force predictions did not depend on the twitch contraction times of the muscles. (49)

Of the four model parameters, A directly modulates the gain of the force. Thus, decreased A for fatigued muscle or muscle placed at short length is expected. The relaxation of the force is primarily determined by τ_1. That is because the role of τ_2 decreases quickly with the force-relaxation decline of C_N, which always precedes the force relaxation. The parameter τ_c is the characteristic time for C_m to peak and to go to zero, however interpretation of

changes across difficult conditions is unclear. Many underlying physiological steps, such as Ca^{2+} binding to and dissociation from troponin, may distort the time course of C_N. In the force equation, the sum of τ_1 and some fractional multiple of τ_2 gives the overall rise time of force. When muscles were stimulated with constant frequency trains, a decreased rise time of force was observed as fatigue onset. However, no difference in rise time was observed between the fatigued and the nonfatigued muscles upon variable frequency train stimulation, which was consistent with previous findings. (49)

For human muscles under fatigue or at short length, the major limitation of the 1998 model is that separate sets of parameter values were needed for CFTs and VFTs. However human muscles held at longer lengths and without fatigue required only one set of parameter values. Yet, the model did not necessarily identify the input pattern that generated the maximal force-time integral for this condition. Similarly, the 1998 model routinely underestimated the forces with long IPIs and overestimated the forces with short IPIs. These shortcomings were attributed to some ignored physiological steps, such as nonuniform amounts of divalent calcium that may be released as each pulse of a stimulus train passes. (49)

As the 1998 two-step model of Ding ignored many physiological details, such as the nonlinear summation of calcium transients in single muscle fibers stimulated with doublets, Ding et al (50) proposed the R model. This was based on the work of Duchateau and Hainaut (53). They investigated the force summation from human adductor pollicis muscles triggered by paired stimuli at

different IPIs ranging from 5 to 200 ms. Those results showed that the forces generated by the doublet trains were greater than the sum of two individual twitches. Furthermore, this force enhancement from the second pulse was highest when the IPI was 5 ms and declined exponentially with increases of the IPI. The enhanced force of the paired stimuli was suggested to be due to the enhanced release of divalent calcium by the second pulse (53). In the R model, a factor R_i was introduced to account for the nonlinear summation. (50) Therefore, Ding et al modified the two-step model by adding a factor

$$R_i = 1 + (R_0 - 1)e^{\frac{-(t_i - t_{i-1})}{\tau_c}} \tag{4-9}$$

where R_i is a scaling term that accounts for the differences in the degree of activation by each pulse relative to the first pulse of the train. The analytic solution of C_N goes to

$$C_N = \frac{1}{\tau_c} \sum_{i=1}^{n} R_i \exp\left(-\frac{t - t_i}{\tau_c}\right) \tag{4-10}$$

for i=1 and R_1=1. The magnitude of the enhancement is characterized by R_0, and its duration is characterized by τ_c.

Below is the complete, R model of muscle force derived by Ding and colleagues. (50)

$$\frac{dF}{dt} = \mathrm{A}\frac{\mathrm{C_N}}{k_m + \mathrm{C_N}} - \frac{F(t)}{\tau_1 + \tau_2 \frac{\mathrm{C_N}}{k_m + \mathrm{C_N}}} \tag{4-11}$$

$$R_i = 1 + (R_0 - 1)e^{\frac{-(t_i - t_{i-1})}{\tau_c}} \quad (4\text{-}12)$$

$$C_N = \frac{1}{\tau_c}\sum_{i=1}^{n} R_i \exp\left(-\frac{t - t_i}{\tau_c}\right) \quad (4\text{-}13)$$

Although the Ding R model accurately predicted isometric force for gastrocnemius and soleus muscles during brief trains of stimulation, it failed to predict force from long-train stimulations. It was found that when the muscle was stimulated with long trains, the model overestimated the higher frequency force output for both fast-contracting gastrocnemius and slow-contracting soleus and underestimated the lower frequency force response for soleus muscle. One of the limitations of this model is that it does not account for parameters that vary with time. It was suggested that better curve fitting and predictions of the data from long trains may require the model to vary several parameters during the contraction. Modeling the forces from the long train stimulation patterns was beyond the scope of this particular study. Thus, the changes to the model that are necessary to predict the force generated under long train stimulation were not explored. Furthermore, the original model cannot predict forces during nonisometric contractions because the force-velocity and length-tension relationships were not factored into the formulation. Finally, Ding and colleagues suggest that the model be modified if it is to predict the response of any muscle during fatigue-inducing repetitive activations. (50) However, they demonstrated that the parameter relationships found for able-bodied muscle did not apply to paralyzed muscle. (51)

The investigators further hypothesized that the model would accurately predict force response to long-train stimulation for patients with spinal cord injury. The hypothesis was test over a wide range of input frequencies and stimulation patterns in both fresh and fatigued states using data collected from paralyzed human quadriceps femoris muscles. It was found that the predictions from the force model explained more than 90% and 80% of the variance of the collected force profiles when the muscles were fresh and fatigued, respectively. Hence, the model was shown to have successfully calculated relationships between force and frequency for fresh and fatigued muscles to three varieties of input trains. (55)

Subsequent to spinal cord injury, paralyzed muscles typically gradually transform from type I to type II fibers, resulting in a predominance of fast fatigable muscle fibers. Fast, type II fibers have faster calcium dynamics, resulting from both faster calcium release and uptake. (157, 158) This has been shown to be consistent with the remarkably decreased τ_c values for paralyzed than for nonparalyzed subjects. Parameter A, the gain, was also significantly smaller for paralyzed subjects. This result is physiologically consistent with decreased sustained contractile force due to atrophy after denervation of muscle. (55)

In the Ding model, R_0 is denoted as the nonlinear summation of the transient current of divalent calcium in single muscle fibers in response to doublet stimulation. Hence, the parameter has been suggested to explain the increase in force generated by inputs containing doublets. Hence, model has shown a greater value of R_0 for paralyzed subjects. That conclusion is also supported by

previous studies that have shown that the paralyzed human thenar muscles of paralyzed subjects have greater force augmentation from doublets than nonparalyzed subjects. Despite the marked structural and functional differences between nonparalyzed and paralyzed quadriceps femoris muscles the model with slight adjustments in the procedure employed in parametric identification, predicted force with comparable accuracy for paralyzed subjects. This suggests the model to be robust. (55)

It was found that, even for paralyzed muscle, the model only needed force responses to two brief stimulation trains to identify the parameter values and to predict force response to inputs over a wide range of frequencies and patterns. The robustness and simplicity of this model render favorable for electrostimulation applications by facilitating parametric identification for each patient rapidly, fast identification of schemes for optimal stimulation, and accurate feedforward estimation. It was, however, recognized that the model only successfully predicted the force in quadriceps femoris muscle at one isometric length and at one angle of the knee joint. (55)

However, a relationship was found between R_0 and k_m. It was determined to be linear with $R_0=k_m+1.04$. Yet, the authors caution that this relationship needs to be investigated further before applying it to other muscles, different study cohorts, or other physiological conditions. According to Ding et al (55), there seems to be physiologic credence to the R_0-k_m relationship, as it warrants examination with respect to the three physiological aspects of muscle fatigue, muscle length, and fiber type. K_m models the calcium sensitivity of the sigmoidal

force-calcium relationship and has a partial contribution from the troponin sensitivity. Hence, a smaller k_m value transduces to increased sensitivity of force to calcium. R_0 models increased calcium release from the SR during fatigue. As a result, k_m and R_0 increase with fatigue from doublet stimulation. Elevated release of calcium with elevated muscle stiffness have been proposed as the primary mechanisms behind the nonlinear summation in force by doublets with respect to twitches A greater R_0 value translates into greater nonlinear summation in force. (55)

According to Frey-Law and Shields (66) chronically paralyzed human soleus force profiles were most accurately predicted by the original Ding R model (50). With that model and a doublet ramp input stimulus, soleus muscle forces from chronically paralyzed human muscle were used for parameter optimization. The predictive accuracy was assessed relative to a less complex model and a linear model for constant, doublet, and dual doublet stimulation trains at 5, 10, and 20 pps. However, to make appropriate comparisons between the models, one parameterization approach was required. The doublet ramp, based on the work of Bobet and Stein (17), is comprised of a range of frequencies (5, 7.5, 10, 15, and 20 pps, with 167 pps doublets) over a duration of less than 1500 milliseconds. This unique waveform provides on average equal time at all stimulation frequencies to ameliorate the bias from any specific frequency. (66)

In the findings of Frey Law and Shields (66), it was remarkable that the more complex Ding model predicted only two specific force properties, time to peak tension (TPT) and half-relaxation time (½RT), better than a second-order

nonlinear force model. This contradicted the assumption that the Ding-type model might represent muscle force properties with greater resolution than less complex models. Experimentally, the doublet produced substantially greater additional force at 5 pps than at 20 pps. The Ding model decreased output from doublets with increasing frequency. The second-order nonlinear model predicted the hysteretic muscle property better than the Ding model despite the presence of R_i, However, the largest differences between this study and the work of Ding et al (50) were for A, τ_2, and R_0. However, A is the force gain, which should vary with differences in activation amplitude, cross-sectional area of muscle, and joint angle. The linear relationship between R_0 and k_m was neither observed nor supported by a sensitivity analysis. (66) The values for τ_2 previously ranged from 124 to 1564 ms in nonparalyzed quadriceps muscle (50-56). In paralyzed human soleus muscle, the optimal values for τ_2 varied from 58 to 78 ms. This discrepancy is likely due to differences in muscle velocity characteristics between the quadriceps and soleus, variations in experimental activation of the muscle, changes in the characteristics of chronically paralyzed muscle, and/or the optimization techniques employed for parameter estimation. (66)

Further work with doublet stimulation found that the force-frequency relationship shifted leftward after spinal cord injury. This is indicative of the enhancements in the twitch-to-tetanus ratio known to exist in paralyzed muscle. Posttetanic potentiation occurred to a greater degree in subjects with paralyzed muscle (20%) than in subjects with nonparalyzed muscle (7%). Upon normalization, contractile speeds reflected well-known changes of paralyzed

muscle in the direction toward fast fatigable muscle. The doublet stimulation strategy provided consistent high-resolution measurements of muscle dynamics that showed remarkable differences between paralyzed and nonparalyzed muscle without causing fatigue. (172)

Table 4-1. List of parameters for Ding muscle force model.

Symbol	Unit	Definition
C_N		Normalized amount of Ca^{2+}-troponin complex
F	N	Mechanical force
t_i	ms	Time of the ith stimulation
N		Total number of stimuli in the train before time t_i
t_p	ms	Time of the pth data point
t_q	ms	Time of the qth set of force model parameter set
τ_c	ms	Time constant controlling the rise and decay of C_N
R_0		Mathematical term characterizing the magnitude of enhancement in C_n from the following stimuli
A	N/ms	Scaling factor
τ_1	ms	Time constant of force decline at the absence of strongly bound cross-bridges
τ_2	ms	Time constant of force decline due to the extra friction between actin and myosin resulting from the presence of cross-bridges
h	ms	Integration step

4.5.2 Fatigue model

Below is an early model of muscle fatigue proposed by Ding and colleagues. It is an extended R model (50, 51).

$$\frac{dF}{dt} = \mathrm{A}\frac{\mathrm{C_N}}{k_m + \mathrm{C_N}} - \frac{F(t)}{\tau_1 + \tau_2 \frac{\mathrm{C_N}}{k_m + \mathrm{C_N}}} \tag{4-14}$$

$$R_i = 1 + (R_0 - 1)e^{\frac{-(t_i - t_{i-1})}{\tau_c}} \tag{4-15}$$

$$\frac{d\mathrm{C_N}}{dt} = \frac{1}{\tau_c}\sum_{i=1}^{n} R_i \exp\left(-\frac{t - t_i}{\tau_c}\right) - \frac{\mathrm{C_N}}{\tau_c} \tag{4-16}$$

$$\frac{d\mathrm{A}}{dt} = \frac{-(\mathrm{A} - \mathrm{A}_{rest})}{\tau_{fat}} + \alpha_{\mathrm{A}} F \tag{4-17}$$

$$\frac{dR_0}{dt} = \frac{-(R_0 - R_{0rest})}{\tau_{fat}} + \alpha_{R0} F \tag{4-18}$$

$$\frac{d\tau_c}{dt} = \frac{-(\tau_c - \tau_{c,rest})}{\tau_{fat}} + \alpha_{\tau_c} F \tag{4-19}$$

Fatigue is a major limitation to the clinical application of neuromuscular electrical stimulation. The electrical stimulation pattern used influences muscle force and fatigue. Determining the activation pattern that maximizes force and

minimizes fatigue for each individual is clinically vital. (38) Mathematical models that predict muscle forces and fatigue generated by a variety of activation patterns would aid the search for optimal patterns. To begin this process, Ding and colleagues introduced a four-parameter fatigue model that, as a extension of their original force model, that predicts the low-frequency muscle fatigue caused by various stimulation patterns on different days during isometric contractions. This fatigue model was shown to be robust by accounting for 90% of the difference in forces produced by several types of fatigue tests. The model forces at the end of fatigue testing were seen to differ from experimental forces by just 9%. Thus, the Ding model of muscle fatigue demonstrated the potential for predicting muscle fatigue in response to a wide range of stimulation patterns. (51)

A fundamental assumption is that τ_c has the same value for fatigued and nonfatigued muscles. Yet, it has been previously observed that there is a prolonged Ca^{2+} transient with fatigued muscles which might result from depressed Ca^{2+} uptake, reduced rate of Ca^{2+} release, and elevated resting intracellular Ca^{2+} concentration. Conversely, the prolonged relaxation, which is controlled by τ_1 and τ_2 in the force model, could also be modeled by the slower Ca^{2+} dynamics with the fatigued muscle. For fatigued muscles, nevertheless, Ding et al fixed τ_1 and τ_0 at the values obtained in the non-fatigued condition and fit the values of the other three parameters (A, R_0, and τ_i) to the experimental forces. (51)

The Ding group found substantial changes in the values of A, R_0, and τ_e as the muscle transitioned from nonfatigued to fatigued states. Their approach to modeling fatigue was to construct a model that could modify the values of the parameters during fatigue. It has been previously shown that, during sustained isometric contractions, the rate and amount of fatigue are proportional to the force-time integral generated by the muscle in response to the fatiguing stimulus. Hence, instantaneous force was used as the driving function in the Ding fatigue model. (51)

The major shortcoming of the Ding fatigue model is that it needs two different stimulus combinations to parameterize the model for nonfatigued and fatigued muscles. This makes it impossible to both model fatigue and to predict muscle forces under different fatigue levels In addition, the Ding fatigue model was validated using data from only human quadriceps femoris muscles with protocols consisting of trains with a wide range of frequencies (10 to 40 pps) and activation patterns (CFT, VFT, and DFT). In general, it was found that the fatigue model predicted well the forces generated by the fatigue protocols with different input patterns on different days. (51)

It was also observed that the fatigue model overestimated the force response to the first train in a constant-frequency protocol and underestimated the responses to the first trains in the variable- and doublet-frequency protocols. Because the fatigue model used the nonfatigued force model parameter values when the initial forces for that session were calculated, the misestimation observed at the onset of the fatigue protocol was due to the inaccuracy of

predictions in the original force model. Modification of the force model and a more sophisticated modeling of R_0 in the fatigue model was recommended. This can include adding another differential equation to enable a shorter time constant to capture the changes in R_0 at the beginning of fatigue. Such modifications may be necessary, according to Ding et al (51), to obtain better predictive ability in inputs of high frequency or those stimuli that contain doublets. This is consistent with the fact that muscle fatigue depends on many factors including extrinsic stimulation parameters such as frequency, duty cycle, and activation patterns. (38, 51)

Further fatigue model development showed that simulated k_m did not saturate in a maximal isometric contraction. Hence k_m was varied because it mathematically defines the voltage sensitivity of the strongly bound cross-bridges in the presence of the calcium-troponin complex. In addition, a pilot study showed that the model produced the best predictions when k_m ranged between 1.5 and 4. Moreover, fatigue in human skeletal muscle is accompanied by changes in the contractile apparatus of the muscle, including a slowing of the calcium dynamics (τ_c), changing in sensitivity of force to calcium (k_m), decreasing gain (A), and decreased force relaxation (τ_1 and τ_2). In addition, enhanced calcium sensitivity of muscle fibers stimulated with doublets to force during fatigue has been observed. This enhancement R_0 decays with the interpulse interval when muscles are fatigued. This ultimately suggests that τ_1 plays a far greater role in modulating force relaxation than does τ_2 during fatigue. (52)

A limitation of the earlier fatigue model was that it did not accurately depict the changes in R_0 at the onset of fatigue. Hence, the Equations 4-20 through 4-22 were inserted:

$$R_0 = R_0^{<1>} + R_0^{<2>} \quad (4\text{-}20)$$

$$\frac{dR_0^{<1>}}{dt} = \frac{-(R_0^{<1>} - R_{0rest}^{<1>})}{\tau_{R0}} - \alpha_{R0} * F \quad (4\text{-}21)$$

$$\frac{dR_0^{<2>}}{dt} = \frac{-(R_0^{<2>} - R_{0rest}^{<2>})}{\tau_{fat}} - \alpha_{R0} * F \quad (4\text{-}22)$$

where $R_{0rest}^{<1>}$ and $R_{0rest}^{<2>}$ were the nonfatigued values. In addition, k_m was fixed for nonfatigued muscle but varied for fatigued muscle. The equation for τ_c was replaced by $d\tau_1/dt=-(\tau_1-\tau_{1rest})/\tau_{fat}-\alpha_{\tau 1}*F$ where $\alpha_{\tau 1}$ was the coefficient for force and τ_1, and τ_{1rest} was the value for nonfatigued muscle. Hence, this version of the fatigue model was modulated by five free parameters α_A, α_{R0}, $\alpha_{\tau 1}$, τ_{fat}, and τ_{R0}. (52)

Furthermore, according to Ding et al (52) overestimation in the model resulted from setting k_m too high. A dynamic k_m yielded values less than one. This allowed for faster progression of C_N than if $k_m=1$. This change improved the prediction of fatigue stimulation with higher-frequency trains. Additionally, to remedy the previous error in assuming exponential behavior for R_0, the additional time constant, τ_{R0}, was added to the model to depict the change in R_0 at fatigue onset. This addition improved the resolution of R_0 and in predicting fatigue profiles taken at peak force.

Table 4-2. List of parameters for early Ding muscle fatigue model for nonparalyzed muscle.

Symbol	Unit	Definition
C_N		Normalized amount of Ca^{2+}-troponin complex
F	N	Mechanical force
t_i	ms	Time of the ith stimulation
N		Total number of stimuli in the train before time t_i
t_p	ms	Time of the pth data point
t_q	ms	Time of the qth set of force model parameter set
τ_c	ms	Time constant controlling the rise and decay of C_N
R_0		Mathematical term characterizing the magnitude of enhancement in C_N from the subsequent stimuli
A	N/ms	Scaling factor
τ_1	ms	Time constant of force decline at the absence of strongly bound cross-bridges
τ_2	ms	Time constant of force decline due to the extra friction between actin and myosin resulting from the presence of cross-bridges
α_A	ms^{-2}	Coefficient for force model parameter A in the fatigue model
α_{R0}	ms^{-1} $^*N$	Coefficient for force model parameter R_0 in the fatigue model
$\alpha_{\tau c}$	N^{-1}	Coefficient for force model parameter τ_c in the fatigue model
τ_{fat}	s	Time constant controlling the recovery of the three force model parameters (A, R_0, and τ_c) during fatigue
h	ms	Integration step

Additional work by Ding and colleagues (53) evaluated the effect of resting

times on fatigue. Three resting times, 500, 750, and 1000 ms, were investigated. The model predicted that fatigue was a decreasing function of the resting time. At a resting time was 750 ms, the model showed that the DFT80 pattern was most fatiguing and the VFT80 pattern was least fatiguing and was consistent with the experiment. This trend was remarkably different when the resting time was less.

One major limitation with this fatigue model was that the input stimulus trains used to verify the model contained only six pulses. Hence, the forces produced were in the rising generation phase, regardless of the input characteristics. Forces produced by trains longer than six pulses, as in FES, showed distinct generation and maintenance phases. It has been shown that the force-generation phase is more energy demanding and the more dominant contributor to muscle fatigue. This suggests that the fatigue model may need to be modified to predict fatigue elicited by stimulation trains with greater than six pulses. (53) Further evaluation by Ding et al (54) showed that the structure the previous force model was robust enough to predict the forces from stimuli lasting about one second. The significance of this work lies in the ability of the model to predict force responses to inputs with a wide range of characteristics as long as fatigue does not onset.

For paralyzed muscle, a later version of the Ding force-fatigue model (55) investigates k_m rather than R_0 as the varying parameter. Hence the auxiliary equations changed to:

$$k_m = k_m^{<1>} + k_m^{<2>} \tag{4-23}$$

$$\frac{dk_m^{<1>}}{dt} = \frac{-(k_m^{<1>} - k_{mrest}^{<1>})}{\tau_{km}} - \alpha_{km} * F \quad (4\text{-}24)$$

$$\frac{dk_m^{<2>}}{dt} = \frac{-(k_m^{<2>} - k_{mrest}^{<2>})}{\tau_{fat}} - \alpha_{km} * F \quad (4\text{-}25)$$

where $k_{mrest}^{<1>}$ and $k_{mrest}^{<2>}$ were the nonfatigued values. In addition, τ_1 was fixed at the nonfatigued value but varied during fatigue. Hence the equation for τ_c was replaced by $d\tau_1/dt=-(\tau_1-\tau_{1rest})/\tau_{fat}-\alpha_{\tau1}*F$ where $\alpha_{\tau1}$ was the coefficient for force and τ_1 and τ_{1rest} was the nonfatigued muscle value. This fatigue model was modulated by the five free parameters of α_A, α_{km}, $\alpha_{\tau1}$, τ_{fat}, and τ_{km} and was found to be robust across stimuli with higher frequencies. The three force-driving coefficients in this fatigue model, α_A, α_{km}, and $\alpha_{\tau1}$, characterize the effect of short-term fatigue on the force-model parameters A, k_m, and τ_1. No correlation was found between any pair of the coefficient set. The lack of correlation suggests that contractile properties of muscle vary significantly during fatigue. The findings further demonstrate that fatigue is a complex physiological process. (55)

The best functional electrical stimulation system necessitates a quantitative model to provide predictive control of stimulation parameters so that they are optimized for different users over a wide range of physiological conditions, muscle groups, and activities. It was hypothesized that the previous model would accurately predict force responses to long stimulation trains for paralyzed subjects. According to Ding et al (56), the revised mathematical model calculated the force responses from various inputs with different characteristics.

The predictions of the model explained greater than 90% and 80% of the variance in the recorded data for fresh and fatigued muscles, respectively. The calculated force-time integrals and peak forces were well-correlated with the experimental correspondents with intraclass coefficients mostly above 0.95.

Compared to data from nonparalyzed muscle, the revised force-fatigue model demonstrated a larger R_0 for paralyzed muscle. This contradicts experimental observations of greater augmentation by doublet force in cat muscle. Yet, it has been shown that the paralyzed human thenar muscles demonstrate increased augmentation of force from doublets than do nonparalyzed muscles. This suggests that paralyzed muscle has a larger R_0 value. Yet, the nonparalyzed muscle data used as control in this study were highly potentiated, whereas the paralyzed muscle data was not. Potentiation has also been demonstrated to decrease the nonlinear summation of force from doublets. (56)

Decreased parameter values for k_m, τ_1, and τ_2 were expected for paralyzed muscle, according to the Ding group (56). However, the findings indicated no difference in these parameter values between the two muscle health states. The absence of differences could have resulted from the potentiation of nonparalyzed muscle but not paralyzed muscle, a confounding among parameters, or both. Potentiation has been demonstrated to elevate the divalent calcium sensitivity in muscle. Hence, potentiated nonparalyzed muscles may have similar k_m values as paralyzed muscle. This is because the potentiation of former has a similar effect on the calcium sensitivity as the greater percentage of

type II fibers does in the latter. Because potentiation does not affect muscle contractile speed, the primary explanation for similar values for τ_1 and τ_2 between experimental groups was suggested as the compensation or confounding effect between τ_c, τ_1, and τ_2. Despite the significant differences between nonparalyzed and paralyzed quadriceps femoris muscles, the model with minor modifications in parameter estimation performed equally between the two experimental groups. This suggests that the model is robust. For either the fresh or fatigued condition, the model only required responses to two brief stimulation trains for parameter estimation and force prediction. However, Ding and colleagues (56) recognize that the particular model only predicted the force responses for quadriceps femoris muscle at one length under isometric conditions at one knee joint angle.

4.5.3 The nature of the problem with the Ding models

The Ding models are being modified with a dynamic characterization of the divalent calcium current to provide better understanding of the physiology of force generation and fatigue in the chronically paralyzed human soleus. This increased understanding will lead to the safer, more effective therapeutic stress protocols for paralyzed lower extremities.

Current models misestimate force and fatigue by assuming that the concentration divalent calcium is constant during a muscle contraction. This assumption appears, at best, to be an empirical derivation. There appears to be no theoretical justification for such an assumption. Hence, it is believed that a dynamic characterization of the calcium current in paralyzed muscle, derived from first principles of mathematics, chemistry, and physics, will yield information

about the underlying physiological mechanisms of fatigue in paralyzed human muscle as a process of evolution that is heretofore unknown. The proce4wssses can be represented mathematically by diffusion functions, which are discussed in the next chapter. Moreover, the underlying physicochemical principles of relevance are autocatalysis, the Principle of Le Chatelier, macromolecular crowding, and fractal power laws of Michaelis-Menten reaction kinetics and are discussed in Appendix A as well as Appendix E.

In the Ding models, the quantity C_N is assumed to behave according to ideal Michaelis-Menten kinetics in muscle force generation. This scheme of reaction kinetics relies on the law of mass action derived from Fickian diffusion and thermodynamically molecular random collision. However, many biologic processes significantly diverge from such conditions. For example, cytoplasm behaves more like a solid than a Newtonian fluid due to its very high solute concentration. This can severely hinder molecular diffusion or collision. (107,191) Hence, the hindrance of molecular mobility requires modifications to the law of mass-action and Michaelis-Menten kinetics to better reflect certain physiologic situations such as calcium dynamics in fatiguing paralyzed muscle.

In the early Ding models (50, 51), the parameters R_0 and k_m are treated as scalar parameters. Yet, they are defined respectively as a quantitative measure of the nonlinear summation of the Ca^{2+} from preceding pulses and the voltage sensitivity of the calcium channels in the sarcoplasmic reticulum. In addition to the empirical derivations, the constructs of the definitions are themselves mathematically inconsistent at best. A scalar is a linear element. There is no

nonlinearity or dynamics associated with such an element. Hence, these parameters would yield better prediction of force and fatigue if they were modified in such a way that is congruent with the physiological reality of equilibrating chemical reactions that occur within a contracting muscle.

To demonstrate the Ding force and fatigue models in MATLAB, profiles for fresh and fatigued muscle were generated using parameters from Frey Law and Shields (66) and Ding (56) via code specially written for this study. In the figures, the force curve is included along with the curve for C_N. For the fatigue model, plots of A, R_0, and τ_c are also included. From this, the behavior of the free parameters in the Ding models may be seen as a function of time.

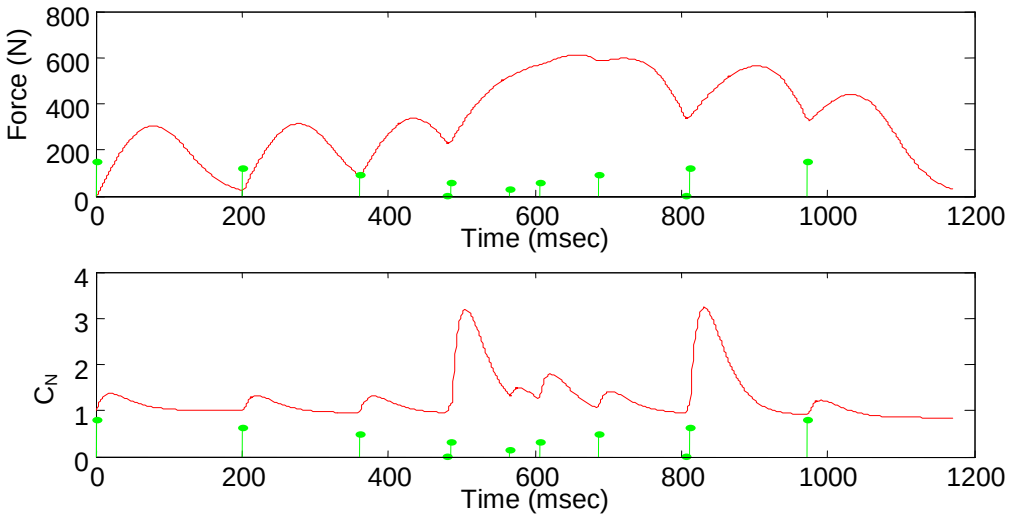

Figure 4-16. Duplication of force response and C_N from a doublet ramp using the Ding force model. This shows that the Ding force model does a reasonable job at calculating C_N even with a constant R_0. However, the peaks in the C_N curve are not uniform in magnitude and do not necessarily correspond as shown in the literature with each pulse of the doublet ramp stimulus.

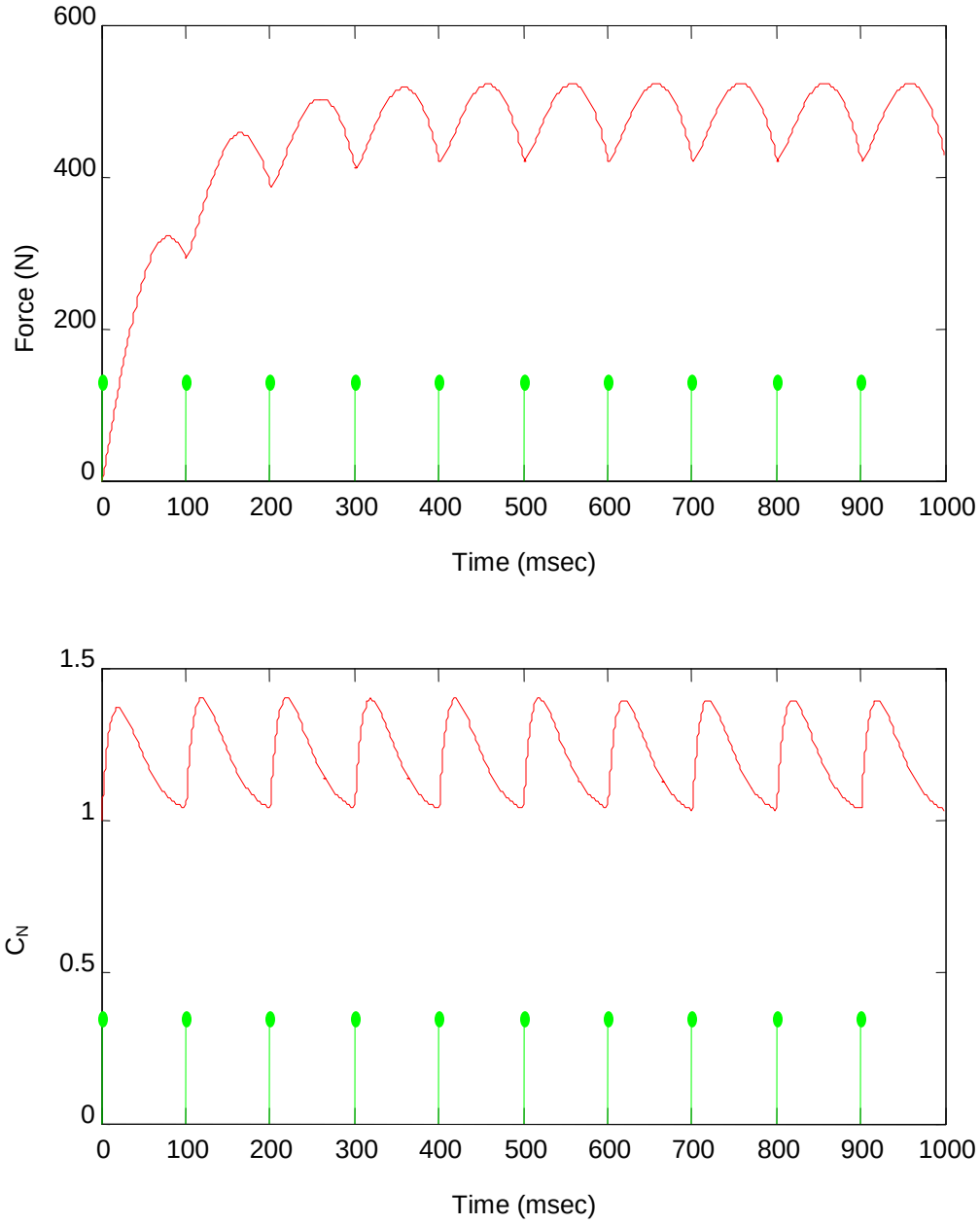

Figure 4-17. Duplication of a fatiguing contraction from a 10 CT input using the Ding fatigue model. It is shown that in the Ding fatigue model, the force tetani remain unfused. Furthermore, the peaks in the C_N curve remain at relatively high magnitude. Nevertheless, the original parameters of Ding et al (56) were used in this simulation. This suggests that an adequate accounting of the calcium dynamics during fatigue is lacking in this model.

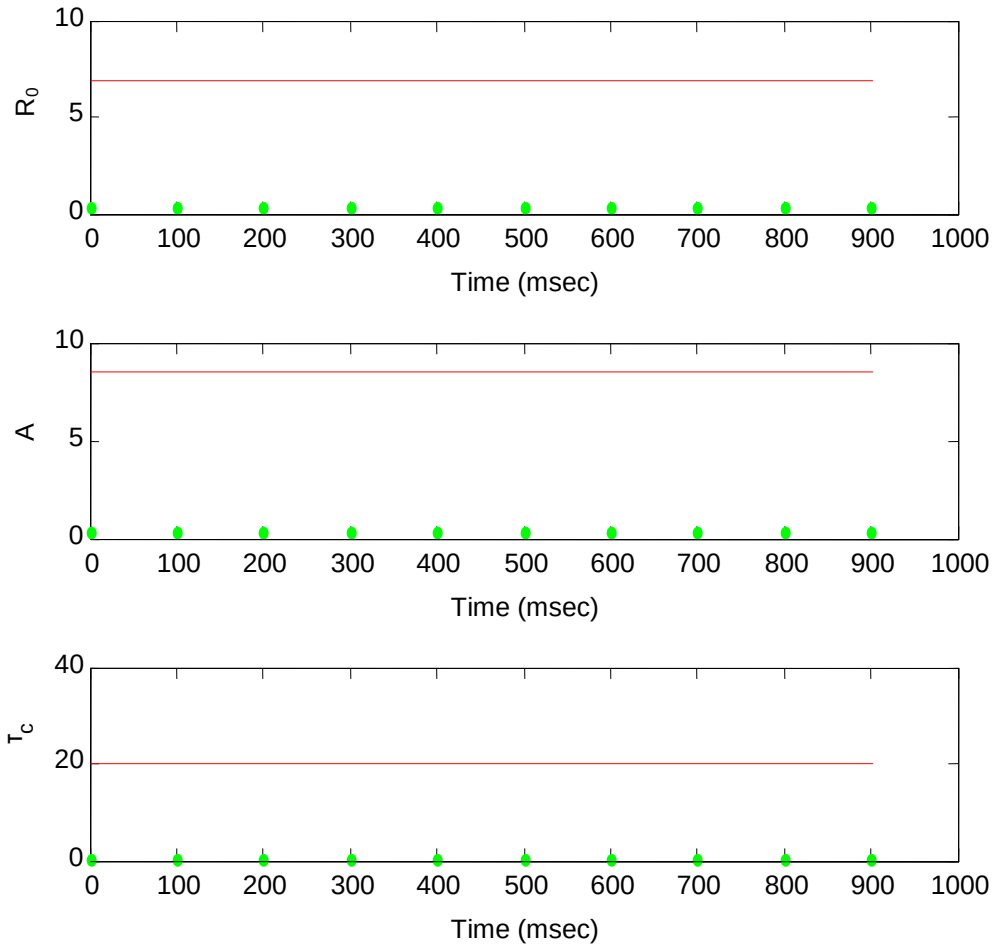

Figure 4-18. Behavior of A, R_0, and τ_c in the Ding fatigue model from a 10 CT input. All parameters remain constant throughout a contraction.

In the Ding fatigue model, the parameters remain constant throughout a fatiguing contraction after a very short transient period. This lack of parameter dynamics may explain the poor performance of the model in predicting fatigue in paralyzed muscle. Large errors are generated as a result (unpublished observations).

4.5.4 Criticism of statistical methods

In the work of Ding et al (48-56), correlation coefficients were calculated to determine goodness-of-fit for the different models. The correlation coefficient by itself may not necessarily be the best way to determine goodness-of-fit. It is not clear in the literature what the Ding models are being correlated with. It may be possible to find correlation between model and a particular subset of parameters. Yet, that would imply that a different set of questions are being asked. The key point to remember for data analysis in these types of studies is that agreement, whether or not correlation is included in a goodness-of-fit metric, between a model and experimental data would be more germane and appropriate.

CHAPTER 5: A THEORY OF CALCIUM CURRENT IN PARALYZED MUSCLE

The goal of this thesis is be test whether the concept missing from present models, and thus the present understanding of muscle physiology, is the dynamic behavior of divalent calcium during induced muscle contraction. Current models assume that the calcium dynamics in electrically stimulated muscle is quasistatic if not constant. In addition, it is hypothesized that the calcium dynamics in denervated muscle are different than the calcium dynamics in intact muscle in fresh and fatigued states. If the behavior of calcium current can be understood as a series of growth, diffusion, and decay processes, muscle force and low-frequency fatigue can be more accurately predicted over the time course of response to neuromuscular electrical stimulation.

5.1 A mathematical construct of growth, diffusion, and decay in muscle

5.1.1 A theory of diffusion

There may be a twofold purpose of diffusion functions. First they may serve as purely mathematical devices which describe the asymptotic approach towards saturation throughout the diffusion process. Hence, the model-building problem is to determine the growth curve that best fits a series of empirical observations over the whole diffusion process. Yet, there is limited value of these models for such purposes since they require a high level of aggregate behavior. Hence, they are unable to convey detailed information about the characteristics of the underlying diffusion process. (113)

The second use of diffusion functions is for making predictions of the continuation of an ongoing diffusion process. In this case, the problem is one of parameter estimation for a specific growth curve at the beginning of an actual process and then making predictions of the continuation by extrapolating the estimated function. However, the use of diffusion functions for prediction involves subtle complications. First, they have the same deficiencies as all extrapolation techniques. They are mechanistic, have minute explanatory power, and are in general wholly deterministic. Yet, the more fundamental problem is selecting the appropriate model. While the form of the overall growth curve is determined by the mathematical function employed, empirical diffusion curves demonstrate a plethora of shapes which are not readily categorized. The question then turns to how best to determine, the type of diffusion function for a particular case. Without basic understanding of underlying assumptions for each model as well as knowledge of specific diffusion characteristics, this choice often a matter of an educated guess. (113)

Two major forms of influence on the individual diffusion process may be distinguished. They are external and internal influence. The distinction arises from the characteristic of the source of influence. External influence denotes the direct influence on the innovation of an individual which a promoter exerts through various activities. It is termed external because it originates outside the set of adopters. Meanwhile, internal influence is the influence that the members of a system exert on each other due to their interaction. Examples of this are the physician who considers employing a new procedure for the first time may want

to first confer on the matter with colleagues and the young woman who wears trendy clothes to impress her peers. (108)

Another well-known growth/diffusion function is the modified exponential function. This model assumes that the instantaneous diffusion rate only varies with the remaining gap to the saturation level. Mathematically, this is stated as dy/dt=ay(N-y). Solving with respect to y and setting the initial condition equal to zero, the following diffusion function is $y(t)=N(1-e^{-at})$. (9, 113)

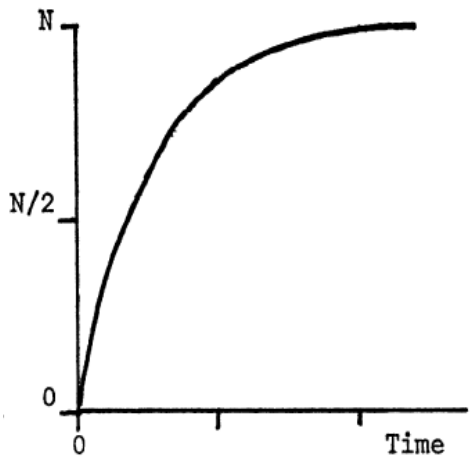

Figure 5-1. The modified exponential function. (113)

In many practical situations, as is demonstrated above, external and internal influence will superpose to yield a specific outcome of diffusion. However, the respective strengths of these two forces are not likely to be equal in all cases. In some situations, the dominant influence may originate from sources

outside the system. In other cases the influence that the constituents of a set exert on each other may dominate. In addition, theory supported by empirical data suggests that the characteristic of an innovation is a vital factor that underlies such differences. For example, a new fertilizer may be subject to intense debate among farmers. Thus, this would show high internal influence. However, this likely would not happen for a new brand of apple juice or laundry soap. (113)

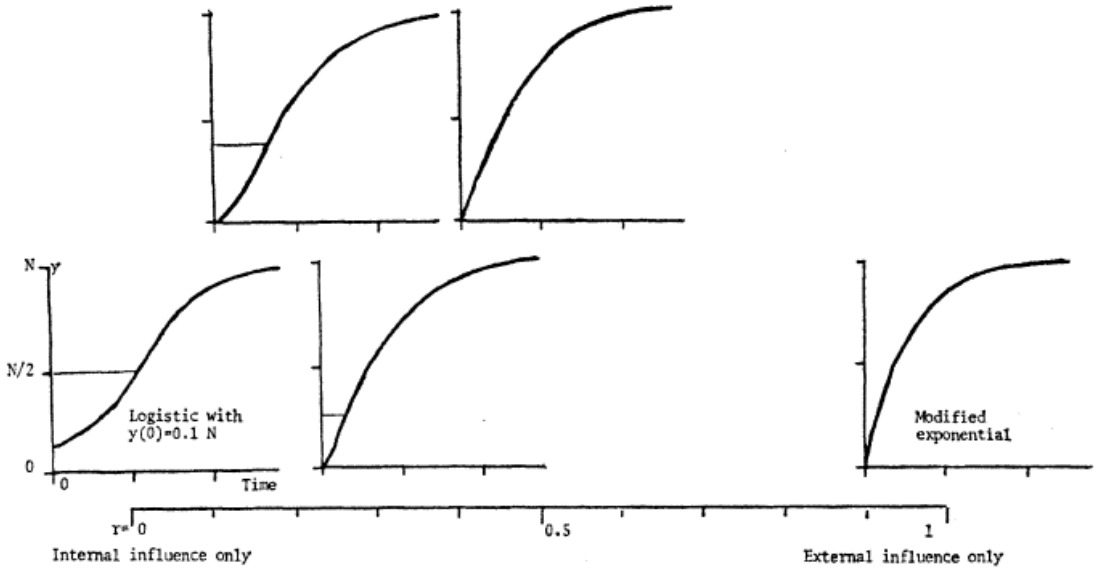

Figure 5-2. Diffusion curves for different combinations of external and internal influence. (113)

Implicit in many models of diffusion or growth is the assumption that diffusion occurs homogeneously, or that the impulse toward adoption remains constant throughout the time span. Lekvall and Wahlbin (108) state explicitly:

> "External and internal influence is assumed to be uniformly distributed…so that adopters and non-adopters are contacted in proportion to their current numbers in each time period."

Since decreasing or increasing stimulus effects may affect the skew of the diffusion curve, models should explicitly incorporate these effects. However, skew may arise from other factors. Hernes (78) classifies skew in the following way: 1) structural heterogeneity, when some capacity is differentially distributed in the population, such as a characteristic which varies among members who are successively exposed to a stimulus, 2) dynamic heterogeneity, when the population changes as the process goes on such as the change in income level, and 3) changing stimulus effect, when the impact of exposure to the stimulus varies with time. This can be thought of as a modulating effect of the stimulus itself over time. Or it can be considered with dynamic heterogeneity, as when non-adopters increase their resistance or susceptibility with repeated stimulation.

With respect to the sources of skew mentioned above, a diffusion process can be thought of in different ways. If the process is described as one of varying stimulus effect, the model can represent exponentially modulated impact. If the process is considered with respect to dynamic heterogeneity, the equation can represent some exponentially changing property of the adopters and non-adopters. However, if the diffusion is considered with respect to structural heterogeneity, the question of whether the distribution of a population property modulates the quality of interaction between adopters and non-adopters must be posed. Even with a constant distribution, the interaction quality may vary as subgroups of different resource levels consume more products. (78)

A general nonsymmetric function can be used to describe an S-shaped curve. It resembles the logistic function. Yet, its point of inflection is not the midpoint between zero and the upper asymptote. If b < 1, the curve has positive or right skew. If b > 1 the curve has negative or left skew. That models a process which is asymptotically faster than the logistic. When b = 1, the function is logistic. It was noted that the function can be flexibly used to generate an S-shaped curve as well as a J-shaped curve. (73) Furthermore, Lekvall and Wahlbin (113) summarized the phenomena with their statement:

> "Generally speaking, if the….network is dominated by external sources of influence the diffusion curve will approach the modified exponential function. If, on the other hand, internal [influence] is the most important influential factor, the curve will tend more towards the logistic type."

In the general case, the two processes described above can be combined in a manner similar to that of Lekvall and Wahlbin (113) and Coleman (34) into a Riccati equation. Often, the right skewing in diffusion processes can be assumed to be the specific outcome of the superposition of external and internal influences. Mathematically, this means that exponential and logistic processes are summed together. The inherent problem in diffusion models is that fitting them to aggregate data does not necessarily validate the models. Unless there is pre-existing knowledge of the strength of external and internal influences relative to each other, there is much difficulty in predicting the shape of a diffusion curve. (113) According to Hernes (78), often the logistic or the modified exponential models are not used in modeling due to poor curve-fitting. Nevertheless the

alternative functions or processes generate curves of the same general skew to the right.

There are many phenomena which can be approximately described by a first-order difference or differential equation. Studies of the dynamics of such models usually consist of determining static equilibrium solutions, and then conducting linearized analyses to ascertain their stability with respect to small disturbances. Explicitly nonlinear characteristics are usually not considered. Modern studies have shown that the very simplest nonlinear difference or differential equations can possess a variegated spectrum of behavior. These spectra can include stable points, cascades of stable cycles, and behavior that is in many ways indistinguishable from sample functions of random processes. (127)

A specific example is afforded by the “logistic” difference equation: $N_{t+1}=N_t(a-bN_t)$. In the limit b=0, it describes a population with purely exponential growth for a > 1. For b≠0, the quadratic nonlinearity generates a growth curve that contains a hump. The steepness of the hump is tuned by the parameter a. Despite its extreme simplicity, in practical applications the equation has the disadvantage that it restricts X to the interval 0<X<1. If X exceeds unity, subsequent iterations diverge towards infinity. This means that the population becomes extinct. Furthermore, F(X) in the equation attains a maximum value of a/4 (at X=0.5). Hence, the equation has significant dynamical behavior only if a<4. However, all trajectories converge to X=0 if a< 1. (127)

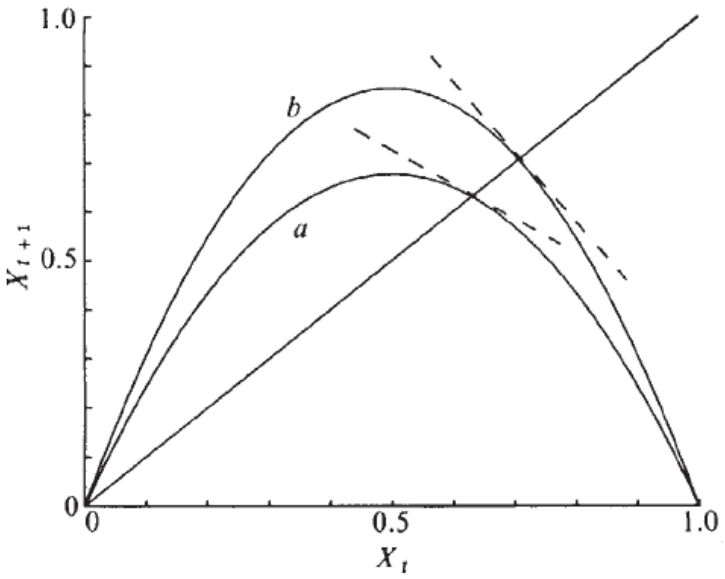

Figure 5-3. Trajectories of the “logistic” difference equation. (127)

In many cases of dissymmetrical sigmoids, however, congruence to observed data is inadequate. Some extensions of the formalism of the logistic law can be made towards a more general autonomous growth function. Buis (24) developed an approach that uses the growth diagram or trajectory. It was developed for the graphic description of the state variation of a growing system and uses: the instantaneous rate and the instantaneous acceleration as germane parameters. The two admissible state representations are derived from either the absolute rate V = dy/dt, or on the relative rate R = (1/y)(dy/dt) which has the effect of a logarithmic transformation. The trajectory is located in plane (V, Γ) or (R, Γ_R), respectively. The last parameter, Γ_R, is denoted as the relative acceleration, dR/dt.

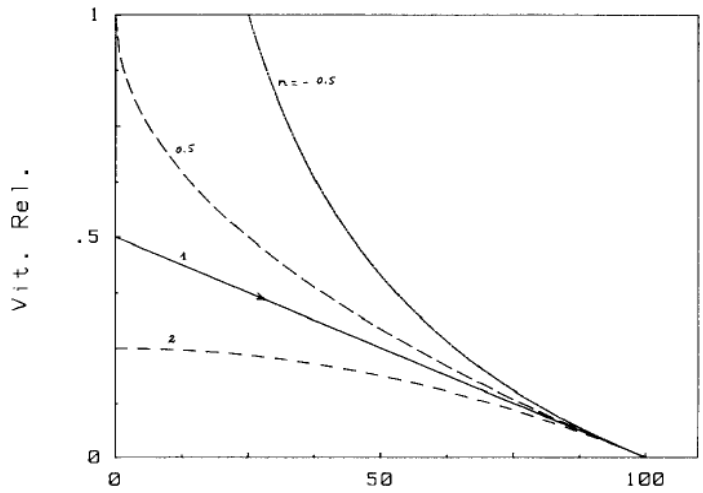

Figure 5-4. Variation of the relative rate, R, for different values of n. The case n=1 corresponds to the Verhulst logistic growth law. (24)

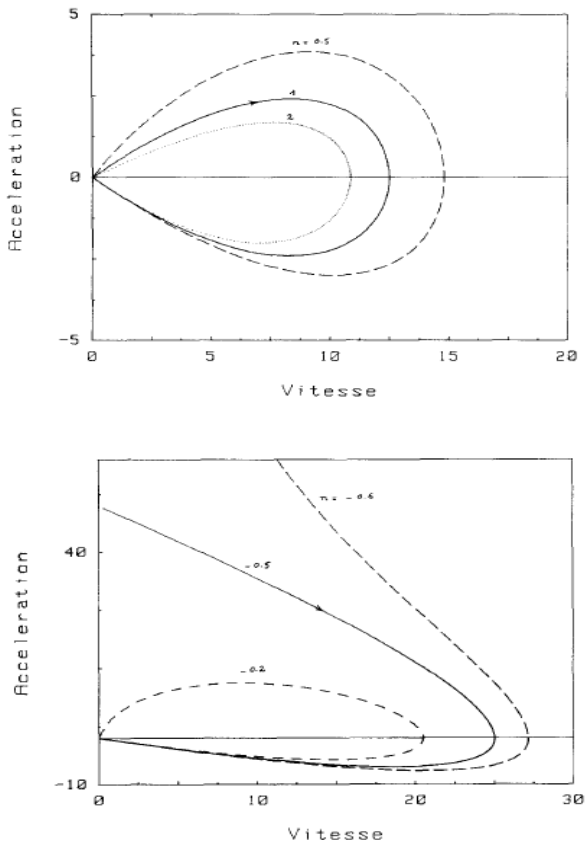

Figure 5-5. Logistic growth diagrams for different values of n. (24)

Buis (24) defines simple logistics as a linear decrease in the instantaneous specific rate of growth in relation to growth variable y:

$$R = k(\mathrm{A} - y) = \mathrm{a}\left(1 - \frac{y}{\mathrm{A}}\right) \tag{5-1}$$

with k, a and A > 0. A is the maximum value. Alternatively, the instantaneous absolute rate V can be expressed by a Riccati differential equation:

$$\mathrm{V} = ky(\mathrm{A} - y) = \mathrm{a}y\left(1 - \frac{y}{\mathrm{A}}\right) = \mathrm{a}y - \left(\frac{\mathrm{a}}{\mathrm{A}}\right)y^2 \tag{5-2}$$

Hence, the logistic law is parameterized in the second equation by a damping term known as the Verhulst “force retardatrice”. (24, 179, 180) In an additive model, V is proportional to y^2. However, in a multiplicative model, V is the product of the derivatives of the geometric and negative exponential laws which approximate logistic behavior. The approximations occur the beginning and at the end of growth, respectively. Thus, the absolute rate, V, can be written as a Taylor series:

$$\frac{dy}{dt} = f(y) = c_0 + c_1 y + c_2 y^2 + c_3 y^3 + ... \tag{5-3}$$

As f(y)=0 for y=0 and y=A, f(y) has two real, positive roots. The equation goes to a quadratic function $f(y)=c_1y-c_2y^2$ with c_1 and c_2 nonegative. Hence, the

logistic law of growth corresponds to a kind of minimum formalism, as meant by Verhulst with the equation for the decrease in R. (24, 179, 180)

5.1.2 Riccati-Bass diffusion model

The Riccati-Bass diffusion model was developed in the late 1960s by Frank Bass (10) and describes the process of how new products get adopted as an interaction between users and potential users. The model is widely used in all types of forecasting. Mathematically, the basic Bass diffusion equation is a Riccati differential equation (158) with constant coefficients. See Appendix A for the derivation of the Riccati differential equation.

The Bass model is formulated in the following manner:

$$\frac{f(t)}{1-F(t)} = p + qF(t) \qquad (5\text{-}4)$$

where:

$f(t)$ is the rate of change of the installed base fraction

$F(t)$ is the installed base fraction

m is the ultimate market potential

p is the coefficient of innovation

q is the coefficient of imitation

Sales $S(t)$ is the rate of change of adoption $f(t)$ multiplied by the ultimate market potential m:

$$S(t) = mf(t) \tag{5-5}$$

$$S(t) = m\frac{(p+q)^2}{p}\frac{e^{-(p+q)t}}{(1+\frac{q}{p}e^{-(p+q)t})^2} \tag{5-6}$$

The time of peak sales t^*

$$t^* = \frac{Ln\frac{q}{p}}{(p+q)} \tag{5-7}$$

In the original model (10), the coefficient p denotes the coefficient of innovation, external influence, or advertising effect. Meanwhile, the coefficient q is defined as the coefficient of imitation, internal influence, or word-of-mouth effect. Typical values of p and q have the following range. The mean value of p tends to be 0.03, and is often less than 0.01. Meanwhile, the mean value of q tends to be 0.38, with a typical range between 0.3 and 0.5

Norton and Bass (142) extended the model for sales of products with continuous repeat purchasing. The model formulated for three generations is below.

$$S_{1,t} = F(t_1)m_1(1-F(t_2)) \tag{5-8}$$

$$S_{2,t} = F(t_2)(m_2 + F(t_1)m_1)(1-F(t_3)) \tag{5-9}$$

$$S_{3,t} = F(t_3)(m_3 + F(t_2)(m_2 + F(t_1)m_1)) \tag{5-10}$$

where $$m_i = a_i M_i$$

M_i is the incremental number of ultimate adopters of the ith generation product

a_i is the average (continuous) repeat buying rate among adopters of the ith generation product

t_i is the time since the introduction of the ith generation product

$$F(t_i) = \frac{1 - e^{-(p+q)t_i}}{1 + \frac{q}{p} e^{-(p+q)t_i}} \qquad (5\text{-}11)$$

It has been found that the p and q terms are generally the same between successive generations. (142)

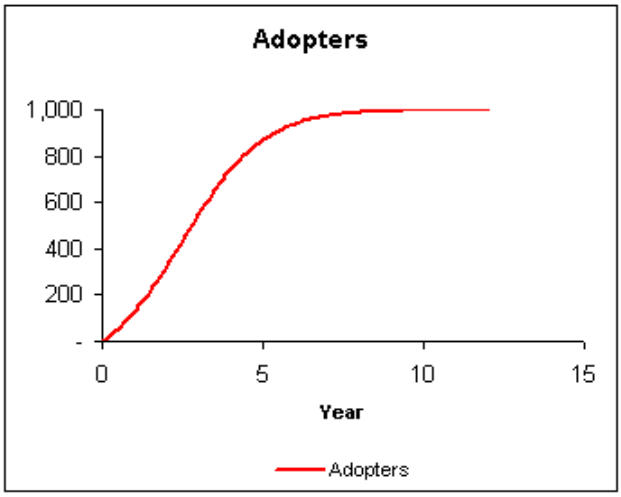

Figure 5-6. Graph of total adopters for product cycle. (10, 142)

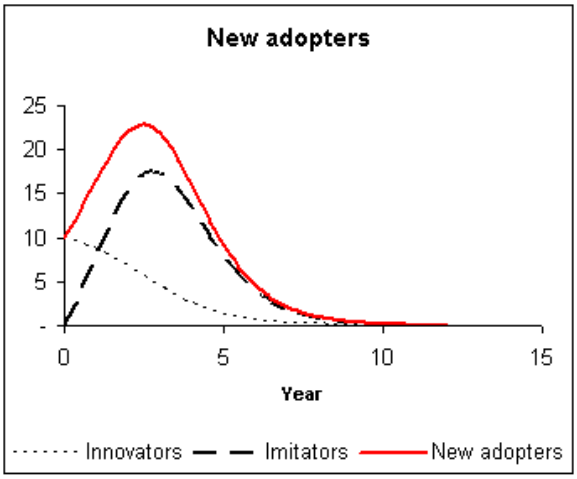

Figure 5-7. Graphs of innovators, imitators, and new adopters for product cycle. (10, 142)

5.2 The role of calcium in force and fatigue in denervated muscle

5.2.1 An early model of calcium current in skeletal muscle

There has been work done that indicates the role of calcium in muscle force and fatigue. The calcium has been assumed to behave as a current.

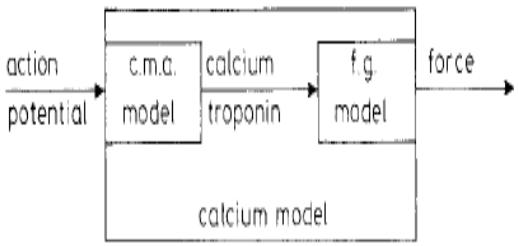

Figure 5-8. Block diagram of calcium mediated activated force generation model. (185)

The calcium mediated activation model (c.m.a.m.) describes the changes of the calcium concentration intracellularly. At rest the calcium is stored mostly in the terminal cisternae of the sarcoplasmic reticulum (SR). When an action potential spreads over the t-tubules, calcium flows into the sarcoplasm and binds to troponin. A resulting calcium-troponin complex facilitates force generation. Dissociation of the complex occurs via low sarcoplasmic calcium concentration by a calcium pump in the longitudinal SR against a calcium gradient. At rest, and after an action potential, calcium flows into the sarcoplasm because of the calcium gradient. In the SR, calcium diffuses back to the cisternae passively. In this model, troponin and calcium carriers are treated as separate compartments due to their binding capacities. Also, a uniform calcium concentration is assumed inside each compartment. This implies that all diffusion processes are virtually instantaneous in each compartment. (185)

The differential equations used to model the calcium concentrations in each compartment arise from the differences between the ionic influx and efflux of these compartments. Also, the system was assumed to be closed so that the amount of calcium, troponin and ATPase would not vary. Biochemically, the amount of ATPase in the SR is so great that its buffer action is significant. According to the model, the ATPase competed strongly with troponin in calcium binding. It was found that the muscle dynamics after the second action potential varies greatly with the degree of calcium occupancy of both the troponin and the ATPase. This model allows for the examination of other parametric influences on excitation-contraction coupling. (185)

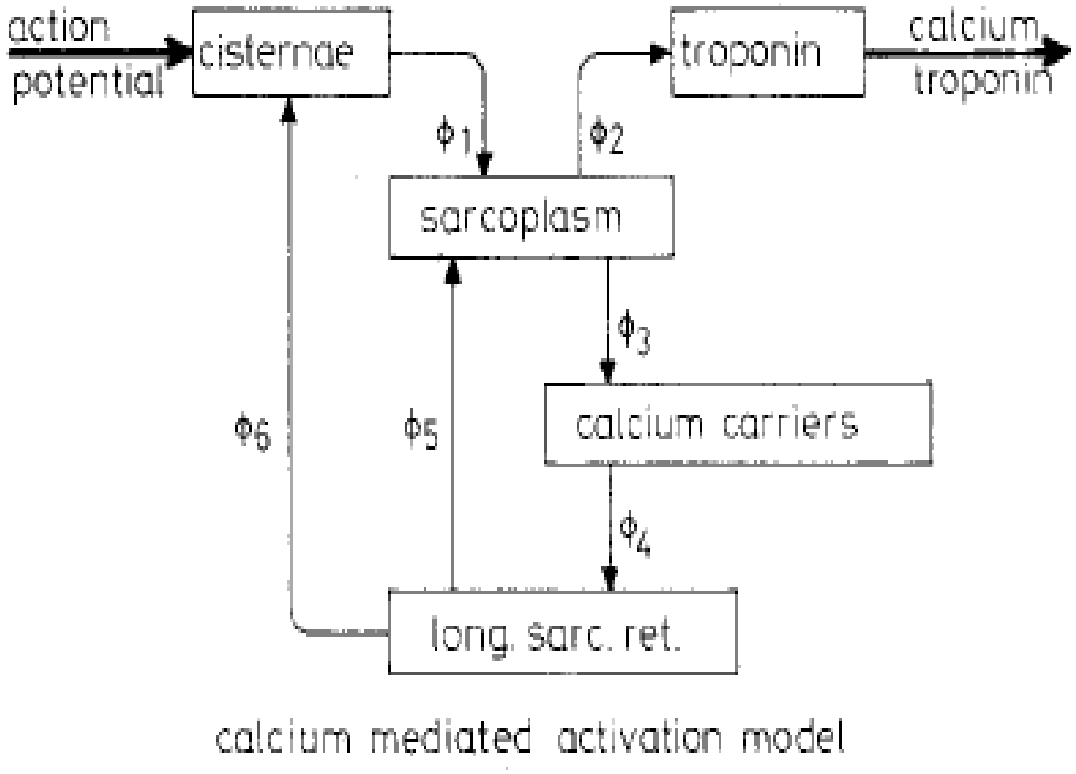

Figure 5-9. Calcium current flow diagram in c.m.am. (185)

5.2.2 The relationship of calcium-troponin binding, calcium channel activation, and voltage sensitivity to force generation in paralyzed muscle

It is hypothesized that the calcium current has a quantal nature. According to del Castillo and Stark (27), variations in calcium concentration had no significant effect on the end-plate sensitivity to depolarization. However, changes in calcium concentration did markedly affect the magnitude of the end-plate voltage. Thus, it was concluded that the quantity of acetylcholine liberated by an individual maximal motor event is directly proportional to the divalent calcium concentration at the neuromuscular junction. (28-31) Based on the above premises, the quantum hypothesis assumes that there is a large number

(n) of quanta stored in the nerve terminal. Each quanta has a certain probability of being released upon nerve stimulation. If the average probability of released is p, the mean number of quanta released per unit of stimulation is defined by m=np A reasonably accurate estimate of p may be obtained from two-pulse experiments in which the amplitude of the second response is depressed. It has been shown that the amplitude of the second response decayed to an initial value exponentially as the interval between the two pulses increased. (126) However, it has been shown that the depression of the end-plate potential produced by low-frequency stimulation over long periods can be accounted for entirely by a reduction in quantal content rather than a change in size. (126, 178)

Repetitive stimulation of muscles elicits contractions that summate nonlinearly, especially when tension saturates at the high-frequency tetanic level. The force-frequency curve under isometric conditions is generally sigmoidal. This indicates an additional nonlinearity at low frequencies. It has also been found that the force from two closely spaced stimuli could be significantly larger and more prolonged compared to a twitch. At low frequencies that generate twitches without fusion, staircase phenomena in both mathematical directions have been observed. This implies a facilitation or depression of the force profiles from successive inputs, as well as posttetanic potentiation of twitches. The length-tension and force-velocity curves of muscle show other well-known nonlinearities. Finally, small magnitude nonlinearities have been recorded that are associated with the bending of myofilament bonds until fracture. (175)

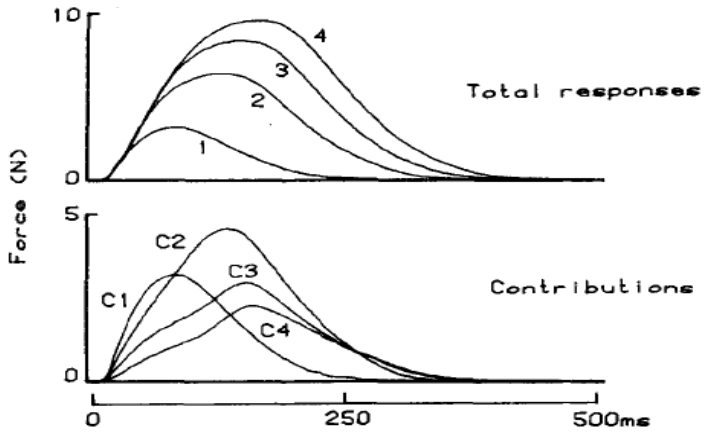

Figure 5-10. Evidence of early depression in the cat soleus in response to subsequent pulses. Note that pulses C2-C4 have progressively longer times to peak force. (175)

Stein and Parmiggiani (175) found two phases of nonlinear summation under a wide range of conditions in fast- and slow-twitch mammalian muscles. Early depression or less-than-linear summation occurs when a second contraction is superimposed on the rising phase of a twitch, and a phase of facilitation or more-than-linear summation is seen later in the time-course of the twitch. The two phases could be different aspects of the same basic phenomenon since the early depression becomes more prominent with repetitive stimulation as the later facilitation becomes less pronounced. (175) Yet, the investigators believed that the two types of nonlinearities arise from distinct mechanisms for several reasons. First, later facilitation was still present with time intervals greater than the contraction time of the muscles that were studied. Meanwhile, early depression was totally eliminated.

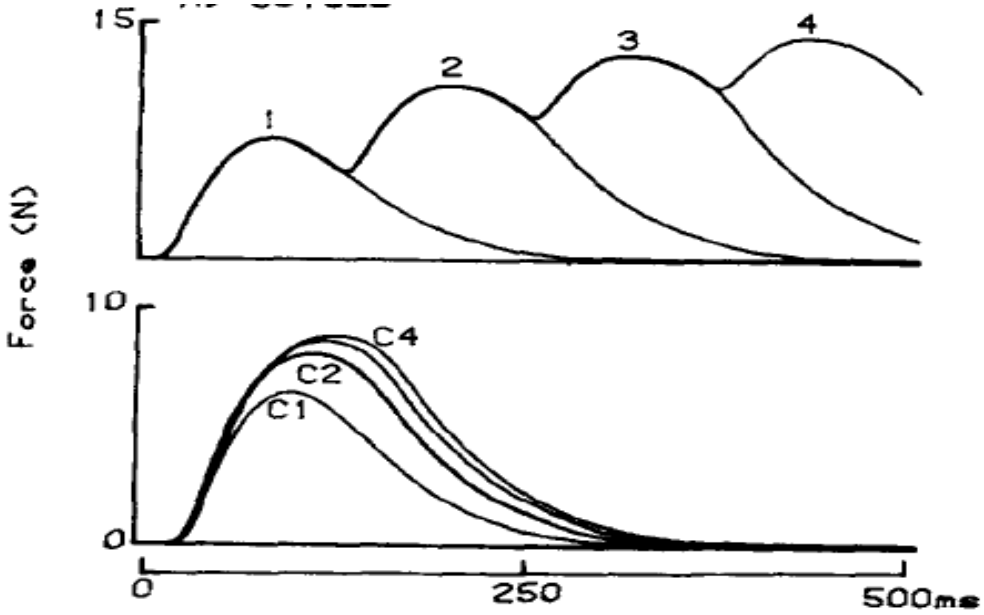

Figure 5-11. Averaged and superimposed twitches in cat soleus. The response of j-1 stimuli was subtracted from j stimuli to document to nonlinear contribution of C_j. (175)

It was found that the increasing depression with additional pulses and variation of the depression with the twitch-to-tetanus ratio under a variety of test conditions were totally consistent with the initial depression due to a saturating process in a muscle. From experiments on amphibian muscle at low temperatures, it was hypothesized that a muscle is maximally activated for a prolonged time period. This is denoted as the “plateau of the active state.” This plateau occludes force generation since a later input could not generate any extra force unless the active state decreased below its plateau level. Nevertheless, it is generally accepted that mammalian muscles at normal temperatures are not at maximal activation from a single input. However, if a second pulse is superimposed on the rise of a twitch, a less-than-linear

summation of generated force initially occurs. This is known as “depression”. (175) As the twitch peaks, this early depression transitions to a subsequent more-than-linear summation. This is known as “facilitation”. Several possible mechanisms have been proposed for the facilitation of force generation from subsequent inputs. (149)

Parmaggiani and Stein (149) found that the facilitation of the tension produced by a subsequent pulse decayed in exponentially as a function of the interpulse interval, regardless of how facilitation was measured. In comparing fast- and slow-twitch muscles, the time-course of the facilitation depended on muscle contraction time. Thus, it was concluded that the same processes that modulate twitch contraction time also likely modulate tension facilitation due to a subsequent pulse. However, tension facilitation is remarkably different for later pulses in a train. While the facilitation due to a second pulse decreases exponentially with the interpulse interval, the optimal interval for third-pulse facilitation is greater than 100 ms in slow-twitch muscles. Comparing fast and slow muscles, the optimal interpulse interval was found to be closely related to the duration of contraction, and was shown to range from 1.26 to 1.5 times the duration of the twitch in the fast and slow muscles investigated. Hence, this suggested again a relationship between the mechanisms that modulate duration of contraction and those that govern tension facilitation. Nevertheless, the investigators envisioned a progressive saturation, instead of sudden occlusion, as additional divalent calcium released by successive stimuli occupy more and more of the sites on troponin.

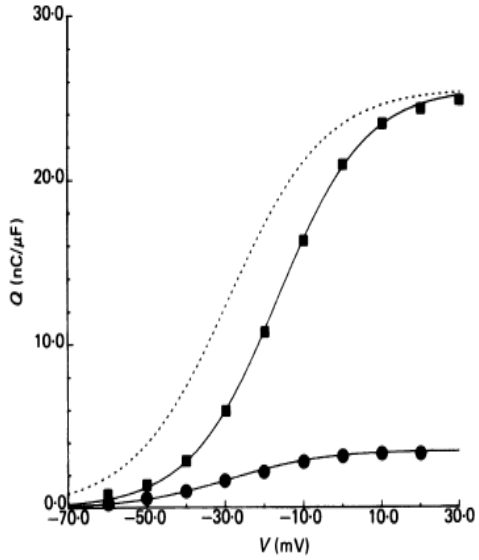

Figure 5-12. Movement of charge in normal rat e.d.l. (squares) and soleus (circles) as a function of voltage. The dashed curve is the soleus curve scaled to maximum and demonstrates the voltage sensitivity differential in the two fiber types. (60)

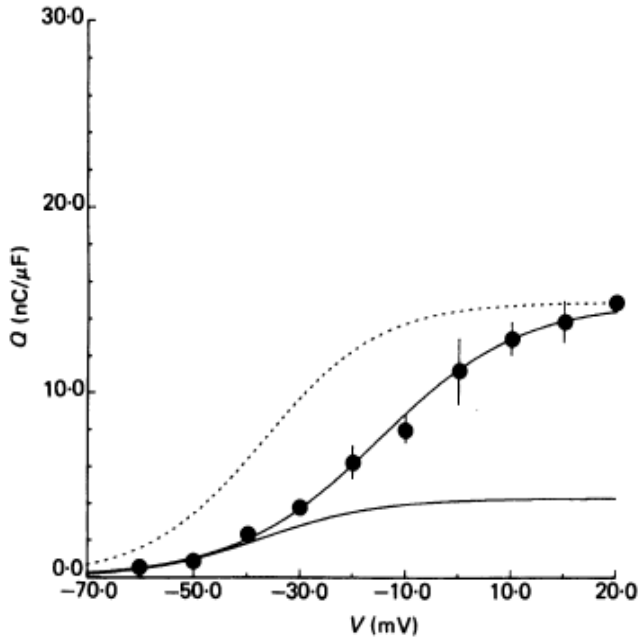

Figure 5-13. Average movement of charge in paraplegic rat soleus (circles) as a function of voltage. The dashed curve is the solid curve scaled to a maximum and demonstrates the change in charge movement in denervated soleus. (60)

The above processes have been suggested to be a first-order Michaelis-Menten reaction. The findings of Dulhunty and Gage (60, 61) also suggest that the baseline calcium current changes between pulses in a stimulus train. As the calcium concentration increases, force increases until the troponin is saturated. Once the troponin is saturated, no more calcium can be bound and contractile force decays.

The calcium current is hypothesized as a function of either the type or quantity of the charge-generating proteins in a membrane. A change in the quality of current likely depends on a turnover of protein subunits in the membranes of the t-tubule or the sarcoplasmic reticulum. It has been observed that the time course of the change in the quantity of current in e.d.l. fibers following nerve section corresponds to the time course of other morphologic adaptations in the sarcotubular membranes following denervation. The role for the indentations in excitation-contraction coupling has been demonstrated by the result that the quantity of indentations in denervated e.d.l. fibers were much lower than in intact fibers. However, it was found that there is little or no change in current in denervated soleus fibers, even with denervation. It was thus concluded that the normal activity pattern in soleus does not modulate the current qualities. However, the higher activity rates of soleus that follow denervation indeed modulate current in the muscle. It was thus shown that denervated e.d.l. fibers adopt the current qualities of intact or denervated soleus fibers. (61) These findings may be applied to paralyzed muscle.

5.2.3 The roles of inactivation of excitation-contraction coupling and voltage sensitivity in decreased force-generating ability, and increased fatigability, in paralyzed muscle

Inactivation of excitation-contraction (EC) coupling is thought to arise in the voltage sensor of the SR because asymmetric current is inactivated during depolarization. It has a time course similar to that of tension inactivation. Inactivation of EC coupling is not caused by calcium depletion from the SR. It is neither caused by inactivation of the calcium release channel or myofilament contractile proteins. Diffusion delays do not explain the difference in time course. If diffusion were rate limiting, force decay would not be depend on voltage and maximum ionic contractures would not have magnitudes as great as in tetanic force. Forces in superficial fibers would inactivate before forces in deeper fibers would activate. The interpretation of the observations was that there are two stages of inactivation in the EC coupling process. It has been denoted that the two states of the voltage sensor in amphibian muscle are 'refractory' and 'denervated'. The refractory state modulates the decay of ionic contracture tension and is rapidly reversed upon repolarization. The denervated state occurs with longer periods of depolarization, with deprivation of external calcium in the presence of divalent calcium channel antagonists. Recovery from the denervated state takes many minutes. (59)

The two states of inactivation can be realized by a state model which extends from previously proposed models. The calcium channel in the terminal cisternae is opened when a voltage-sensitive protein in the t-tubules is converted from a precursor state, P, to an active state, A. The conversion to A depends on

the initial formation of an intermediate state, Q. This followed by rapid dissociation of calcium which transforms Q to A. The two-step transition from P to A, which is dependent on calcium, explains the effects of low external concentrations of calcium on muscle contraction. However, during prolonged depolarization, A is slowly transformed to an inactive state, I, and then to an additional inactive state Y. Based on that reasoning, it was thus proposed that the transformation of I to Y involves the dissociation of additional divalent calcium. That is because the denervated state is reached more easily in low concentrations of calcium. The formation of A changes the conformation of the calcium release channel in the terminal cisternae from a closed to an open state. (59, 112-119)

Dulhunty (59) noted the remarkable morphologic similarities and homology between the sodium channel and the dihydropyridine receptor calcium channel and suggested that fast and slow inactivation are modulated by similar mechanisms. This implied that the possibility that one component of EC coupling inactivation happens in the coupling process between the voltage sensor and calcium release channel did not exist. Another remarkable comparison between the inactivation of sodium channels and the voltage sensor for EC coupling is that, in mammals, both happen at more negative membrane voltages in fast-twitch fibers than in slow-twitch fibers. This suggested that the voltage sensitivity of inactivation in the two different proteins might be modulated by the membrane environment.

A fundamental property of denervated muscles is the inability to sustain force during tetanus contraction. Hence, a voltage-sensitive mechanism may be involved in this dysfunction. It was previously hypothesized that such a mechanism involved in tetanic contraction, such as the dihydropyricline (DHP)-sensitive L-type calcium channels, may adapt upon denervation in mammalian fibers. Delbono and Stefani (40) found that numbers of indentations change in parallel to the magnitude of current following denervation. This is because the quantities of membrane indentations in denervated muscle fibers were shown to remarkably decrease from those in intact muscles. This suggests that calcium channels themselves cannot be ruled out and the cause of shifts in membrane voltages. However, the decrease in voltage sensors detected by reduced calcium current at various stages of the denervation process was suggested to cause the decrease in mechanical force in mammalian skeletal muscle.

Delbono and Stefani (40) found that the calcium current amplitude increased during the first days of denervation and then decreased with respect to intact fibers. In the second week post-denervation, the maximum current was observed to significantly reduce. This led to the question of whether or not the number of voltage sensors actually decreases by observing binding of different calcium channel antagonists over time. Since it was known that the functioning channels, based on the probability of open channels, could be much less than the channels recorded by assay, this study implied that the number of DHP receptors reduces after two weeks of denervation.

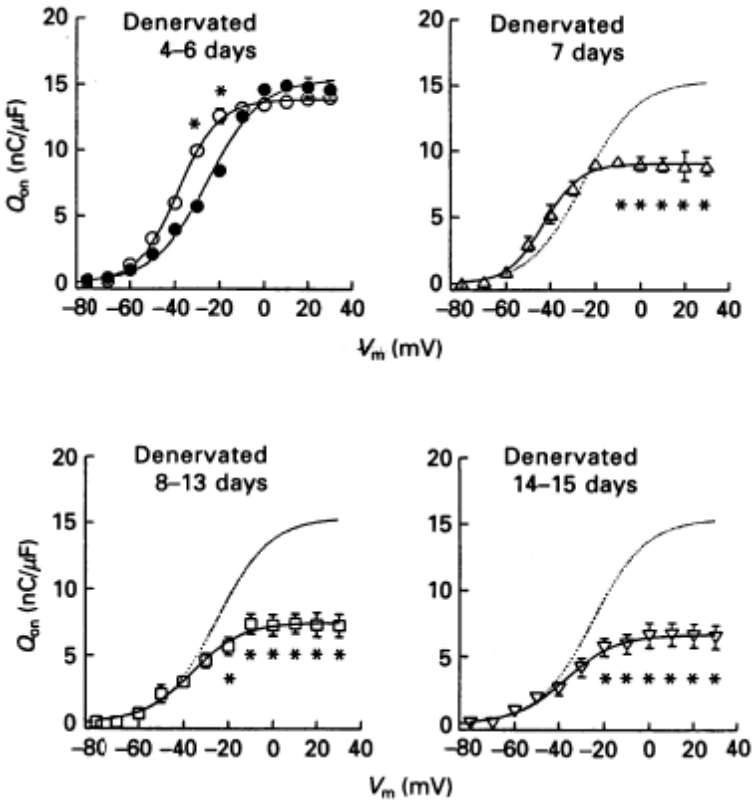

Figure 5-14. Changes in the charge-voltage relationship in rat extensor digitorum longus at various stages of denervation. (40)

A significant decrease of the maximum force of tetanic contractions may be explained from the fact that fibers with smaller diameter have lower membrane capacitance because of the decreased contribution of the sarcotubular membrane. The increase in the tubular membrane fraction increases the membrane notwithstanding a significant decrease in fiber diameter. The volume fraction change of the sarcotubular system may explain the lack of celerity of calcium activation in states of denervation.

Additionally, Delbono and Stefani (41) showed that inactivation of calcium current in denervated fibers had faster recovery and a delayed onset. This makes

the calcium current harder to inactivate in whole muscle. It was suggested that proteolysis during denervation may decrease the function of a typical inactivating gate in some calcium channels. It was noted that denervated skeletal muscle contains a higher concentration of calcium than in intact muscle. This was suggested to arise from the decrease in Ca^{2+}-ATPase activity which triggers proteolysis. (35, 41, 59) It was shown that inactivation of calcium in denervated soleus fibers had a faster recovery time course as well as a slower onset of inactivation. This renders divalent calcium in denervated muscle harder to inactivate. There was only a partial voltage dependence of the calcium inactivation and it was shifted leftward. These changes in the voltage dependence of calcium current inactivation differ from sodium current inactivation in denervated fibers of the rat. The maximum calcium current recovered with an exponential time course during the interpulse interval at -90 mV. Yet, the recovery from inactivation was shown to be quicker after denervation than in intact fibers. It was hypothesized that, at that voltage, most of the channels are closed rather than inactivated however. (41)

Paralyzed muscle fatigue dynamics can be inferred from those of denervated muscle. Since the calcium current in paralyzed muscle is reduced, this implies that the calcium released from each pulse in a stimulus train is also reduced. As paralyzed muscle also contains excess calcium from proteolysis of fibers, this implies that troponin saturates much more quickly during an elicited contraction. Rapid saturation of troponin would generate maximal force more quickly. Yet, maximal force cannot be sustained due to the morphological

degradation of the calcium channels. Hence, even with the excess calcium in the myoplasm, force in paralyzed muscle decays because there is degraded contractile machinery in the fibers. (41, 59) Furthermore, inactivation of EC coupling likely contributes to muscle fatigue. The rate of inactivation in fast-twitch fibers corresponds with the damped tension during high-frequency stimulation. (35)

CHAPTER 6: METHODS

The goals of this thesis are to ascertain which model structure as well as which parameterized closed-form model is best for predicting force as well as predicting fatigue in paralyzed human soleus across different muscle/state combinations over time of stimulation. In doing so, an assessment of the predictive value of the information will be performed. At the completion of the work, there will be a more definitive view of the predictive value of different models of force and fatigue in paralyzed human soleus as well as an enhanced understanding of muscle physiology.

6.1 Human subjects

Data collection of force and fatigue profiles was performed in the Clinical Measurement Laboratory at The University of Iowa Hospitals and Clinics (UIHC). Subjects with paralysis qualified for the study if they have had complete paralysis at the level of T12 or above for at least two years. Two of the investigators supervising this study (RKS, LFL) work extensively with SCI subjects and have assisted in the identification of the subjects from the laboratory. Subjects of both sexes and all races were considered for enrollment. Since spinal cord injury occurs primarily in young to middle-aged adults, only subjects greater than 18 years of age were enrolled. These subjects had no other medical conditions and be greater than 18 years of age.

Subjects with paralysis were recruited by personal contact, telephone or mail by physical therapy staff after a review of records to determine their time

after injury. Subjects were excluded from the study if they were unable to provide informed consent. Subjects who are paralyzed were excluded if they presented with medical problems other than spinal cord injury.

Informed consent was obtained from each subject. Each subject was then asked to fill out a questionnaire that identifies demographics and injury history. Electrical stimulation of the soleus with doublet ramp stimuli then commenced. For all stimulation trials, the paralyzed subject remained in his or her wheelchair. Rest periods of five minutes occurred between each input train. A force-fatigue profile was retrieved and stored during the duration of each different input. Profiles were stored both on hard drive as well as optical disk. The time for the acquisition of these data was approximately 30 minutes per session.

This protocol was submitted to the Investigational Review Board of The University of Iowa for approval. This study does not involve biohazard materials. Subject confidentiality has been strictly honored. Subjects of either gender have not been identified by name in publications or presentations at scientific sessions. The risks of the study were outlined in the consent form.

6.2 Experimental setup, instrumentation, recording procedures, and data collection

The equipment used to collect the data in this study consists of custom-designed electronic equipment for collection, recording, and analysis of real-time human paralyzed muscle force and fatigue data described in the following subsections. It is located in the Clinical Measurement Laboratory of the University of Iowa Hospitals and Clinics (UIHC). No other equipment was used in this protocol.

6.2.1 Experimental setup

The torque measurement system is designed to measure the plantarflexion torque with a subject in the seated position with the knee and ankle at 90'. Adjustability of the heel cup, force transducer, and axis of rotation allows the force transducer (AWU-250, Genisco technology) to be positioned under the first metatarsal head. The foot plate axis of rotation is aligned with the anatomic axis of the ankle. Stabilization of the heel to the foot plate during torque production is provided by a rigid ankle cuff directing three vectors of force through the calcaneus via turnbuckles. A double strap secured over the femur provides additional stabilization of the heel in the foot plate assembly during plantarflexion

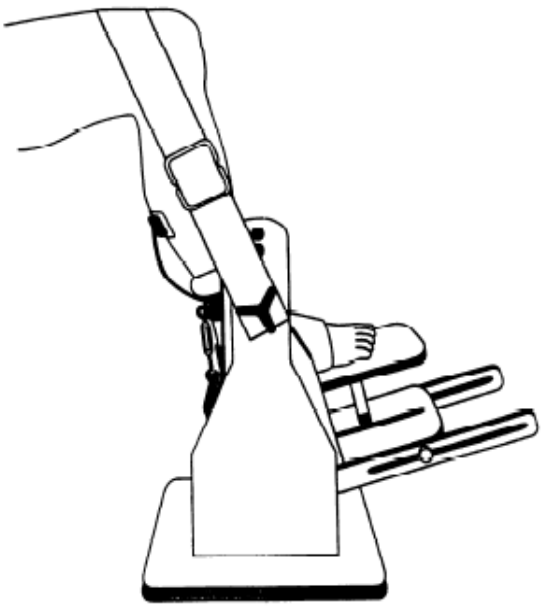

Figure 6-1. Torque measurement apparatus including adjustable axis of rotation, stabilization cuff, and femoral strap. (66)

. Figure 6-1 shows a schematic of the torque measurement system. Calibration of the torque measurement system is to be done with known loads. By induction from previous work, the calibration yields a linear regression equation with a correlation value (R^2 of 0.99. The force transducer is electronically coupled to a multichannel recorder. Various indices of calibration are to be calculated for this protocol.

6.2.2 Instrumentation

Two silver-silver chloride electrodes (8 mm in diameter, with an inter-electrode distance of 20 mm) will record soleus compound muscle action potential activity to verify supramaximal activation. Each electrode will contain an on-site pre-amplifier with a gain of 36. The signal will be further amplified by a GCS 67 amplifier (Therapeutics Unlimited, Iowa City, IA, USA) with adjustable gain from 500 to 10,000. The amplifier utilizes a high impedance circuit (greater than 15 MΩ at 100 Hz), with a common mode rejection ratio of 87 dB at 60 Hz and a bandwidth of 40-4000 pulses per second.

A custom-designed constant current stimulator and isolation unit has a current range from 0 to 200 mA with current variations of less than 5% and total voltage capability of 400 V. It will be triggered by digital pulses from a data-acquisition board (Metrabyte DAS 16F, Keithley Instruments Inc., Cleveland, OH, USA) housed in a microcomputer under custom software control. The stimulation intensity will be supramaximal which is about 50% greater the intensity required to produce a maximum compound muscle action potential. Stimulation inputs are to be delivered via a double-pronged stimulation electrode

secured over the tibial nerve with the use of a gel pad that adheres to the back of the leg.

6.2.3 Recording procedures

The skin over the soleus muscle was scrubbed with alcohol, and the electrode was applied 2 cm lateral to the midline at one-third the distance from the lateral malleolus to the fibular head. After visual inspection of the M-waves, the electrode may have needed to be slightly repositioned in order to accentuate the biphasic waveform. Each subject had the right foot placed in the torque measuring device and secured so that the ankle will be at 90º. The wheelchair of the subject was rolled forward until the knee is also flexed to 90º. The knee was positioned at ninety degrees of flexion and the ankle was secured to the test apparatus in the neutral joint position. The tibial nerve was activated using a double pronged stimulation electrode that was secured on the calf. The test position minimized the contribution of the gastrocnemius to the plantarflexor torque.

The splinted dual pronged nerve electrode was used to stimulate the tibial nerve in the popliteal fossa, using computer driven pulse sequences generated by the custom-made constant-current stimulator using 250 μsec pulsewidths. The placement of the electrode was optimized to produce the largest soleus M wave peak to peak amplitude. Stimulation intensities were then increased to approximately 1.5 times greater than required for a maximum M wave to ensure supramaximal stimulation throughout the protocol.

All data collected were the force signal profiles for each input, and the EMG response for each input. The force, EMG and stimulation trigger signals were recorded simultaneously into ASCII text files and later analyzed using MATLAB 7.0 software (The Mathworks, Natick, MA). All data were digitized at 1000 samples per second.

6.2.4 Data collection

Via the equipment described in Subsection 6.2.1, soleus force-fatigue data collected from four paralyzed trained limbs and four paralyzed untrained limbs from subjects with chronic, complete SCI was used in this study. All subjects were otherwise healthy. Written informed consent, as approved by the institutional review board, was obtained prior to collection of the force data.

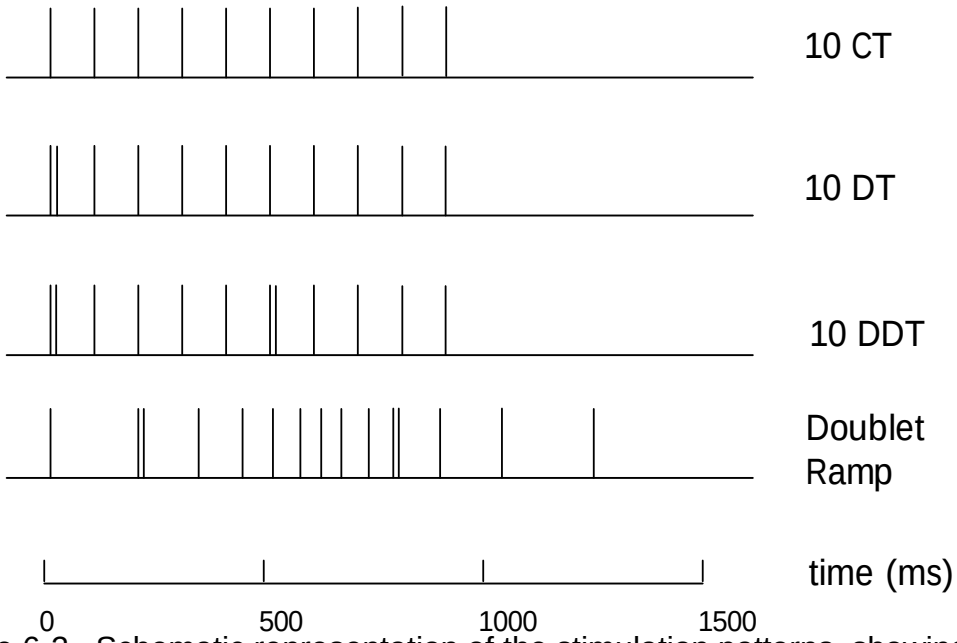

Figure 6-2. Schematic representation of the stimulation patterns, showing only the 10 pps series and the doublet ramp used for parameter determination for each model. (66).

Following the work of Frey-Law and Shields (66), and with the assumed physiologic approximation of paralyzed trained muscle to nonparalyzed muscle, the stimulation protocol begins with a series of 1 pps twitches to determine the optimal electrode placement and ensure supramaximal levels of activation. Five warm-up contractions, 7-pulse trains (20 pps trains, 330 msec on: 670 msec off) applied at 1 train/sec, were then given to ensure the soleus muscle was in a more potentiated state, without inducing fatigue. Following the warm-up, a pre-programmed stimulation trains were then performed. The set consists of: a doublet ramp of 15 pulses with interpulse intervals (IPIs) of 200, 6, 127, 100, 67, 67, 50, 50, 67, 67, 6, 94, 133, and 200 ms (1234 ms duration, Figure 6-2).

Following the method of Shields and Dudley-Javoroski (162), with the assumed physiologic approximation of paralyzed trained muscle to nonparalyzed muscle, the fatigue protocol uses supramaximal intensity to elicit contractions. The stimulator is programmed to deliver a train of 10 pulses (15 pps; 667 ms duration) every 2 seconds. A bout of stimulation consists of 125 trains. Subjects complete four bouts of stimulation during a session. The bouts of stimulation are separated by rest periods of 5 minutes.

6.3 Validation protocols

6.3.1 Introduction

When electric current is applied to any biologic tissue, its physicochemical equilibrium is perturbed. As a result, by the principle of Le Chatelier (8), the biologic tissue changes state to minimize the perturbation of its equilibrium. In the case of muscle, regardless of presence or absence of pathology, the

equilibrium depends on the increase or decrease of free calcium in the sarcoplasmic reticulum. As a muscle is extrinsically stimulated at low frequencies over a prolonged period of time, it contracts until there is insufficient free calcium to sustain a contraction at a given level of force. This decay in contractile ability is known as low-frequency fatigue. Another contraction cannot begin until the equilibrium of free divalent calcium the muscle is reestablished at sufficient levels. (1, 73, 130, 163)

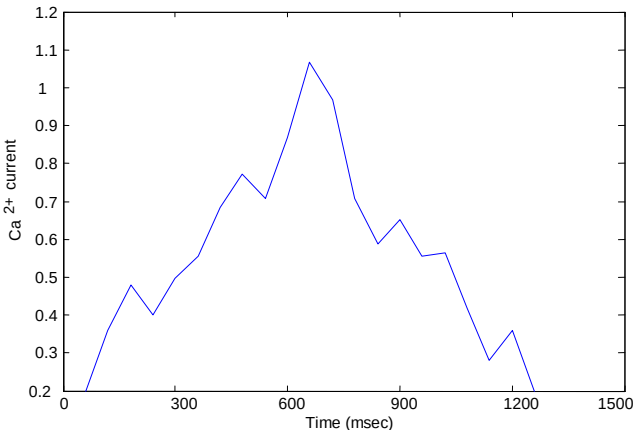

Figure 6-3. Hypothetical C_N curve from a Riccati-Bass diffusion function for R_0 resulting from a doublet ramp input. It varies with time and accounts for nonlinear summation of activation from each pulse.

To capture the dynamics of the autocatalytic periodic reactions (112-119) that modulates muscle force and fatigue in the Ding models (48-56), a Riccati-Bass R_0 and k_m are respectively hypothesized to account for the gradual occlusion of troponin by calcium (149), the macromolecular crowding of CaTr in the sarcoplasm (163), and for asymmetrical movement of charge predicted by

exponential functions upon electrical stimulation (41, 60). The contractile machinery in muscle can be represented as a stop transducer with reversed polarity. Its behavior can thus be characterized by dynamic R_0 or k_m modeled with a decreasing Riccati-Bass diffusion function that maintains constant probabilities of actions in its coefficients for each contraction. (10, 142) As the activation curve for R_0 flattens between each pulse, the nonlinear summation for R_i, as well as the force, in the entire stimulus train also decays.

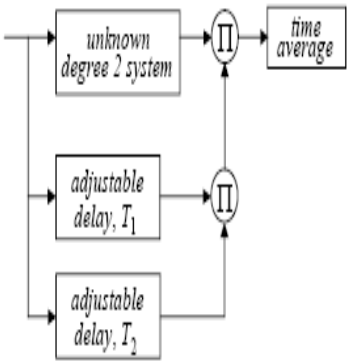

Figure 6-4. Assumed structure of muscle in Conaway models. (9)

6.3.2 Determining differences in force-fatigue model structure

Therre os much recent literature that cite the Ding (48-46) work. Hence, it appears that the Ding models can be modoified in myriad ways. One such way is to incorporate the Riccati equation to characterize different physiologic processes iin predicting force and low-frequency fatigue in the chronically parluzed human soleus..

6.3.2.1 Physiological rationale

This is the first force-fatigue model structure to incorporate mathematical diffusion functions to describe major physiologic processes that occur during a muscle contraction. In this study, the problem is one of parameter estimation for a specific decay curve at the beginning of an actual process and then making predictions of the continuation by optimizing the estimated function. (113) Furthermore, two forms of influence on the different diffusion processes are distinguished. They are external and internal sources of influence. (108) This phenomena is reflected by the particular coefficients of the Riccati equation that is included in each of the Conaway models. In each model, the external influence comes from the extrinsic calcium applied to the muscle that causes calcium to move. Internal influence is a function of the relevant structures in the sarcoplasmic reticulum, specifically calcium channels, to behave according to certain aggregate probabilities in different states.

Furthermore, a nonsymmetric function can generate a sigmoidal curve similar to the logistic function. Yet, its point of inflection is not necessarily the midpoint between zero and the upper asymptote. If $b > 1$ the curve has negative or left skew. That models a process which is asymptotically faster than described by the logistic function. (73) Even with a constant distribution, the interaction quality may vary as muscles of different training states require different levels of calcium to contract. In both Conaway models, the external and internal processes described above have been combined into a Riccati equation such that the exponential and nonsymmetric sigmoidal processes are

superposed. In addition, the diffusion laws in the models are modulated by a damping term. (24, 179, 180) Hence, it is hypothesized that R_0 and k_m are both products of the derivatives of nonsymmetric sigmoidal and negative exponential damping laws which asymptotically approach logistic behavior. Thus, in the Conaway models, the Riccati-Bass diffusion model (10) describes the external and internal processes of muscle force and fatigue. And, since Norton and Bass (142) extended the model to predict activity in subsequent cycles, it is hypothesized that the Riccati-Bass coefficients are constant for each contraction in a bout of stimulation. Finally, it is inferred that the underlying processes involved in the calcium binding or activation of extrinsic stimulation still behave according to a power law of Michaelis-Menten kinetics (162) in each contraction in fresh and fatigued states in paralyzed muscle.

Thus, the learning objectives for modifying the Ding model of muscle fatigue are as follows. It is hypothesized that modification of the original Ding models via an additional differential equation that more accurately predicts R_0 as a function of time in fresh muscle, and R_0 as a power law function of k_m in fatigue. The proposed additional differential equation will be first-order, ordinary, and nonlinear of the Riccati class. With the assumption that R_0 and k_m are time-varying quantities, this modified model structure is to provide the resolution necessary to account for the autocatalytic, periodic process of calcium release in the fresh state as well as inactivation of calcium channels and EC coupling in fatigue. A more accurate calculation of k_m and R_0 will allow greater resolution in predicting force at various stages of the fatigue process. It will be especially

interesting to see how it works in the untrained human paralyzed soleus in a fatigued state due to its compromised biologic environment.

6.3.2.2 Closed-form parameterized models

By including more realistic calcium dynamics described by a Riccati-Bass function, it is hypothesized that the structure of the Conaway force-fatigue models yields a more robust model of muscle force generation, with respect to different inputs, than does the structure of the Ding force-fatigue models.

The modified force model will be better able to predict force since it is assumed that calcium current follows a Riccati-Bass growth/diffusion/decay pattern (10) in muscle. It is furthermore assumed that the excitation-contraction machinery acts as a stop transducer between electrical inputs and muscle force. With these dynamic assumptions, the differential equation to calculate R_0 as a time-varying quantity goes to $dR_0/dt=-(\lambda_1+\lambda_2 R_0)(1-R_0)$, with λ_1 as the calcium-troponin association affinity and λ_2 as the calcium-troponin dissociation affinity. The numerical values of the Riccati-Bass coefficients will be determined via parameter estimation. However, following Norton and Bass (142), they will be assumed to be constant over an entire stimulation bout.

With the additional Riccati differential equation for the parameter R_0, below is the complete, modified Ding model of muscle force. It will hereafter be referred to as the Conaway model of muscle force.

$$\frac{dF}{dt} = A\frac{C_N}{k_m + C_N} - \frac{F(t)}{\tau_1 + \tau_2 \frac{C_N}{k_m + C_N}} \tag{6-1}$$

$$R_i = 1 + (R_0 - 1)e^{\frac{-(t_i - t_{i-1})}{\tau_c}} \tag{6-2}$$

$$\frac{dC_N}{dt} = \frac{1}{\tau_c}\sum_{i=1}^{n} R_i \exp\left(-\frac{t-t_1}{\tau_c}\right) - \frac{C_N}{\tau_c} \tag{6-3}$$

$$\frac{dR_0}{dt} = -(\lambda_1 + \lambda_2 R_0)(1 - R_0) \tag{6-4}$$

Table 6-1. List of parameters for the Conaway muscle force model.

Symbol	Unit	Definition
C_N		Normalized amount of Ca^{2+}-troponin complex
F	N	Mechanical force
t_i	ms	Time of the ith stimulation
N		Total number of stimuli in the train before time *t*
t_p	ms	Time of the pth data point
t_q	ms	Time of the qth set of force model parameter set
τ_c	ms	Time constant controlling the rise and decay of C_N
A	N/ms	Scaling factor
τ_1	ms	Time constant of force decline at the absence of strongly bound cross-bridges
τ_2	ms	Time constant of force decline due to the extra friction between actin and myosin resulting from the presence of cross-bridges
k_m		Sensitivity of strongly bound cross-bridges to the change in calcium current
h	ms	Integration step
λ_1	ms^{-1}	Affinity for calcium and troponin to bind after the first pulse during a stimulated contraction
λ_2	ms^{-1}	Affinity for calcium and troponin to dissociate after the first pulse during a contraction

With the introduction of the Riccati-Bass equation for R_0, this will improve upon the Ding model of muscle force generation by allowing for nonlinearity in

the divalent calcium concentration during stimulation. The time-dependent Riccati-Bass model describes the manner in which extra calcium in muscle from applied external stimulation current behaves between pulses. The differential equation must be negative to model the change in calcium-troponin binding from subsequent pulses in a stimulus train as a decaying process. Since the Riccati-Bass equation is frequently used in forecasting, it is reasoned that it may be used to predict force in human muscle. With the Riccati-Bass equation, nonlinearity to the second order may be examined for the autocatalytic process of periodic calcium release in fresh muscle contraction, especially when there is no force decay from fatigue. A more exact initial R_0 may then be used to calculate R_i and, ultimately, rate-limiting C_N during later stages of force generation at higher stimulate on frequencies and in response to special pulse forms such as doublets.

In addition, with the assumptions of decreasing calcium sensitivity and stop transducer behavior of the excitation-contraction machinery for fatigue, the differential equation to calculate the variable k_m goes to $dk_m/dt=-(\mu_1+\mu_2 k_m)(1-k_m)$, with μ_1 as the probability that calcium channel will activate and μ_2 as the probability that calcium channel will inactivate. The numerical values of the Riccati-Bass coefficients will be determined via parameter estimation. However, they will be assumed to be constant over an entire stimulation bout. This new variable will then be used to calculate R_0 as a power law function, and hence R_i and C_N, in the force prediction algorithm.

Therefore, it is proposed that the R_i term will be modeled as a varying quantity with an additional time constant that is markedly lesser than τ_c at initial conditions. In addition, to model fatigue with even more physiologic realism, the rate-limiting equation in the Ding model would need to account for leaked calcium and hence decreasing C_N during stimulation. In addition, this rate-limiting step needs to account for the calcium channel inactivation which results in higher concentrations of calcium. It is thus hypothesized that R_0 behaves as a power law function of a possibly fractal-like k_m during paralyzed muscle fatigue. The time constant τ_{leak} is introduced to account for the exponentially decreasing R_i that arises due to calcium leakage during fatigue, such that a combined time constant would be $\tau_{fatigue}=1/(\tau_c+\tau_{leak})$. It is assumed that R_i, due to a decaying k_m, would decrease in fatigue. Hence, incorporating the novel parameter τ_{leak} into R_i would give $R_i = 1+(R_0-1)e^{-(ti-t[i-1])*1/(\tau c+\tau leak)}$ or $R_i = 1+(R_0-1)e^{-(ti-t[i-1])*1/(\tau fatigue)}$.

The physiologic interpretation of the modification is that as calcium leaks out of fatiguing muscle, the differences in the degree of activation would decrease as the contractile apparatus is no longer able to sustain maximal force due to remodeling of the ryanodine receptors. Yet, fatigue does not happen instantaneously. Some investigators argue that fatigue begins immediately upon initial contraction. Hence, to be physiologically plausible, τ_{leak} should be so large such that $\tau_{fatigue}\approx\tau_{leak}$ for large values of τ_{leak}. Thus, it is hypothesized that the voltage sensitivity, as well as the interpulse summation of force, decreases markedly in fatigue.

With the additional time-dependent Riccati-class differential equation for the variable k_m, and the assumptions of calcium leak, increased inactivation, and possible fractal-like kinetics, below is the complete, modified Ding-type model of muscle fatigue. It will hereafter be referred to as the Conaway model of muscle fatigue.

$$\frac{dF}{dt} = \mathrm{A}\frac{\mathrm{C_N}}{k_m + \mathrm{C_N}} - \frac{F(t)}{\tau_1 + \tau_2 \dfrac{\mathrm{C_N}}{k_m + \mathrm{C_N}}} \tag{6-5}$$

$$\frac{d\mathrm{C_N}}{dt} = \frac{1}{\tau_{fatigue}} \sum_{i=1}^{n} \exp\left(-\frac{t - t_i}{\tau_{fatigue}}\right) - \frac{\mathrm{C_N}}{\tau_{fatigue}} \tag{6-6}$$

$$R_i = 1 + (R_0 - 1)e^{\frac{-(t_i - t_{i-1})}{\tau_c}} \tag{6-7}$$

$$R_0 = \mathrm{a}k_m{}^{b} + c \text{ , with b} \neq 0, 1 \tag{6-8}$$

$$\frac{d\mathrm{A}}{dt} = \frac{-(\mathrm{A} - \mathrm{A}_{rest})}{\tau_{fat}} + \alpha_{\mathrm{A}} F \tag{6-9}$$

$$\frac{d\tau_1}{dt} = \frac{\tau_1 - \tau_{1rest}}{\tau_{fat}} + \alpha_{\tau 1} F \tag{6-10}$$

$$\frac{dk_m}{dt} = -(\mu_1 + \mu_2 k_m)(1 - k_m) \tag{6-11}$$

$$\frac{1}{\tau_{fatigue}} = \frac{1}{\tau_c + \tau_{leak}} \tag{6-12}$$

This fatigue model is governed by eight parameters: A (N/ms), $\alpha_{\tau 1}$ (N^{-1}), τ_{1rest} (ms), τ_2 (ms), τ_{leak} (ms), a, b, and c. The value τ_{1rest} is the value of τ_1 when

muscles are not fatigued. F is the isometric force. Experimental forces will be used in Equations 6-7 through 6-10 during parameter identification. However, once the fatigue model is parameterized, forces predicted by Equation 6-5 will be used to test the ability of the model to predict fatigue. Equation 6-11 models the decreasing voltage sensitivity during fatigue. However, the equation must be negative to model the decay appropriately. In addition, the voltage sensitivity must be modeled appropriately to account for the differences between the probability of activation (μ_1) and probability of inactivation (μ_2). Hypothetical examples of Riccati-Bass voltage sensitivity at extremum probability ratio points are given below.

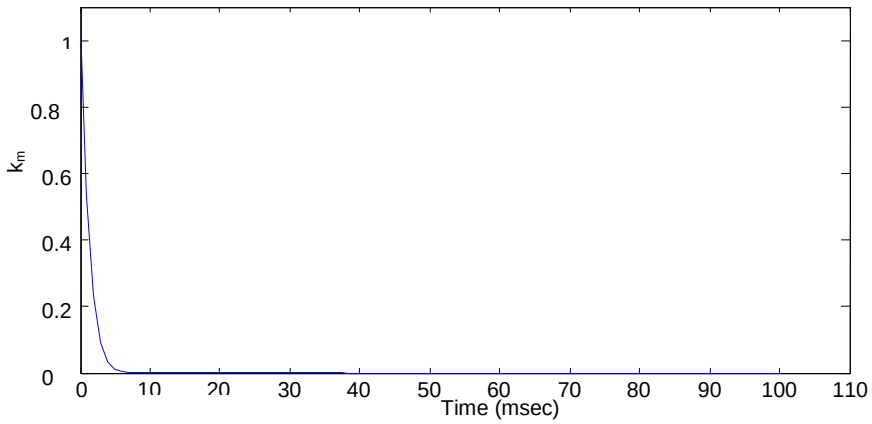

Figure 6-5. Hypothetical Riccati-Bass voltage sensitivity with μ_2/μ_1=1.001. For small ratios of μ_2 to μ_1, the voltage sensitivity changes so rapidly that the muscle inactivates quickly. Hence, fatigue would onset very suddenly.

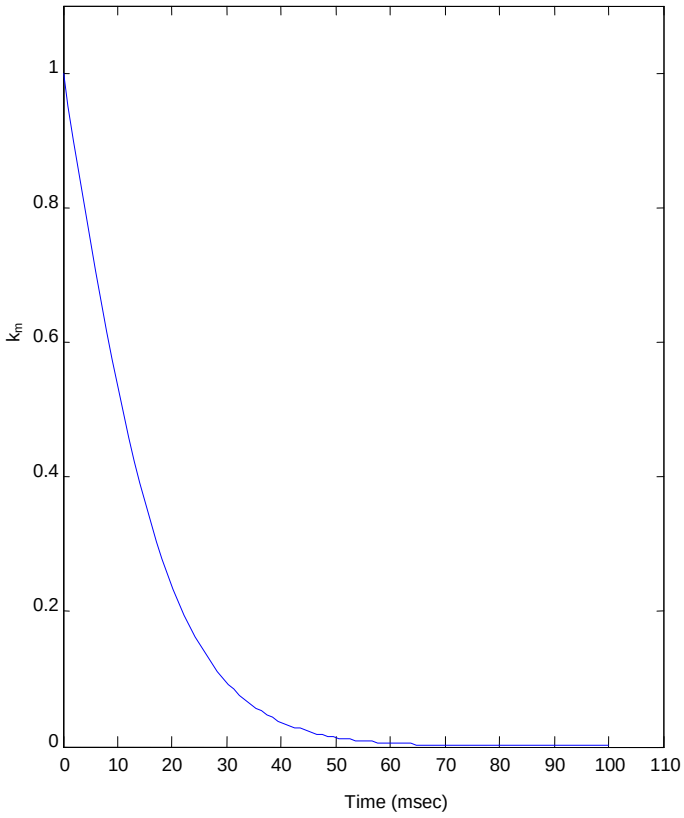

Figure 6-6. Hypothetical Riccati-Bass voltage sensitivity with μ_2/μ_1=10.01. For large ratios, the muscle inactivates at a slower pace. Fatigue would onset very slowly. If that were physiologic reality, however, muscles would easily be damaged due to overwork from the lack of a refractory period.

Furthermore, an analysis was done to investigate the nature of power laws (162) of Riccati-Bass functions (10) to determine whether the R_0-k_m relationship could be fractal. Such behavior was previously unknown. Curiosity arose when the value of b in $R_0=ak_m^b+c$ did not change much, if at all, in preliminary optimizations of the Conaway fatigue model. Nevertheless, a working value for b has been found to be in the range of 1.0-1.5 in repeated optimizations.

b=1

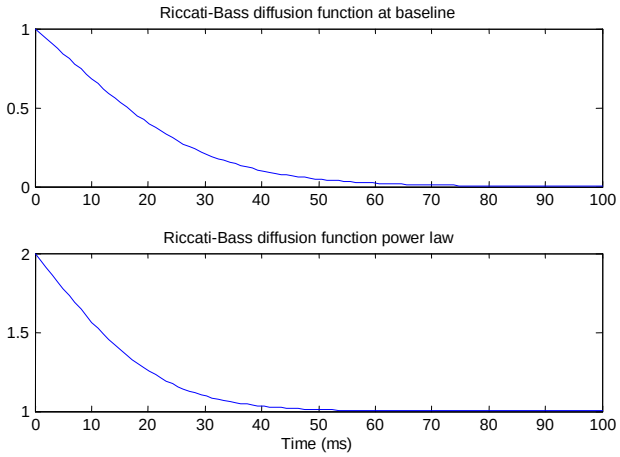

b=1.5

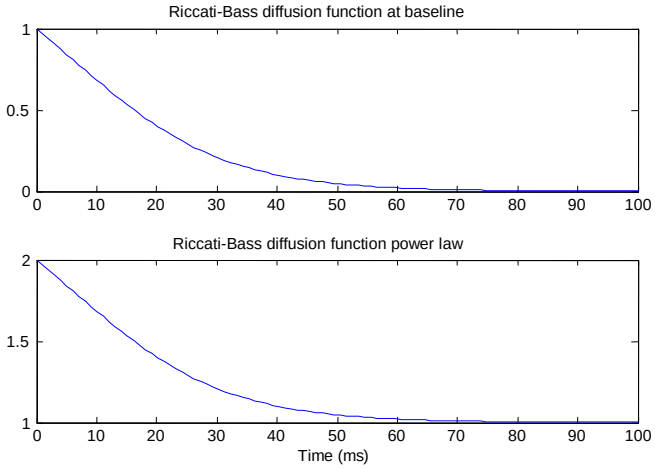

Figure 6-7. Power law analysis of Riccati-Bass functions for b=1.0, 1.5. Increases in b shift the curves rightward and accelerate inflection.

The limited power law analysis shows that power law functions of Riccati-Bass equations are time-shifted sigmoids with increasing decay and accelerated inflection. To apply this finding to the R_0-k_m relationship (56), the optimal value

of b must be chosen such that the relationship remains nonlinear and the modeled delay in the calcium channels is optimized.

Table 6-2. List of parameters for Conaway muscle fatigue model.

Symbol	Unit	Definition
C_N		Normalized amount of Ca^{2+}-troponin complex
F	N	Mechanical force
t_i	ms	Time of the ith stimulation
N		Total number of stimuli in the train before time *t*
t_p	ms	Time of the pth data point
t_q	ms	Time of the qth set of force model parameter set
τ_c	ms	Time constant controlling the rise and decay of C_N
A	N/ms	Scaling factor
τ_1	ms	Time constant of force decline at the absence of strongly bound cross-bridges
τ_2	ms	Time constant of force decline due to the extra friction between actin and myosin resulting from the presence of cross-bridges
$\alpha_{\tau 1}$	N^{-1}	Coefficient for force model parameter τ_1 in the fatigue model
α_A	N^{-1}	Coefficient for force model parameter A in the fatigue model
τ_{fat}	s	Time constant controlling the recovery of the parameter τ_1 during fatigue
τ_{leak}	ms	Time constant to account for the exponentially decreasing C_N that arises due to calcium leakage during fatigue
$\tau_{fatigue}$	ms	Superposition of τ_c and τ_{leak}, $1/\tau_{fatigue}=1/(\tau_c+\tau_{leak})$
a		Coefficient of k_m
b		Exponent of k_m
c		Intercept of R_0
h	ms	Integration step
μ_1	ms^{-1}	Probability that calcium channel will activate
μ_2	ms^{-1}	Probability that calcium channel will inactivate

6.3.2.3 Data analysis

Using unconstrained optimization parameter values, differences in mean squared error and correlation with respect to the experimental data will be compared between the Conaway and Ding force models for various inputs. If the Conaway models, with unconstrained optimization parameter values, produce on average less mean squared error and greater correlation than the Ding models, then that would suggest that the structure of the Conaway models is a more accurate model structure to explain muscle biophysics than the structure of the Ding models. Specifically, such findings would suggest that calcium dynamics, and hence muscle force generation and maintenance, in paralyzed human soleus varies as a Riccati-Bass process that maintains constant probabilities of actions in its coefficients for each contraction and for various inputs. (10, 142) Furthermore, it would mean that the structure of the Conaway models is a more accurate and physiologically plausible predictor of force and fatigue than is the structure of the Ding models.

Table 6-3. Initial optimal parameter sets for Ding and Conaway force-fatigue models.

Muscle state	Muscle model	Fixed parameters	Free parameters
Fresh	Ding	τ_c=20 ms R_0=6.9	A, k_m, τ_1, τ_2
Fresh	Conaway	τ_c=20 ms λ_1=0.01, λ_2=0.03 A is scaled	k_m, τ_1, τ_2
Fatigue	Ding	τ_c=20 ms, k_m=0.06 τ_2=62.7 ms	A, R_0, τ_1
Fatigue	Conaway	τ_c=20 ms, τ_{1rest}=28.3 ms τ_2=62.7 ms μ_1=0.38, μ_2=0.5 a=1, b=1.5, c=1 A is scaled	$\alpha_{\tau 1}$, τ_{leak}, τ_{fat}

Using unconstrained optimization parameter values, differences in mean squared error and correlation with respect to the experimental data will be compared between the Conaway and Ding force models for inputs with frequencies greater than 5 pps. If the Conaway model, with constrained optimization parameter values, produces on average greater correlation to the experimental data than does the Ding model, then that would mean that the Conaway force model is a more accurate predictor of force at frequencies greater than 5 pps than is the Ding force model.

6.3.3 Muscle force protocol

The second objective of this thesis involves the comparison of two mathematical models to predicting force in fresh paralyzed human soleus. Given one closed-form parameterized model and one modified closed-form parameterized model, it is to be determined which model best predicts force in fresh paralyzed human soleus. If a given model can be found to accurately model and predict force, this could lead to further insight into the calcium dynamics of force in stimulated muscle, and ultimately, to design stress protocols that prevent fatigue. In addition, since trained paralyzed muscle behaves like nonparalyzed muscle (164), insights about the physiologic differences in force generation between nonparalyzed and paralyzed muscle can be garnered through this effort. Statistical tools will be used to compare predicted force versus experimentally generated force for each model. The models will then be compared against each other for curve fit and error indices.

6.3.3.1 Physiological rationale

Post-denervation changes that occur in muscle include altered fatigability and speed properties, neuromuscular transmission (33, 170), relationship between torque and frequency (170), low frequency fatigue (33, 168, 170), effects of training (169, 170), and post-fatigue potentiation (171). It is commonly though the human chronically paralyzed soleus has similar physiology to a fast-fatigable Type IIb fiber muscle.

Ding and colleagues (50) demonstrated the validity of a mathematical model that predicts the force generated by rat skeletal muscles during brief fused and unfused isometric contractions. The Ding force model consists of three coupled differential equations. The first two equations model the calcium dynamics and the third equation models force dynamics. The model parameters were estimated from brief trains of regularly spaces pulses that produce unfused muscle responses. Using these parameters, the model will be able to predict isometric forces from a variety of other stimulation patterns. Comparing experimental and modeled force indices have suggested a close fit between the model and the experiment data. It has since been shown that numerous physiological parameters calculated by the model have agreed with values obtained independently by other investigators.

The learning objectives for modifying the Ding force model are as follows. It is hypothesized that modification the Ding model of muscle force via an additional differential equation more accurately predicts R_0 as a function of time. Additionally, it is hypothesized that a certain combination of k_m, τ_1, and/or τ_2

yields the least prediction error while optimizing to realistic physiologic values. This would suggest several things. First, the voltage sensitivity of the SR calcium channels modulates force generation at low frequencies in paralyzed muscle during an extrinsically induced contraction. This would suggest a possible pathway to low-frequency fatigue in paralyzed human soleus and would imply that there are accelerated degradations of the calcium channels in the sarcoplasmic reticulum in paralyzed muscle during extrinsic contraction. Further, improved curve fit and reduced prediction error, by additionally optimizing on τ_1 and/or τ_2, would suggest that the lack of strong cross-bridge bonds and/or increased force decay due to cross-bridge friction modulate force generation in paralyzed muscle as stimulation input frequency increases.

6.3.3.2 Closed-form parameterized model of muscle force

To investigate the behavior of the Conaway force model in MATLAB, profiles for fresh muscle stimulated with inputs of different frequencies were generated using parameters from Frey Law and Shields (66) via code specially written for this study. In the figures, the force curve is included along with the curve for C_N. Plots of R_0 in fresh muscle are also shown.

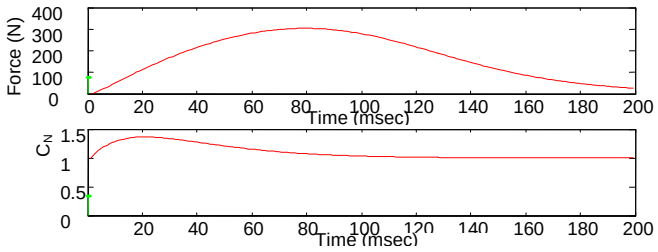

Figure 6-8. Duplication of force response and C_N from a twitch using the Conaway force model for one contraction. Since R_0 was found to be constant for this input, no plot is given for that curve.

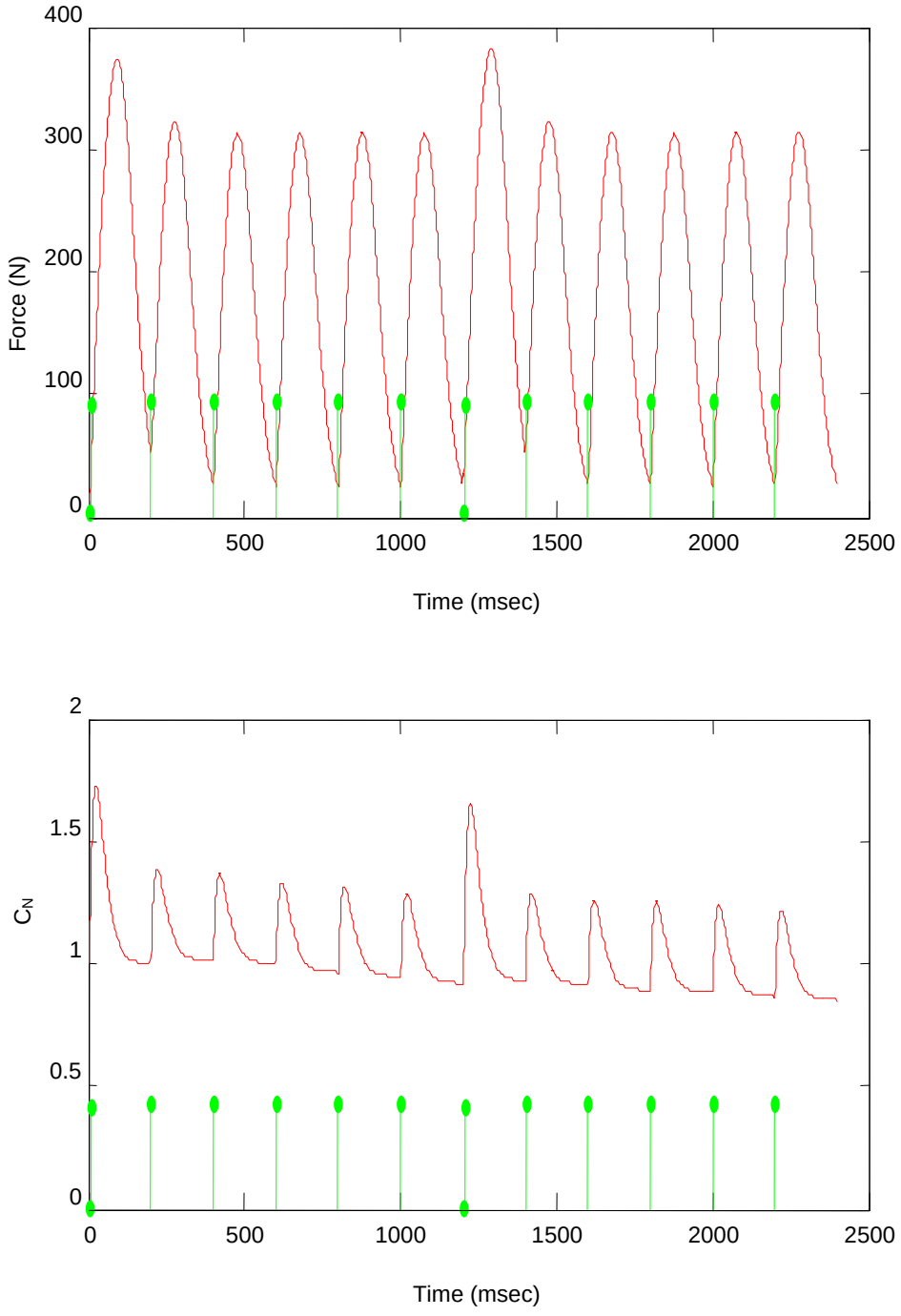

Figure 6-9. Duplication of force response and C_N from a 5 DDT input using the Conaway force model for two contractions.

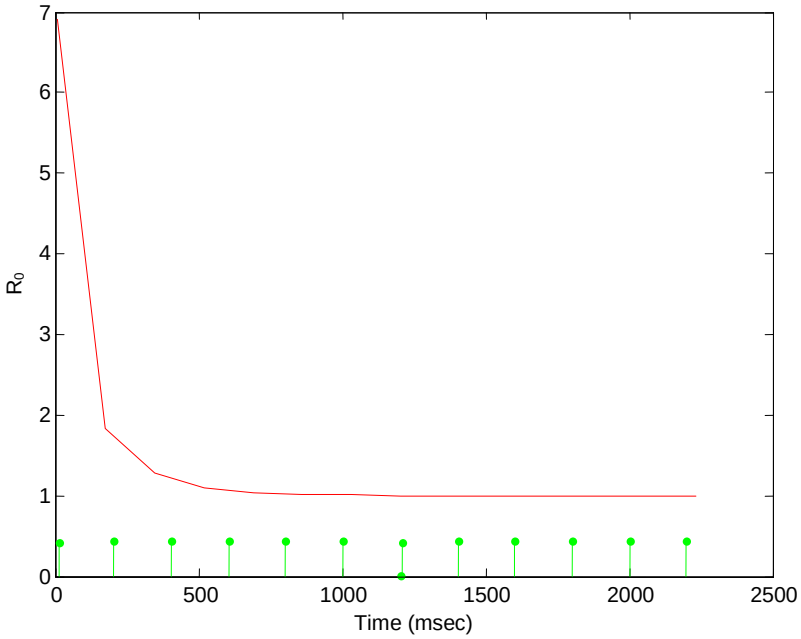

Figure 6-10. Behavior of R_0 from a 5 DDT input using the Conaway force model for two contractions. Note its sharp decrease.

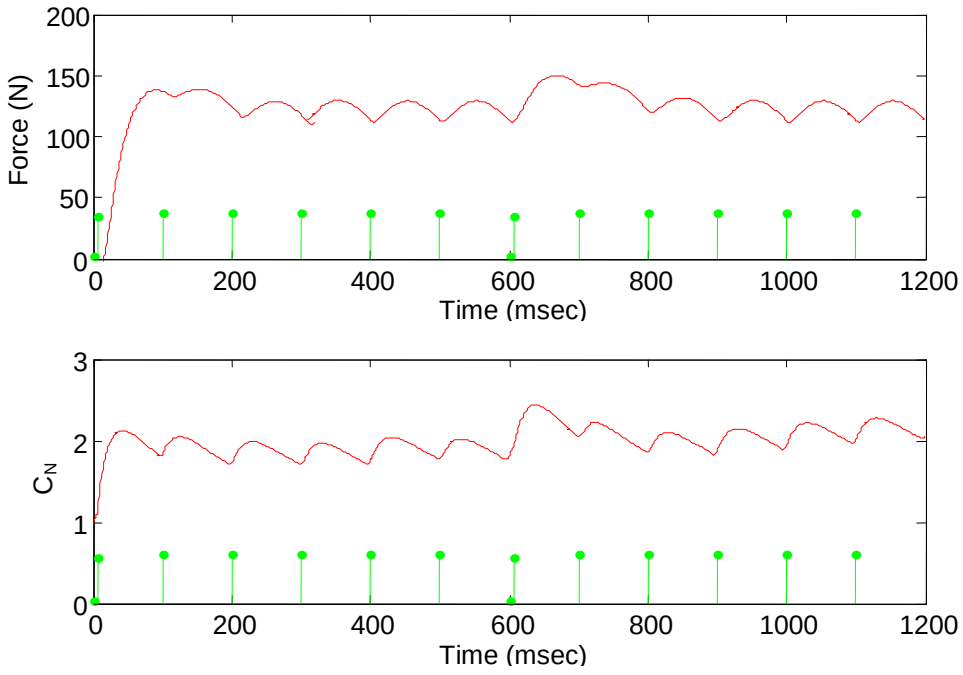

Figure 6-11. Duplication of force response and C_N from a 10 DDT using the Conaway force model for one contraction.

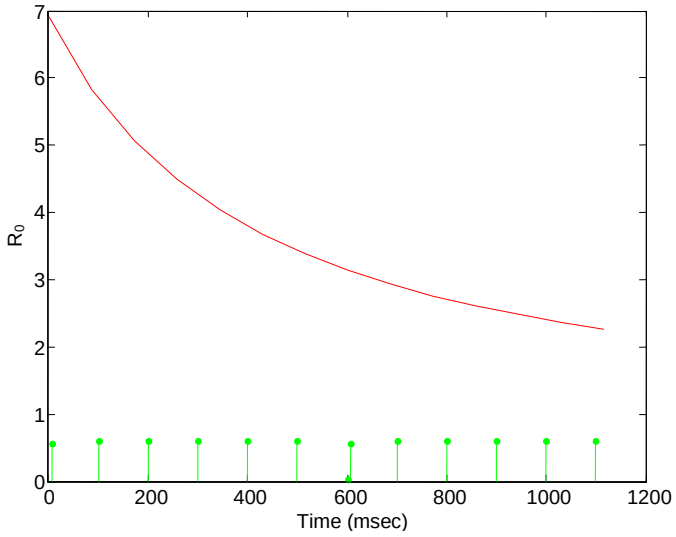

Figure 6-12. Behavior of R_0 from a 10 DDT input using the Conaway force model for one contraction. Note its increased lag in inflection.

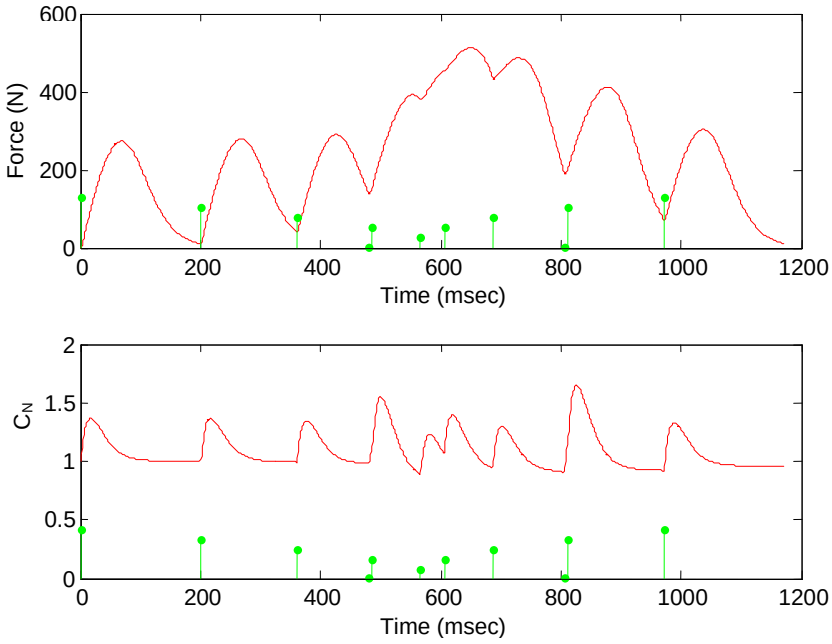

Figure 6-13. Duplication of force response and C_N from a doublet ramp using the Conaway force model for one contraction.

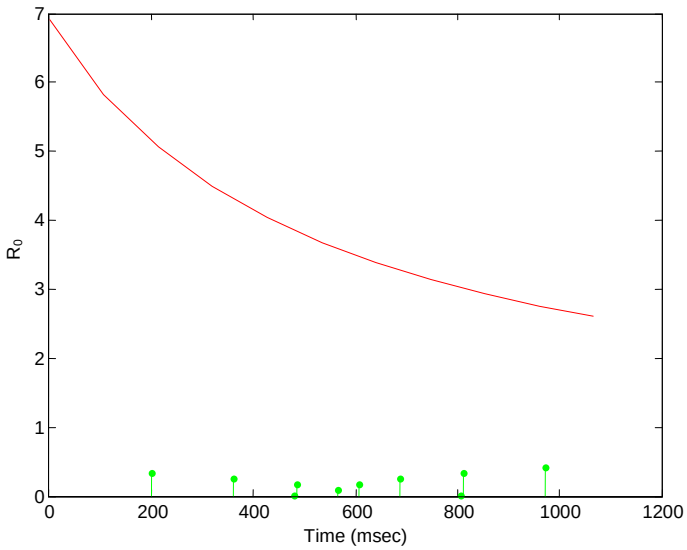

Figure 6-14. Behavior of R_0 from a doublet ramp input using the Conaway force model for one contraction. Note the smoothness of the curve

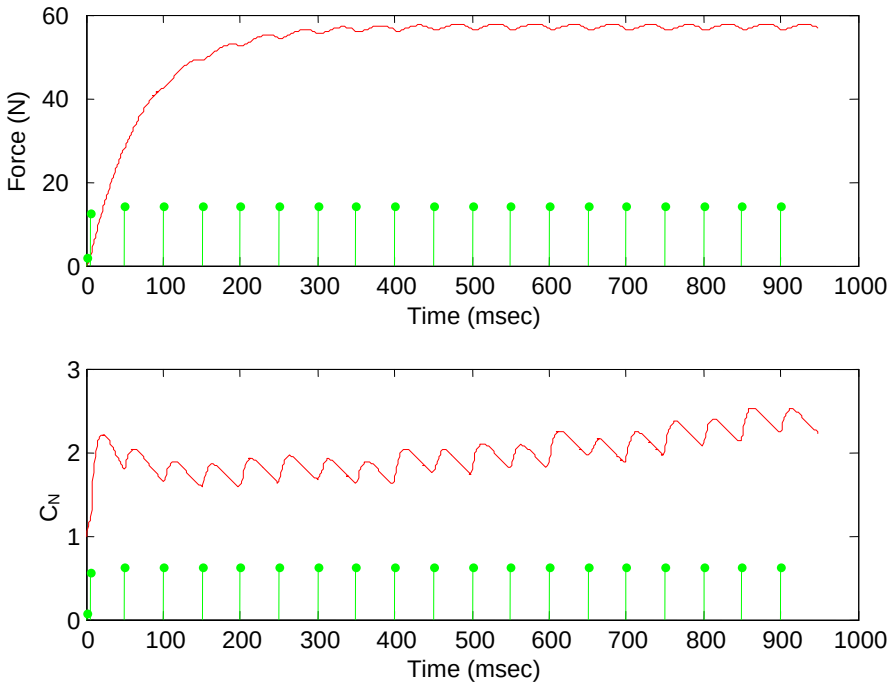

Figure 6-15. Duplication of force response and C_N from a 20 DDT input using the Conaway force model for one contraction.

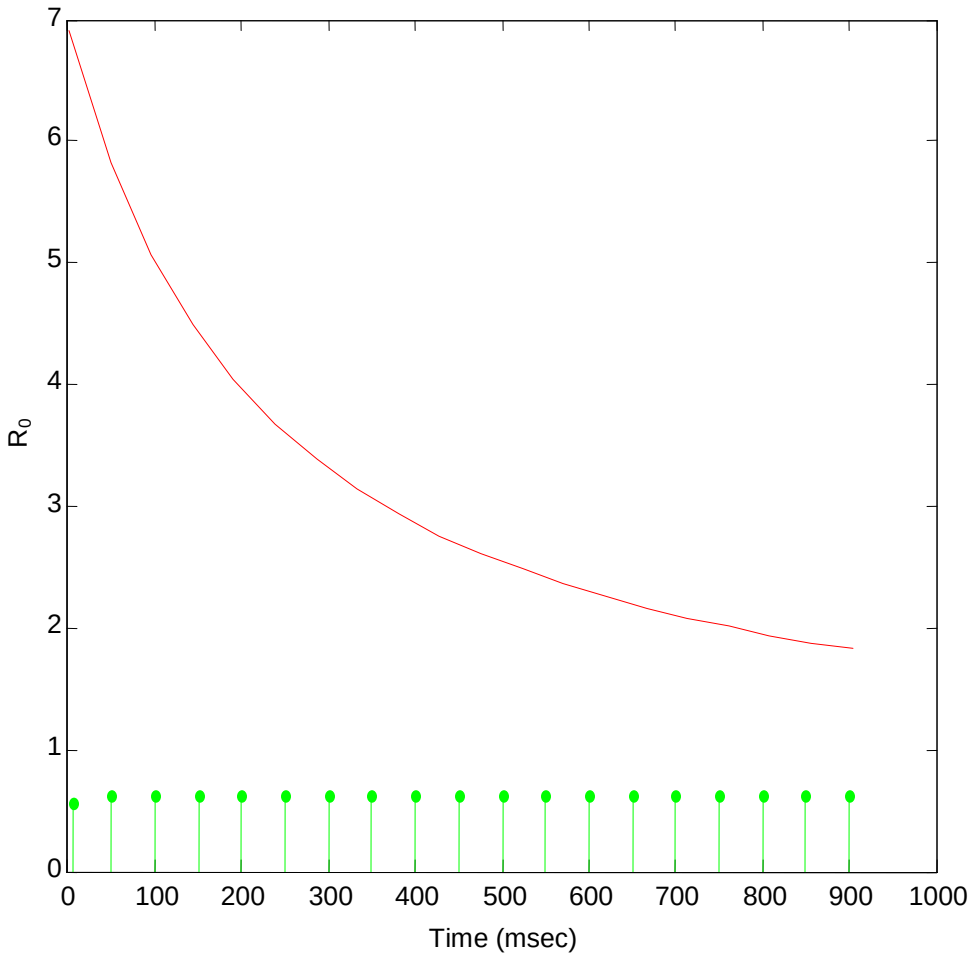

Figure 6-16. Behavior of R_0 from a 20 DDT input using the Conaway force model for one contraction. Note its increased lag and earlier inflection.

The preceding analysis confirms that the Conaway model generates curves similar to the Ding model for predicting force in fresh muscle from different types of inputs. In addition, the model, with a dynamic R_0, calculates the C_N curve more uniformly. The peaks in the C_N correspond as demonstrated in the literature with each pulse of the doublet ramp stimulus. Finally, as the frequency

of stimulation increases, the R_0 curve smoothens during the period of contraction. This implies that the Riccati-Bass equation for R_0 simulates the underlying calcium dynamics, and in turn leads to modeled muscle force generation, in a way that is physiologically plausible.

Of particular interest is the behavior of the individual free parameters of the simulated fasciculating contractions caused by higher frequencies (10 to 20 pps). (42) It is specifically hypothesized that the cross-bridge friction (τ_2) is the dominant process in generating force at higher frequencies in paralyzed fresh muscle. If τ_2 is shown to generally increase as a function of contraction index at increasing frequencies, it would demonstrate that it is the dominant free parameter in the Conaway force model. This would mean that cross-bridge friction is the dominant process that modulates force generation at higher frequencies in muscle.

6.3.3.3 Data analysis

Using constrained optimization parameter values, differences in predictive errors will be compared between different optimizations of the Conaway force model for stimulation inputs of 10 CT, doublet ramp, as well as 20 DDT and distinct parameter sets involving combinations of k_m, τ_1, and τ_2 The test statistic will be the Akaike final prediction error. The parameter set that generates the least prediction error and returns parameters within ranges reported elsewhere will be judged as optimal. It will be interesting to see if there are any differences between trained and untrained muscle, or which parameters, if any, are dominant at higher frequencies. Specifically, positive findings would mean that force

summation, and hence muscle force generation and maintenance, in paralyzed human soleus change as a function of increasing frequency.

6.3.4 Muscle fatigue protocol

The third objective of this thesis involves the comparison of two mathematical models to predicting fatigue in paralyzed human soleus. Given one closed-form parameterized model and one modified closed-form parameterized model, it is to be determined which model best predicts fatigue in paralyzed muscle. If a given model can be found to accurately model and predict fatigue, this could aid in the implementation of safe therapeutic limb stress protocols for persons with chronic spinal cord injury. In addition, since trained paralyzed muscle behaves like nonparalyzed muscle (164), insights about the physiologic differences in the process of muscle fatigue between nonparalyzed and paralyzed muscle can be garnered through this effort. Statistical tools will be used to compare predicted force versus experimentally generated force for each model. The models will then be compared against each other for curve fit and error indices.

6.3.4.1 Physiological rationale

Impeded calcium release from the sarcoplasmic reticulum has been identified as a factor in muscle fatigue in isolated fibers. (2, 3, 4) Transformation of skeletal muscle from slow to fast leads to long duration muscle fatigue from electrical stimulation at low frequencies. This has been seen the chronically paralyzed soleus muscle. (163, 165) Low-frequency fatigue occurs via a compromise in the excitation-contraction coupling mechanism which impedes the

release of divalent calcium. This impeded release of calcium ions by the SR has been hypothesized to contribute to fatigue from continuous activation at low frequencies for long periods of time (115, 120, 192). Since repetitive activation decreases the concentration of calcium ions intramuscularly, the amount of free ion available for myosin phosphorylation diminishes. (2, 177)

During exercise, however, defects in calcium release have been suggested to impair muscle function. It has been shown that during exercise in rodents and humans, RyR1 is progressively PKA-hyperphosphorylated, S-nitrosylated, and depleted of molecules including the RyR1-stabilizing subunit calstabin1. This results in "leaky" calcium channels that lead to a decrease in exercise tolerance in rodents. It has been shown that rodents with deleted calstabin1 exhibited markedly impaired exercise tolerance. A small molecule that prohibits depletion of calstabin1 from the RyR1 increased force generation and exercise tolerance. It also decreased calpain activity and levels of plasma creatine kinase. This suggests a possible mechanism by which calcium leaked from calstabin1-depleted RyR1 channels leads to impaired signaling, muscle damage, and decreased exercise tolerance. (11) The RyR is a homotetramer and half of all these complexes are proximal to the DHPR. In addition, it has been shown that RyR channels are dense square structures arranged in regular rows such that the adjacent channels contact one another at the corners. Fast and slow skeletal muscle fibers predominantly have the RyR1 isoform. However, fast fibers have higher RyR density. (12, 123, 170)

The calcium dependence of RyR activity is achieved by several different mechanisms. The RyR is activated by low concentration and inhibited at higher concentration. It has been suggested that there are various modes of calcium handling in the variety of fiber types that differentially affect the activity of the RyR. When the RyR is depolarized by the t-tubule, the released calcium ions may cause a positive feedback release cycle followed by a negative feedback release cycle. Direct interaction of the DHPR in the t-tubules of the RyR is believed to modulate excitation-contraction coupling. This occurs via a structural change in the DHPR that elicits a structural change in the RyR. That is the event which finally triggers the opening of calcium release channels. Biochemical evidence for a link between the two receptors has been reported. Ryanodine receptors interact with a variety of accessory proteins believed to modulate the activity of these calcium release channels. These proteins include S100 protein, CaM, 60-kDa CaM-dependent protein kinase, calsequestrin, and calstabin. (12, 123, 173)

According to Bellinger et al (11), binding of calstabin1 to RyR1 stabilizes the closed state of the calcium channel and facilitates coupled gating between neighboring channels that amplifies the transient current. Pharmacologic depletion of calstabin1 from RyR1 has been shown to decouple adjacent channels and causes leaks. In nonparalyzed muscle, this can inhibit contraction via depolarization. Genetic alteration of calstabin1 binding in RyR1 was shown to decrease excitation-contraction coupling and reduces the maximal voltage-gated release of divalent calcium with no change to its store content. It was shown that

knockout of calstabin1 specific to skeletal muscle decreased the voltage-gated Ca^{2+} release in the SR. In murine extensor digitorum longus, decreased maximal tetanic contraction and a shift to the right in the relationship between force and frequency were recorded. Yet alteration in SR calcium content or release was not indicated. This suggested that calstabin1 modulates gain from excitation-contraction coupling in fast-twitch skeletal muscle. Moreover, leakage of SR calcium via RyR1 channels was further hypothesized to cause muscle damage during intense stimulation by activating calpain which was shown to increase after intense stimulation.

In addition, as calcium channels inactivate, EC coupling is impaired. Delbono and Stefani (40, 41) found that calcium inactivation in paralyzed fibers had an increased recovery, and a decreased speed of inactivation. This renders inactivation of paralyzed muscle more difficult, since the voltage dependence of the calcium channel inactivation was partially shifted leftward due to proteolysis. It is also known there is a parallel change in the numbers of indentations and the amount of charge movement after denervation. (61) Furthermore, inactivation of EC coupling is not caused by calcium depletion from the sarcoplasmic reticulum or inactivation of the calcium release channel or contractile proteins. The resistance to inactivation of tension indicates a characteristic of the voltage-sensitive molecule. (59)

6.3.4.2 Closed-form parameterized model of muscle fatigue

To investigate the behavior of the Conaway fatigue model in MATLAB, profiles for simulated fatigued muscle were generated using parameters from

Ding (56) via code specially written for this study. In the figures, the force curve is included along with the curve for C_N. A plot of k_m in fatigued muscle is shown. In addition, plots of variation for A, $\alpha_{\tau 1}$, τ_{leak}, and τ_{fat} are also shown to demonstrate the sensitivity that the fatigue force and C_N curves have to the free parameters. This will semiquantitatively show which, if any, of the free parameters may be dominant in the Conaway fatigue model.

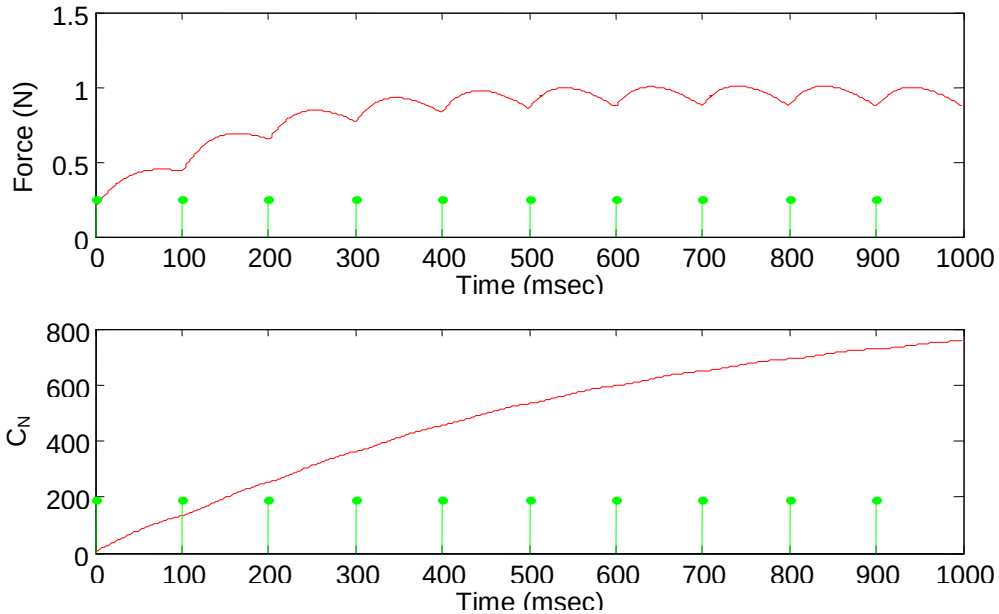

Figure 6-17. Duplication of a fatiguing contraction and C_N from a 10 CT input using the Conaway fatigue model for one contraction. It is shown that in the Conaway fatigue model, the force tetani fuse and decrease in magnitude. Furthermore, the C_N curve smoothens and goes to an asymptotic limit. This implies that the Conaway fatigue model may account for decaying, autocatalytic processes in fatigued paralyzed muscle.

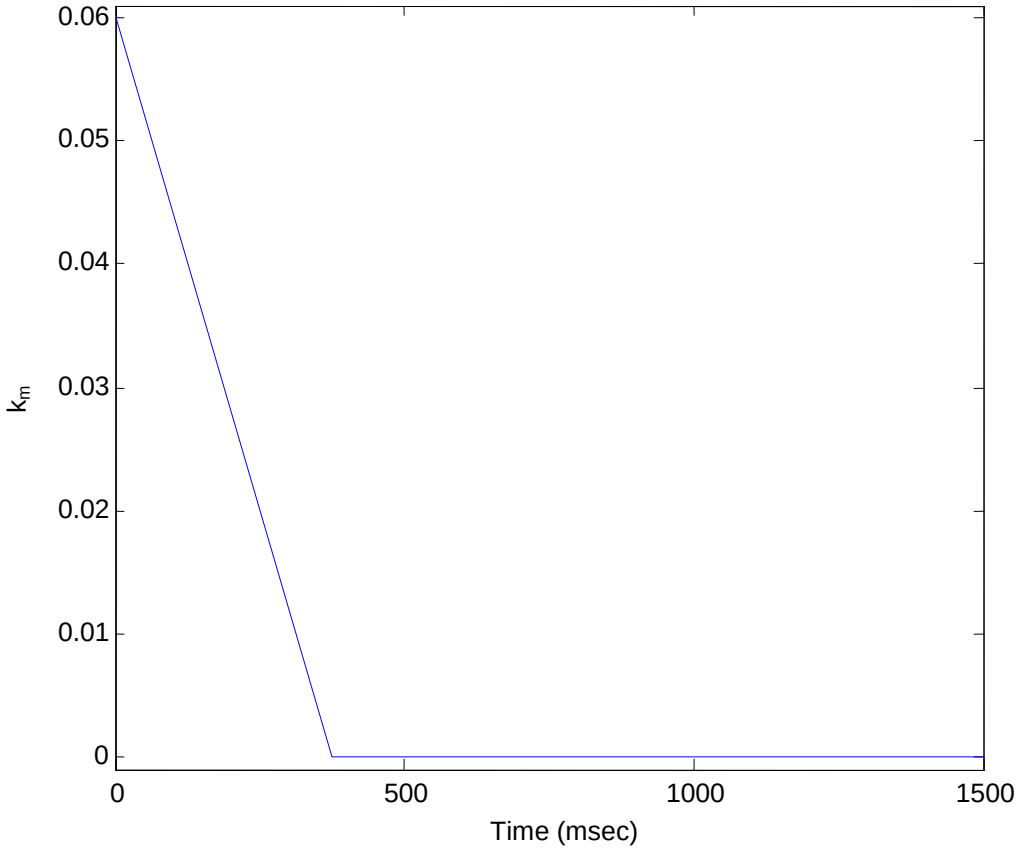

Figure 6-18. Behavior of k_m in the Conaway fatigue model for one contraction. It is shown that, in the Conaway fatigue model, k_m decays over a period of contraction. However, in the Ding model, k_m is a fixed parameter constant throughout a contraction.

In a related task, the effects of the free parameters are also explored through simulation. Of interest is the effect that τ_{leak} and $\alpha_{\tau 1}$ have on C_N. Observation of those simulated effects on the modeled force investigates previous assertions that calcium leak from the SR, as well as the lack of strongly bound cross-bridges, are the dominant factors in low-frequency fatigue in

paralyzed muscle. This will yield fruitful information on what threads to pursue in data analysis. Extrema of parameter ranges are shown for brevity.

τ_{leak}=0:

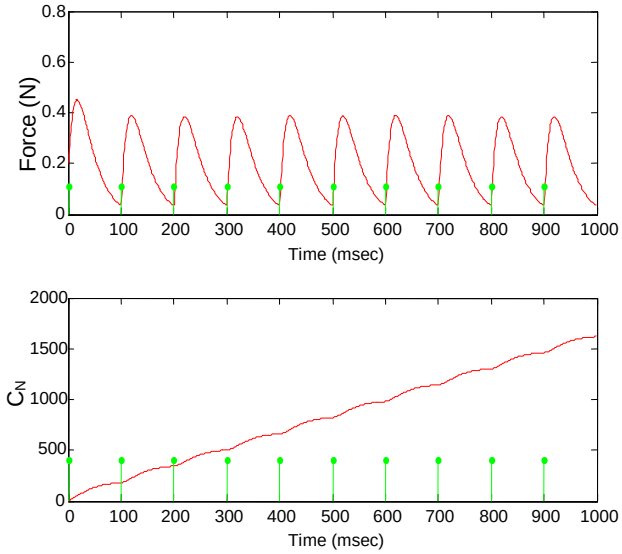

τ_{leak}=100:

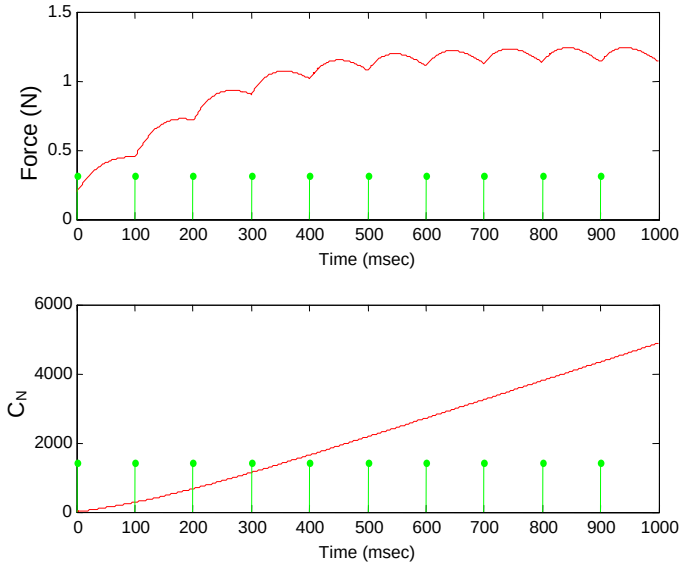

Figure 6-19. Effects of variations in τ_{leak} on the curves for force and C_N in the Conaway fatigue model for one contraction. The parameter τ_{leak} has the most effect on the shape of the curves by simulating fasciculations.

α_{T1}=0:

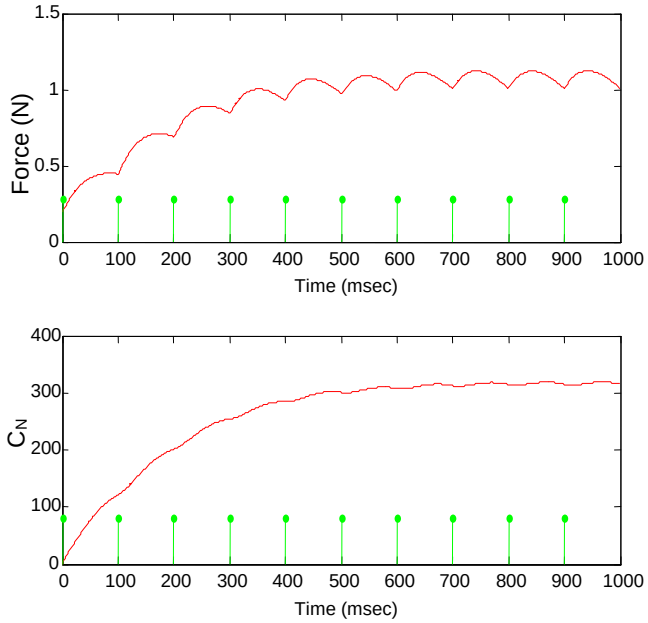

α_{T1}=5:

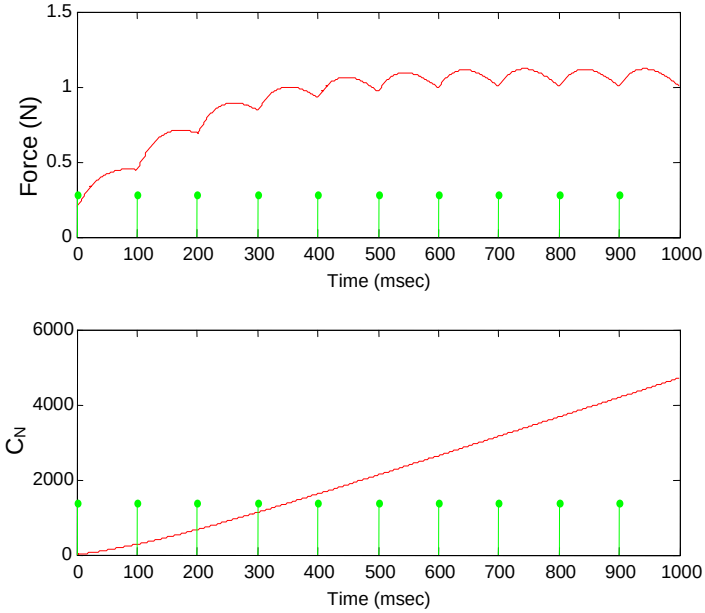

Figure 6-20. Effects of variations in α_{T1} on the curves for force and C_N in the Conaway fatigue model for one contraction. When α_{T1} is large, the concavity of the C_N curve inverts.

A=0.05 to 0.20:

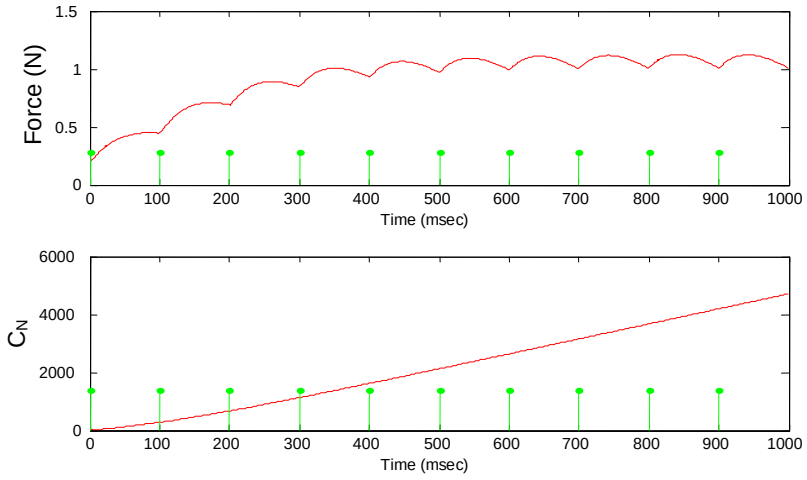

Figure 6-21. Effects of variations in A on the curves for force and C_N in the Conaway fatigue model for one contraction. The parameter A has the least effect on the shape of the curves.

In Figures 6-19 through 6-21, it is shown that τ_{leak}, quite remarkably, has the most influence on the predictive curves for force and C_N in the Conaway fatigue model. When that parameter is 0, the modeled tetani in the output do not fuse. As seen previously, unfused tetani results from the Ding model. Hence, as τ_{leak} increases, the fusion of the tetani in the simulated contraction gets smoother. Meanwhile, the parameter $\alpha_{\tau 1}$ influences the shape of C_N the most. It is very remarkable to see that when the particular parameter is 0, the concavity of the C_N curve inverts. Since that parameter directly modulates τ_1, the time constant of lack of strong cross-bridges, the means physiologically that the lack of strongly-bound cross-bridges does have a role in fatigue. It may be secondary to the

calcium leak. Nevertheless, $\alpha_{\tau 1}$ cannot be excluded from Hill-Huxley type of fatigue model. It is also seen that the parameter A has the least influence on the curves for force and C_N. Hence, the overall dominance of τ_{leak} on curve shaping implies that, consistent with the Principle of Le Chatelier (8), calcium leak current (11) has a major influence on fatigue in excessively stimulated paralyzed muscle. Hence, by including these changes, as well as a time constant to account for calcium leak induced by extrinsic electrical stimulation, the Conaway model will predict muscle fatigue better than the original Ding model.

6.3.4.3 Data analysis

The Conaway fatigue model will be investigated to understand the physiology of the muscle fatigue process. Fatigue data from Subjects 17 and 18 will be used in the analysis to test hypotheses. Optimizing on all model parameters without constraints, differences in mean squared error with respect to the experimental data will be compared between the Conaway and Ding fatigue models for inputs of 15 pps at 667 ms duration. If the Conaway model produces on average less mean squared error than the Ding model, then that would mean that the Conaway model is a more accurate predictor of muscle fatigue than the Ding model. Specifically, such findings would suggest that low frequency fatigue in paralyzed human soleus that arises from extrinsic stimulation is dependent upon a decaying muscle activation which is a power law function of time-varying voltage sensitivity.

Using the optimal, constrained parameter set, values will be calculated for each contraction in trained and untrained muscle. Trends of means and

standard deviations will be determined to ascertain how each parameter, especially τ_{leak}, behaves as a function of contraction index during fatigue. Specifically, it is hypothesized that calcium leak increases as a function of contraction index during fatigue. If τ_{leak} is shown to generally increase as a function of contraction index during fatigue, while the other parameters behave erratically, it would demonstrate that it is the dominant free parameter in the Conaway fatigue model. This would mean that calcium leak is the dominant process that modulates fatigue in muscle.

6.4 Solution techniques, parameterization approach, error calculation, and statistical methods

Solution techniques, parameterization approaches, and calculation of error, and statistical techniques for this study are described in this section. The results in the next chapter will show the data analyzed according to statistical techniques discussed.

6.4.1 Solution techniques

In the general case, nonlinear summation is accomplished by solving a differential equation. For the Riccati equation, solutions have the form of y(t)=F(t)/G(t) and have been specifically shown to have the following Taylor series expansion. (39)

$$y_0=t^3/3+t^7/63+2t^{11}/2079+... \qquad (6\text{-}13)$$

Moreover, the solution of the Riccati equation in a neighborhood of any point y_{00} is:

$$(t - t_0) = \Sigma_{n=2}^{\infty} \mathrm{A}_r (y_0 - y_{00})^r \qquad (6\text{-}14)$$

More specifically, the Levenburg-Marquardt algorithm (LMA) interpolates between the Gauss-Newton algorithm and the gradient descent method. (68, 114, 125) The LMA is more robust than the GNA. Hence, it converges even with a large error in estimation. Nevertheless, for well-behaved functions and reasonable initial parameter values, the LMA tends to converges more slowly than the GNA. The primary use of the LMA is found in the least squares curve fitting problem. The problem is formulated in the following way. Given a set of empirical data pairs (t_i, y_i), the parameters **p** of the model curve f(t|**p**) are to be optimized so that the sum of the squares of the deviations from the experimental values

$$s(p) = \sum_{i=1}^{m} [y_i - f(t_i \mid p)]^2 \qquad (6\text{-}15)$$

converges to a minimum.

Like other numeric schemes of minimization, the Levenburg-Marquardt algorithm is an iterative technique. To begin a minimization, an initial guess for the parameter vector **p** must be provided. In many instances, a typical estimate like $\mathbf{p}^T$=(1,1,...,1) is satisfactory. However, in other situations, the algorithm converges only if the initial estimate is already fairly proximal to the final solution. In each step of the iteration, the parameter vector **p** is overwritten by a new estimate **p** + **q**. To determine **q**, the functions f_i(**p** + **q**) are estimated by

linearization such that **f**(**p** + **q**) ≈ **f**(**p**) + **Jq** where **J** is the Jacobian of **f** at **p**. (68, 114, 125)

At a minimum of the sum of squares S, $\nabla_q S = 0$. Differentiating the square of the right hand side of the equation above and setting to zero leads to ($\mathbf{J}^T\mathbf{J}$)**q** = $-\mathbf{J}^T\mathbf{f}$ from which **q** can be found by taking the inverse of $\mathbf{J}^T\mathbf{J}$. However, the crux of Levenburg-Marquardt is to replace this equation by a 'damped version' ($\mathbf{J}^T\mathbf{J}$ + λ.**I**)**q** = $-\mathbf{J}^T\mathbf{f}$. This non-negative damping factor λ is changed at each iterative step. If S decreases rapidly, a smaller damping factor can be used. This would bring the algorithm closer to Gauss-Newton. However, if an iteration gives insufficient reduction in the residual, the factor can be increased giving a step closer to the gradient descent direction. Furthermore, if a calculated step length or the decrease in the sum of squares to the current-valued parameter vector **p** misses predefined limits, the iteration is terminated and the final parameter vector **p** is taken as the solution. (68, 114, 125)

A myriad of quasi-heuristic arguments have been suggested for the best choice for the damping factor λ. Theory has shown the reasons that guarantee local convergence of the algorithm for some of the choices. However, these choices can make the global convergence of the algorithm very slow proximal to the optimum. Hence, the absolute value of any choice depends on the scaling of the initial problem. Marquardt recommended initializing with a value λ_0 and a factor v>1. Initially setting $\lambda=\lambda_0$, the residual sum of squares S(**p**) is computed after one step from the initial point with the damping factor of $\lambda=\lambda_0$ and secondly with λ/v. If both of computed residual sums are worse than the starting point, the

damping increases by successive multiplication by v. This continues until a better point is determined with a new damping factor of λv^k for some k. However, if the damping factor λ/v results in decreased residual, this is taken as the new value of λ and the process continues. Yet, if using λ/v gave a larger residual sum but using λ resulted in a better residual, the damping factor does not change. Thus, the new optimum becomes the value obtained with λ as damping factor. (68, 114, 125)

In a 2006 paper (6), the matrix Riccati differential equation (MRDE) for the linear quadratic singular system was solved via neural networks. The purpose was to achieve optimal control with decreased computation by comparing the solutions of the MRDE obtained from traditional methods such as Runge-Kutta and Runge-Kutta-Butcher, as well as the nontraditional method of neural networks. Using the Levenburg–Marquardt algorithm, it was shown that the accuracy of neural network solution was qualitatively better than traditional methods. The advantage of the network approach is that, once training occurs, the solution may be instantaneously calculated at any number of points while minimizing computing time and memory with uniform accuracy. Hence, it was shown that trained neural networks provide compact expression of the analytical solution in the finite domain.

6.4.2 Parameterization

All models will be parameterized using a single predetermined stimulation pattern, the doublet ramp. (55, 66) To appropriately compare results between models, one parameterization approach is necessary. The model parameters

will be mathematically optimized using the MATLAB optimization toolbox function, lsqnonlin, a least squares approach using the Levenberg-Marquardt method. The lsqnonlin function minimizes the sum of the squares of the differences between model and experimental forces at each point in time. In addition, the models require a stiff differential equation solution algorithm for appropriate convergence of the optimization.

6.4.3 Error calculation

The Akaike Final Prediction Error (FPE) criterion, according to the MATLAB 7.x Reference Manual (The MathWorks, Natick, MA), provides a measure of model quality by testing the model on different parameter sets. After several different models are computed, they can be compared using this criterion. According to theory, the most accurate model has the least FPE. The Akaike FPE is thus defined by the following equation:

$$FPE = V\left(\frac{1+\frac{d}{N}}{1-\frac{d}{N}}\right) \tag{6-16}$$

where V is the squared error loss function, d is the number of optimized parameters, and N is the number of points in the data set. The squared error loss function V is defined by the following equation:

$$V = \det\left(\frac{1}{N}\sum_{1}^{N}\varepsilon(t,\theta_N)(\varepsilon(t,\theta_N))^T\right) \tag{6-17}$$

where θ_N represents the estimated parameters.

Using the optimal parameter values determined for each subject and model, force train predictions from doublet ramps and inputs of varying

frequencies with and without doublets, and fatiguing bouts for trained and untrained human paralyzed soleus muscle will be produced. The Akaike Final Prediction Error (FPE) criterion provides a measure of model quality by simulating the situation where the model is tested on different parameter sets. After several different models are computed, they can be compared using this criterion. According to theory, the most accurate model has the least FPE. The reason for that is that agreement, not correlation, between a model and experimental data is what is sought. Actual numerical values of force are not important for this study. The question to be answered is, "How well does a model agree with experiment?" That leads to the question fundamental to this study, "Which model agrees best with experiment?"

The Akaike FPE from the MATLAB 7.0 Optimization Toolbox (The Mathworks, Natick, MA) will evaluate the fit of each optimization of each model relative to experimental for both limbs in each test state. Therefore, the Akaike FPE will be determined for each candidate optimal parameter set against data from nonparalyzed and paralyzed muscle in fresh and fatigued states. In all cases, the optimal parameter set will be the one that generates the least Akaike FPE while returning the most realistic parameter values.

6.4.4 Statistical methods

Statistical techniques including paired t-tests, single factor analysis of variance, repeated measure two-way analysis of variance, will be used in this study. By comparing the parameter values between trained and untrained muscle in fresh and fatigued states, differences between nonparalyzed and

paralyzed muscle can be ascertained. Using the paired t-tests, differences in model structure as well as specific model ability (Ding vs. Conaway) can be ascertained. Using analysis of variance, parametric variation will be calculated and compared for frequency (5 pps vs. > 5 pps), training status (trained versus untrained) and contraction index in fresh muscle. In fatigued muscle, analysis of variance will be used to examine parametric behavior as a function of contraction index and training status (trained and untrained). All statistics will be done in Excel 2007 (Microsoft, Redmond, WA). The level of significance will be set at 0.05.

CHAPTER 7: RESULTS

7.1 Introduction

In this chapter, the results of this study are given. First, the Conaway models of muscle force and fatigue are validated and tested for robustness with data from trained and untrained limbs. Next, the Ding and Conaway models are compared in predictive ability using various statistical metrics. Then, the role of the parameter τ_2 in the Conaway force model is investigated. Finally, the role of the parameter τ_{leak} in the Conaway fatigue model is investigated. The findings will answer the major hypothesis of the study about whether an adequate characterization of the dynamics of divalent calcium during contraction is what is missing from models of muscle force and fatigue.

7.2 Validation and testing of the Conaway models

The Conaway models of muscle force and fatigue are validated in this section. In addition, the models are shown to be robust using various inputs in untrained and trained muscles in different subjects.

7.2.1 Conaway force model

With initial values (τ_c=20, τ_1=28.3, τ_2=62.7, k_m=0.06, λ_1=0.38, λ_2=0.5), the Conaway force model is validated using data from a 5 DT with beginning doublet in the untrained limb of subject 18. The model is then shown to be robust by using twitch, a10 DT input, and a 20 CT input in the untrained muscle of Subject 18 as well as with a doublet ramp input in the trained limb of Subject 27.

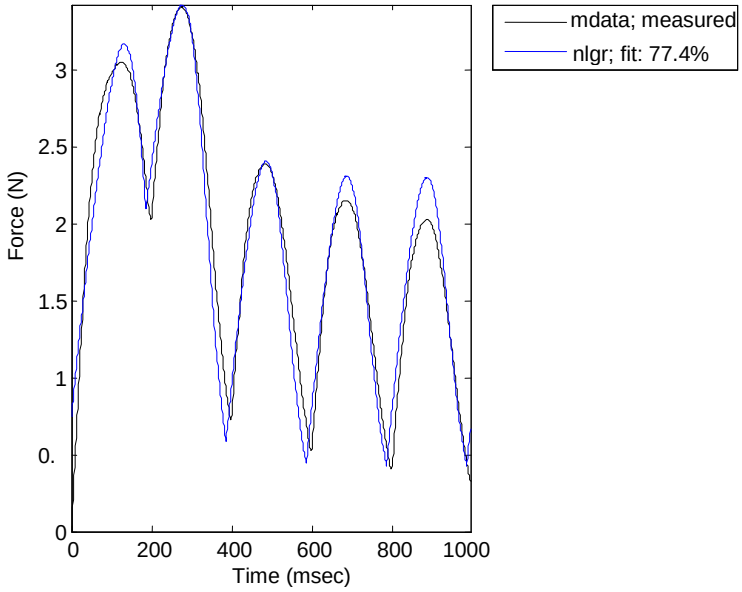

Figure 7-1. Validation of Conaway force model with 5 pps train with beginning doublet in trained muscle in Subject 18. The model had 77.4% agreement with the data.

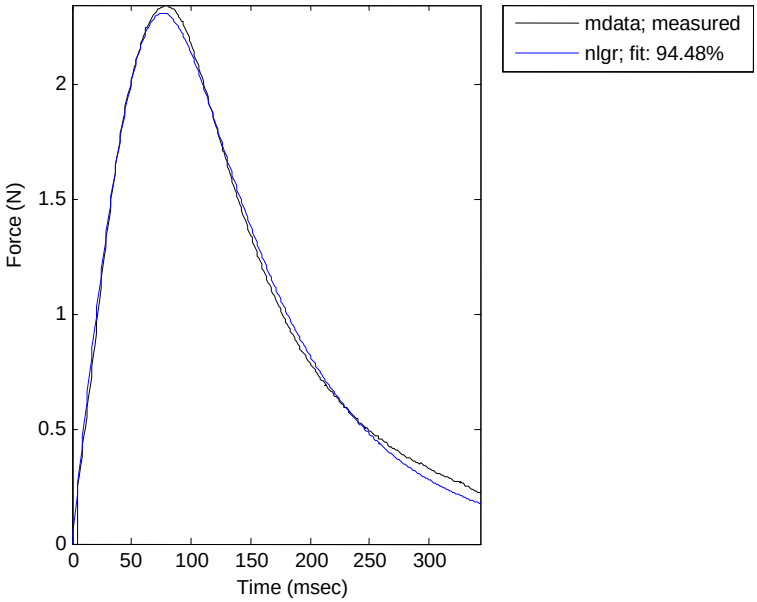

Figure 7-2. Twitch in trained muscle in Subject 18. The model had 94.48% agreement with the data.

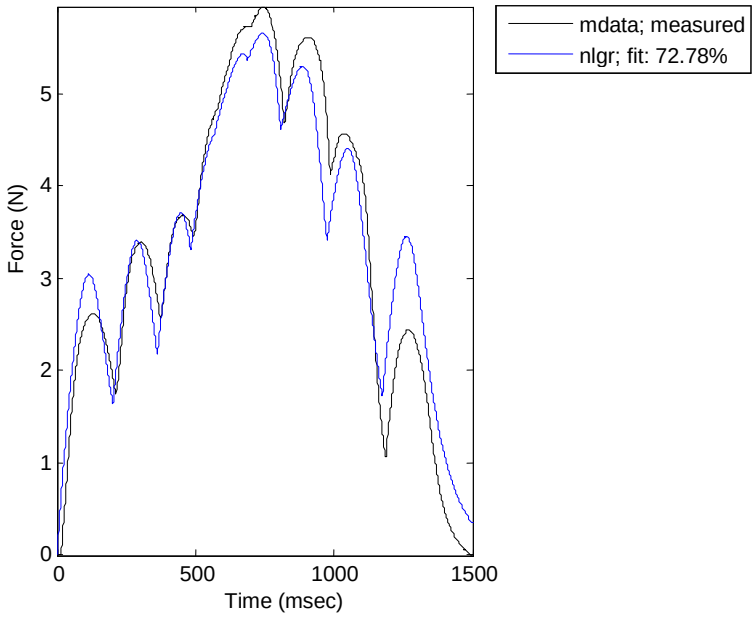

Figure 7-3. Doublet ramp in trained muscle in Subject 27. The model had 72.78% agreement with the data.

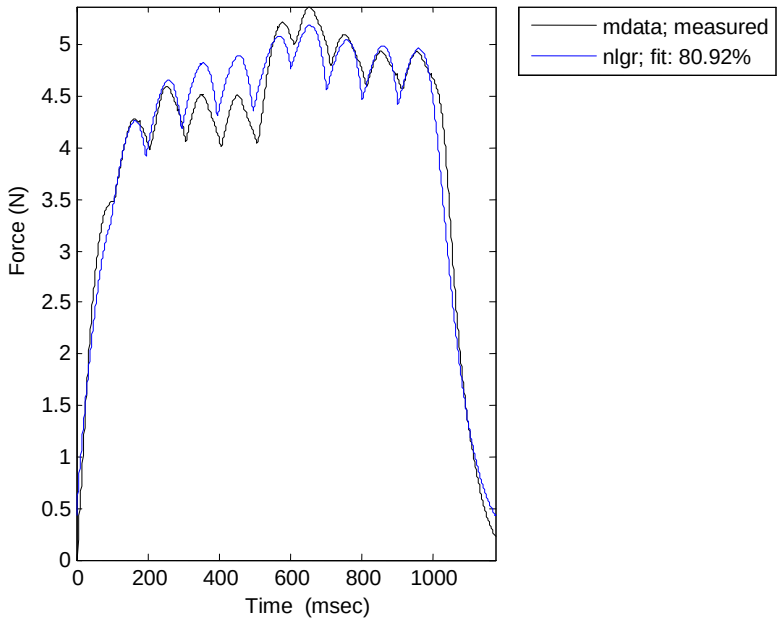

Figure 7-4. 10 DT stimulation in untrained muscle in Subject 18. The model had 80.92% agreement with the data.

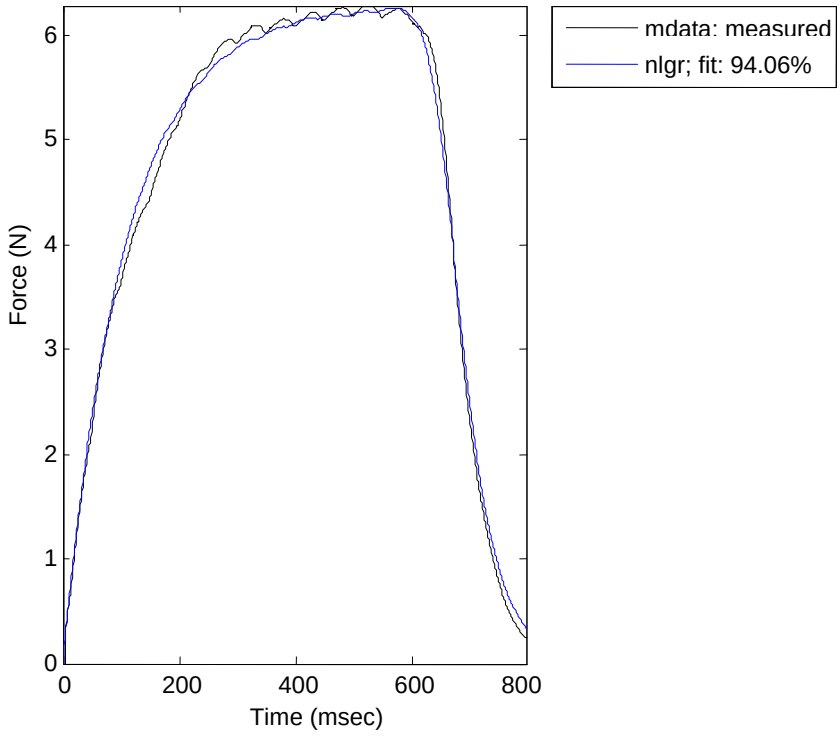

Figure 7-5. 20 CT in untrained muscle in Subject 18. The model had 94.06% agreement with the data.

It is thus shown that the Conaway force model is robust for different inputs. The curve fits range from 72.78 to 94.48 percent.

7.2.2. Conaway fatigue model

With initial values (τ_c=20, τ_{1rest}=28.3, τ_2=62.7, τ_{fat}=47.9, $k_m(0)$=0.06, $\alpha_{\tau 1}$=0.003, μ_1=0.38, μ_2=0.5, a=1, b=1,5, c=1), the Conaway fatigue model is validated for both limbs in Subject 18. The input is set to 10 CT (15 pps, 667 ms).

Table 7-1. Parameter values for Conaway fatigue model validation in trained limb in Subject 18.

Parameter	Optimized value	Standard Deviation	Free or fixed	Range
τ_2	62.7	0	Fixed	[0 ∞]
τ_c	20	0	Fixed	[0 ∞]
a	1	0	Free	[0,50]
B	1.5	0	Free	[0,10]
c	1	0	Free	[0,10]
τ_{1rest}	28.3	0	Fixed	[0,10]
τ_{fat}	28.5647	9.95897	Free	[0,50]
$\alpha_{\tau 1}$	4.4955	1.78964	Free	[0 50]
μ_1	0.38	0	Fixed	[0 ∞]
μ_2	0.5	0	Fixed	[0 ∞]
τ_{leak}	87.473	7.50893	Free	[0, 1000]
A	0.0347338	0.0052389	Free	[0 ∞]

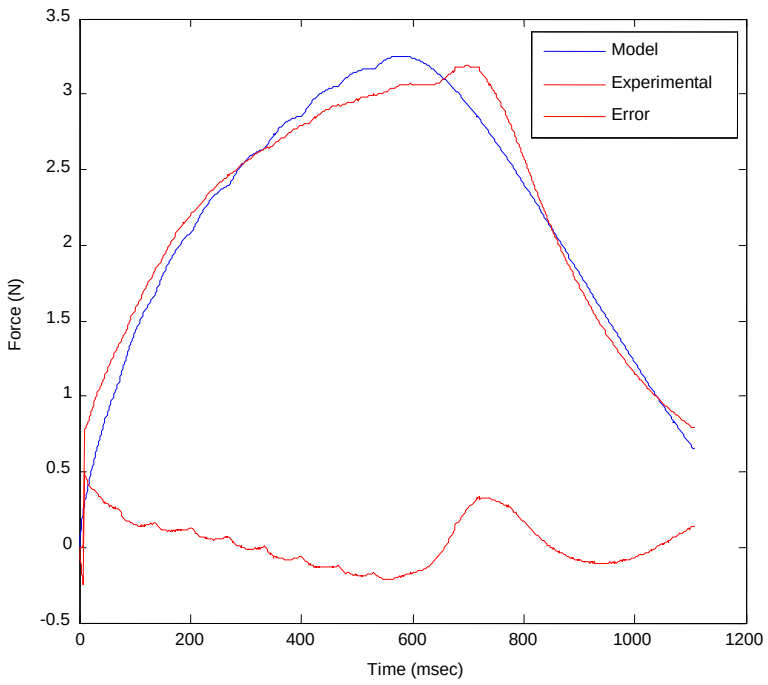

Figure 7-6. Fatigue in trained limb of Subject 18. The agreement of the Conaway model with the experimental data is 0.982282.

Table 7-2. Parameter values for Conaway fatigue model validation in untrained limb in Subject 18.

Parameter	Optimized value	Standard deviation	Free or fixed	Range
τ_2	62.7	0	Fixed	[0 ∞]
τ_c	20	0	Fixed	[0 ∞]
a	1	0	Free	[0,50]
b	1.5	0	Free	[0,10]
c	1	0	Free	[0,10]
τ_{1rest}	28.3	0	Fixed	[0 ∞]
τ_{fat}	30.5407	7.41266	Free	[0,50]
$\alpha_{\tau 1}$	5.14556	1.4505	Free	[0 50]
μ_1	0.38	0	Fixed	[0 ∞]
μ_2	0.5	0	Fixed	[0 ∞]
τ_{leak}	95.7433	7.56264	Free	[0, 1000]
A	0.123803	0.00397493	Free	[0 ∞]

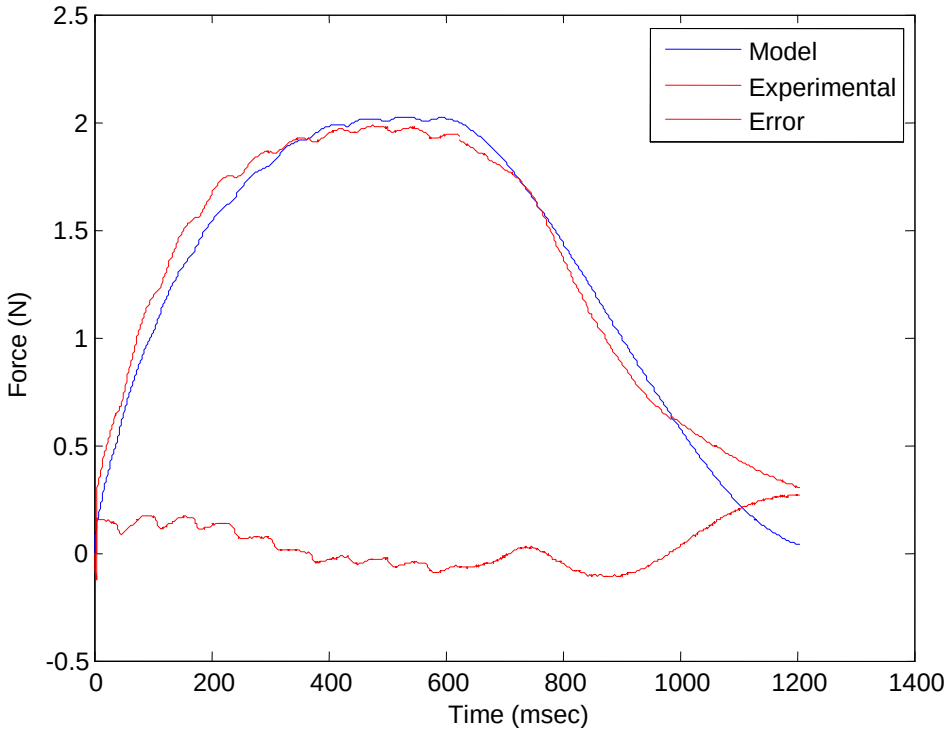

Figure 7-7. Fatigue in untrained limb of Subject 18. The agreement of the Conaway model with the experimental data is 0.9990524.

Table 7-3. Comparison of error statistics in Conaway fatigue model validation for trained and untrained limb. The Conaway fatigue model has very low error, in all metrics, for both trained and untrained muscle.

Muscle training Status	Mean Squared Error	Mean Absolute Error:	Correlation Coefficient	95% CI	r^2	p-value
Trained	0.161416	0.0257231	0.982282	(0.980085 0.98424)	0.9648	<0.001
Untrained	0.112667	0.0369234	0.990524	(0.989395 0.991533)	0.981137	<0.001

7.3 Determining differences in force and fatigue model structures

7.3.1 Global comparison between Ding and Conaway model structures

Table 7-4. Prediction measures across various inputs, training status, and fatigue states from both models in unconstrained optimization.

Model/Subject/Training/Input (Unconstrained optimization)	Mean Squared Error	Mean Absolute Error	Correlation Coefficient	95% CI	r^2	p-value
Ding 18 trained 5 DDT	0.259469	0.0714151	0.709223	(0.681905 0.734565)	0.502997	<0.001
Conaway 18 trained 5 DDT	0.271594	0.0710973	0.672219	(0.642153 0.700221)	0.451879	<0.001
Ding 18 untrained 10 DT	0.28267	0.138498	0.715163	(0.675599 0.750619)	0.511458	<0.001
Conaway 18 untrained 10 DT	0.212569	0.103256	0.849276	(0.826456 0.86931)	0.721269	<0.001
Ding 18 trained 20 CT	0.271539	0.155377	0.757612	(0.722992 0.788436)	0.573976	<0.001
Conaway 18 trained 20 CT	0.204272	0.120135	0.874776	(0.855515 0.891619)	0.765232	<0.001
Ding 18 untrained fatigue	0.761985	0.438124	0.37476	(0.325149 0.422314)	0.140445	<0.001
Conaway 18 untrained fatigue	0.045919	0.000529374	0.997035	(0.996681 0.997352)	0.99408	<0.001

5 DDT=5 pps with dual doublet
10 DT=10 pps with beginning doublet
20 CT=20 pps continuous train

Using unconstrained optimization parameter values, various statistics have been calculated. Differences in mean squared error and correlation with respect to the experimental data have been compared between the Conaway and Ding models for various inputs.

Table 7-5. Comparison of average mean square error and average correlation coefficient in Ding and Conaway model structures under unconstrained optimization.

Model Structure	Average Mean Squared Error (95% CI)	Average Correlation Coefficient (95% CI)
Ding	0.463259 ± 0.432941	0.648606 ± 0.255369
Conaway	0.178981 ± 0.138586	0.874781 ± 0.214206

From the 95% confidence intervals of the means for both metrics from each model, it is seen that the Conaway model structure has less average mean squared error and greater correlation than the Ding model structure of muscle force across different inputs and subjects. Furthermore, a two-sided paired t-test with four degrees of freedom for the average mean squared error at $\alpha=0.05$ yields $t=1.88825$. That is less than the critical value $t=2.776445$. For the correlation coefficient, a two-sided paired t-test with four degrees of freedom at

α=0.05 yields t=-1.94385. That is considerably less than the critical value t=2.776445. Hence, the hypotheses regarding the Conaway model having greater correlation to experimental data, and less mean squared error than does the Ding model are not rejected.

7.3.2 Comparison between Ding and Conaway force models

Table 7-6. Prediction measures from the Ding and Conaway force models for inputs with frequencies greater than 5 pps in unconstrained optimization in trained muscle from Subject 18.

Model/Input	Mean Squared Error	Mean Absolute Error	Correlation Coefficient	95% CI	r^2	p-value
Ding 10 CT	0.326737	0.138498	0.538285	(0.496847 0.577274)	0.289751	<0.001
Conaway 10 CT	0.016872	0.01583	0.848331	(0.806825 0.889838)	0.719665	<0.001
Ding 10 DT	0.441139	0.305584	0.450897	(0.408164 0.491659)	0.203308	<0.001
Conaway 10 DT	0.06579	0.017	0.870632	(0.816685 0.924398)	0.75800\	<0.001
Ding 20 CT	0.271539	0.155377	0.757612	(0.722992 0.788436)	0.573976	<0.001
Conaway 20 CT	0.014578	0.016597	0.959027	(0.95243 0.965624)	0.919733	<0.001
Ding 20 DT	0.28267	0.138498	0.715163	(0.675599 0.750619)	0.511458	<0.001
Conaway 20 DT	0.070897	0.03773	0.723194	(0.618077 0.828311)	0.52301	<0.001

10 CT=10 pps continuous train
10 DT=10 pps with beginning doublet
20 CT=20 pps continuous train
20 DT=20 pps with beginning doublet

Using unconstrained optimization parameter values, various statistics have been calculated. Differences in mean squared error and correlation with

respect to the experimental data have been compared between the Ding and Conaway force models for inputs with frequencies greater than 5 pps in trained and untrained muscle.

A one-sided paired t-test with three degrees of freedom for the average mean squared error at α=0.05 yields a p-value of 0.001902907. For the correlation coefficient, a one-sided paired t-test with three degrees of freedom at α=0.05 yields a p-value of 0.037650013. Both p-values are less than 0.05. Hence, the hypotheses regarding the Conaway model having greater correlation, and less mean squared error, to experimental data in trained muscle than does the Ding model are not rejected.

Table 7-7. Prediction measures from the Ding and Conaway force models for inputs with frequencies greater than 5 pps in unconstrained optimization in untrained muscle from Subject 18.

Model/Input	Mean Squared Error	Mean Absolute Error	Correlation Coefficient	95% CI	r^2	p-value
Ding 10 CT	0.345966	0.208889	0.531295	(0.489438 0.570709)	0.282274	<0.001
Conaway 10 CT	0.386246	0.21118	0.576794	(0.281677 0.871791)	0.332622	<0.001
Ding 10 DT	0.389072	0.239113	0.370379	(0.320528 0.418183)	0.13718	<0.001
Conaway 10 DT	0.018002	0.016788	0.809217	(0.74039 0.878044)	0.654833	<0.001
Ding 20 CT	0.271539	0.155377	0.757612	(0.722992 0.788436)	0.573976	<0.001
Conaway 20 CT	0.01361	0.019836	0.940613	(0.926062 0.055164)	0.884753	<0.001
Ding 20 DT	0.28267	0.138498	0.715163	(0.675599 0.750619)	0.511458	<0.001
Conaway 20 DT	0.212569	0.103256	0.849276	(0.826456 0.86931)	0.721269	<0.001

10 CT=10 pps continuous train
10 DT=10 pps with beginning doublet
20 CT=20 pps continuous train
20 DT=20 pps with beginning double

For the correlation coefficient, a one-sided paired t-test with three degrees of freedom at α=0.05 yields a p-value of 0.048310047. Hence, only the hypothesis regarding the Conaway model having greater correlation to experimental data in untrained muscle than does the Ding model at frequencies greater than 5 pps is not rejected. The statistical significance is weak, however.

A single factor analysis of variance was performed to test for differences between model mean squared errors at a significance of 0.05. With the p-value at 0.000909, it is shown that there is a highly significant difference between the predictive abilities between the Ding and unconstrained Conaway force models. Remarkably, the training status contributed little to the error variance. The difference of the error generated by the models was the primary source of mean squared error variance.

Table 7-8. Single factor analysis of variance for mean squared error between Ding and Conaway force models.

Source of Variation	*SS*	*df*	*MS*	*F*	*P-value*	*F crit*
Model	0.289618	1	0.289618	19.11658	0.000909	4.747225
Training	0.181801	12	0.01515			
Total	0.471419	13				

7.3.3 Comparison between Ding and Conaway fatigue models

Optimizing on all model parameters without constraints, differences in mean absolute error and correlation with respect to the experimental data will be compared between the Conaway and Ding fatigue models for inputs of 15 pps at 667 ms duration. Significance will be set at α=0.05. Error threshold will be set at 0.1. The model with least mean absolute error and greatest correlation across all trials in untrained muscle will be judged as best-fitting. The comparative results from the Ding and unconstrained optimized Conaway fatigue models in the untrained limb are shown below. The parameters in the Ding model (56) are set to {A_{rest}=11.0, R_{0rest}=0.45, τ_{crest}=20, τ_1=28.3, τ_2=62.7, k_m=0.06, α_A=-0.004, α_{R0}=0.002, $\alpha_{\tau c}$=0.003}.

Table 7-9. Parameter values for Conaway fatigue model validation in trained limb in Subject 18.

Parameter	Initial value	Optimized value	Free or fixed	Range
τ_2	20	69.1274	Free	[0,1000]
τ_c	62.7	20	Free	[0,50]
a	1	1	Free	[0,10]
B	2	2	Free	[0,10]
C	1	1	Free	[0,10]
τ_{1rest}	28.3	115.928	Free	[0,1000]
τ_{fat}	47.9	41.3017	Free	[0,50]
$\alpha_{\tau 1}$	0.003	2.6607	Free	[0 50]
μ_1	0.38	0.01	Free	[0,50]
μ_2	0.5	0.03	Free	[0,50]
τ_{leak}	20	75.0349	Free	[0, 100]
A	0.085	0.0347338	Free	[0 ∞]

Ding Model

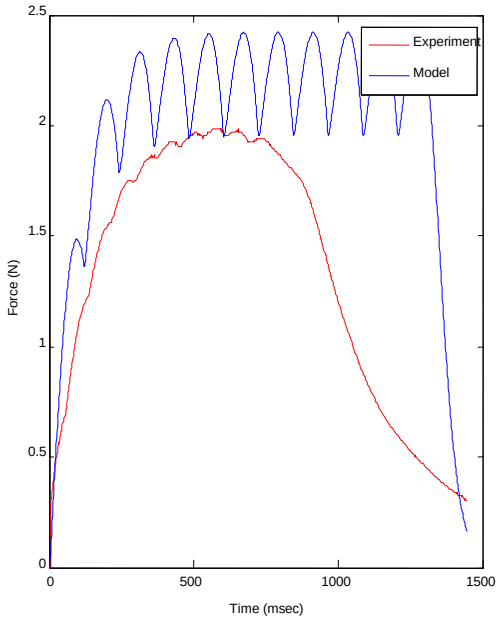

Conaway Model

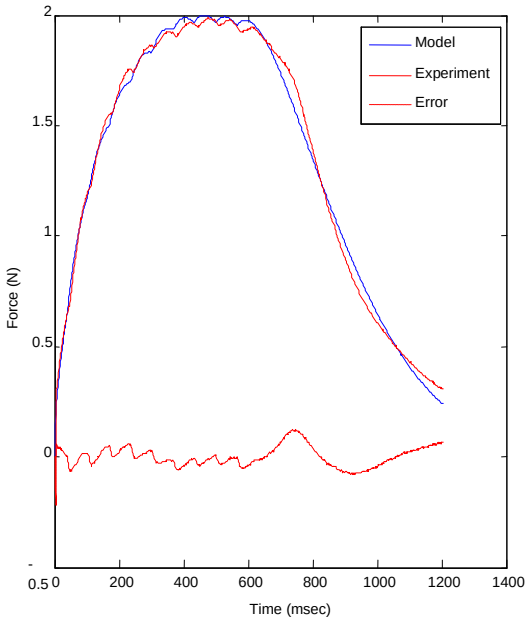

Figure 7-8. Comparison between Ding and unconstrained Conaway fatigue models in Subject 18 untrained limb.

Table 7-10. Comparison of error statistics between Ding and unconstrained Conaway fatigue models in trained and untrained limbs in Subject 18.

Fatigue model/ Training state	Mean Squared Error	Mean Absolute Error	Correlation Coefficient	95% CI	r^2	p-value
Ding Trained	0.74072	0.407835	0.686276	(0.653777 0.716248)	0.470975	<0.001
Conaway Trained	0.160551	0.018093	0.980598	(0.978194 0.98274)	0.96153	<0.001
Ding Untrained	0.761985	0.438124	0.37476	(0.325149 0.422314)	0.140445	<0.001
Conaway Untrained	0.045919	0.000529374	0.997035	(0.996681 0.997352)	0.99408	<0.001

Table 7-11. Single factor analysis of variance for mean squared error between Ding and Conaway fatigue models. The difference in model predictive ability is highly significant.

Source of Variation	*SS*	*Df*	*MS*	*F*	*P-value*	*F crit*
Model	0.419995	1	0.419995	123.6309	0.007992	18.51282
Training	0.006794	2	0.003397			
Total	0.426789	3				

A single factor analysis of variance was performed to test for differences between model mean squared errors at a significance of 0.05. With the p-value at 0.007992, it is shown that there is a highly significant difference between the predictive abilities between the Ding and unconstrained Conaway fatigue models. Remarkably, the training status contributed little to the error variance. The difference of the error generated by the models was the primary source of mean squared error variance. Hence, the hypothesis is not rejected.

7.4 The role of τ_2 in the Conaway force model

Using constrained optimization parameter values and trained muscle data from Subject 18, differences in predictive errors have been compared between different optimizations of the Conaway force model for stimulation inputs of 10 CT, doublet ramp, as well as 20 DDT and parameter sets involving combinations of k_m, τ_1, and τ_2 The test statistic is the Akaike final prediction error.. The parameter set that generates the least prediction error and returns parameters within ranges reported elsewhere will be judged as optimal.

7.4.1 10 CT

Table 7-12. Optimized parameter values for Conaway force model using $\{k_m, \tau_1, \tau_2\}$ with 10 CT input

Parameter	Initial value	Optimized value	Standard deviation	Free or fixed	Range
τ_c	20	20	0	Fixed	[-∞,∞]
A	0.085	0.037987	0.00011458	Free	[-∞,50]
k_m	0.06	0.00349555	0.94091e-005	Free	[0.0005, 0.2]
τ_1	28.3	37.8078	0.468708	Free	[10,100]
τ_2	62.7	184.905	1.82687	Free	[0,1000]
λ_1	0.38	0.38	0	Fixed	[-∞,∞]
λ_2	0.5	0.5	0	Fixed	[-∞,∞]

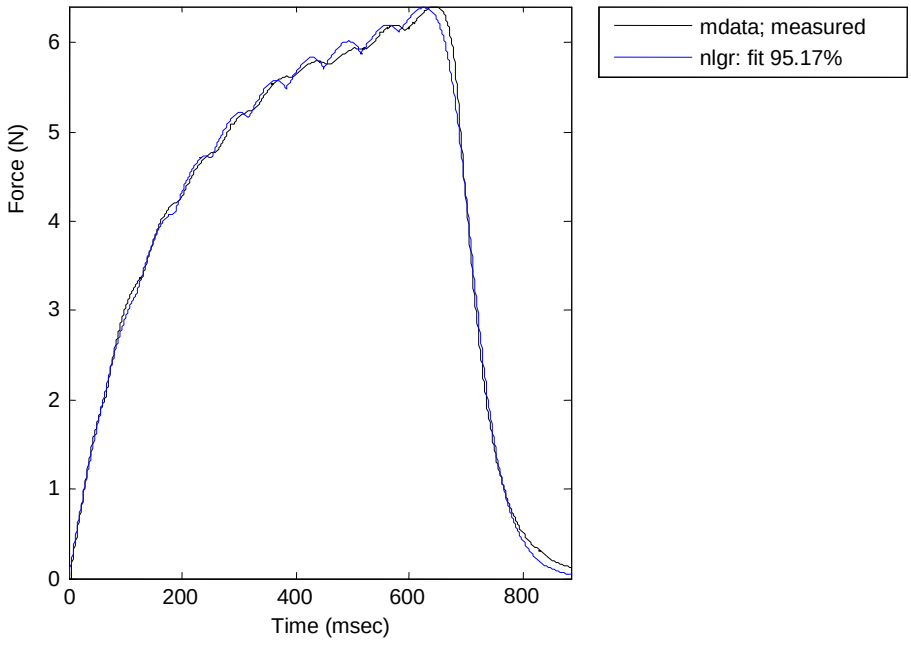

Figure 7-9. 10 CT optimized on $\{k_m, \tau_1, \tau_2\}$. The fit of the optimized model is 95.17%. However, the value for τ_2 is out of the range reported in the literature.

Table 7-13. Optimized parameter values for Conaway force model using $\{k_m, \tau_1\}$ with 10 CT input.

Parameter	Initial value	Optimized value	Standard deviation	Free or fixed	Range
τ_c	20	20	0	Fixed	[-∞,∞]
A	0.085	0.0528972	0.000431944	Free	[-∞,50]
k_m	0.06	0.00190744	0.000240562	Free	[0.0005, 0.2]
τ_1	28.3	60.4474	2.25155	Free	[10,100]
τ_2	62.7	62.7	0	Fixed	[-∞,∞]
λ_1	0.38	0.38	0	Fixed	[-∞,∞]
λ_2	0.5	0.5	0	Fixed	[-∞,∞]

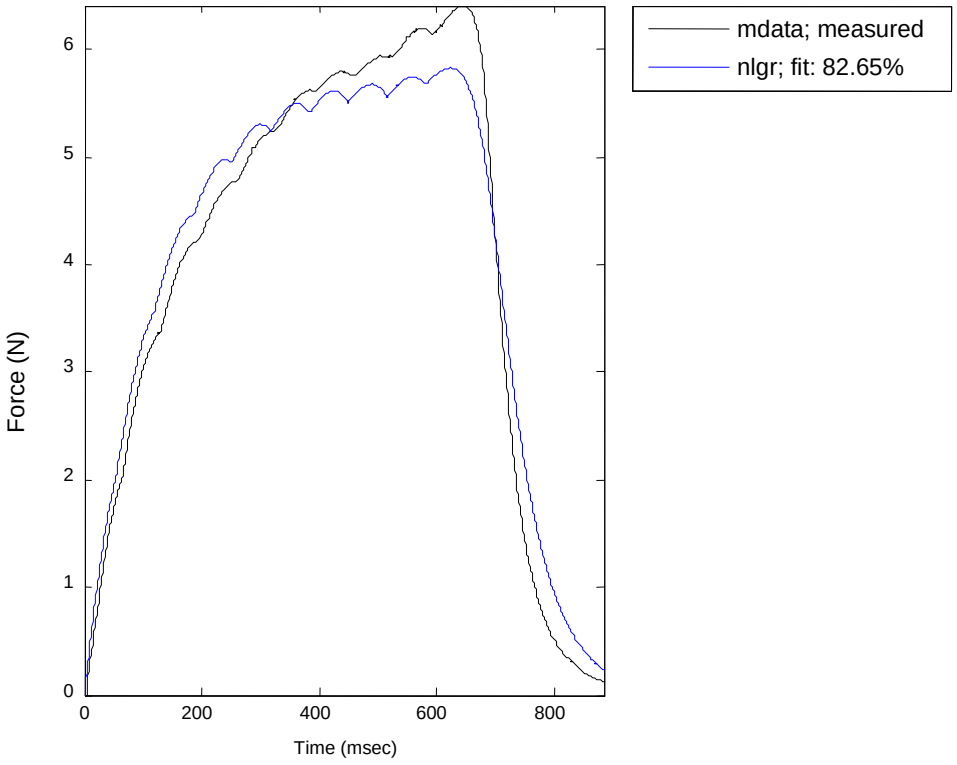

Figure 7-10. 10 CT optimized on $\{k_m, \tau_1\}$.The fit of the optimized model is 82.65%. However, the free parameter values are consistent with the literature

Table 7-14. Optimized parameter values for Conaway force model using $\{k_m\}$ with 10 CT input

Parameter	Initial value	Optimized value	Standard deviation	Free or fixed	Range
τ_c	20	20	0	Fixed	[-∞,∞]
A	0.085	0.0618124	0.000292747	Free	[-∞,50]
k_m	0.06	0.00117368	4.96623e-005	Free	[0.0005,0.2]
τ_1	28.3	28.3	0	Fixed	[-∞,∞]
τ_2	62.7	62.7	0	Fixed	[-∞,∞]
λ_1	0.38	0.38	0	Fixed	[-∞,∞]
λ_2	0.5	0.5	0	Fixed	[-∞,∞]

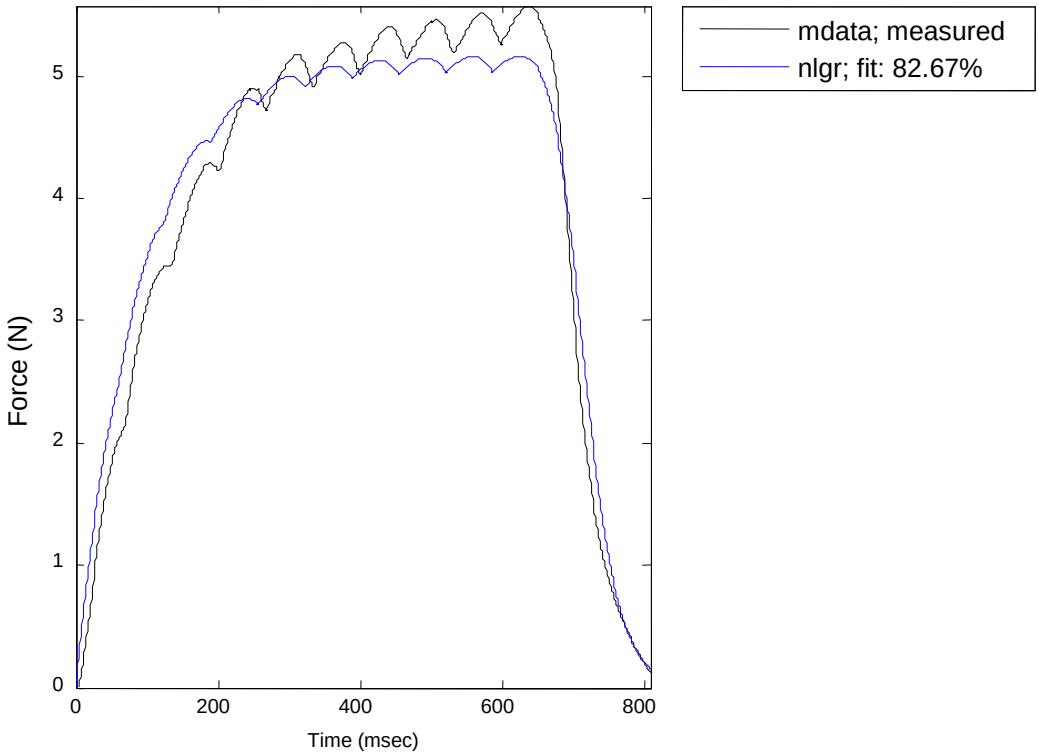

Figure 7-11. 10 CT optimized on $\{k_m\}$. The fit is 82.67%. However, the parameter values do not make sense physiologically. The parameter k_m decreases dramatically in this optimization.

Table 7-15. Loss functions and Akaike FPEs for the three optimized Conaway force models for 10 CT input. Note that $\{k_m, \tau_1, \tau_2\}$ generates the least prediction error. However, $\{k_m, \tau_1\}$ gives the most realistic values.

Optimizing parameter set	$\{k_m, \tau_1, \tau_2\}$	$\{k_m, \tau_1\}$	$\{k_m\}$
Loss Function	0.0103751	0.168472	0.117346
Akaike final prediction error	0.0104688	0.169613	0.117926

7.4.2 Doublet ramp

Table 7-16. Optimized parameter values for Conaway force model using $\{k_m, \tau_1, \tau_2\}$ with doublet ramp input

Parameter	Initial value	Optimized value	Standard deviation	Free or fixed	Range
τ_c	20	0		Fixed	[-∞,∞]
A	0.085	0.326646	0.000280742	Free	[-∞,50]
k_m	0.06	0.000509338	1.53478e-005	Free	[0.0005,0.2]
τ_1	28.3	25.9221	1.00108	Free	[10,100]
τ_2	62.7	198.15	2.83668	Free	[20,1000]
λ_1	0.38	0.38	0	Fixed	[-∞,∞]
λ_2	0.5	0.5	0	Fixed	[-∞,∞]

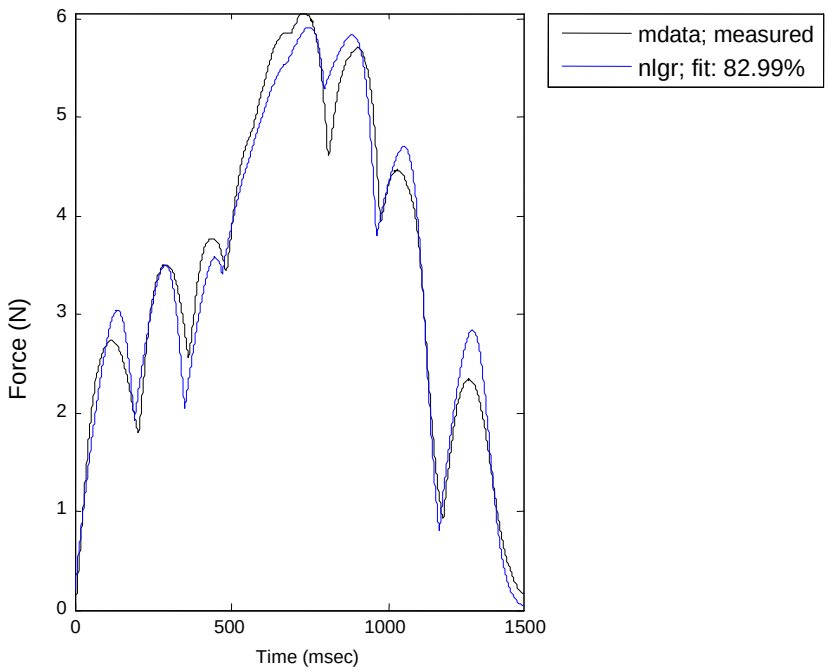

Figure 7-12. Doublet ramp optimized on $\{k_m, \tau_1, \tau_2\}$. The fit of the model is 82.99%. However, the optimized values for k_m and τ_2 are well outside of reported ranges.

Table 7-17. Optimized parameter values for Conaway force model using $\{k_m, \tau_1\}$ with doublet ramp input

Parameter	Initial value	Optimized value	Standard deviation	Free or fixed	Range
τ_c	20	20	0	Fixed	[-∞, ∞]
A	0.085	0.047387	0.000568711	Free	[-∞,50]
k_m	0.06	0.000144649	0.000123907	Free	[0.0005,0.2]
τ_1	28.3	84.3839	2.76143	Free	[10,100]
τ_2	62.7	62.7	0	Fixed	[-∞, ∞]
λ_1	0.38	0.38	0	Fixed	[-∞, ∞]
λ_2	0.5	0.5	0	Fixed	[-∞, ∞]

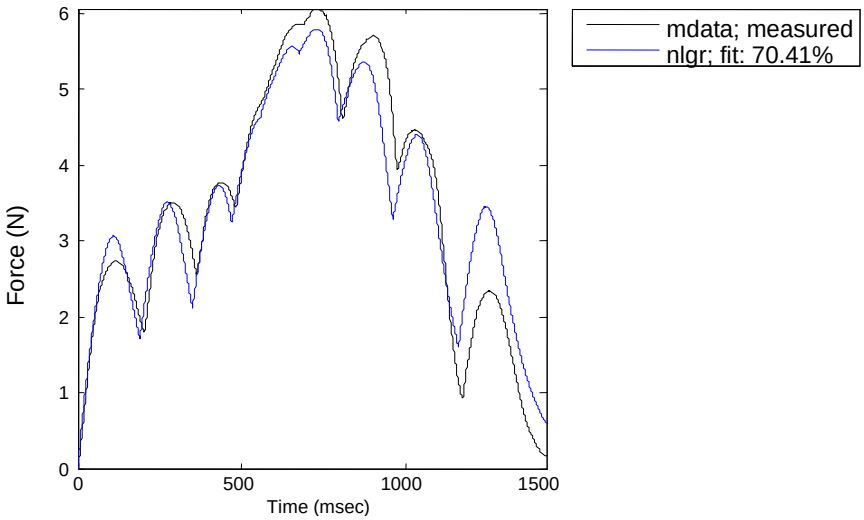

Figure 7-13. Doublet ramp optimized on $\{k_m, \tau_1\}$. The model fit is 70.41%. However, the optimized parameter values are within ranges reported in the literature.

7.4.3 20 DDT

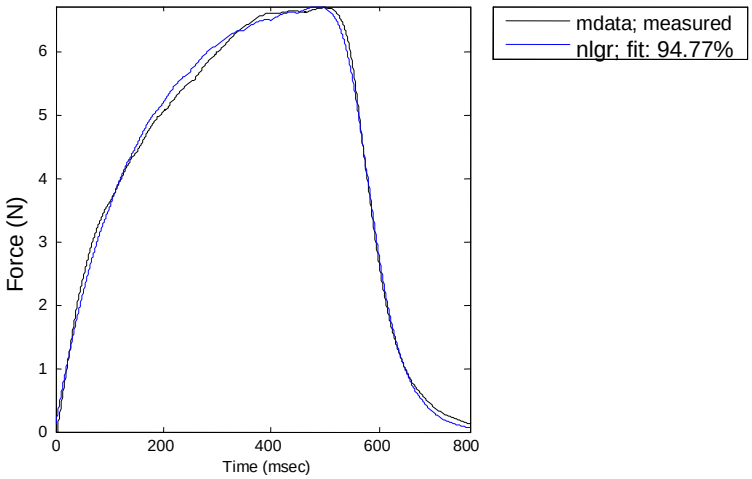

Figure 7-14. 20 DDT optimized on $\{k_m, \tau_1, \tau_2\}$. The model fit is 94.77%. In addition, the optimized free parameter values are within reported ranges.

Table 7-18. Optimized parameter values for Conaway force model using $\{k_m, \tau_1\}$ with 20 DDT input

Parameter	Initial Value	Optimized value	Standard deviation	Free or fixed	Range
τ_c	20	20	0	Fixed	[-∞,∞]
A	0.085	0.11319	0.00502644	Free	[-∞,50]
k_m	0.06	0.0891981	0.00972664	Free	[0.0005,0.2]
τ_1	28.3	100	3.33277	Free	[10,100]
τ_2	62.7	62.7	0	Fixed	[-∞,∞]
λ_1	0.38	0.38	0	Fixed	[-∞,∞]
λ_2	0.5	0.5	0	Fixed	[-∞,∞]

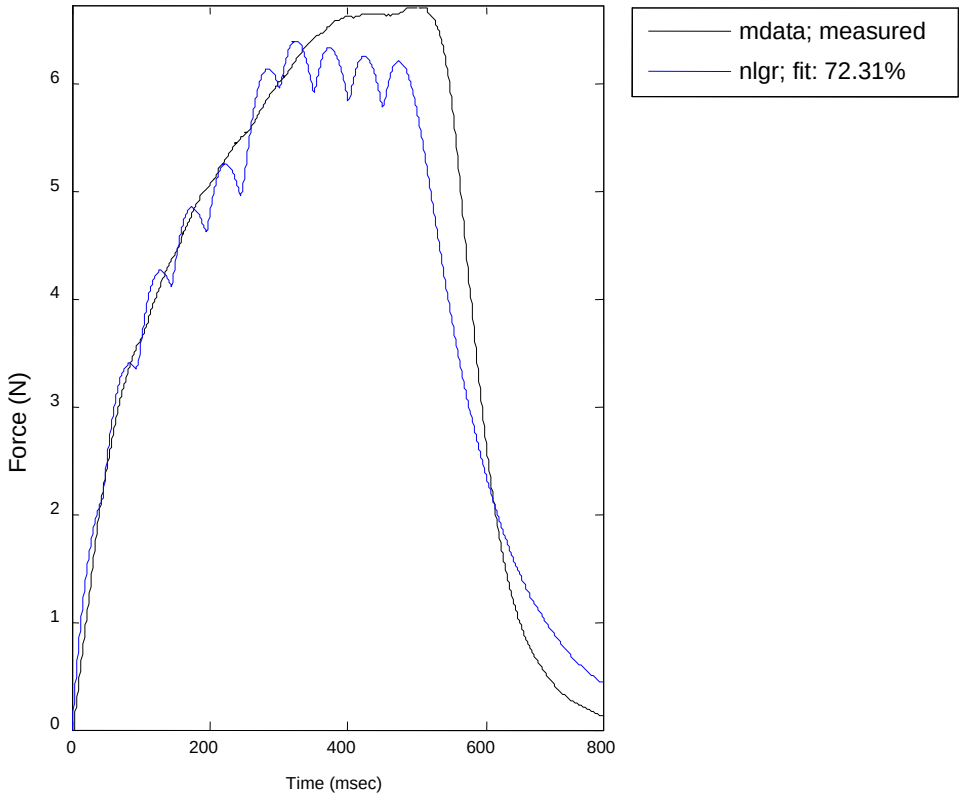

Figure 7-15. 20 DDT optimized on $\{k_m, \tau_1\}$.The model fit decreases to 72.31%. In addition, the value for τ_1 does not fall within previously reported ranges.

Table 7-19. Loss functions and Akaike FPEs for the two optimized Conaway force models for 20 DDT input. It is shown that for the 20 DDT input, the set $\{k_m, \tau_1, \tau_2\}$ generates the least prediction error while returning realistic physiologic values.

Optimizing parameter set	$\{k_m, \tau_1, \tau_2\}$	$\{k_m, \tau_1\}$
Loss Function	0.01628	0.637144
Akaike final prediction error	0.0164491	0.6421091

7.4.4. Parametric behavior in modeled trained and untrained muscle

Below is a graphical analysis of the behavior of optimized parameter values of the set $\{k_m, \tau_1, \tau_2\}$ as functions of input frequency and contraction index for Subject 18. This shows how the parameters change in the Conaway model of fresh paralyzed trained and untrained human soleus during a bout of stimulation. Interpretations of the parametric variations will yield insights into and suggest new hypotheses about the physiology of chronically paralyzed human muscle. These insights will lead to future *in vitro* experiments to confirm such hypotheses.

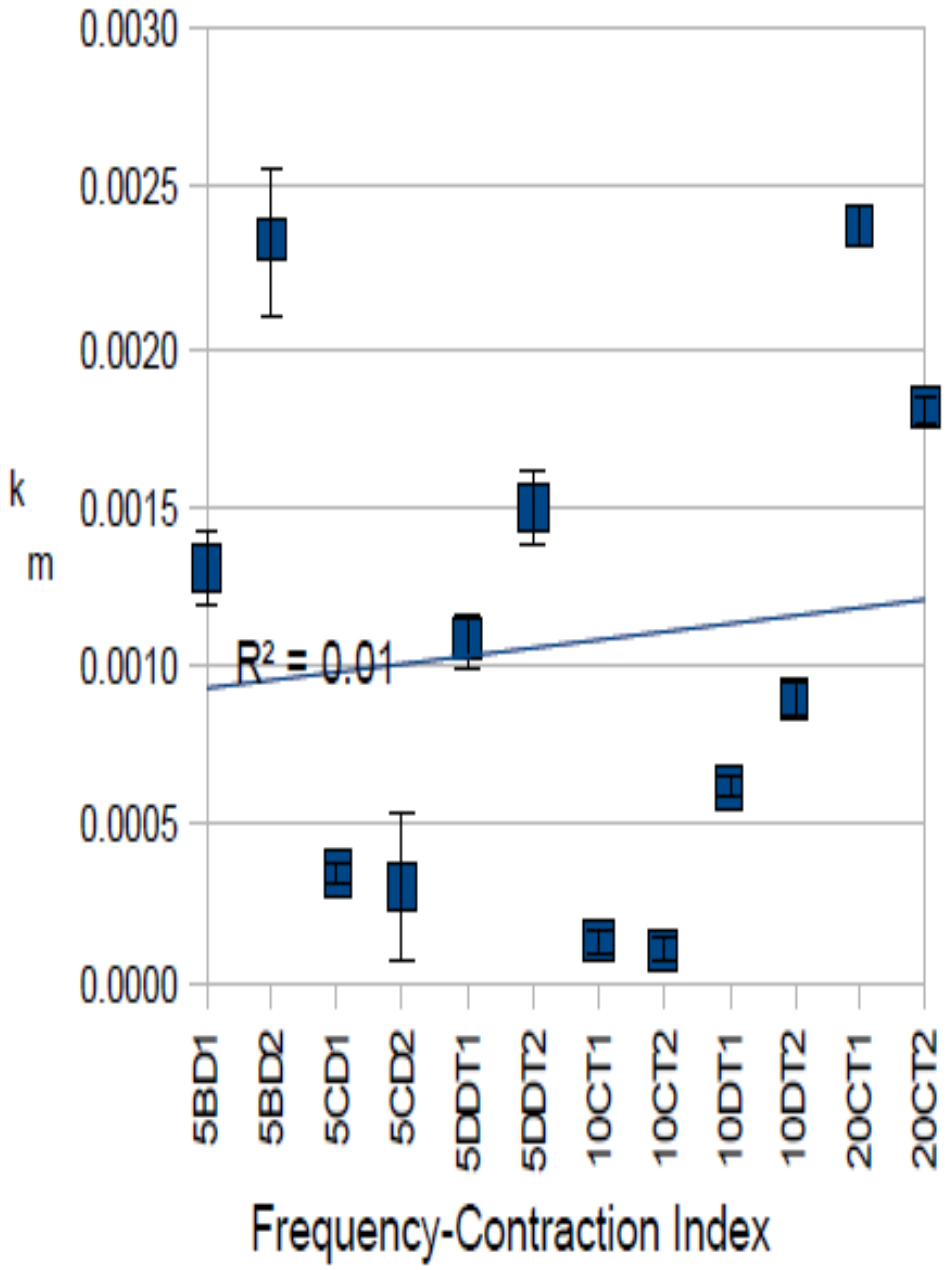

5 BD=5 pps with beginning doublet
5 CD=5 pps with center doublet
5 DDT=5 pps with dual doublet
10 CT=10 pps continuous train
10 DT=10 pps with beginning doublet
20 CT=20 pps continuous train

Figure 7-16. Behavior of k_m as a function of frequency and contraction in trained muscle.

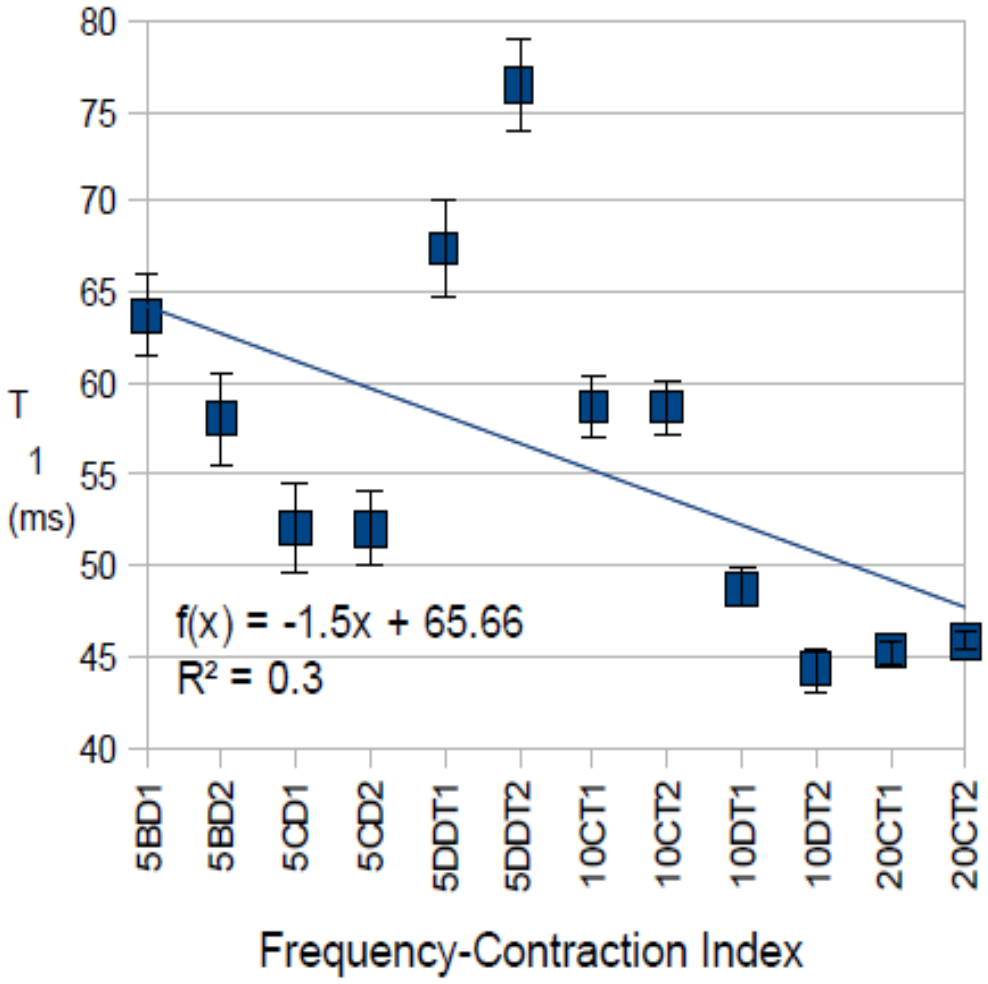

5 BD=5 pps with beginning doublet
5 CD=5 pps with center doublet
5 DDT=5 pps with dual doublet
10 CT=10 pps continuous train
10 DT=10 pps with beginning doublet
20 CT=20 pps continuous train

Figure 7-17. Behavior of τ_1 as a function of frequency and contraction in trained muscle.

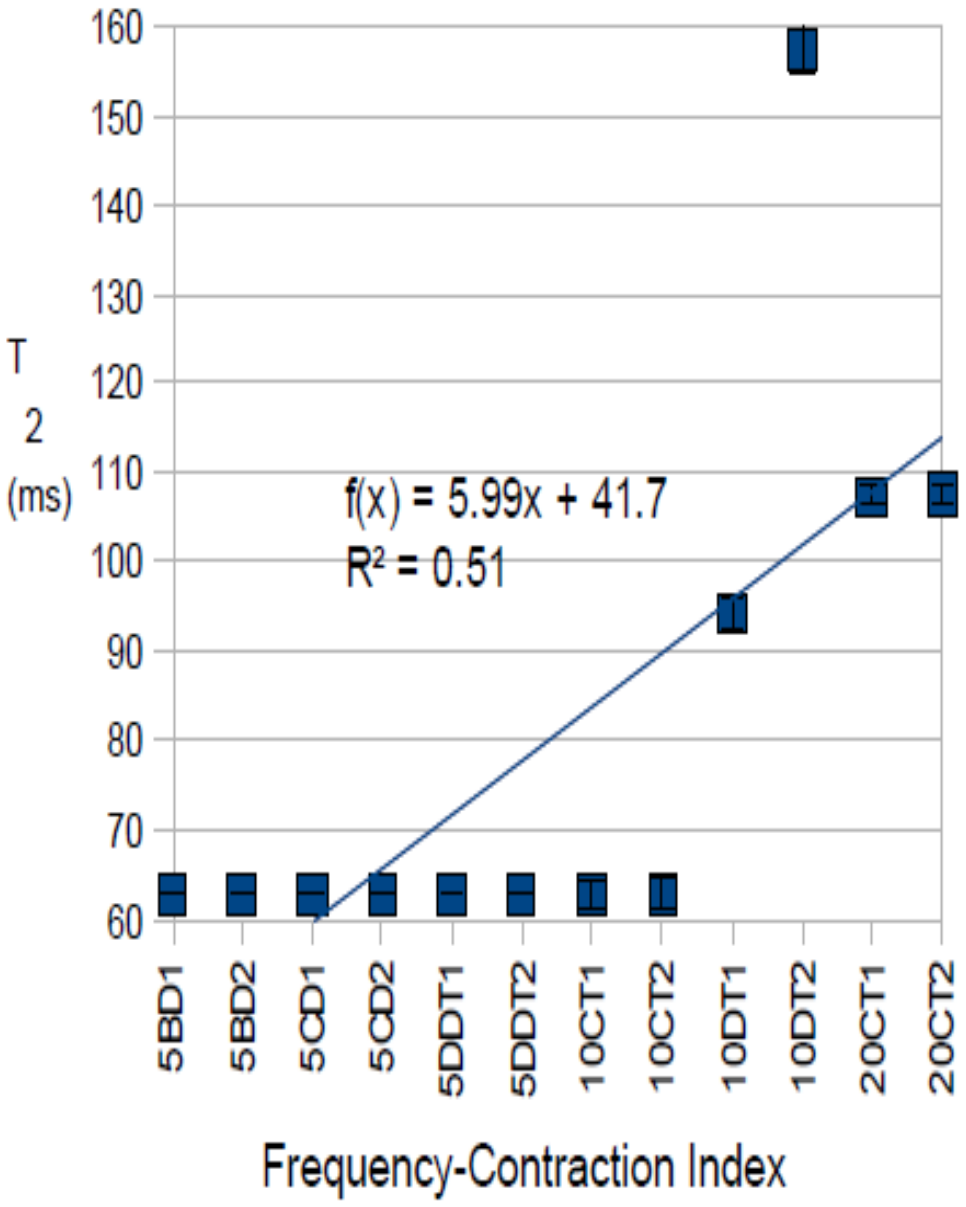

5 BD=5 pps with beginning doublet
5 CD=5 pps with center doublet
5 DDT=5 pps with dual doublet
10 CT=10 pps continuous train
10 DT=10 pps with beginning doublet
20 CT=20 pps continuous train

Figure 7-18. Behavior of τ_2 as a function of frequency and contraction in trained muscle.

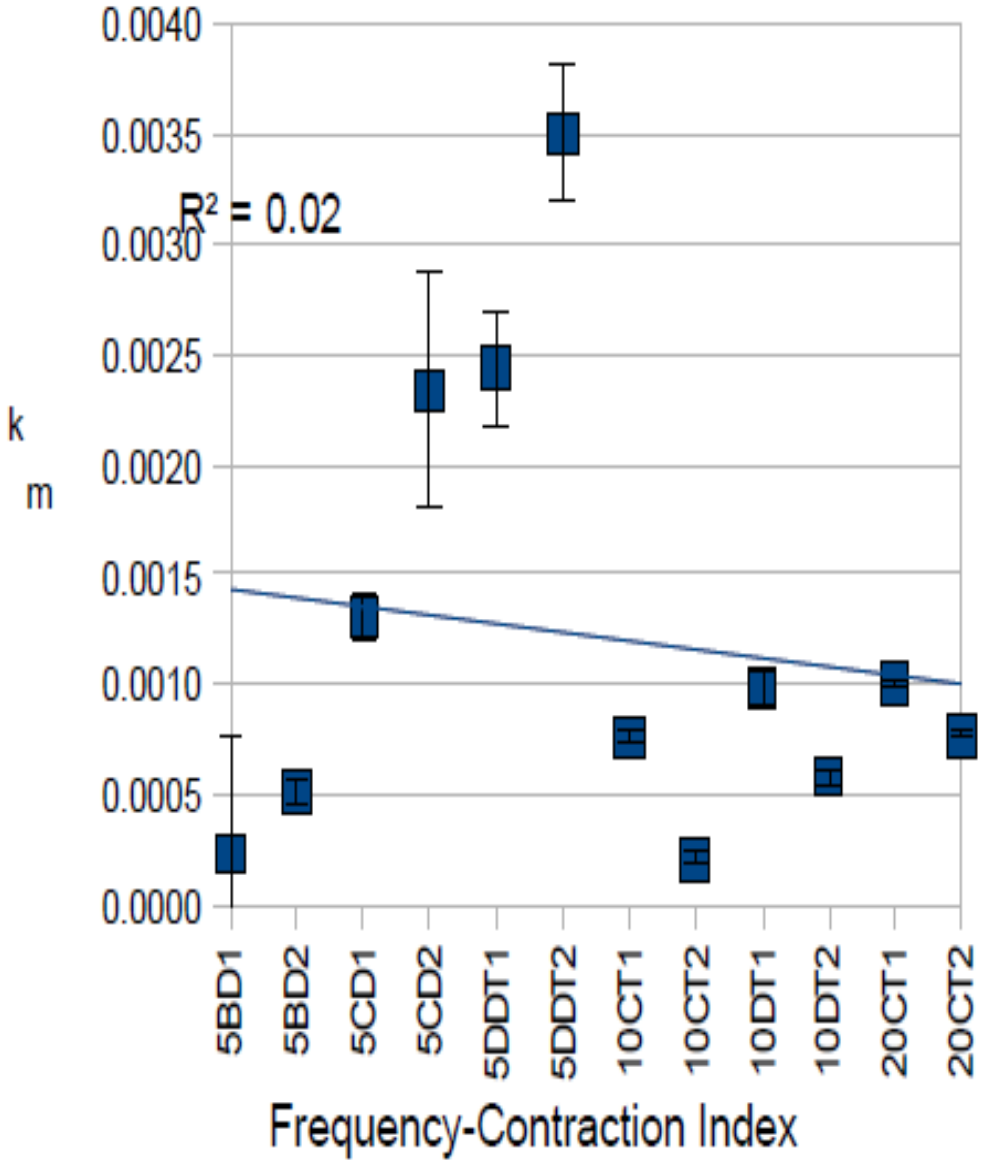

5 BD=5 pps with beginning doublet
5 CD=5 pps with center doublet
5 DDT=5 pps with dual doublet
10 CT=10 pps continuous train
10 DT=10 pps with beginning doublet
20 CT=20 pps continuous train

Figure 7-19. Behavior of k_m as a function of frequency and contraction in untrained muscle.

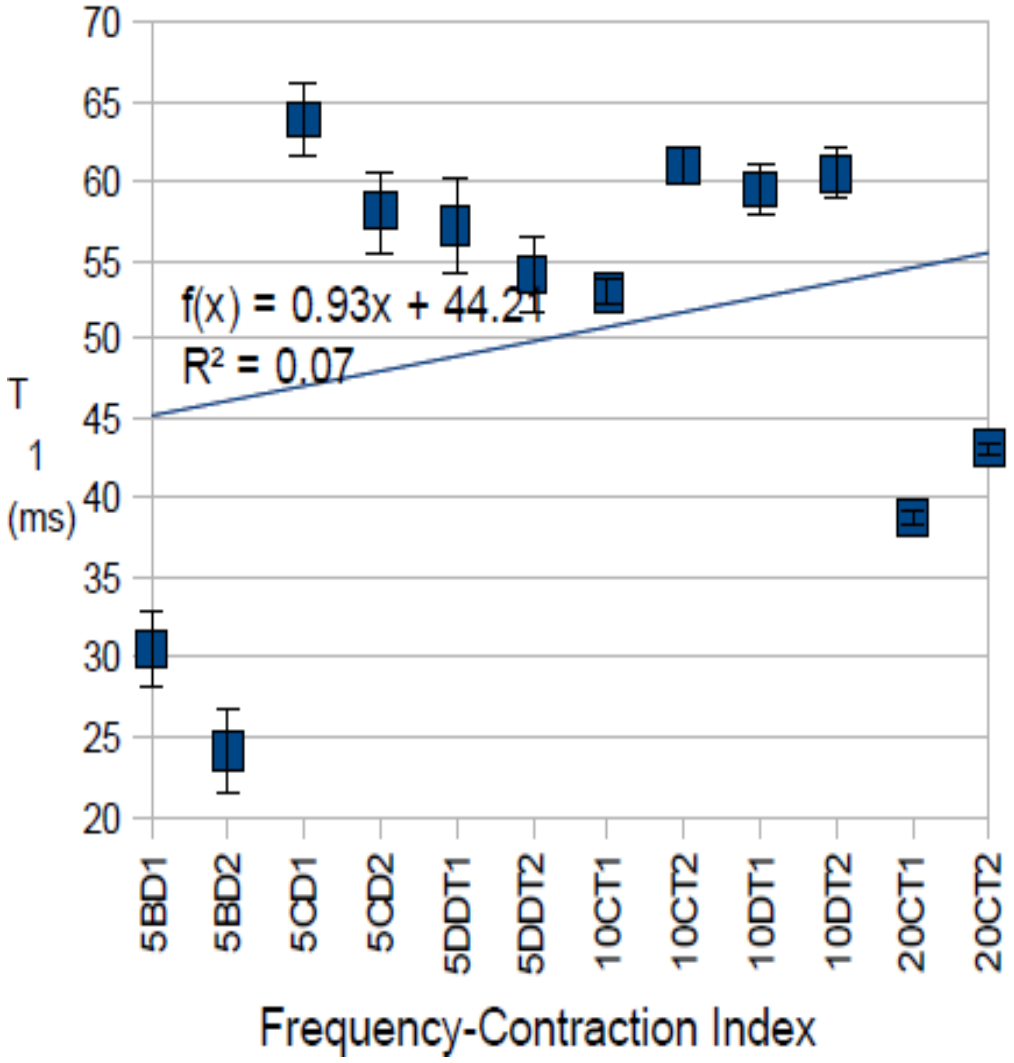

5 BD=5 pps with beginning doublet
5 CD=5 pps with center doublet
5 DDT=5 pps with dual doublet
10 CT=10 pps continuous train
10 DT=10 pps with beginning doublet
20 CT=20 pps continuous train

Figure 7-20. Behavior of τ_1 as a function of frequency and contraction in untrained muscle.

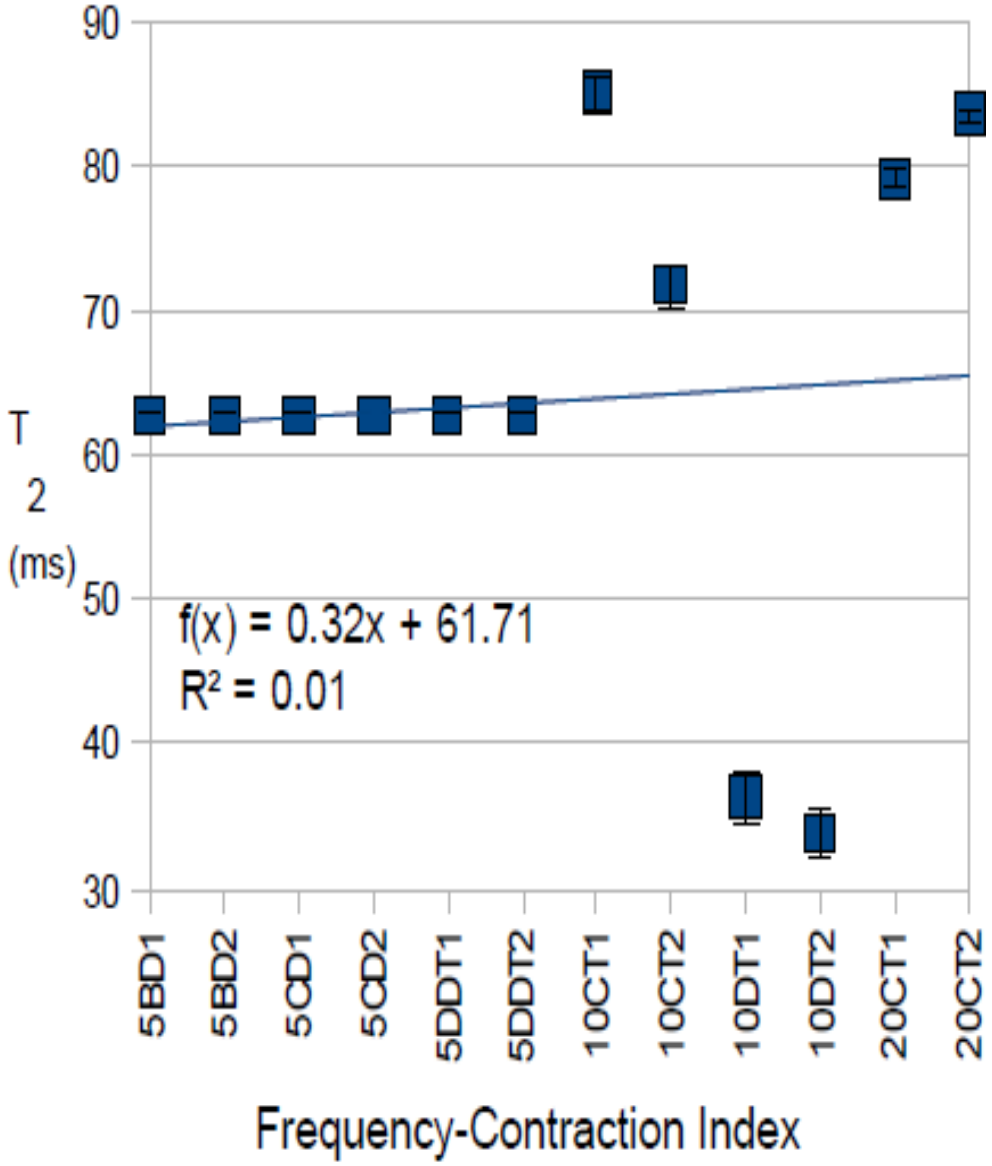

5 BD=5 pps with beginning doublet
5 CD=5 pps with center doublet
5 DDT=5 pps with dual doublet
10 CT=10 pps continuous train
10 DT=10 pps with beginning doublet
20 CT=20 pps continuous train

Figure 7-21. Behavior of τ_2 as a function of frequency and contraction in untrained muscle.

Table 7-20. Free parameters in Conaway force model found using Subject 18 trained fresh muscle. Note how they vary with the frequency-contraction index. There are no discernable trends for k_m and τ_1.

Frequency-contraction	k_m	$k_m \sigma$	τ_1	$\tau_1 \sigma$	τ_2	$\tau_2 \sigma$
TW1	0.056356	0.0030345	92.6698	0.527527	62.7	0
TW2	0.025194	0.000755089	89.9141	0.70367	62.7	0
TW3	0.039287	0.000891217	93.8319	0.539341	62.7	0
5BD1	0.000238	0.00052842	30.4305	2.27201	62.7	0
5BD2	0.00052	7.42019E-05	24.0571	2.70777	62.7	0
5CD1	0.001307	0.000110394	63.7291	2.27936	62.7	0
5CD2	0.002333	0.00054015	58.0519	2.5451	62.7	0
5DDT1	0.002442	0.000262759	7.0926	2.91389	62.7	0
5DDT2	0.003508	0.000315385	54.0877	2.34614	62.7	0
10CT1	0.000759	2.90621E-05	53.0067	0.799308	84.9806	1.19596
10CT2	0.000207	2.71403E-05	60.9035	1.14939	71.6926	1.40497
10DT1	0.000981	7.51937E-05	59.387	1.64141	37.2828	1.85178
10DT2	0.00058	4.21264E-05	60.422	1.55763	33.8664	1.67538
20CT1	0.001003	1.71797E-05	38.7531	0.403607	79.108	0.536626
20CT2	0.000772	1.06972E-05	43.15123	0.323722	83.544	0.452029

TW=Twitch
5BD =5 pps with beginning doublet
5CD=5 pps with center doublet
5DDT=5 pps with dual doublet
10CT=10 pps continuous train
10DT=10 pps with beginning doublet
20CT=20 pps continuous train

Table 7-21. Free parameters in Conaway force model found using Subject 18 untrained fresh muscle. Note how they vary with the frequency-contraction index. There are no discernable trends for k_m and τ_1.

Frequency-contraction	k_m	$k_m \sigma$	τ_1	$\tau_1 \sigma$	τ_2	$\tau_2 \sigma$
TW1	0.000648	2.46696E-05	100.573	0.902726	62.7	0
TW2	0.007656	2.76542E-05	100.814	0.865475	62.7	0
TW3	0.007421	0.000220802	87.6133	0.705944	62.7	0
5BD1	0.001307	0.000110394	63.7291	2.27936	62.7	0
5BD2	0.002333	0.000234269	58.0519	2.5451	62.7	0
5CD1	0.00034	3.27406E-05	52.0672	2.4078	62.7	0
5CD2	0.000301	0.00023277	51.9914	2.03897	62.7	0
5DDT1	0.001079	0.00008793	67.472	2.5692	62.7	0
5DDT2	0.001496	0.00011603	77.4633	2.47875	62.7	0
10CT1	0.000128	3.32747E-05	58.7336	1.63862	62.7	1.62628
10CT2	0.000104	3.42764E-05	58.7336	1.450544	62.7	1.71819
10DT1	0.000615	0.000030896	48.6946	1.05463	94.0249	1.60997
10DT2	0.00089	5.15635E-05	44.259	1.19176	157.46	2.59865
20CT1	0.002377	7.53411E-05	45.2349	0.577079	107.261	1.008143
20CT2	0.001809	4.39106E-05	45.7827	0.507517	107.52	0.952346

TW=Twitch
5 BD=5 pps with beginning doublet
5 CD=5 pps with center doublet
5 DDT=5 pps with dual doublet
10 CT=10 pps continuous train
10 DT=10 pps with beginning doublet
20 CT=20 pps continuous train

7.4.5 Analyses of variance for k_m, τ_1, and τ_2

Determining a dominant parameter is done via two-way analysis of variance with replication for each of the three free parameters in the Conaway force model.

Table 7-22. Two-way analysis of variance with replication for k_m. No factor is statistically significant.

Source of Variation	*SS*	*Df*	*MS*	*F*	*P-value*	*F crit*
Input frequency	2.03E-06	1	2.03E-06	2.612643	0.12168	4.351243
Training status	1.46E-07	1	1.46E-07	0.187386	0.669734	4.351243
Frequency*Training	1.09E-06	1	1.09E-06	1.40183	0.250299	4.351243
Within	1.55E-05	20	7.77E-07			
Total	1.88E-05	23				

Table 7-23. Two-way analysis of variance with replication for τ_1. No factor is statistically significant.

Source of Variation	*SS*	*df*	*MS*	*F*	*P-value*	*F crit*
Input frequency	67.20733	1	67.20733	0.539702	0.471083	4.351243
Training status	193.4658	1	193.4658	1.55361	0.227005	4.351243
Frequency*Training	388.0999	1	388.0999	3.116602	0.092763	4.351243
Within	2490.532	20	124.5266			
Total	3139.305	23				

Table 7-24. Two-way analysis of variance with replication for τ_2. Neither the training status nor the interaction between frequency and training status has statistical significance. However, the factor of input frequency is significant statistically.

Source of Variation	*SS*	*df*	*MS*	*F*	*P-value*	*F crit*
Input frequency	2180.089	1	2180.089	4.845452	0.039628	4.351243
Training status	1703.392	1	1703.392	3.785949	0.065875	4.351243
Frequency*Training	1703.392	1	1703.392	3.785949	0.065875	4.351243
Within	8998.493	20	449.9247			
Total	14585.37	23				

It is thus shown that τ_2 is the dominant free parameter in the Conaway force model at frequencies higher than 5 pulses per second.

7.5 The role of τ_{leak} in the Conaway fatigue model

The Conaway fatigue model has been investigated further to understand the physiology of the muscle fatigue process. Fatigue data from Subjects 17 and 18 were used in the analysis to test hypotheses. Below are graphical plots of optimized parameter values for trained and untrained muscle in fatigue as they vary with contraction index. The goal is to investigate how each parameter behaves in both training states as a function of index of contraction in a bout of stimulation.

7.5.1 Parametric plots for modeled trained muscle

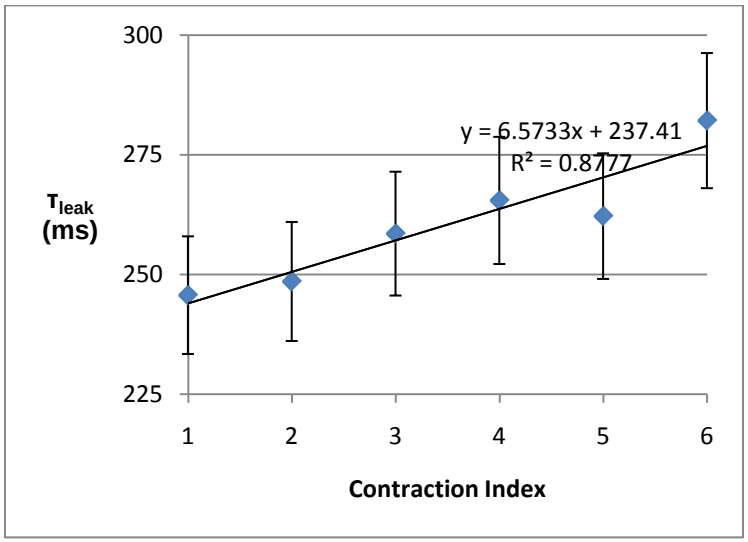

Figure 7-22. Behavior of τ_{leak} as a function of contraction index in trained muscle in Subject 17.

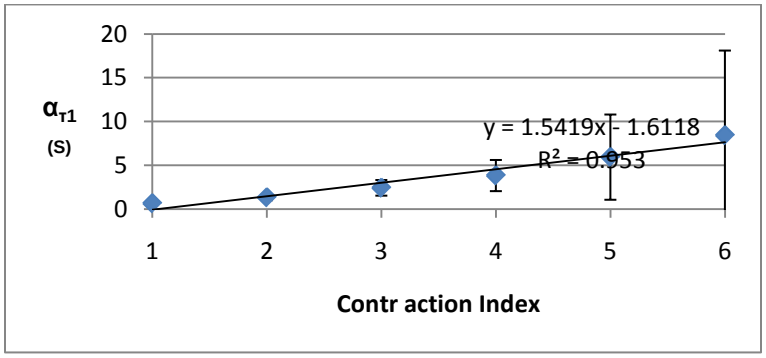

Figure 7-23. Behavior of $\alpha_{\tau 1}$ as a function of contraction index in trained muscle in Subject 17.

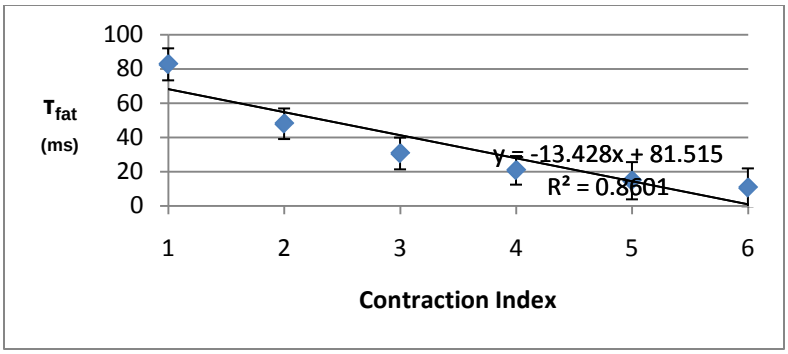

Figure 7-24. Behavior of τ_{fat} as a function of contraction index in trained muscle in Subject 17.

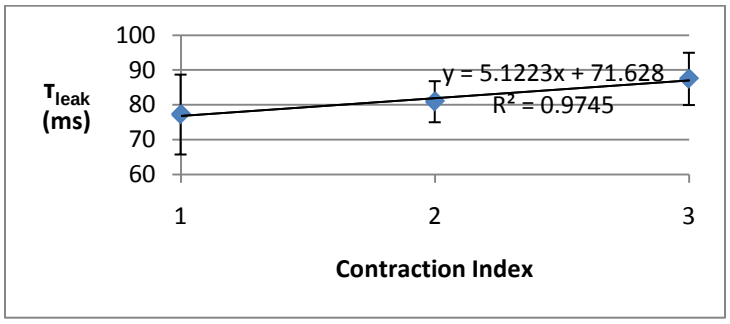

Figure 7-25. Behavior of τ_{leak} as a function of contraction index in trained muscle in Subject 18.

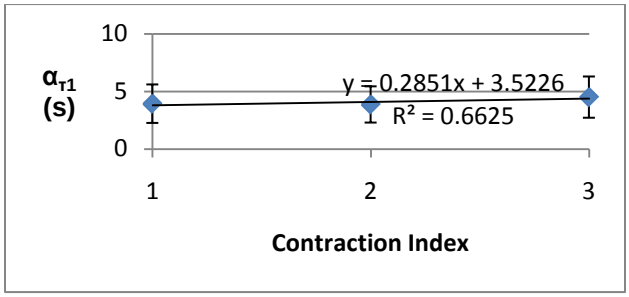

Figure 7-26. Behavior of $\alpha_{\tau 1}$ as a function of contraction index in trained muscle in Subject 18.

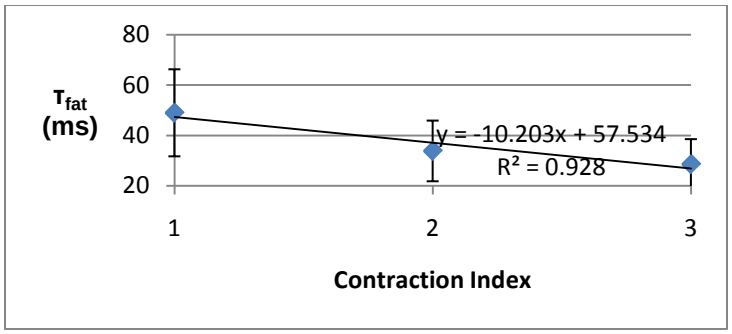

Figure 7-27. Behavior of τ_{fat} as a function of contraction index in trained muscle in Subject 18.

7.5.2 Parametric plots for modeled untrained muscle

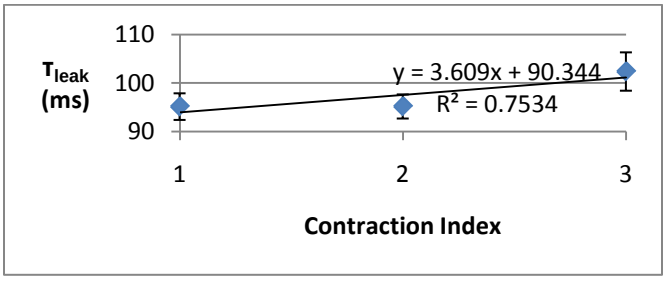

Figure 7-28. Behavior of τ_{leak} as a function of contraction index in untrained muscle in Subject 17.

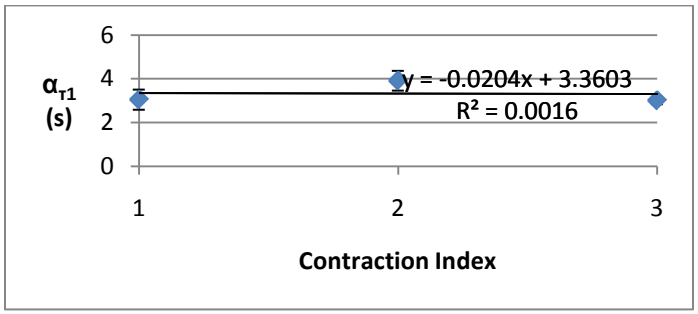

Figure 7-29. Behavior of $\alpha_{\tau 1}$ as a function of contraction index in untrained muscle in Subject 17.

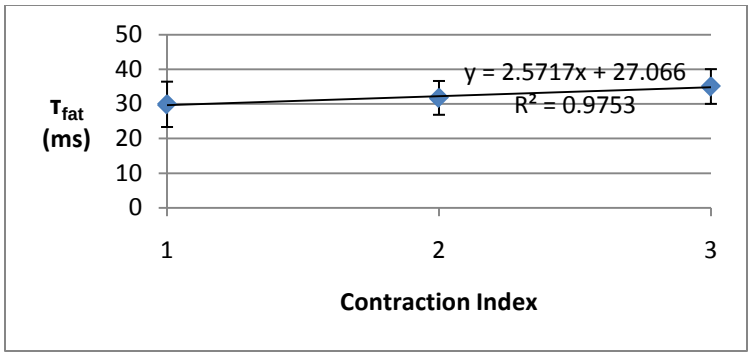

Figure 7-30. Behavior of τ_{fat} as a function of contraction index in untrained muscle in Subject 17.

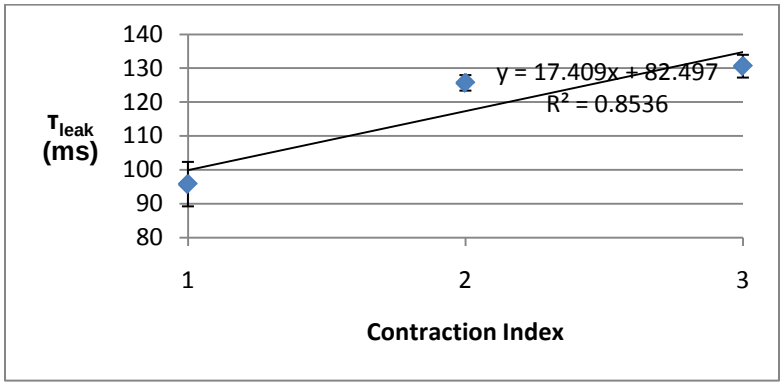

Figure 7-31. Behavior of τ_{leak} as a function of contraction index in untrained muscle in Subject 18.

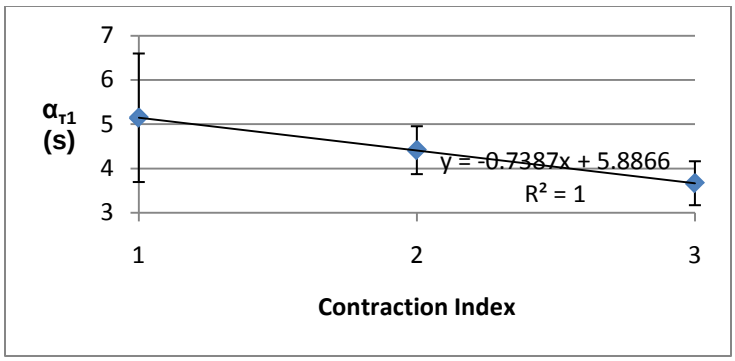

Figure 7-32. Behavior of $\alpha_{\tau 1}$ as a function of contraction index in untrained muscle in Subject 18.

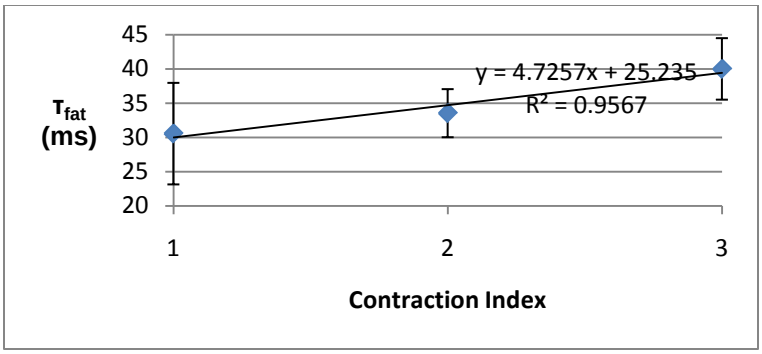

Figure 7-33. Behavior of τ_{fat} as a function of contraction index in untrained muscle in Subject 18.

It is noted that in the Conaway fatigue model, τ_{leak} increases with little change in variance as a function of contraction index. This is seen in both trained and untrained muscle. Contrarily, the variances of the other two free parameters fluctuate wildly as a function of contraction index.

Table 7-25. Free parameters in Conaway fatigue model found using Subject 17 trained fatigued muscle. Note how they vary with the contraction index. The standard deviations for $\alpha_{\tau 1}$ and τ_{fat} increase with each contraction. Hence, those parameters have little influence in fatigue. The parameter τ_{leak} is dominant.

Contraction	τ_{leak}	τ_{leak} σ	$\alpha_{\tau 1}$	$\alpha_{\tau 1}$ σ	τ_{fat}	τ_{fat} σ
1	245.676	4.73417	0.67884	0.102152	82.6344	9.34955
2	248.536	5.13729	1.35213	0.320982	47.9305	8.93
3	258.528	7.38156	2.44676	0.891975	30.5755	9.27007
4	265.454	7.22485	3.84758	1.77835	20.7245	8.35242
5	262.178	8.07727	5.94942	4.86385	14.661	10.8726
6	282.119	9.69667	8.43335	9.68127	10.5671	11.3016

Table 7-26. Free parameters in Conaway fatigue model found using Subject 18 untrained muscle. Note how they vary with the contraction index. The standard deviations for $\alpha_{\tau 1}$ and τ_{fat} increase with each contraction. Hence, those parameters have little influence in fatigue. Again, the parameter τ_{leak} is dominant.

Contraction	τ_{leak}	τ_{leak} σ	$\alpha_{\tau 1}$	$\alpha_{\tau 1}$ σ	τ_{fat}	τ_{fat} σ
1	95.7433	7.56264	5.14556	1.4505	30.5407	7.41266
2	125.641	2.29066	4.41374	0.5405	33.5256	3.51211
3	130.561	3.36306	3.66808	0.49578	39.9921	4.48909

7.5.3 Analyses of variance for τ_{leak}, $\alpha_{\tau 1}$, and τ_{fat}

Table 7-27. Two-way analysis of variance with replication for τ_{leak}. The analysis shows that the interaction term between contraction index and training has the greatest contribution to the variance in τ_{leak}. All factors are statistically significant.

Source of Variation	*SS*	*df*	*MS*	*F*	*P-value*	*F crit*
Contraction Index	16715.17	1	16715.17	150.3158	1.82E-06	5.317655
Training	10427.81	1	10427.81	93.76599	1.08E-05	5.317655
Index*Training	26732.22	1	26732.22	240.3969	2.98E-07	5.317655
Within	889.6027	8	111.2003			
Total	54763.81	11				

A two-way analysis of variance with replication was performed to determine if there are differences in τ_{leak}, $\alpha_{\tau 1}$, and τ_{fat} between the first three contractions of a fatiguing bout across trained and untrained limbs. The reason the particular contraction index difference was selected for analysis is due to the limited amount of data. There were six contractions in the trained muscle file and

only three contractions in the untrained file. Hence, a common factor had to be selected for any analysis to make sense.

Table 7-28. Two-way analysis of variance with replication for $\alpha_{\tau 1}$. The two main factors are statistically significant.

Source of Variation	*SS*	*df*	*MS*	*F*	*P-value*	*F crit*
Contraction Index	10.2121	1	10.2121	23.65861	0.001249	5.317655
Training	3.444628	1	3.444628	7.98025	0.022324	5.317655
Index*Training	1.711338	1	1.711338	3.964695	0.081627	5.317655
Within	3.453153	8	0.431644			
Total	18.82122	11				

Table 7-29. Two-way analysis of variance with replication for τ_{fat}. No factor is statistically significant. Hence, it has the least influence of the three free parameters in the Conaway fatigue model.

Source of Variation	*SS*	*df*	*MS*	*F*	*P-value*	*F crit*
Contraction Index	149.3073	1	149.3073	0.70685	0.424906	5.317655
Training	430.0303	1	430.0303	2.035846	0.191469	5.317655
Index*Training	272.5415	1	272.5415	1.290264	0.28888	5.317655
Within	1689.834	8	211.2292			
Total	2541.713	11				

From the above statistics, it is shown that τ_{leak} is the dominant free parameter in the Conaway fatigue model. Remarkably, for τ_{leak}, the contraction index and the interaction between the contraction index and training status had much lesser contributions to the variance. Moreover, since the interaction factor has its p-value less than that of the contraction index by an order of magnitude, the interaction is the most significant. For $\alpha_{\tau 1}$, however, the training status and

the interaction between the contraction index and training status had much lesser contributions. Furthermore, since the contraction index has its p-value less than that of the training status by an order of magnitude, the contraction index is the most significant. These results are totally unexpected!

CHAPTER 8: CONCLUSION

8.1 Evaluating the specific aims

8.1.1 Major findings

This study provides the first systematic evaluation of models that include calcium dynamics for predicting force and low-frequency fatigue in electrically stimulated, chronically paralyzed human muscle. There are three major findings of this study. First, it was found that, by including a Riccati-Bass diffusion function for R_0 and k_m in modeling force and fatigue respectively, the structure of the Conaway models predicts force and low-frequency fatigue with less mean squared error than do the Ding models. Second, the cross-bridge friction is the most influential factor in generating force in fresh muscle at frequencies greater than 5 pps. Finally, the calcium leak current is the most influential factor in low-frequency fatigue in paralyzed muscle. Hence, the specific aims of this study have been successfully answered.

The hypotheses that the structure of the Conaway model produces less prediction error, and greater curve fit, than the Ding model structure are not rejected. The findings show that the structure of the Conaway model is more robust in predicting force from different inputs in fresh muscle as well as predicting force in fatigued muscle. Furthermore, there are certainly noticeable differences between trained and untrained muscle as well. The Conaway force model has better predictive ability for frequencies greater than 5 pps. Similarly, the Conaway fatigue model has significantly better ability, with average curve fits

to the experimental data around 95%, than the Ding model does to predict fatigue. Remarkably, in fresh and fatigued muscle, the training status generally contributed little to the error variance. The difference of the error generated by the force and fatigue models was the primary source of mean squared error variance. The difference in model predictive ability is highly significant statistically.

8.1.2 Interpretations, discoveries, and insights

The Conaway force-fatigue model structure is the first to incorporate Riccati-Bass diffusion functions (10, 142) to describe underlying physiologic processes. With external and internal components, these processes are characterized by λ_1 and λ_2 in the Conaway force model and μ_1 and μ_2 in the Conaway fatigue model. The external influence comes from the extrinsic calcium applied to the muscle that causes calcium to move. Internal influence is a function of the relevant structures and ions in the sarcoplasmic reticulum, namely calcium channels and free calcium, which behave according to specific aggregate probabilities in different states.

However, the respective strengths of these two influences are unequal, with the second parameter always being greater than the first. In fresh muscle, the affinity for calcium and troponin to dissociate after the first pulse during a stimulated contraction was always greater than the affinity for calcium and troponin to bind after the first pulse during a stimulated contraction. Meanwhile, in fatigued muscle, the probability that calcium channels will inactivate was always greater than the probability that calcium channels will activate. It has been shown

that the quality of a functional state is a vital factor that underlies such differences. (113) In fact, an implicit assumption of many muscle force-fatigue models is the assumption that diffusion occurs homogeneously, or that the tendency towards binding or activation remains constant throughout a contraction. (108) The diffusion processes are functions of time-varying inputs, and hence, the models are exponentially modulated. However, the processes must also be considered with respect to the structural heterogeneity of a muscle membrane, either with or without pathology. Hence, the question of whether the assumed mathematical distribution of free divalent calcium or activated calcium channels properly modulates the modeled force must be posed. Figures 7-1 through 7-7 show that the assumed distribution is valid and that the Conaway model structure is robust.

It was hypothesized that the structure of the Conaway force-fatigue models yields a more robust model of muscle force generation, with respect to different inputs, than does the structure of the Ding force-fatigue models. Using the 95% confidence intervals of the means for mean squared error and correlation coefficients from each model, Table 7-5 shows that the Conaway model structure performs markedly better than the Ding model structure does at force prediction. Indeed, the confidence intervals do not overlap. Furthermore, Tables 7-6 and 7-7 show that single-factor analysis of variance for Ding and Conaway force models shows that the difference in model structure accounts for over 60% of the variation in the mean squared error in trained and untrained muscle. In addition, according to Table 7-8, single factor analysis of variance for

mean squared error between Ding and Conaway fatigue model shows that the difference in model structure accounts for over 98% of the variation in the mean squared error. Hence, these statistics show that that including the Riccati-Bass equation in models of muscle force and fatigue, even under unconstrained optimization, makes a vast improvement in the predictive ability of the Hill-Huxley nonlinear muscle model because specific biochemical processes that occur during a contraction are accounted for in a manner that is more realistic physiologically.

Furthermore, since Norton and Bass (142) extended the model to predict activity in subsequent demand cycles, it has been shown that the structure of the Conaway models holds for each contraction in a bout of stimulation, for both trained and untrained muscle, and that the coefficients are generally the same between successive generations. (See Appendices G and H for complete stimulation bouts.) It is thus shown in Figures 7-1 through 7-5 that, for fresh muscle, ascertainment of a physiologically realistic Conaway force model optimization for various inputs in fresh paralyzed muscle is facilitated via the model stabilization provided by the Riccati-Bass equation for R_0. A variable R_0 accounts for the early depression and facilitation from autocatalytic calcium-troponin binding, via differences between association and dissociation affinities, during an extrinsically induced contraction. (149, 175) This reflects the net release of calcium during prolonged stimuli and includes the formation of cross-bridges. (149) Moreover, for fatigued muscle, Figures 7-6 and 7-7 show that determination of a physiologically realistic Conaway fatigue model optimization is

facilitated via the model stabilization provided by the Riccati-Bass equation for k_m. A dynamic k_m accounts for the change in voltage sensitivity (59-61) via differences between calcium channel activation and inactivation probabilities during a fatiguing contraction. (40, 41) This reflects the net current movement (59-61) and allows calcium leak from the SR (11) in the fatigue process to be modeled in each contraction as well. Hence, these two different modeled processes imply that the assumption of the excitation-contraction mechanism acting as a stop transducer (103) is valid.

Once a muscle can no longer maintain maximum force, it hysteretically returns to equilibrium due to the change in concentration of free calcium in the sarcoplasm. The biophysical interpretation of the mathematics of calcium diffusion in muscle is that for every molecule of CaTr, there will be a specific instant in time when the state converges to a ‘‘limit of stability‘. The amount transformed from the aggregate CaTr in a specific time unit depends on the characteristic of the species-specific limit, and on the number of perturbations in the state of the aggregate. (116-119) It is known that in a system in which consecutive reactions occur in the presence of a product of autocatalysis, essential conditions exist that allow oscillating processes with damping, especially in the case of two consecutive reaction of equal period in dynamic equilibrium such that energy is minimized in the global system. (117-119) In the case of extrinsic contraction of a paralyzed muscle, the autocatalytic calcium-troponin formation and dissociation reactions lag each other hysteretically in a bistable state. (193) Therefore, by the Principle of Le Chatelier (8, 118, 119,

193), it is concluded that CaTr formation or dissociation is a function of the free calcium available in the sarcoplasm during a contraction.

Previous work (66) optimized the Ding force model on all free parameters for all contractions. Optimization on all free parameters for each contraction in a bout of stimulation is not physiologically realistic and can fail to capture dynamics. Using trained muscle data of Subject 18, the question of what is the most realistic free parameter set with which to optimize the Conaway force model came to the foreground. Among the parameter sets $\{k_m, \tau_1, \tau_2\}$, $\{k_m, \tau_1\}$, and $\{k_m\}$, it is shown in Figure 7-10 that the second set yielded the most realistic values for the doublet ramp and the 10 CT input, even though the three-parameter set had the least prediction error. However, there is not much difference in the fit of curves optimized on $\{k_m, \tau_1\}$ and $\{k_m\}$. This suggests that the lack of strong cross-bridge bonds, in addition to changes in the voltage sensitivity in the calcium channels in the SR, modulate force generation in paralyzed muscle at low frequencies. The reason for this is that, functionally and morphologically, trained paralyzed muscle has more integrity. (163-165) The biologic milieu may represent a difference in the amount of protein or it may indicate how far the protein molecules are embedded into the lipid phase of the membrane. The different voltage sensitivities in trained and untrained muscle could be explained if the voltage-sensitive protein in the fibers of trained soleus were more deeply embedded in the membrane and saw a different part of the electric field. There are fewer indentations in nonparalyzed soleus fibers. Upon denervation, the quantity of indentations increases. Furthermore, the calcium transient is smaller

in untrained than trained muscle. This could result from a decreased membrane area in the terminal cisternae available for calcium release. Or, it may result from decreased calcium capacity per unit volume of sarcoplasmic reticulum in untrained muscle. Since the proteins in the contractile machinery of soleus fibers require less calcium for activation, this suggests a holistic adaptation of the soleus sarcoplasmic reticulum of storing less calcium and releasing decreased amounts of calcium upon activation. (60)

However, for a 20 DDT input, according to Table 7-19, the set $\{k_m, \tau_1, \tau_2\}$ yields the least final prediction error with parameter values closest in agreement to those reported in the literature (66). This suggests that with stimulation of paralyzed muscle at higher frequencies, cross-bridge friction increases as a muscle tries to generate force more rapidly. Hence, the tetani fasciculate with increasing smoothness. This finding indicates the catch-like property of muscle as well as the process of ionic crowding (8) of free calcium in the SR as a paralyzed muscle transitions to low-frequency fatigue.

It was hypothesized that cross-bridge friction changes as a function of frequency and index contraction in fresh muscle. Figures 7-16 through 7-18 show that, in trained muscle, the voltage sensitivity (k_m) is generally oscillatory after the fourth contraction (first 5 pps with beginning doublet input), the time constant of force decay from lack of strong cross-bridge bonds (τ_1) generally decreases after two twitches and reaches minimum value after the second 20 pps with doublet input, and the time constant of force decay due to cross-bridge friction (τ_2) is constant until it increases when inputs of 10 pps with doublets and

higher are given. However, Figures 7-19 through 7-21 show that, in untrained muscle, the voltage sensitivity (k_m) is generally constant after the fifth contraction (second 5 pps with beginning doublet input), the time constant of force decay from lack of strong cross-bridge bonds (τ_1) generally decreases after the twitches yet levels out with a 5 pps with center doublet input, and the time constant of force decay due to cross-bridge friction (τ_2) is constant until it increases when inputs of 10 pps without doublet and higher are given.

Since the calcium current in paralyzed muscle is reduced, this implies that the calcium released from each pulse in a stimulus train is also reduced. In addition, because paralyzed muscle also contains excess calcium from proteolysis of fibers, this implies that troponin saturates much more quickly during an elicited contraction. Rapid saturation of troponin would generate maximal force and cause muscle equilibration more quickly. Yet, maximal force cannot be sustained due to the morphological degradation of the calcium channels. Hence, even with the excess calcium in the myoplasm, force in paralyzed muscle decays because there is degraded contractile machinery in the fibers. This explains the decay in τ_1 as a function of input frequency shown by the plots. Rather than instantaneous occlusion, the results imply that the cross-bridges form in this way until the troponin is saturated at 20 pps. (117, 149, 163)

The behavior of τ_2 can be explained from the fact that later inputs at low frequencies rose with the same time delay as the twitch. Hence, this confirms the earlier hypothesis of progressive saturation of troponin by additional divalent calcium in the myoplasm. In the presence of divalent calcium, this inhibitory

domain moves away from actin and tropomyosin displaces. Activation of myosin binding to the actin facilitates additional cross-bridge formation through increased calcium binding or by directly altering actin conformation. Hence, cross-bridge friction increases asymptotically as calcium-troponin binding increases autocatalytically. (12, 73, 112, 130)

Determining a most influential parameter was done via two-way analysis of variance with replication for each of the three free parameters in the Conaway force model and is shown in Tables 7-22 through 7-24. For k_m and τ_1, it is shown that no one of the factors are statistically significant. Meanwhile, the analysis for τ_2 shows that neither the training status nor the interaction between frequency and training status has statistical significance. However, the factor of input frequency is very significant statistically. This confirms what was found in the model-fitting optimization analysis. Yet, the within group factor accounted for 62% of the variation. This could be due to experimental error or physiological differences between subjects. It is thus conditionally concluded that the cross-bridge friction is the most influential physiologic process in force generation in paralyzed muscle at frequencies higher than 5 pulses per second.

As the input frequency of the electrical stimulus increases, the muscle contractions progressively become more fused and the muscle generates greater torque. (42, 163) Once the muscle tetani are fully fused, any frequency increase afterwards elicits infinitesimal changes in force and its underlying generative processes. The parameter-frequency curve for muscle will be shifted to the left of the parameter-frequency curve for fast muscle. Since previous work has shown

that increases in volume fraction of the sarcolemma in soleus fibers following denervation release more calcium, this shifts the tension-membrane voltage curves of actin and myosin to the left. (149, 163) Assuming untrained muscle to be acute post-paralyzed muscle and trained muscle as an approximation to nonparalyzed muscle, this would explain the differences in the parametric points of change with respect to frequency-contraction index. Biochemically, myosin phosphorylation increases when fibers transform from slow to fast from disuse (20, 21). As the calcium concentration in the SR decreases from repetitive activation, decreased free divalent calcium is available to phosphorylate myosin light chains. (2, 176) Hence, the cross-bridge friction increases. Since untrained paralyzed muscle behaves more like fast muscle than does trained paralyzed muscle, this explains why the model parameters, and the underlying physiologic processes, change at lower frequencies in untrained muscle than they do in trained muscle.

In fatigued muscle, with the Riccati-Bass structure (10, 142) for k_m, it is inferred that the underlying processes involved in the calcium binding or activation of extrinsic stimulation still behave according to power laws of Michaelis-Menten kinetics in each contraction in fatigued paralyzed muscle. Hence, the power law formalism (162) is indeed valid for the Conaway fatigue model. With a value for b around 1.5, it means that, according to the Conaway fatigue model, the R_0-k_m relationship could be fractal. Physiologically, this can be interpreted as increased delay in the SR calcium channels sensing strongly bound cross-bridges from the calcium current during fatigue in paralyzed muscle.

As a result, the more-than-linear enhancement from additional pulses in a stimulus train is further decreased. This implies decreased force-generation in a paralyzed muscle because the excess free calcium remains unbound due to decreased sarcotubular volume. (40)

It was further hypothesized that calcium leak from the SR during an extrinsically induced contraction is the primary contributor to fatigue from extrinsic stimulation in paralyzed muscle. Additionally, this process was thought to be amplified in untrained paralyzed muscle. Finally, it was hypothesized that calcium leak increases as a function of contraction during fatigue. It is shown in Figures 7-25 and 7-28 that in fatigued trained and untrained muscle, τ_{leak} increases with not much variance as a function of contraction. Meanwhile, the variances of the other two free parameters fluctuate wildly. This means that τ_{leak} is the most influential parameter in the Conaway fatigue model. This means that calcium leak from the sarcoplasmic reticulum is the most influential process in muscle fatigue. Furthermore, in Table 7-27, two-way analysis of variance with replication for τ_{leak} shows that the interaction term between contraction index and training accounts for almost 50% of the variance in τ_{leak}. This means that calcium leaks out of the SR increases multiplicatively as a function of training status and every additional contraction in fatigue. Finally, Figure G-7 shows that peak force decays with every additional contraction. That means that there is potentiation as described by Shields et al (171) occurring as a paralyzed muscle fatigues.

Bellinger et al (11) show that remodeling of the RyR1 macromolecular complex during exercise, consisting of PKA hyperphosphorylation at Ser-2844,

RyR1 *S*-nitrosylation, PDE4D3 depletion, and calstabin1 depletion, likely plays a role in determining exercise capacity. Several biochemical changes have been identified in the RyR1 macromolecular complex consistent with leaky RyR1/Ca^{2+} channels. Muscle-specific deficiencies of either calstabin1 or PDE4D3 in exercise defects in mice have been shown in the remodeling of the RyR1 complex. This remodeling is characterized by depletion of calstabin1 and PDE4D3 from the RyR1 complex, and has been linked to impaired exercise performance. This explains the differences in parametric variations between muscle training states seen in the results. It may be that because trained paralyzed muscle behaves like nonparalyzed muscle (163, 164), there is more calcium leak occurring in trained muscle than in untrained muscle. This is because trained muscle has a greater sarcotubular volume fraction. Therefore, the cross-bridge activity and other modulating factors in trained muscle may behave differently than those in untrained muscle.

This is also supported by the fact that kinetics of cytoplasmic reactions follow anomalous rate laws with macromolecular crowding as a major factor. Reactants are constrained in space in crowded environments microscopically by forces such as steric hindrance and electromagnetic interactions which can occur intermolecularly. The reaction volume available for a calcium ion is modulated by number, size and shape of all other ions in the SR. Regardless of the quantity of available troponin, collisions between calcium ions and troponin will be much less numerous than collisions between calcium ions. (163) Hence, due to the excess

release from extrinsic stimulation and denervation proteolysis, the calcium ions repel each other rendering a muscle unable to sustain maximal force.

Two-way analysis of variance with replication for $\alpha_{\tau 1}$ shows, in Table 7-28, that the two main factors of training and contraction are statistically significant for the coefficient for force model parameter τ_1 in the fatigue model. Together, they account for almost 73% of the parameter variance. That means that the change in maximally sustained force is a function of contraction index as well as training status. Furthermore, two-way analysis of variance with replication for τ_{fat} shows that no factor is statistically significant for the time constant controlling the recovery of the cross-bridges during fatigue. Hence, it is concluded that maintenance of cross-bridge friction has the least influence of the physiologic processes in fatigue in paralyzed muscle.

This result can be explained be the following process. The affinity of the contractile proteins for calcium may increase in paralyzed muscle. Further evidence to support a role for the indentations in excitation-contraction coupling is provided by the fact that there is a parallel change in the numbers of indentations and the amount of charge movement after denervation. (61) Inactivation of EC coupling is not caused by calcium depletion from the sarcoplasmic reticulum or inactivation of the calcium release channel or contractile proteins. The resistance to inactivation of tension indicates a characteristic of the voltage-sensitive molecule. (59)

However, Delbono and Stefani (41) found that calcium inactivation in paralyzed fibers had an increased recovery, and a decreased speed of

inactivation. This renders inactivation of paralyzed muscle more difficult, since the voltage dependence of the calcium channel inactivation is partially shifted leftward due to proteolysis. Hence it is plausible to suggest that this process may degrade the functioning of a typical inactivating gate in some of the calcium channels. As a result, formation of strong cross-bridges necessary to maintain maximal force is impeded. Moreover, impaired release of calcium ions by the SR and a change in the sensitivity of the calcium receptor have been suggested as contributors to low-frequency fatigue. (115, 120, 191) Hence, as soleus transforms, upon denervation, from premost influentially slow fiber type to that of fast-fatigable fibers (72, 77, 164), the relaxation phase is prolonged in the fatigued state.

Hence, it is inferred that, as the chronically paralyzed soleus fatigues from stimulation, calcium channel remodeling and inactivation of EC coupling from ionic crowding accelerate with each subsequent contraction. In turn, this means that as more calcium leaks out, further channel remodeling and inactivation occur in a positive feedback cycle until maximal sustained force decays. The calcium channel remodeling indicates electromechanical hysteresis. As the calcium channels remodel due to calcium leak, they acquire different conformations as energy from the sarcoplasmic reticulum is lost. Hence, with decreased potential energy, the muscle loses the ability to sustain maximal force. Furthermore, inactivation of EC coupling indicates chemical hysteresis. As the excess calcium ions flow around a sarcomere, the voltage-sensitive troponin molecules in the SR change conformations and lose the ability to generate force. Thus, relaxation is

prolonged. Clinically, that means that if there is overstimulation, the degrading biochemical processes will continue until the muscle is most likely damaged beyond repair.

8.1.3 Problems and weaknesses in the study

One major weakness of this study is that there is no demonstrable modeling of the transition between nonfatigued and fatigued states in a muscle. In this study, muscle behavior has been inferred solely from differences in optimal sets of parameters. The protocol assumes that nonfatigue and fatigue are separate discrete states. It would be more realistic to model muscle behavior along a continuum. If this were done, an index of muscle fatigue could be developed for clinical use in therapeutic stimulation protocols.

There are other deficiencies in this study. First, the sample size and input range are very small. The Conaway models need to be validated over a much larger population of subject and a wide spectrum of inputs to establish their generalizability and reliability as well as their clinical applicability. This would require substantial data collection from multiple centers.

Furthermore, the Conaway models need to be tested for robustness with stochastic inputs such as pseudorandom n-ary sequences. Were this done, higher-order information, such as Wiener kernels, about muscle properties could be obtained. This would aid in developing input-output relationships between stimuli and generated forces in paralyzed muscle

8.2 Future work to address long-term goals

There are many directions in which this modeling work can be extended.

It would be fruitful to apply the Conaway models to human muscle force and fatigue data from subjects who have other neurological impairments such as Parknson's disease, stroke, traumatic brain injury, and cerebral palsy. If such investigations were pursued, a more complete picture of muscle physiology may be obtained.

8.2.1 Directions in modeling

Currently, there is no demonstrable modeling of the transition between nonfatigued and fatigued states in a muscle as functions of frequency and index of contraction. It would be more realistic to model muscle behavior along a continuum with a generalized force-fatigue model. To achieve this, the R_0-k_m constitutive power law relationship from the Conaway fatigue model can be applied to the Conaway force model. Evidence to support this comes from the reverse engineering result that the Conaway fatigue model can be optimized to fit, with 95% agreement, a 20 DDT force profile from fresh muscle (unpublished observation). This observation suggests a novel way to investigate the transition to fatigue. If a generalized Conaway force-fatigue fatigue model can be constructed, its parameters can be optimized to determine the frequency of stimulation at which the relationship between nonlinear enhancement and voltage sensitivity, as well as the calcium leak, become influential in maximal force maintenance or lack thereof in paralyzed muscle.

In addition, the relationship between nonlinear summation and calcium channel voltage sensitivity (R_0-k_m) needs to be investigated for its possible fractal nature in both fresh and fatigue states. To do this, however, Lyapunov

exponents would need to be calculated. If a fractal relationship is found to exist, it would say a great deal about the kinetics in a paralyzed muscle during a contraction, as well as its morphology. In addition, such findings would yield further insight on how to characterize the transition between fresh and fatigued states in a paralyzed muscle using a closed-form parameterized mathematical model that employs nonlinear differential equations in its structure.

This modeling work may be extended to other neurological impairments such as stroke. To date, it is unknown how a post-stroke paretic muscle behaves as it goes into fatigue. It is assumed that paretic muscle behaves similarly to paralyzed muscle, yet with possible differences. Using muscle force-fatigue data from paretic human subjects, it is proposed that the abilities of the Ding models to predict force and low-frequency fatigue would be compared to the predictive ability of the Conaway models. The results from paretic human subjects would be compared to the results from paralyzed human subjects to garner a much more comprehensive understanding of muscle physiology in different mechanisms and states of neuromuscular pathology.

8.2.2 Suggested experiments in vitro

In paralyzed single crayfish muscle fibers and frog semitendinosus immersed in a calcium gradient, force output from sinusoidal length changes in the frequency range of 0.25-133 Hz can be studied. From this, three processes can be shown in the interaction of myosin with actin in fully activated preparations. They would be a low-frequency phase advance, a middle-frequency delay, and a high-frequency advance. These processes can be used

as probes to study the chemomechanical decoupling of fatigability. (115, 120, 183, 191)

A high resolution method for determining the complex stiffness of "fatigued" single muscle fiber can be implemented by immersing them in excess calcium and oscillating the fiber length sinusoidally. The resulting force amplitude and phase shift are observed and interpreted in terms of chemomechanical energy transduction. In "fatigued", fast skeletal muscle fibers of rabbit, frog, and crayfish, reaction rate processes can be discovered. These would show ATP hydrolysis and associated energy transduction since they are not present in fresh muscles. Results of complex stiffness data from different muscles in different species would elicit better understanding of fatigue mechanisms across a broad spectrum of varying phylogeny. (115, 120, 183, 191)

8.2.3 Clinical applications

It is expected that these results will be used in the design of better neuro-muscular electrical stimulators. It is envisioned that future revisions of the model will be incorporated into a real-time NMES controller that will predict and prevent fatigue that arises from different mobility tasks in individuals with spinal cord injury.

The insights about the physiology of muscle fatigue in chronically paralyzed muscle can be used to develop clinical indices to asses muscle integrity in the neurologically impaired. With appropriate validation of the Conaway models in paretic muscle, a standard battery of tests based on the calcium dynamics in muscle fatigue may be developed. Such tests may be used

to develop therapeutic strategies to preserve muscle integrity for different mechanisms and degrees of neurological impairment including cerebral palsy, stroke, traumatic brain injury, and spinal cord injury.

8.3 Summary

Several conclusions are drawn from this study. First, it is concluded that including the Riccati-Bass equation in models of muscle force and fatigue, makes a vast improvement in the predictive ability of the Hill-Huxley nonlinear muscle model of Ding because certain biochemical processes are accounted for in a manner that is more realistic physiologically. Such additions stabilize the original models and makes them robust. Physiologically, it is concluded that calcium-troponin formation or dissociation is a function of the free calcium available in the sarcoplasm during a contraction. Furthermore, the lack of strong cross-bridge bonds, in addition to changes in the calcium channel voltage sensitivity in the sarcoplasmic reticulum, modulates force generation in paralyzed muscle at low frequencies. However, the cross-bridge friction is the most influential physiologic factor in force generation in paralyzed muscle at frequencies higher than 5 pulses per second. Furthermore, calcium leak from the sarcoplasmic reticulum is the most influential process in paralyzed muscle fatigue. The process of muscle fatigue occurs as calcium channel remodeling and inactivation of excitation-contraction coupling from ionic crowding accelerate with every additional contraction.

The fundamental question to be considered is whether expansion-contraction equations can approximate curvilinear motion when the former is far

more rapid in one direction or a small angle than in others. Since the expansion-contraction equations and their solutions are simple, finding theorems for these approximations could simplify the study of physiologic processes. (57) Because the Riccati-Bass equation generates sigmoidal diffusion functions, it is argued from the literature that they can be applied to many other physiologic processes. Furthermore, it is at best inappropriate to assume that physiologic processes behave as scalar functions since biochemical reactions occur in all directions in a volume. Thus, including the fundamental construct of the diffusion function in physiological systems theory by extending this powerful equation to different clinical problems and associated underlying models is of great societal importance and urgency. Better assessments will lead to optimal therapeutics. Therapeutics that better enable function will decrease health care costs and increase the societal contributions made by individuals with SCI. In the modern economy, every bit of savings is exponentially helpful in a logistic manner.

APPENDIX A: THE RICCATI EQUATION

A.1 The Riccati equation and its extensions

A.1.1 Introduction

At the close of 1720, the Venetian nobleman Count Jacopo Francesco Riccati proposed two new differential equations. In modern symbols, these equations can be written as follows:

$$x' = ax+bt^m \tag{A-1}$$

$$x' = ax+bt+ct^2 \tag{A-2}$$

where *m* is a constant and *t* is the independent variable. (16)

Originally, Riccati focused on the geometric problem of a pair of coordinates (α,β) describing planar motion by a first-order linear differential equation such as:

$$\begin{bmatrix} \dot{\alpha} \\ \dot{\beta} \end{bmatrix} = \begin{bmatrix} w_{11} & w_{12} \\ w_{21} & w_{22} \end{bmatrix} \begin{bmatrix} \alpha \\ \beta \end{bmatrix} \tag{A-3}$$

The question to be answered was: which equation governs the slope x=β/α? It was shown to be

$$x' = ax^2 + bx + c \tag{A-4}$$

where $a=-w_{12}$, $b=w_{22}-w_{11}$, $c=w_{21}$.. (16, 158)

A.1.2 The Bernoulli equation

In mathematics, an ordinary differential equation of the form

$$y' + P(x)y = Q(x)y^n \tag{A-5}$$

is called a Bernoulli equation when n≠1, 0. (13) Dividing by y^n yields

$$\frac{y^1}{y^n} + \frac{P(x)}{y^{n-1}} + Q(x) \tag{A-6}$$

A change of variables is made to transform into a linear first-order differential equation.

$$w = \frac{1}{y^{n-1}} \tag{A-7}$$

$$w' = \frac{1-n}{y^n} y' \tag{A-8}$$

$$\frac{w'}{1-n} + P(x)w = Q(x) \tag{A-9}$$

The substituted equation can be solved using the integrating factor

$$M(x) = e^{(1-n)\int P(x)dx} \tag{A-10}$$

A.1.3 The general Riccati equation

Riccati (158) responded to the challenge posed by Daniel Bernoulli to solve his equation by saying:

> "Reductio aequationum differentialum secundi ordinis plerumque est adeo perplexa, atque involuta, ut Analystam minus attentum frequentissime eludat. Dum syntheticae viae insistimus, & a primis fluxionibus ad altiorem gradum ascendimus, cum assumatur tanquam constans vel nota differentia, vel nulla, eae difficultates, de quibus sermo erit, vix occurrunt;

quae tamen evitari nequeunt, si problema aliquod proponatur secunda elementa involvens & analytica methodo procedendum sit. Infinitas dari formulas differentio-differentiales, ad quas pervenitur, nulla adhibita constante, nemo profecto ignorat: totidem quoque exhiberi posse, ad quas pervenire non conceditur, nisi constante in subsidium vocata, acutiores non latet Analystas: at quomodo ab invicem dignosci queant, & qua ratione tractandae sint, non ita compertum neque obvium puto; cum tamen sublimioris Geometriae officium sit inspicere, quousque, & quibus in circumstantis expressiones istae solutionem admittant."

In the translation by Bruce (158), that means:

"The reduction of differential equations of the second order generally is especially involved and complicated, and usually the reduction eludes the less attentive analyst. While we are pursuing the path of synthesis, and when we rise from the first fluxion [derivative] to the higher level, since we can assume that either there is agreement with a known differential, or else nothing is to be agreed upon, then these difficulties for which something needs to be said hardy occur. This cannot be avoided, if some problem is proposed involving elements of the second degree, and one has to proceed by an analytical method. There are boundless second order or differentio-differential equations that can be given, and for which there appears to be no solution, and nobody is ignorant of that: likewise, there are just as many that can be solved that are only revealed to the more acute analysts, and for which we may concede that a solution can only be found by calling on their aid. But how are these differential equations to be distinguished from each other, and by what means are they to be solved? I think that the answer to this question is neither known nor obvious; for it is still the task of the more sublime mathematicians to examine these things at some future time, and to consider in what circumstances these expressions admit of a solution."

Riccati (158) continues his argument with the following proposition.

"Reductio aequationum differentialum secundi ordinis plerumque est adeo perplexa, atque involuta, ut Analystam minus attentum frequentissime eludat. Dum syntheticae viae insistimus, & a primis fluxionibus ad altiorem gradum ascendimus, cum assumatur tanquam constans vel nota differentia, vel nulla, eae difficultates, de quibus sermo erit, vix occurrunt;

quae tamen evitari nequeunt, si problema aliquod proponatur secunda elementa involvens & analytica methodo procedendum sit. Infinitas dari formulas differentio-differentiales, ad quas pervenitur, nulla adhibita constante, nemo profecto ignorat : totidem quoque exhiberi posse, ad quas pervenire non conceditur, nisi constante in subsidium vocata, acutiores non latet Analystas : at quomodo ab invicem dignosci queant, & qua ratione tractandae sint, non ita compertum neque obvium puto; cum tamen sublimioris Geometriae officium sit inspicere, quousque, & quibus in circumstantis expressiones istae solutionem admittant. “

That is translated as:

“For example, let there be a curve constructed in which some power *m* of the abscissa *x* is set out in order along a line in the ratio of the second order differentials of the ordinates *y* and inversely as the similar differentials of the same abscissae, by which means the curve is set out by a differential equation of the second order.“ (158)

The analysis starts with the general ordinary differential equation

$$\frac{dy}{dx} = f(x, y) \tag{A-11}$$

Approximating f(x,y) while x is kept constant gives

$$f(x, y) = P(x) + Q(x)y + R(x)y^2 + \ldots \tag{A-12}$$

Riccati (158) looked at the approximation to the second degree and considered equations of the type

$$\frac{dy}{dx} = P(x) + Q(x)y + R(x)y^2 \tag{A-13}$$

He claimed that no curve exists when the transition is made from the first derivative to the second derivative, unless some constant is initially given in the first order differential equation. Furthermore, Riccati asserted that it is impossible for such an equation to be modified except by the addition of equal terms to both sides, or by the substitution of other functions. Conversely, transitioning from the second derivative to the first derivative, an infinite family of curves exists with a specific first-order constant that satisfy the constraints of the original problem. (158)

The above equation is the General Riccati Equation. It is nonlinear and does not fall under the category of any of the classical differential equations. In order to solve a Riccati equation, it is necessary to have a particular solution. Riccati proposed that all second-order differential equations can be reduced to first order differential equations with or without a specified constant and in which the second derivatives have been determined via quantities of finite magnitudes as long as the proposed equation for each does not diverge from its own indefinite integrals. (19, 39, 90, 154)

A.1.4 Solution of the general Riccati equation

More generally, Riccati (158) examined the equation: $x^n dq=du+u^2dx:q$ with the exponent *m* given as arbitrary and the quantity $q=x^n$ is substituted. At the end of the treatise, he posed the question of what ratio should *n* be so that separation of variables will allow solving the equation only by quadratures.

In his 1733 treatise, Euler (65) responded to the question posed by Riccati with the following answer. The Riccati equation is indeed integrable when n is

either 0 or a positive whole number, so the whole thing itself can be integrated. For truly this happens whenever n=-4K/(2K+1), with K denoting some positive whole number. Hence the equation, if the exponent of x itself is –n/(n+1), can be reduced to $ax^n\,dx = dy+y\,dx$. That equation is integrable if n=-4K/(2K+1). Thus, these are the cases in which separation of variables in the Riccati equation can occur.

The correspondence between Riccati equations and second-order linear ODEs has a number of consequences. If one solution of a second order ODE is known, then it is known that another solution can be obtained by a simple integration. The same holds true for the Riccati equation. In fact, if one can find one particular solution y_1, the general solution is obtained as $y=y_1+u$. (19, 90)

A.1.5 Growth and diffusion models

Via a Riccati equation without a constant term, P represents population size and t represents time, this model is given by the differential equation (90):

$$\frac{dP}{dt} = rP\left(1-\frac{P}{K}\right) \tag{A-14}$$

where the constant r defines the growth rate and K is the carrying capacity. The solution to the equation (with P_0 being the initial population) is

$$P(t) = \frac{KP_0e^{rt}}{K + P_0(e^{rt} - 1)} \tag{A-15}$$

where

$$\lim_{t \to \infty} P(t) = K \tag{A-16}$$

P(t) is known as a logistic function. A logistic function models the S-shaped growth curve of some set of elements P. Initially, growth is approximately exponential. As saturation begins, the growth decreases until stopping at maturity. As shown in the graph, the unchecked growth is modeled as a percentage rate term +rKP. As the population grows, some members of P interfere with each other in competition for some critical resource which can be called the saturation point, modeled by K. This competition decreases the growth rate until P ceases to grow at the point of maturity. (90, 100, 150)

A logistic function is defined by the mathematical formula:

$$y = \frac{\mathrm{a}+\mathrm{me}^{-\frac{t}{r}}}{a + ne^{-\frac{t}{r}}} \tag{A-17}$$

for real parameters a, b, m, n, and τ. (85, 94, 145)

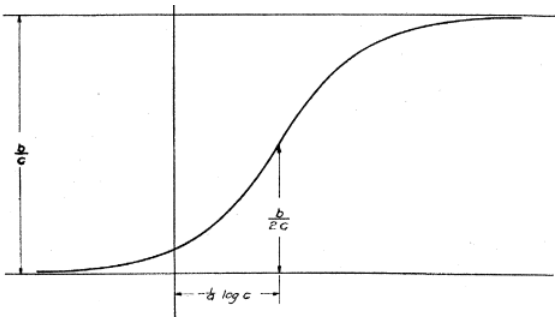

Figure A-1. General logistic curve with inflection point at (-ln c/a, b/2c). (150)

A special case of the logistic function that exists with a=1, b=1 m=0, n=1, t=1,

$$y = \frac{1}{1+e^{-t}} \qquad \text{(A-18)}$$

is called a sigmoid. The name comes from the sigmoidal shape of its graph. Also known as the standard logistic function, it is encountered in a wide variety of technical domains, including chemistry, physics, engineering, health science, probability, statistics, biomathematics, economics, psychology, and sociology.

The sigmoid function solves the first-order non-linear differential equation y'=y(1-y) with the boundary condition P(0)=0.5. (90, 100)

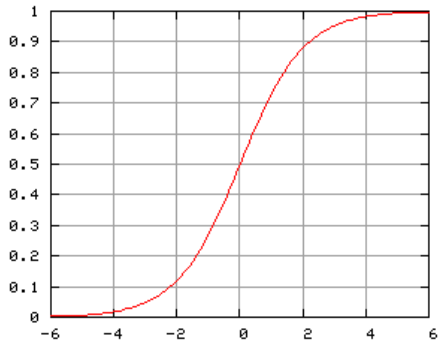

Figure A-2. Sigmoid function.

The sigmoid curve exponentially grows for negative t, slows to linear growth of slope 1/4 near t = 0, and approaches y = 1 with exponential decay. As the inverse of the natural logit function, the sigmoid can to convert the logarithm

of odds into a probability. Conversion of log-likelihood ratio of two alternatives also exhibits sigmoidal behavior. (85) Furthermore, if $y=M/(1+e^{-t/\tau})$, that gives $y/2=M(1-e^{-t/\tau})/2(1+e^{-t/\tau})=\frac{1}{2}M \tanh(t/\tau)$. This result is the hyperbolic tangent function. (22)

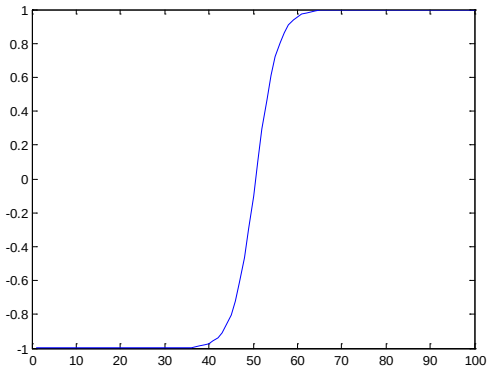

Figure A-3. Hyperbolic tangent function with $\tau=1$.

One application of the logistic equation is a common model of population growth. The model states that the rate of reproduction varies proportionally to the existing population as well as to the amount of available resources, all else being equal. Thus the second term describes the competition for available resources, which tends to limit the population growth. (9, 99, 100)

The physiologist T. Brailsford Robertson published results using the sigmoidal curve to describe various cases of individual growth in animals, plants, and man. Robertson denoted his curve as the “autocatalytic” or self-accelerating curve. That was because it was identical to that used to describe chemical

reactions in which one of the products had the property of increasing the rate of further reaction. (160) Robertson showed that the growth of living matter is phenomenologically autocatalytic. The growth of all organisms can be represented approximately as the resultant of two monomolecular autocatalytic reactions. The rather close similarity in mathematical form and behavior between chemical and physiologic processes was surprising. That is because the factors which ultimately limit autocatalysis are decreased concentration of the reactants and increased concentration of the products. The original theory was later extended to cover growth in protozoan and bacterial populations (161). Actually, the term “autocatalytic” referred just to the accelerating growth phase. However it later referred to the whole S-curve. This repeated loose designation had the result that the autocatalytic curve was equated with the logistic curve. (99)

Growth of the simplest organism is a complicated phenomenon from the different levels of biological consideration. However, certain aspects have been found amenable to quantitative analysis and have generated insight into the relationships between growth and metabolism. The relationship between metabolic rate and body size can be investigated either intraspecifically or interspecifically. (14)

The relationship between the metabolic rate and body size can be articulated in the equation:

$$M = bW^{a} \qquad \text{(A-19)}$$

where M is the metabolic rate per unit time, W the body weight, and a and b are constants. This is a special case of the allometric formula which expresses the

dependence on body size for an enormous amount of biological data. (14) Further, this formula can be expressed in an alternative way:

$$\log U = \log b + a \log W \qquad \text{(A-20)}$$

With Riccati or logistic characteristics, the Bertalanffy equation, $dW/dt=aW^m-bW^n$, states that the result of metabolic and catabolic processes in organism behaves allometrically. The process rates can be expressed as a power function of body mass. This assumption was justified, since first approximations of all physiological rates can be expressed in allometric or power formulas. In addition, the organism in growth changes at the numerous biological levels. The catabolism means, however, the constant loss of building material as it occurs in any given living organism. Biochemically, this means the turnover of proteins. (14)

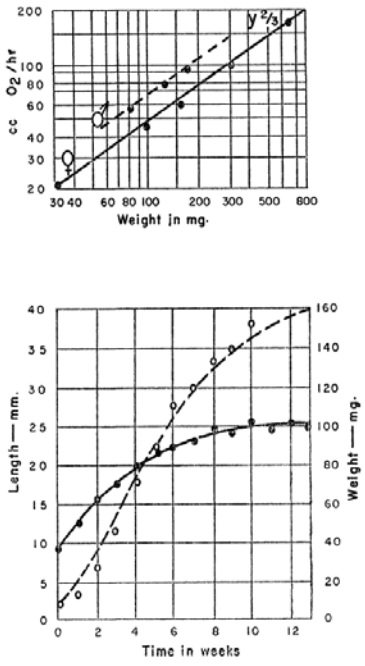

Figure A-4. Allometric metabolic (top) and growth curves (bottom). (14)

In contrast, another type of growth curve can be generated in which anabolism and catabolism occurs at the same rate. Hence, growth rates will always increase. The larger an animal becomes, it grows faster. In this case, growth is exponential and does not reach a steady state. However, there is one organism whose growth curve is unique. Since the Bertalanffy growth formulas are applicable to myriad species, the growth curve shapes are identical. Hence, the same curve can represent the growth of different species by using different scales for body size and time. If, however, the growth curve of man is entered, it appears to be unique. (14)

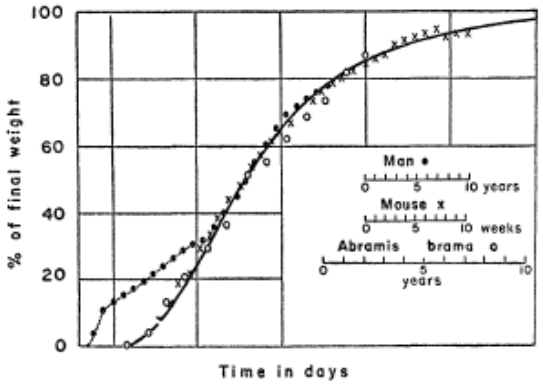

Figure A-5. Comparative growth curves for fish, mouse, and man. (14)

Bertalanffy (14) noted that the second part of the growth curve of man, starting with puberty, adheres to the general pattern. However, the first part of the curve is wholly different. In the early developmental years, the curve is greatly elongated. It is as if a new growth cycle is superposed on the typical growth pattern. Although this variation is present in the growth cycles of

nonhuman mammals, only in humans does it yield a unique curve shape. This growth curve is connected with perturbations in the hormonal homeostasis and is demonstrated in pathologies, such as pubertas praecox in human pituitary dysfunction, when puberty takes place at an early age. Hence, the singular growth curve of humans is a mathematical realization of the delay in human development which has been asserted to be a basic factor in not only human evolution but also human uniqueness.

The following analysis investigated power laws of Riccati-Bass functions to examine possible fractal behavior (10, 162) in the Conaway fatigue model. Curiosity arose when the value of b in $R_0=ak_m^b+c$ did not change much, if at all, in optimizing the Conaway fatigue model. Increasing functions are presented for illustrative purposes.

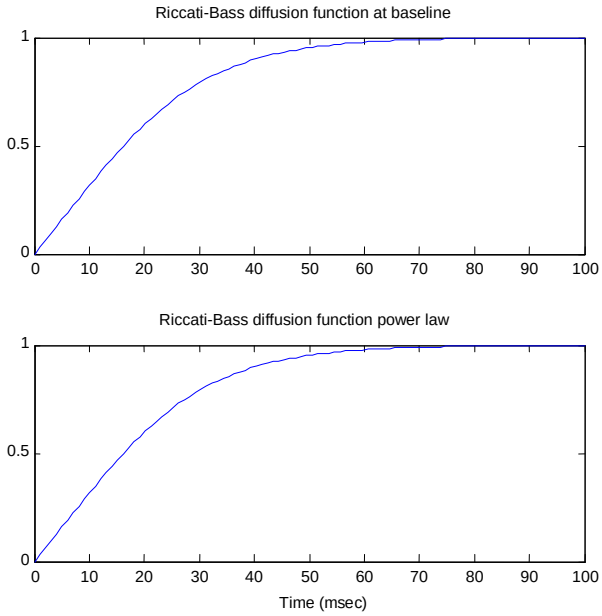

Figure A-6. Riccati-Bass diffusion function and associated power law with b=1.

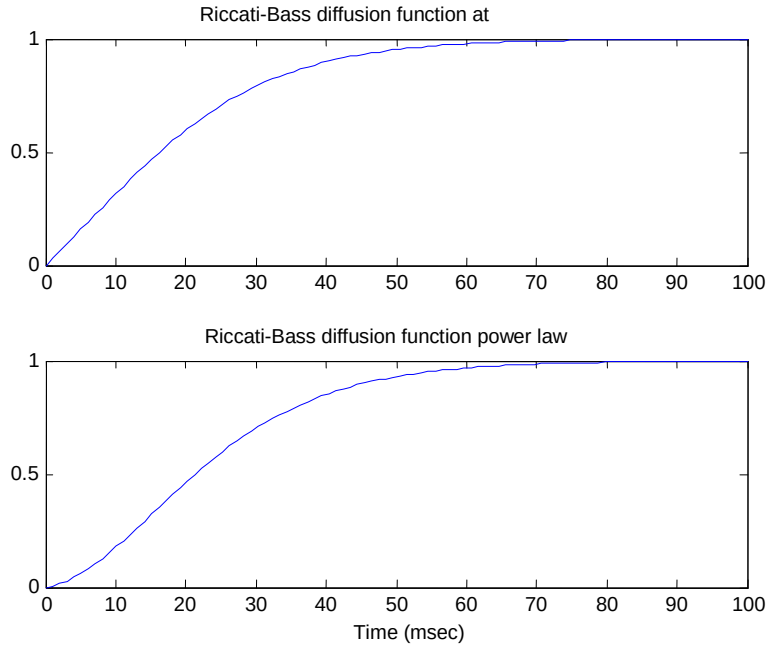

Figure A-7. Riccati-Bass diffusion function and associated power law with b=1.5.

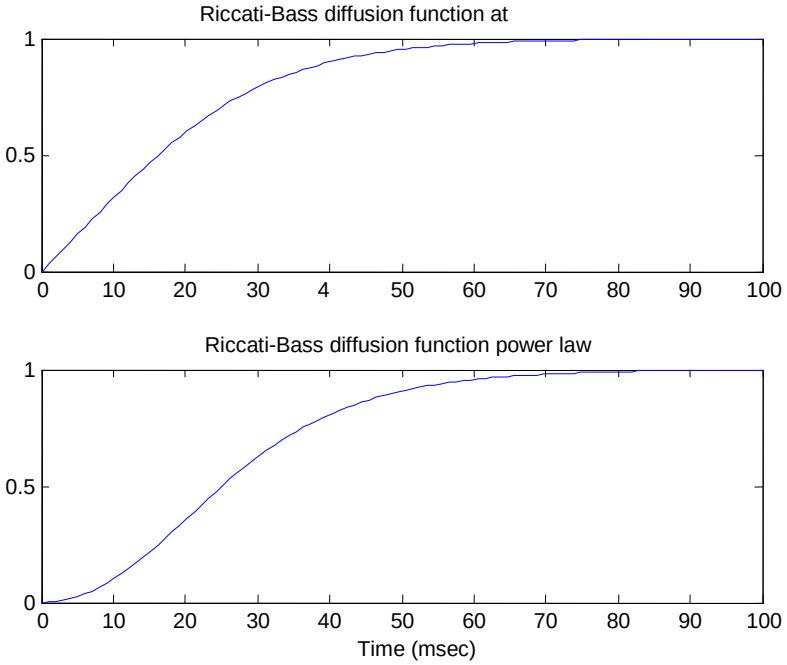

Figure A-8. Riccati-Bass diffusion function and associated power law with b=2.

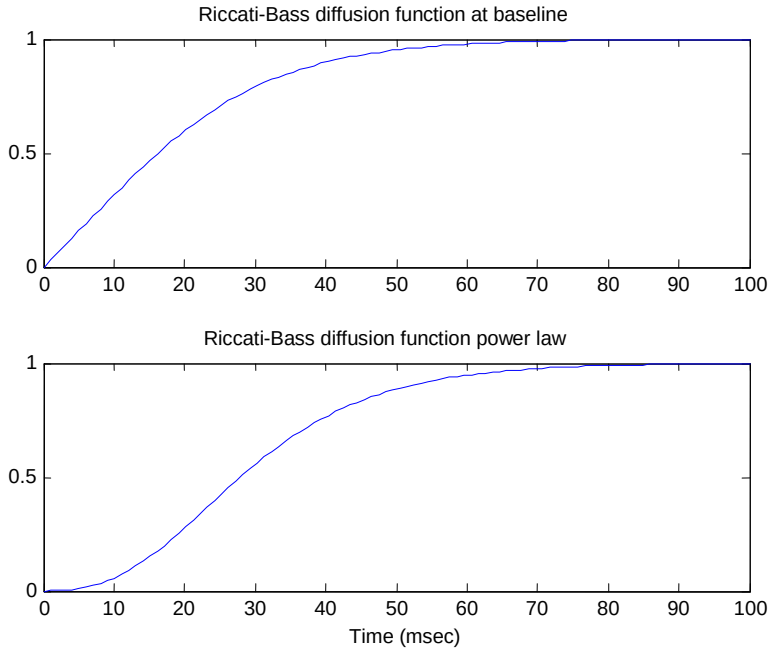

Figure A-9. Riccati-Bass diffusion function and associated power law with b=2.5.

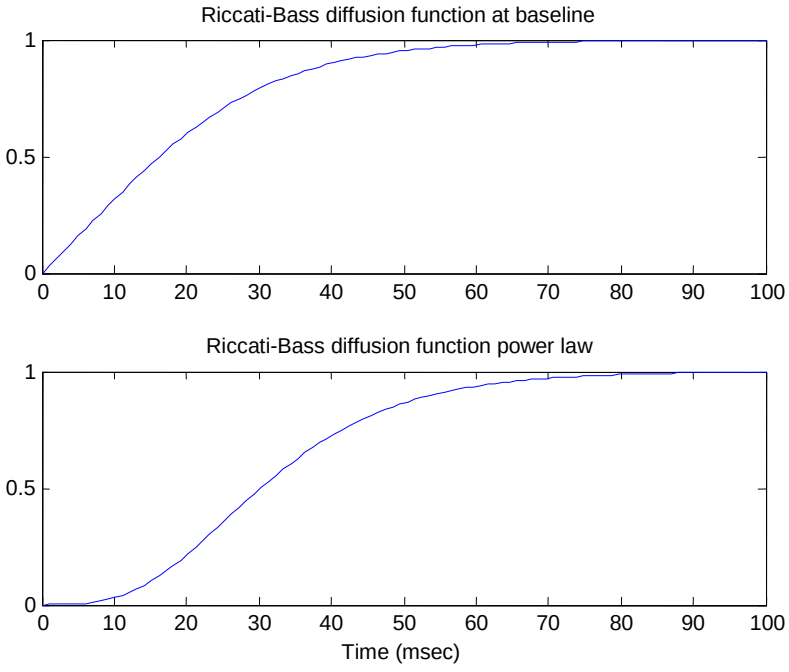

Figure A-10. Riccati-Bass diffusion function and associated power law with b=3

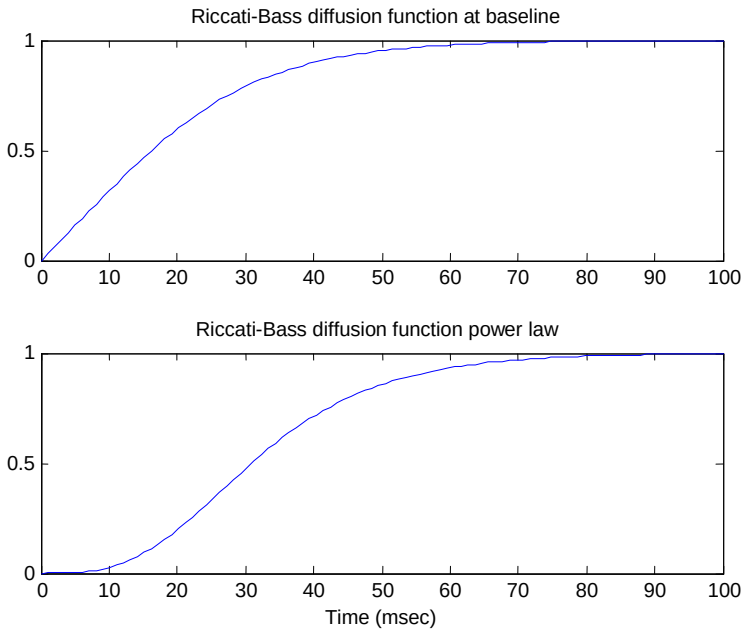

Figure A-11. Riccati-Bass diffusion function and associated power law with b=π.

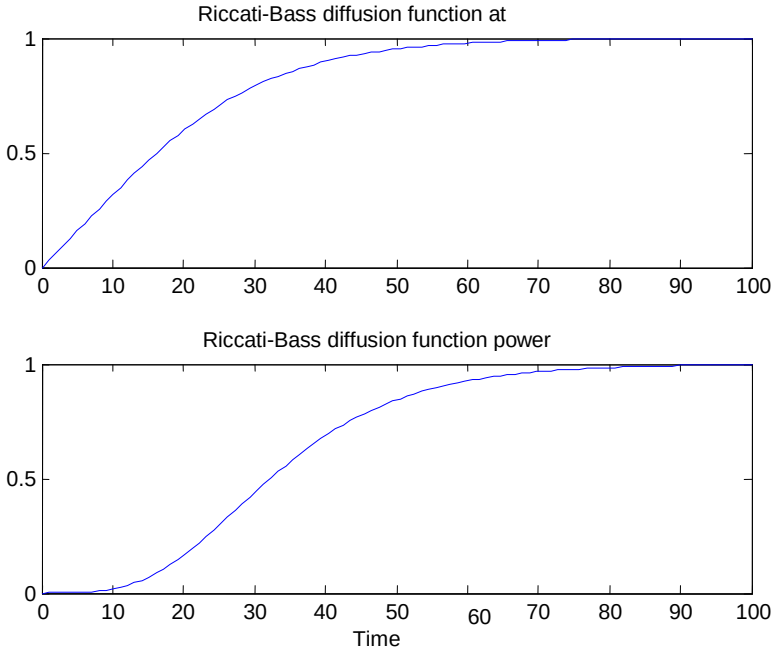

Figure A-12. Riccati-Bass diffusion function and associated power law with b=3.5.

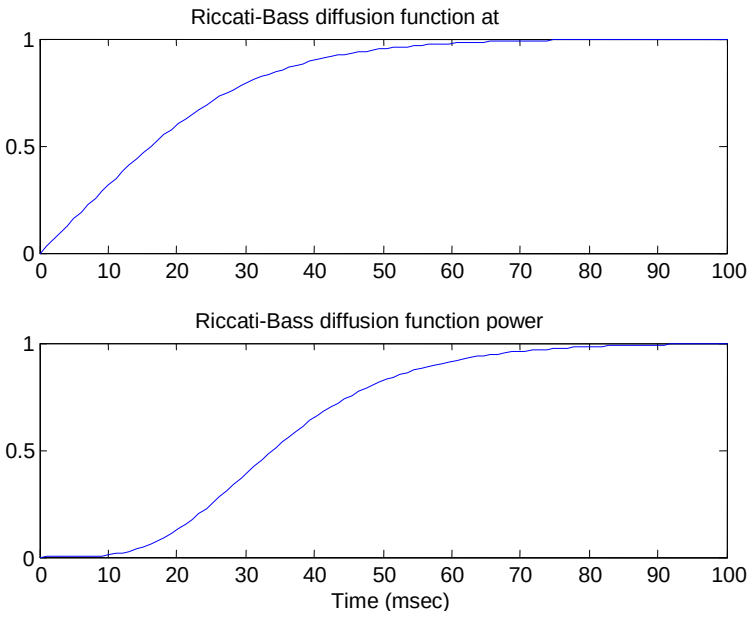

Figure A-13. Riccati-Bass diffusion function and associated power law with b=4.

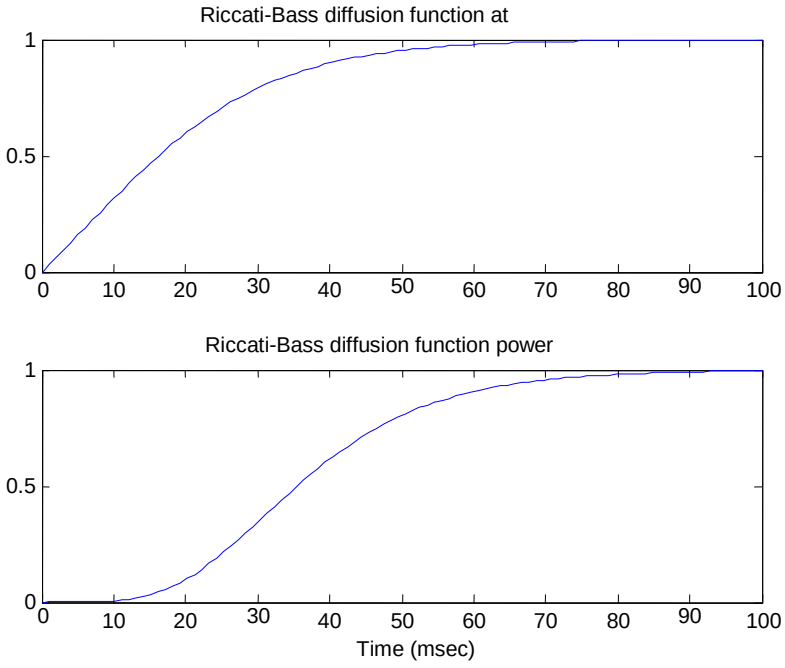

Figure A-14. Riccati-Bass diffusion function and associated power law with b=4.5.

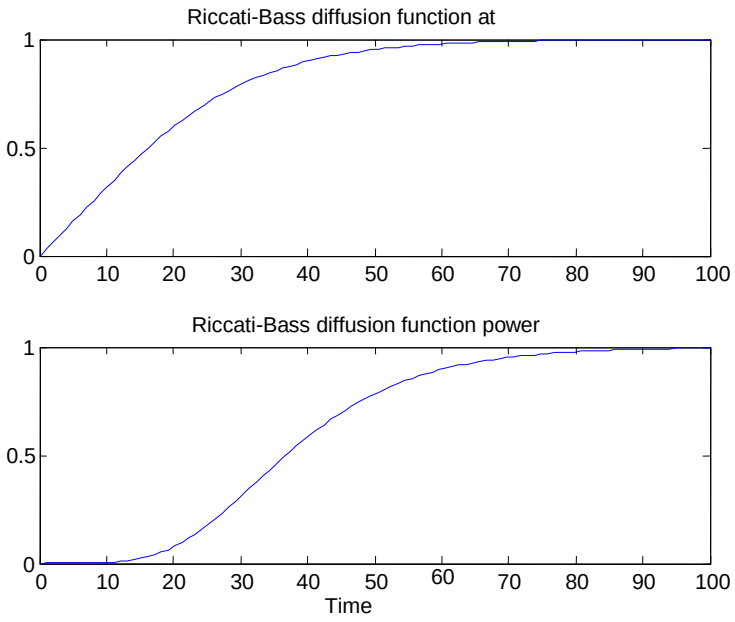

Figure A-15. Riccati-Bass diffusion function and associated power law with b=5.

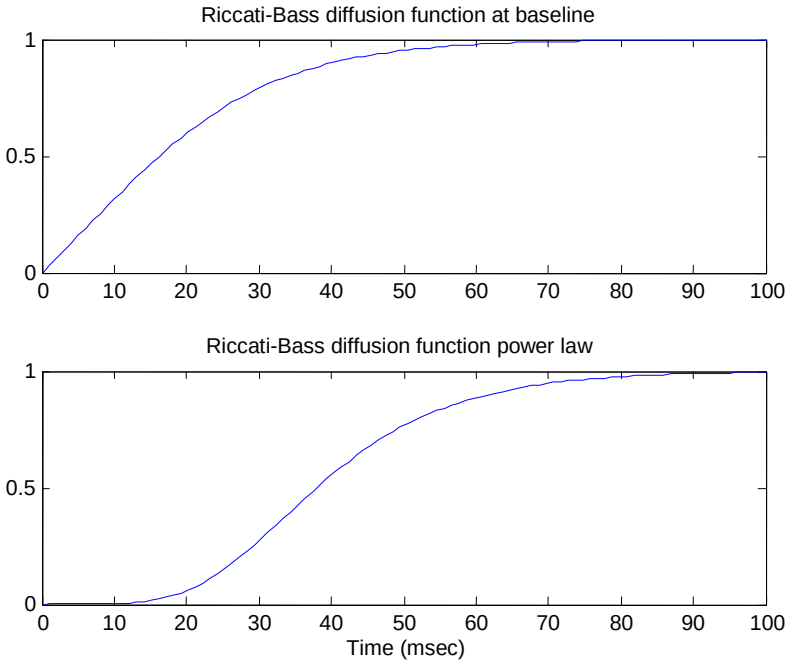

Figure A-16. Riccati-Bass diffusion function and associated power law with b=5.5.

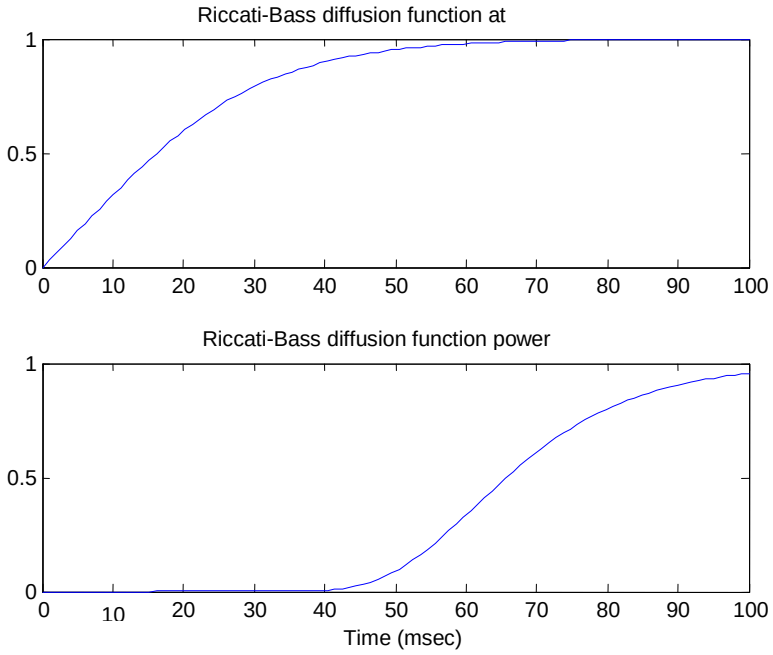

Figure A-17. Riccati-Bass diffusion function and associated power law with b=50.

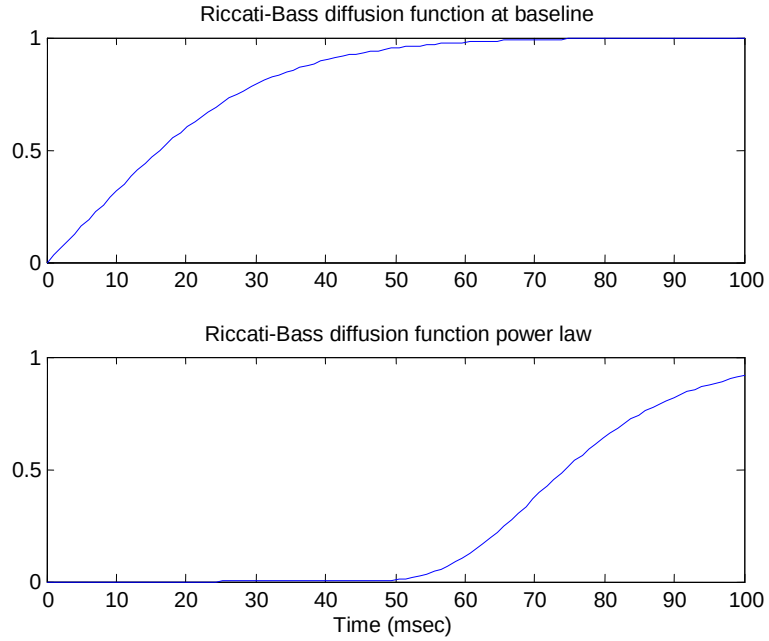

Figure A-18. Riccati-Bass diffusion function and associated power law with b=100.

The preceding analysis shows that power laws of Riccati-Bass functions are time-shifted sigmoids with increasing delay and inflection. To apply this finding to the R_0-k_m relationship, the optimal value of b had to be chosen such that the relationship remains nonlinear and the modeled delay in the calcium channels is minimized. For the Conaway fatigue model using the available data, a working value for b has been found to be in the range of 1.5-2 in repeated optimizations. Physiologically, this can be interpreted as increased delay in sensing strongly bound cross-bridges from the calcium current during fatigue in paralyzed muscle. As a result, the more-than-linear enhancement from additional pulses in a stimulus train is further decreased. This implies decreased force-generation of a muscle because the excess free calcium remains unbound.

A.2 Applications of the general Riccati equation

A.2.1 Biomedical applications of the general Riccati equation

There are many applications of the General Riccati Equation in biology and medicine. As will be seen, different processes behave according to the exact same dynamics, yet have different interpretations and implications. Various biomedical phenomena are discussed below.

A.2.1.1 The dose-response relationship

The dose (or exposure)-response relationship describes the change in effect on an organism caused by varying levels of exposure, known as doses, to a stressor. A stressor may be biologic, chemical, economic, electromagnetic, mechanical, thermal, or psychosocial. In individuals, this relationship may play

out such that a small amount of stressor has no detectable effect, whereas a large amount is fatal. In populations, this dynamic is seen by measuring the number of people affected at different stressor levels. Studying dose response dynamics is paramount to establishing "safe" and "hazardous" levels and dosages for pharmacologic agents, possible pollutants, and other stimuli to which human beings are exposed. The conclusions garnered from these studies are often used to set public policy. (67, 155)

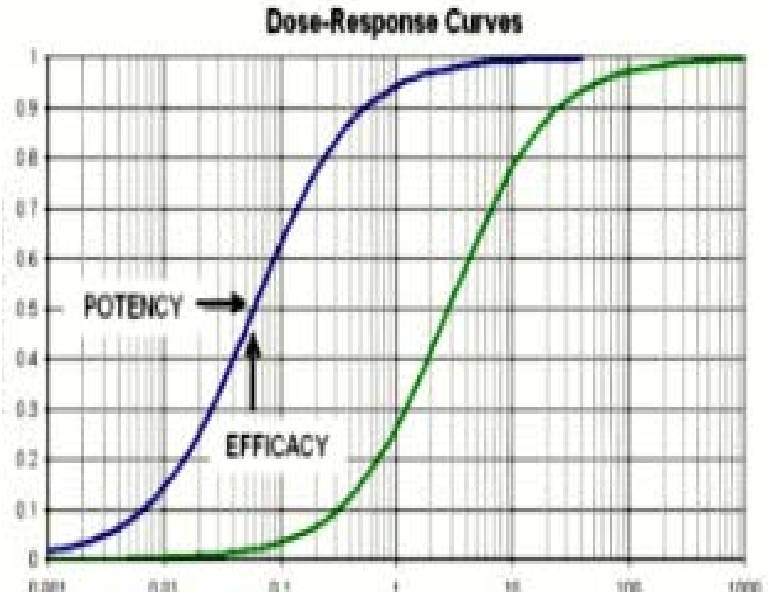

Figure A-19. Dose-response curves for two different stressors. Note that the potency/efficacy point changes as the curve shifts in the abscissa. (155)

A dose-response curve is a Cartesian graph depicting the relationship of the magnitude of a stressor, such as the amount of a drug or frequency of

electromagnetic stimulation, to the response of the organism. Usually, the measured response is mortality. However, other endpoints, such as efficacious blood concentration of a drug or muscle force from passive electrostimulation can be examined. The logarithm of the measured dose is commonly plotted as the abscissa and the response is plotted as the ordinate. As such, the curve is typically a sigmoid, with the middle part having the greatest slope. (67, 155)

The first nonzero response point on a dose-response curve is denoted as the threshold-dose. At increased doses, negative side effects appear and intensify. A stronger stressor makes a steeper curve. In quantitative cases, the ordinate is commonly scaled as percentage of users exhibiting a standard response, usually mortality. Evaluation of the dose-response relationship is central to toxicologists. There is a graded dose-response relationship in an individual. Meanwhile, the dose-response relationship in the population is quantal. Graded doses of a substance ingested by an individual usually result in a magnified response with increased dose. However, when the dose-response relationship is quantal, the population fraction affected goes up with increased dose. The relationship is quantal because the specified state is either absent or present in a given individual. This quantal dose-response phenomenon is used to calculate the median lethal dose (LD_{50}) of all chemicals that humans are exposed to. (101, 122, 144) As Paracelsus (148), sometimes called the father of toxicology, wrote:

> "Alle Ding sind Gift, und nichts ohne Gift; allein die Dosis macht, daß ein Ding kein Gift ist."

The maxim translates into English as

> "All things are poison and nothing is without poison, only the dose permits something not to be poisonous."

A.2.1.2 Epidemiologic models

In models of epidemics in a large population with many different individuals, diversity must be defined by several key qualifiers that are germane to the infection under consideration. For most common childhood diseases that confer long-lasting immunity, such as measles, mumps, and rubella, it common to partition the population into compartments. Known as the SIR model, standard convention defines these three compartments as S for susceptible, I for infectious, and R for recovered hence immune. The letters can also indicate the number in each compartment as a function of time. For a particular disease in a given population, these functions may be calculated to predict and control outbreaks. (5, 26)

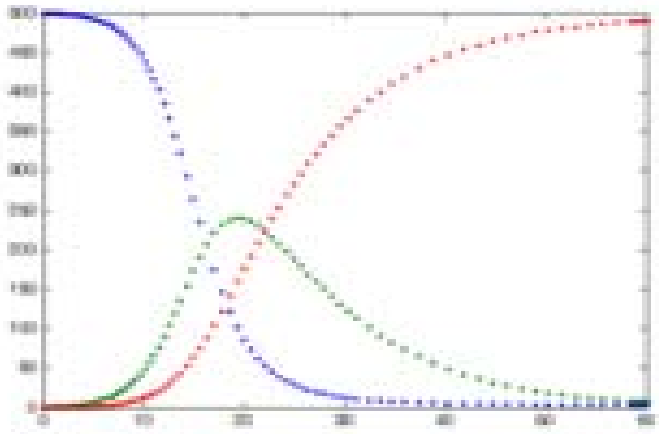

Figure A-20. SIR epidemic model. The epidemic stops when the number of susceptibles drops. Blue=Susceptible, Green=Infected, and Red=Recovered (26)

Since the numbers in each compartment may fluctuate over time, the model is taken to be dynamic. The quality is most remarkable in an endemic with a short infectious phase, such as measles or mumps prior to the availability of vaccination. (5) Such diseases tend to have cyclic patterns as S(t) varies over time. In an epidemic, the number of those susceptible decreases rapidly as infection transmits. Thus, infectious and recovered compartments fill up. As a result, the disease cannot be transmitted again until the babies born into the susceptible compartment reach a critical number. (26)

An outbreak of an epidemic is usually a far more rapid process than the vital population dynamics. Hence, to study the immediate costs of a single epidemic, the birth-death processes may be neglected. (26) Thus the SIR model can be expressed by a nonlinear system of differential equations given by:

$$\frac{dS}{dt} = -\beta IS \tag{A-21}$$

$$\frac{dI}{dt} = \beta IS - vI \tag{A-22}$$

$$\frac{dR}{dt} = vI \tag{A-23}$$

From the linear combination:

$$\frac{dS}{dt} + \frac{dI}{dt} + \frac{dR}{dt} = 0 \tag{A-24}$$

it follows that S(t)+I(t)+R(t)=N. Mathematically this expresses the constancy of population N and implies that the equation may be studied for only two of three variables. (26) Also, infectious disease dynamics depends on the following ratio:

$$R_0 = \frac{\beta}{v}. \tag{A-25}$$

This is known as the basic reproduction number. (5) The role of R_0 is extremely important in modeling epidemics of infection. Rewriting the differential equation for infectious individuals gives:

$$\frac{dI}{dt} = (\beta S - v)I. \tag{A-26}$$

Hence, if

$$R_0 > \frac{1}{S(0)} \tag{A-27}$$

then:

$$\frac{dI}{dt}(0) > 0 \tag{A-28}$$

therefore, with a baseline level of susceptibles, R_0, there will be a typical epidemic outbreak with an increase in infections. (5, 26)

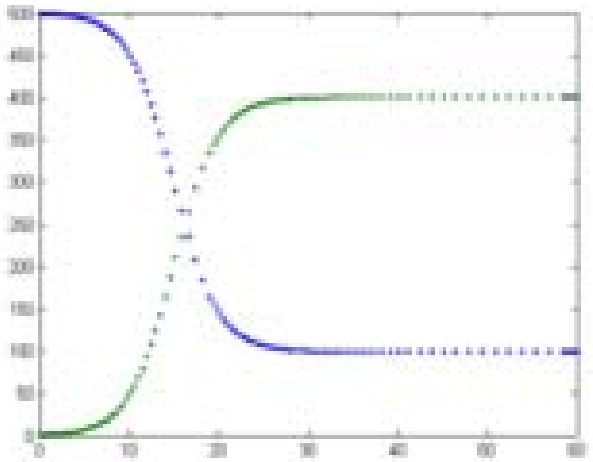

Figure A-21. SIS epidemic model. Susceptibles and infected equilibrate. (26)

However, some infections, such as the common cold, do not afford long-lasting immunity. These infections do not have a recovered state. Hence, individuals remain susceptible after infection. This is known as an SIS epidemic model. (5, 26) This gives the model:

$$\frac{dS}{dt} = -\beta SI + \gamma I \tag{A-29}$$

$$\frac{dI}{dt} = \beta SI - \gamma I \tag{A-30}$$

Denoting N to be the total population leads to:

$$\frac{dS}{dt} + \frac{dI}{dt} = 0 \Rightarrow S(t) + I(t) = N \,. \tag{A-31}$$

Hence, it follows that:

$$\frac{dI}{dt} = (\beta N - \gamma)I - \beta I^2 \,. \tag{A-32}$$

Thus, in an SIS system, the infection dynamics are governed by a Riccati (logistic) differential equation (5, 26), so that for all I(0) > 0,

$$\frac{\beta N}{\gamma} \le 1 \Rightarrow \lim_{t \to +\infty} I(t) = 0 \tag{A-33}$$

$$\frac{\beta N}{\gamma} > 1 \Rightarrow \lim_{t \to +\infty} I(t) = \frac{\beta N - \gamma}{\beta} \tag{A-34}$$

A.2.1.3 Biochemistry, physiology, and psychophysics

There are many oxygen-transporting proteins found in various species that have logistic dynamics. For example, in the muscle tissue of humans and other vertebrates, myoglobin gives muscle its distinct color of red or dark gray. However, it is a monomer that lacks the ability for cooperative binding. As a result, myoglobin stores oxygen rather than transports it. In addition, as the most common oxygen-transporting protein behind hemoglobin, hemocyanin is in the blood of many arthropods and molluscs. In place of iron heme groups this protein uses copper functional groups and is blue upon oxygenation. Finally, some marine invertebrates and annelids employs hemerythrin for oxygen transport. This Fe-containing non-heme protein is pink or violet when oxygenated and clear when deoxygenated. (112)

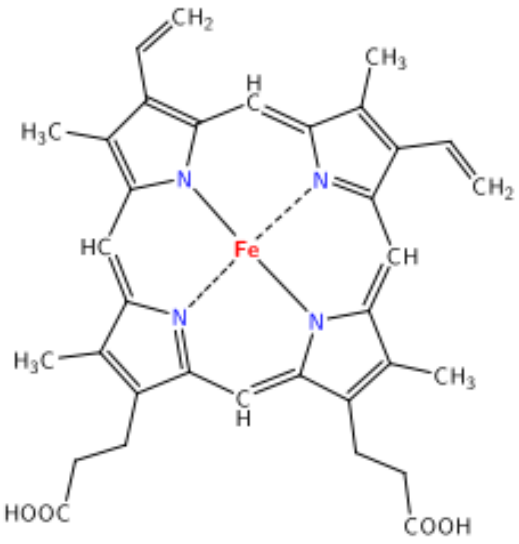

Figure A-22. Heme group. (73, 112)

Hemoglobin (Hb) is the iron-containing metalloprotein for oxygen transport in the red blood cells of vertebrates, including humans. The protein comprises about 97% of the mammalian red blood cell solid mass, and about 35% of the total mass. Hemoglobin transports oxygen from the lungs or gills to the body and releases the oxygen for cell consumption. (73, 112)

The typical adult human hemoglobin molecule is a structure of four globular protein subunits which are composed of a protein chain tightly associated with a heme group. Each protein chain arranges into a connected globin fold arrangement, which is the identical folding motif used in similar proteins such as myoglobin. This motif contains a heterocyclic ring in which the heme group is tightly bound. A heme group consists of an iron ion held in a porphyrin. The Fe ion is the site of oxygen binding and coordinates with the four coplanar nitrogen atoms in the center of the ring. In "end-on bent" geometry, one oxygen atom binds Fe and the other oxygen atom angles outward. In the absence of oxygen, a distorted octahedron is formed via a very weakly bonded water molecule which fills the site. The iron ion exists either as Fe^{2+} or Fe^{3+}. However, Fe^{3+} cannot bind to oxygen. Thus, Fe exists in the +2 oxidation state for oxygen binding. An enzyme reactivates Fe^{3+}-hemoglobin by reducing the iron center.Furthermore, in addition to the oxygen ligand which binds hemoglobin cooperatively, other ligands include competitive inhibitors such as carbon monoxide as well as allosteric ligands such as carbon dioxide. (73, 112)

In the normal adult tetrameric hemoglobin, oxygen binds in a cooperative process. The Hb-O binding affinity increases via the oxygen saturation of the

hemoglobin. The first oxygen bound modulating the binding site geometry for the next oxygen in a way conducive to binding. This is achieved through steric conformational changes of the hemoglobin protein complex. Thus, the oxygen binding curve of hemoglobin is sigmoidal, instead of the typical hyperbolic curve seen with noncooperative binding. Hence, the oxygen-binding capacity of Hb decreases in the presence of CO since it binds preferentially to the oxygen site. In similar fashion, hemoglobin also has competitive binding affinity for cyanide, sulfur monoxide, nitrogen dioxide, and hydrogen sulfide without changing the oxidation state of heme. Yet they suppress oxygen binding and cause grave toxicity. (73, 112)

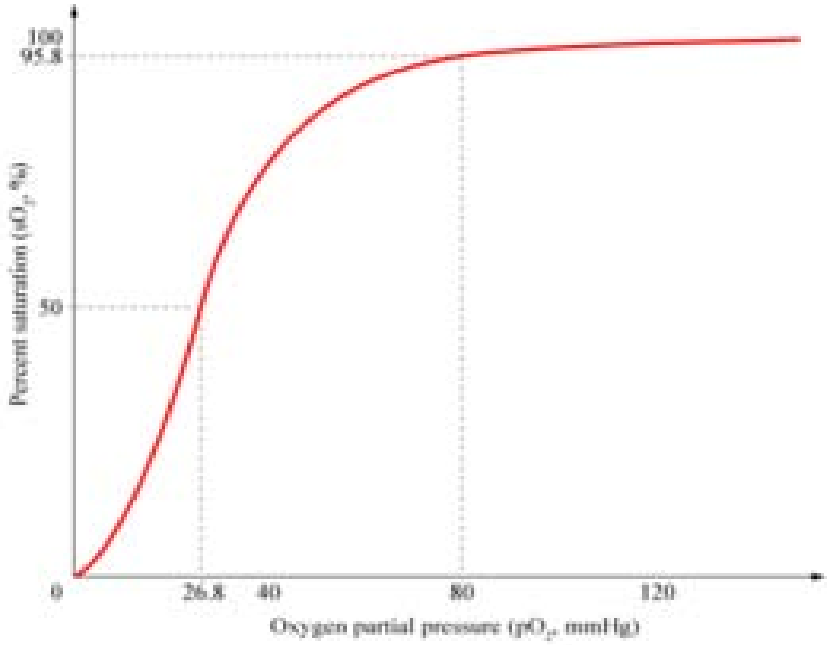

Figure A-23. Hemoglobin oxygen-dissociation curve. (73)

Carbon dioxide binds to a different site than the one for oxygen on the hemoglobin and dissolves more readily in deoxygenated blood. This facilitates its removal from the body through metabolism and ventilation via increased CO_2 affinity in venous blood. This is denoted as the Haldane effect. (73, 112) The enzyme carbonic anhydrase modulates this to give the following series of reactions.

$$CO_2+H_2O \rightarrow H_2CO_3 \rightarrow HCO_3^-+H^+$$

Thus, blood with more CO_2 is more acidic. Hemoglobin binds H^+ and carbon dioxide and changes protein conformation. This enables the release of oxygen. Hydrogen ions bind at various places along the protein. Meanwhile, CO_2 binds at the alpha-amino group of the Hb and forms carbamate. Decreased affinity of Hb for O_2 by the binding of bicarbonate and acid shifts the oxygen saturation curve rightward. Conversely, decreased carbon dioxide in the pulmonary capillaries releases CO_2 and protons from hemoglobin shifts the oxygen saturation curve leftward. (73, 112)

Characterization of the input-output properties of sensory neurons and their models is commonly done via frequency response functions. The response curves are most often sigmoidal and have two special points. The first point is the threshold below which the neuron does not respond, $r_{min.}$. Meanwhile, the second point is the signal level at which the response saturates, r_{max}. The range between threshold and saturation is known as the dynamic range D. By

convention, the dynamic range [r_{min}, r_{max}], is logarithmically transformed into the interval [0, 1]. (71, 110, 146)

The concept of "just noticeable difference" has been widely studied in psychophysics and is implicitly involved in understanding neuronal signal optimality. (71) From the response function, R(s), and the minimum detectable response change, Δs, the just noticeable difference in the signal, can be calculated. If the response curve is sigmoidal, it is seen that the signal varies along the dynamic range. Thus, the just noticeable differences in the signal are detected in the steepest part of the response curve. Hence, the optimal signal intensity is in that region. (110)

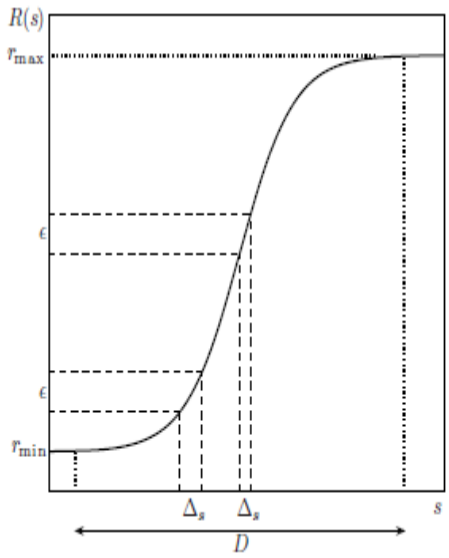

Figure A-24. A schematic example of a response function. The dynamic range D, threshold response r_{min} and maximal discharge r_{max} are illustrated. The size of the corresponding "just noticeable difference" in the signal, Δs, depends on the slope of the response function. It is smallest where the slope is highest. (110)

A psychometric function depicts the relationship between a parameter of a physical stimulus and the responses of a person to a certain quality of that stimulus. The psychometric function is usually sigmoidal. The percentage of correct responses is displayed on the ordinate with range 0 to 100% and the physical parameter on the abscissa. The inflection point of the sigmoid function or midpoint between the chance level and 100% is usually taken as sensory threshold. A common psychometric example is a hearing test with tones of different intensities and frequencies.

One vital sensory modality is nociception. Nociception is defined as "the neural processes of encoding and processing noxious stimuli." (1, 73, 97) It is the afferent activity elicited in the nervous system by stimuli that could damage tissue. This activity is initiated by nociceptors. Also known as pain receptors, nociceptors are able to detect changes in mechanical, thermal or chemical homeostasis above a physiologic threshold. Upon stimulation, a nociceptor transmits a signal along the neuraxis, and in aggregation, elicits a variety of autonomic responses may also include the somatosensory experience of pain in sentient beings. Nociceptors require a minimum level of stimuli to generate a signal in the spinal cord. In some pathological conditions, excitation of nociceptors increases as the noxious stimulus prolongs. This is known classically as hyperalgesia. (1, 73, 97)

Related to nociception is sensitization. Sensitization is an example of non-associative learning in which the progressive amplification of a response follows repeated administrations of a stimulus, such as when a person rubs her arm

continuously. After a while, this tonic stimulation will create a warm sensation that will eventually turn painful. The pain is the result of the progressively amplified synaptic response of the peripheral nerves warning the person that the repetitive stimulation is harmful. Sensitization is thought to facilitate learning, adaptive as well as maladaptive, in the organism. One specific type of sensitization is central sensitization. This is a process in which neurons of nociception in the dorsal horns of the spinal cord become sensitized by peripheral tissue pathology. Since it involves tissue damage and inflammation, this type of sensitization has been postulated as possibly having causality for chronic pain conditions. (1, 73, 97) This is represented graphically in Figure A-20 as a leftward shift in the classic sigmoidal curve of pain versus stimulus intensity.

Clinically, allodynia is a painful response to a typically non-painful stimulus and can be either static or dynamic. Unlike, referred pain, it is dysesthetic. There are different kinds or types of allodynia. Static mechanical allodynia is pain in response to light touch or pressure. Dynamic mechanical allodynia is pain in response to rubbing or brushing. Meanwhile, thermal allodynia is pain due to typically mild skin temperatures in the affected area. However, hyperalgesia is an increased sensitivity to noxious stimuli, which may be caused by damage to nociceptors or peripheral nerves, or temporarily, as a response to infection. Hyperalgesia can be experienced either focally or diffusely. However, psychophysiological studies of conditioning have established that it is possible to acquire a learned hyperalgesia of diffuse form. The focal form is typically associated with disease or injury and divided into two subtypes. Primary

hyperalgesia denotes pain sensitivity directly in the damaged tissues. Meanwhile, secondary hyperalgesia denotes pain sensitivity in the surrounding tissues that are not damaged. (1, 73, 97)

Hyperalgesia and allodynia are often symptoms of disease and may be evolutionary adaptations for enhanced protection of vulnerable tissues. Increased sensitivity for pain may, nevertheless, continue long after the noxious stimulus has disappeared. When that happens, pain exists as a disease in its own right. Changes of neural signal processing may contribute to hyperalgesia and allodynia, either solely or in part. However, sensitization of nociceptive nerve endings rarely outlasts the initial noxious stimulus. Rather, the sensitization is restricted to the area of injury or inflammation and is considered adaptive. (1, 73, 97)

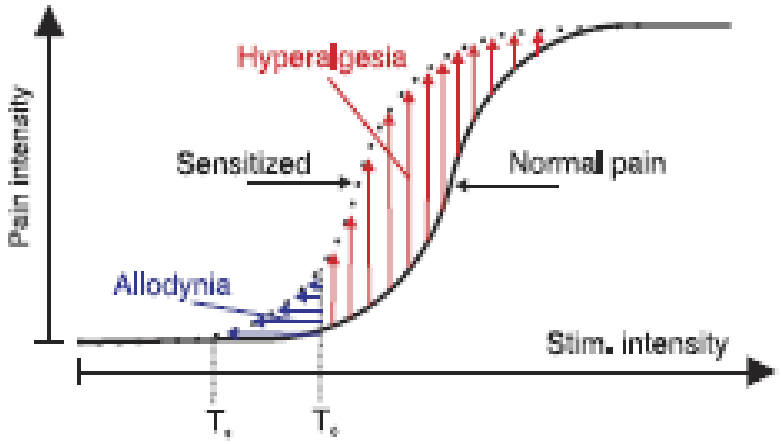

Figure A-25. Classical definitions of sensitization, hyperalgesia, and allodynia. (73, 97)

A.2.2 Applications of the general Riccati equation in engineering and physical science

As with biomedicine, the General Riccati Equation appears in various fields of physical science and engineering. The applications are diverse. However, the fundamental dynamics are identical. Several examples are discussed below.

A.2.2.1 Autocatalysis

In a system with time-varying physical conditions, certain constituent elements may have a transitory existence. Each element lasts just so long as its local conditions continue within certain limits. Although the ‘‘life period” of each individual element may be finite, an aggregate of a number of such elements may have a prolonged existence. They may even increase if the changes in the system state do not exceed certain limits, and that there is replacement. (116, 118, 119)

The kinetics of many biochemical and physiological processes may be considered as isothermal, isobaric mononuclear chemical reactions. Often, these reactions are autocatalytic (116, 118, 119):

$$A \leftrightarrows A' \qquad \text{(A-35)}$$

Consider a large number *n* as a time fraction of a total number N of molecules, such that all these *n* molecules have approximately the same age, then the differential decrease among these will be the same as for the aggregate. Thus, the equation of the reaction kinetics may generally have the form of first-order ordinary differential equations such as:

$$\frac{dP}{dt} = -kP \tag{A-36}$$

which is a first-order ordinary linear differential equation. Since the ages of the P_0' molecules originally present at time t=0 are generally unknown and can be neglected in calculation, equations may be derived which will calculate the derivative of aggregate formation asymptotically. (116, 118, 119)

The physical interpretation of these equations rests on the assumption that the condition of each molecule at a given instant varies incrementally from the mean state of all molecules of the aggregate. For every molecule of A, there will be a specific instant in time when the changes in state converge to a ‘‘limit of stability“. At that given instant, a molecule of A no longer exists and changes into a molecule of A'. The amount transformed from the aggregate A in a specific time unit depends on the characteristic of the “limit of stability” of the molecule A, and on the number of perturbations in the state of the aggregate. Variations in either of these factors will in turn determine how rapidly molecules are transformed from the original aggregate. (116, 118, 119)

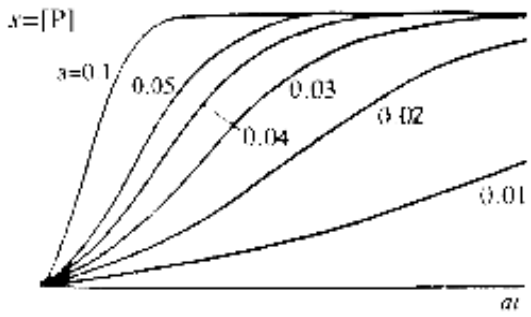

Figure A-26. Family of autocatalytic curves for different initial concentrations. An increase in reactant concentration accelerates the autocatalysis. (119)

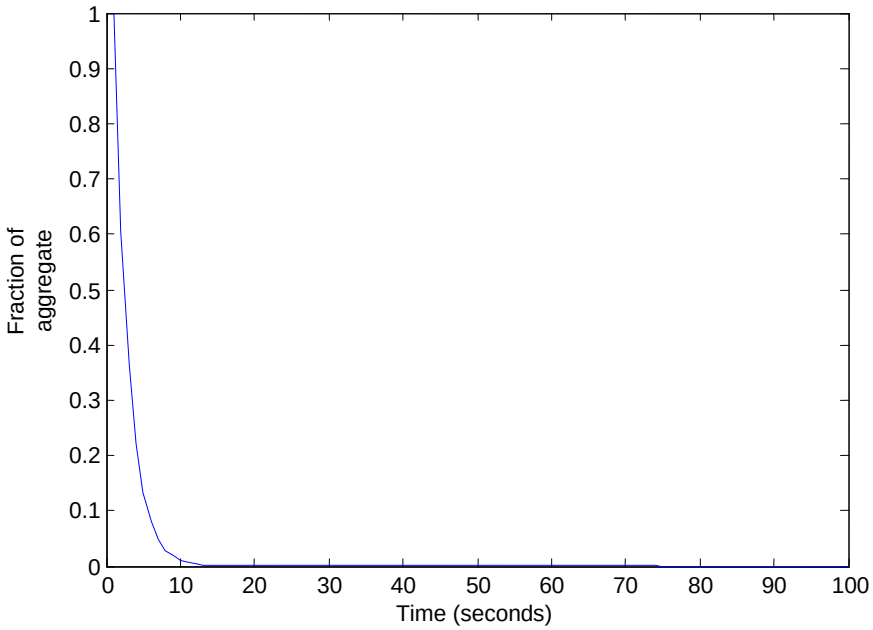

Figure A-27. Limit of stability for conversion of aggregate A to A' in an autocatalytic reaction.

A chemical reaction is said to be autocatalytic if the product of the reaction itself is its own catalyst. A set of chemical reactions are defined as "collectively autocatalytic" if several of those reactions produce catalysts for enough of the other reactions to be self-sustaining after initial energy input. (15, 117)

The second order autocatalytic reaction rate law $A + B \rightarrow 2B$ is $v = k[A][B]$.

The concentrations of A and B vary in time via the following functions:

$$[A] = \frac{[A]_0 + [B]_0}{1 + \frac{[B]_0}{[A]_0} e^{([A]_0 + [B]_0)kt}} \qquad \text{(A-37)}$$

and

$$[B] = \frac{[A]_0 + [B]_0}{1 + \frac{[A]_0}{[B]_0} e^{-([A]_0 + [B]_0)kt}} \qquad \text{(A-38)}$$

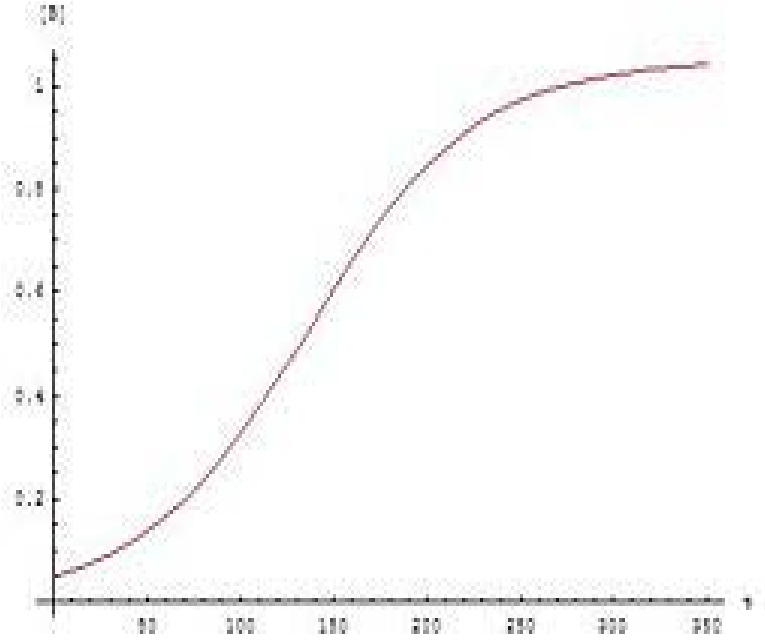

Figure A-28. Variation of product concentration as a function of time in an autocatalytic reaction. (117, 193)

The typical dynamics for autocatalytic reactions is sigmoidal. These reactions initiate slowly due to little catalyst present. As the reaction rate increases, the reaction occurs with increased catalyst. It slows down as the reactant amounts decrease. If the concentration of a reagent varies sigmoidally, the reaction is generally autocatalytic. (15, 117) In addition to clock reactions (117, 193), examples of autocatalytic reactions include the spontaneous degradation of aspirin into salicylic acid and acetic acid.

A.2.2.2 The Kalman filter and recursive Bayesian estimation

Kalman filters are assumed to be Markov chains built on linear operators perturbed by white noise. The system state is represented as a real number vector. At each discrete time step, a linear operator is applied to generate the next state with some noise mixed in. Information from the controls laws may be included if known. After this, an additional noisy linear operator generates the observable outputs from a hidden state. (96)

To use a Kalman filter for internal state estimation of a process based on a sequence of noisy observations, the process must be modeled according to the constraints of the filter. Hence, the matrices $\mathbf{F_k}$, $\mathbf{H_k}$, $\mathbf{Q_k}$, $\mathbf{R_k}$, and sometimes $\mathbf{B_[}$ must be specified for each time-step k as shown below. (96)

The Kalman filter is unusual in being a pure time domain filter. Most filters, such as a low-pass filter, are frequency domain operators which are transformed to the time domain to be implemented. In a Kalman filter, the true state is taken as an unobservable Markov process. Hence, the observed states of the hidden Markov model are the measurements. (96)

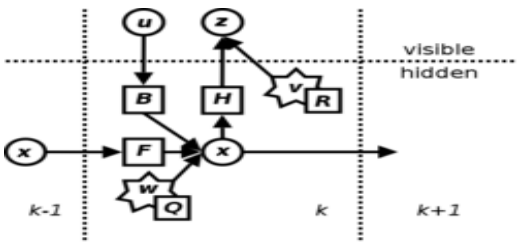

Figure A-29. Model underlying the Kalman filter. Circles are vectors, squares are matrices, and stars represent white noise. (96)

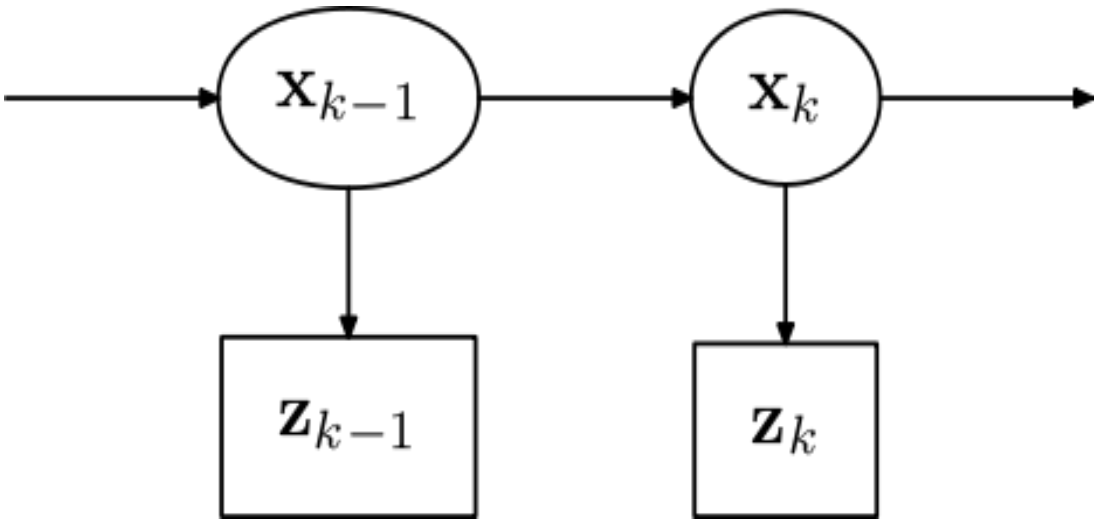

Figure A-30. Markov process with **X** as visible measurements and **Z** as hidden state. (91)

Because of the Markov assumption, the true state is conditionally independent of all earlier states given the immediately previous state.

$$p(x_k \mid x_0, \ldots, x_{k-1}) = p(x_k \mid x_{k-1}) . \quad \text{(A-39)}$$

Likewise the measurement at the k_{th} time step depends only upon the current state. It is conditionally independent of all other states.

$$p(z_k \mid x_0, \ldots, x_k) = p(z_k \mid x_k) . \quad \text{(A-40)}$$

Hence, the probability distribution over all states of the hidden Markov model is given by:

$$p(x_0, \ldots, x_k, z_1, \ldots, z_k) = p(x_0) \prod_{i=1}^{k} p(z_i | x_i) p(x_i | x_{i-1}) . \quad \text{(A-41)}$$

This is also known as recursive Bayesian estimation. (96)

A.2.2.3 Optimal control

Widely used in control theory and control systems engineering, the Kalman filter is a recursive estimator that models the state of a dynamic system from a set of measurements with noise. It solves the linear-quadratic-Gaussian control problem (LQG). Solution is achieved in conjunction with the linear quadratic regulator (LQR). These three tools generally solve the most fundamental problems in control theory. An example would be radar or computer vision. Such applications provide accurate information about the position and velocity of an object, which is continuously updated, from erroneous observations about its location. (96)

Related to Kalman filtering and recursive Bayesian estimation, optimal control addresses the problem of determining a control law for a given system under certain constraints of optimality. An optimal control problem is comprised of a cost functional that depends on state and control variables. As a set of differential equations that describe the control variable trajectories that minimize the cost functional, the optimal control law can be derived from either the necessary condition of the Pontryagin maximum principle, or by solving the sufficient-condition Hamilton-Jacobi-Bellman equation. (23)

Optimal control problems are solved in the following abstract way. The continuous-time cost functional is minimized by

$$J = \Phi(x(t_0), t_0, x(t_f), t_f) + \int_0^{t_f} \mathcal{L}(x(t), u(t), t) dt \quad \text{(A-42)}$$

subject to the first-order differential constraints

$$\dot{x}(t) = \mathrm{a}(x(t), u(t), t), \tag{A-43}$$

the algebraic path constraints

$$b(x(t), u(t), t) \leq 0, \tag{A-44}$$

and the boundary conditions

$$\phi(x(t_0), t_0, x(t_f), t_f) \tag{A-45}$$

where $\mathbf{x}(t)$ is the state, $\mathbf{u}(t)$ is the control, time t is the independent variable, t_0 is the initial time, and t_f is the terminal time. The terms Φ and $\mathcal{L}$ are denoted as the endpoint cost and Lagrangian, respectively. The path constraints are in general inequalities and thus may not be equal to zero at optimal solution. This implies that an optimal control problem with the above formulation may have multiple solutions. (23)

A special case of the general nonlinear optimal control problem solved by Kalman is the linear quadratic (LQ) optimal control problem. The LQ problem is solved as follows. The quadratic continuous-time cost functional

$$J = \frac{1}{2} x^T(t_f) S_f x(t_f) + \frac{1}{2} \int_{t_0}^{t_f} (x^T(t) Q(t) x(t) + u^T(t) R(t) u(t)) d\, t \tag{A-46}$$

is minimized subject to the linear first-order differential constraints

$$\dot{x}(t) = A(t)x(t) + B(t)u(t), \tag{A=47}$$

and the initial condition

$$x(t_0) = x_0 \,. \tag{A-48}$$

A particular form of the LQ problem that arises in many control system problems is that of the linear quadratic regulator (LQR) where matrices are zero, t_0 is 0, and t_f is ∞. (23) The LQR problem is formulated as follows. The infinite horizon quadratic continuous-time cost functional

$$J = \frac{1}{2}\int_0^{\infty} (\mathrm{x}^T(t)\mathrm{Q}\mathrm{x}(t) + \mathrm{u}^T(t)\mathrm{R}\mathrm{u}(t))dt \tag{A-49}$$

is minimized subject to the linear time-invariant first-order differential constraints

$$\dot{x}(t) = \mathrm{A}\mathrm{x}(t) + \mathrm{B}\mathrm{u}(t), \tag{A-50}$$

and the initial condition

$$x(t_0) = x_0 \,. \tag{A-51}$$

It has been shown in classical optimal control theory that the LQ optimal control law has the feedback equation

$$\mathrm{u}(t) = -\mathrm{K}(t)\mathrm{x}(t) \tag{A-52}$$

where $\mathbf{K}(t)$ is a properly dimensioned matrix, given as

$$\mathrm{K}(t) = \mathrm{B}\mathrm{R}^{-1}\mathrm{B}^T\mathrm{S}, \tag{A-53}$$

and $\mathbf{S}$ is the solution of the matrix differential Riccati equation. (23) The matrix differential Riccati equation is given as

$$\dot{\mathrm{S}} = -\mathrm{S}\mathrm{A} - \mathrm{A}^T\mathrm{S} + \mathrm{S}\mathrm{B}\mathrm{R}^{-1}\mathrm{B}^T\mathrm{S} - \mathrm{Q}\,. \tag{A-54}$$

For the finite horizon LQ problem, the Riccati equation is integrated backward in time using the terminal boundary condition $\mathbf{S}(t_f) = \mathbf{S}_f$. However, in the LQR problem, the differential Riccati equation is replaced with the algebraic Riccati equation which is

$$0 = -\mathrm{SA} - \mathrm{A}^T\mathrm{S} + \mathrm{SBR}^{-1}\mathrm{B}^T\mathrm{S} - \mathrm{Q}. \qquad \text{(A-55)}$$

Since the algebraic Riccati equation comes up in infinite horizon problem, the matrices $\mathbf{A}$, $\mathbf{B}$, $\mathbf{Q}$, and $\mathbf{R}$ are all constant. The positive definite or positive semidefinite solution of the ARE is used to compute the feedback gain. (23)

A bang-bang controller switches suddenly between binary states and may be realized in any situation with hysteresis, such as a furnace, and arise in optimal control problems. In discrete form, the Heaviside step function is an example of bang-bang control. (103)

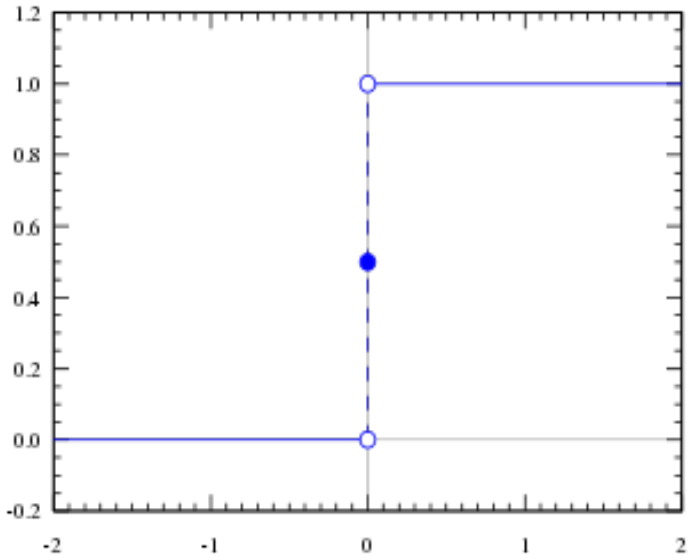

Figure A-31. Heaviside step function.

A smooth approximation of the Heaviside step function is the logistic function:

$$H(x) \approx \frac{1}{2} + \frac{1}{2}\tanh(kx) = \frac{1}{1+\mathrm{e}^{-2kx}} \tag{A-56}$$

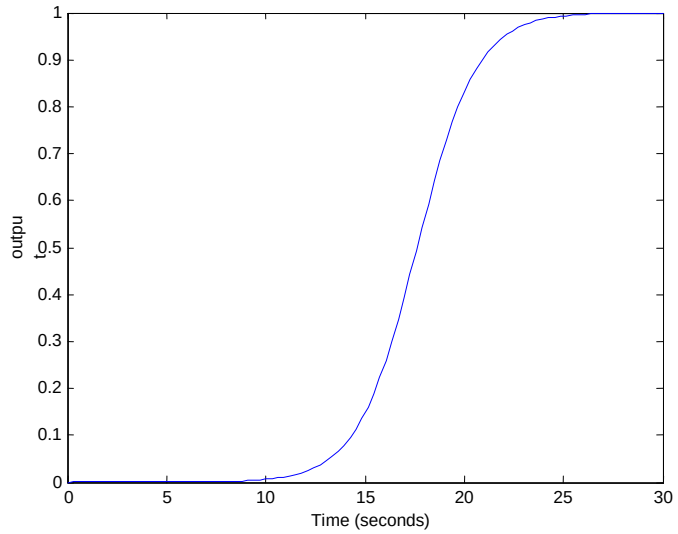

Figure A-32. Smooth approximation to Heaviside step function.

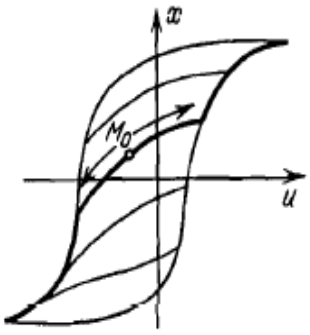

Figure A-33. Set of trajectories in a costate vector in an optimal control scheme. (103)

A.2.3 Socioeconomic applications of the general Riccati equation

One of the most popular uses of the Riccati differential equation and its subcases is in socioeconomic modeling. The problems addressed range from natural resource demand forecasting to modeling world population growth. Several applications are discussed sequentially.

A.2.3.1 Models of population growth

The Malthusian growth model, or the simple exponential growth model, is a model exponential growth based on a constant rate of compound interest, $P=P_0e^{rt}$. The model is named after the Reverend Thomas Malthus. He wrote An Essay on the Principle of Population (124), one of the seminal books on population biology. In the Essay, Malthus bases his entire argument on the following mathematical assumptions:

> "Assuming then my postulata as granted, I say, that the power of population is indefinitely greater than the power in the earth to produce subsistence for man."
>
> "Population, when unchecked, increases in a geometrical ratio. Subsistence increases only in an arithmetical ratio. A slight acquaintance with numbers will shew the immensity of the first power in comparison of the second."

This model is often referred to as The Exponential Law and is widely considered in population ecology as the first principle of population dynamics. At best, it can be described as an approximate physical law as it is generally known that nothing can grow at a constant rate as time goes to infinity (177). Philosopher Antony Flew, in his introduction of the Essay, noted a "certain limited

resemblance" between Malthus' law of population and Newtonian mechanics (119).

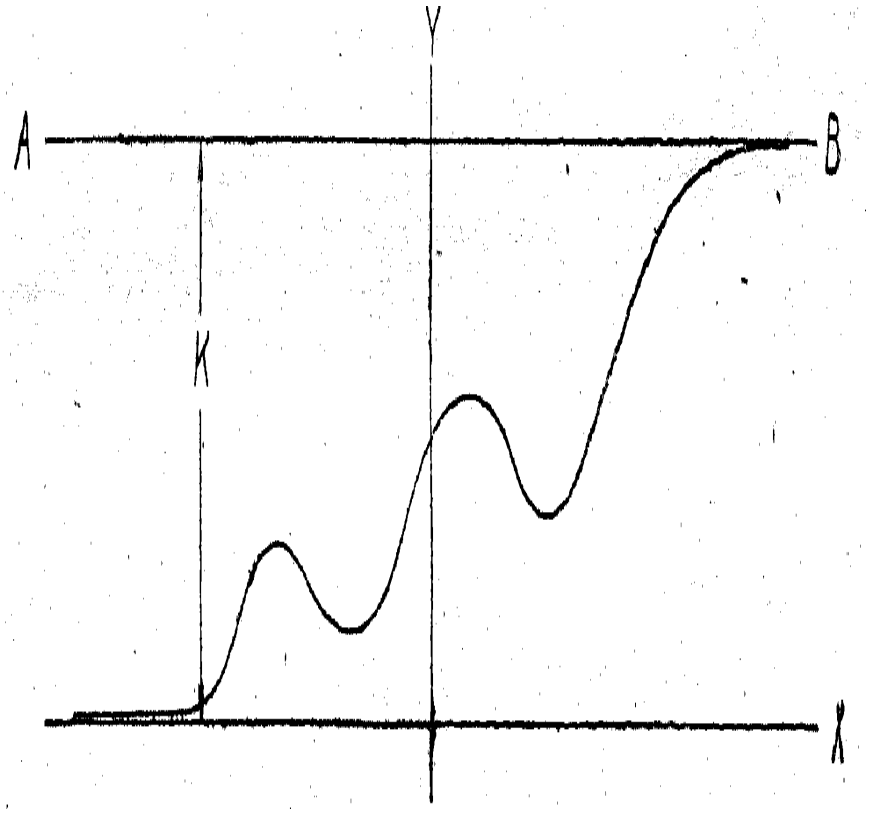

Figure A-34. General curve of population growth. (117, 122, 150)

Specifically for biological populations, the variable X tends to increase from one generation to the next when it is small. It tends to decrease when it is large. Hence, the nonlinear function F(X) frequently has the following properties. The initial value is 0. F(X) is monotonically increasing through the range 0 to A and attains its maximum value at X=A and monotonically decreasing as X increases

past X=A. In addition, F(X) will generally contain one or several parameters of phenomenological significance that modulate the nonlinear characteristics. (127)

A.2.3.2 Other economic and social behavior

Socioeconomic applications of the Riccati or logistic equation include models for the relationship between quantity and price, for theories of business cycles, and for the temporal sequences described by many other economic indices. The general difference or differential equation is also applicable to the social sciences. For example, in learning theory, X may be the number of bits of information that can be remembered after an interval *i*. Or, in the spread of rumors in societies of varying forms, X can be the count of people who have heard the rumor after time t. (127)

Another socioeconomic application of the Riccati equation was presented when Bass (10) published "A new product growth for model consumer durables" in 1969. Prior work described the different phases of new product adoption. The rapid, recent growth in online social networks has led to an increased use of the Bass diffusion model, which estimates the size and rate of growth of these social networks. It is also used is forecasting demand for natural resources. (147)

From a purely empirical perspective, according to Lekvall and Wahlbin (113), most real-world growth curves typically have an asymmetric S-shape with a longer upper shank of the *"S"*. As another variant of the logistic equation, the Gompertz function generates such a diffusion curve with right skew. This function may be written in the following form: $y(t)=N(a^b)^t$. As shown below, the right skew arises from inflection point below N/2 on the curve. (70, 113)

Applications of Gompertz curves include annuity projections (70). These are processes where costs are initially high with slow uptake, followed by a period of rapid growth, followed by a decreased uptake as saturation occurs. In addition, the curves are used to model population in a confined space with limited resources.

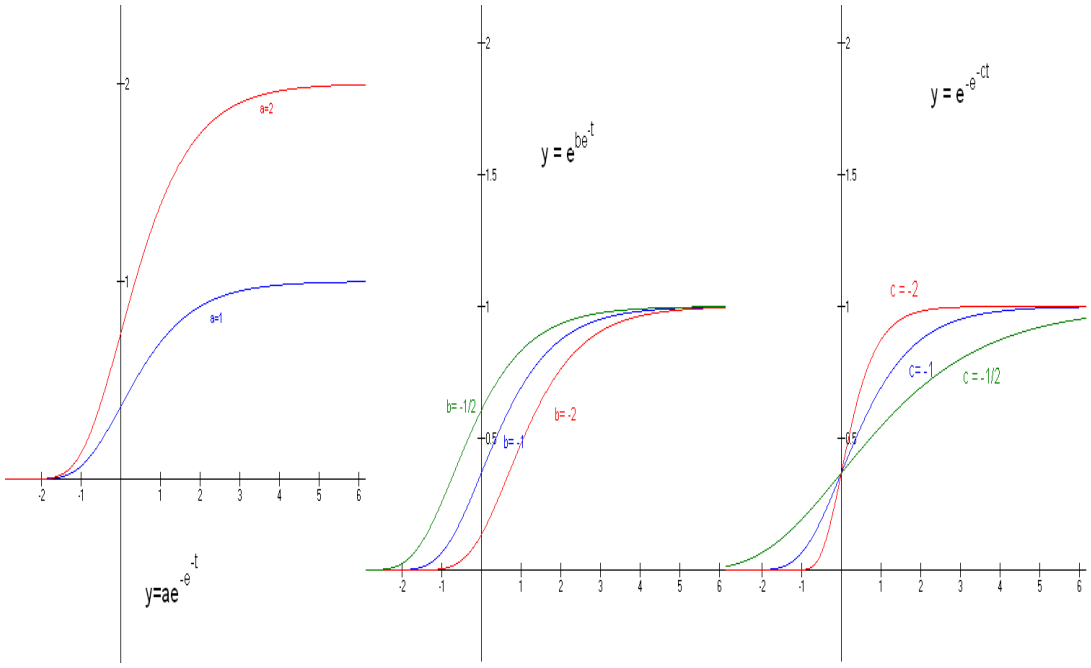

Figure A-35. Gompertz curves. (70)

A.3 Implications

The apparent ubiquity of the Riccati equation in all areas of science has many implications about how the Universe works as well as how science and technology should be conducted by society. A few salient points are given for contemplation in the section. By consideration of these arguments a paradigm

shift that enables more accurate science and more reliable technology may be initiated by many.

A.3.1 Towards a paradigm based on fundamental laws

After Riccati, the equation was studied by many others such as Euler and Liouville. However, the equation did not achieve paramount importance until the twentieth century, when the fields of calculus of variations and optimal control were being developed. Calculus of variations traces its origins to Fermat's principle of least time. However, the bellwether problem was the celebrated brachistochrone problem of the shortest distance along a curve that was stated by Galileo and solved by John Bernoulli. Upon solution of that problem, many other variational problems were studied in succeeding centuries. The problems have spanned from calculating cycloidal motion to determining nautical paths in stationary ocean currents. (16)

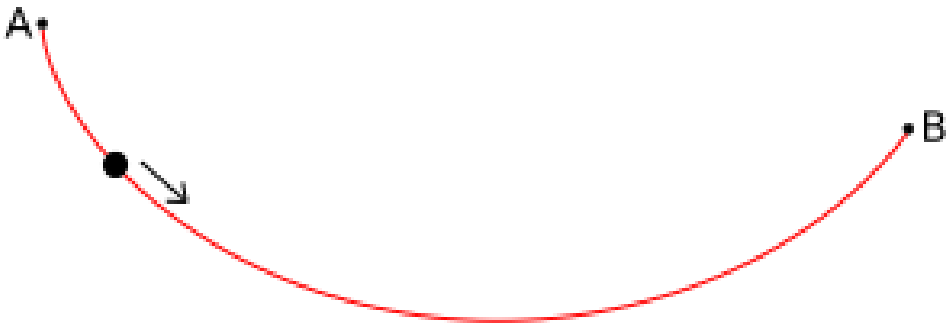

Figure A-36. A brachistochrone is the shortest distance along a curve. (16)

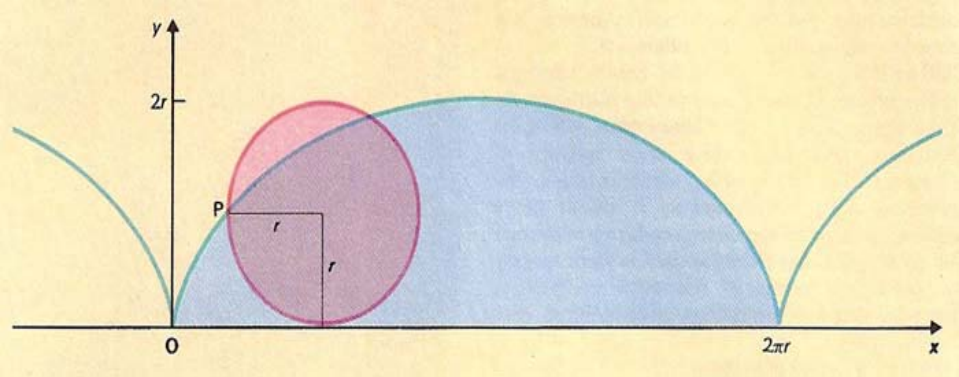

Figure A-37. The cycloid (blue) and its generating circle (red). (16)

As the calculus of variations primarily developed in the first half of the twentieth century, optimal filtering and control gained prominence with the work of Kalman during the 1960s. The fundamental problem in this field is a functional optimization problem as well. However, the novelty was the presence of exogenous variables which affects the dynamics of state-space phenomena. Because the model was so generalizing, plants, devices, and processes no longer needed conceptual distinction and just became known as “a system”. Hence, all the physicality was relegated primarily to the preliminary phases of modeling. It has been noted that the independent variable in variational calculus is usually spatial, whereas the independent variable of optimal control is temporal. (16)

According to Banks (9), the mathematical frameworks that underlie growth/diffusion phenomena are based on relatively few concepts. In addition to the models of Malthus and Verhulst, Fick established a principle that the diffusion rate of a solute in a liquid depends on the spatial gradient of the concentration of

the solute. Nevertheless, the Gompertz (70) and Verhulst (179, 180) equations are generalizations of the 1798 Malthus principle. Hence, there are many models of growth, transfer, and diffusion processes that derive from the Riccati equation. According to Banks (9):

> "It is abundantly clear that advances in growth-transfer-diffusion phenomena are being made at an increasing pace by a growing number of people in many disciplines. By whatever set of indices we might use to measure the growth such activity of progress, it seems safe to say that we have not yet arrived at an inflection point of the growth curve of this activity."

The logistic equation, as a special case of the Riccati equation when P(x)=0, was first put forth by PF. Verhulst (180) in 1838 upon reading Malthus' essay. Verhulst derived the logistic equation to describe the asymptotic growth of a biological population based on the work of his mentor, Adolphe Quetelet. (99) In 1835, Quetelet proposed that the resistance to the growth of a population varied proportionally to the square of the speed of its increase. With that principle, a direct physical analogy could be drawn to the resistance that a medium exerts on a body travelling through it (156). Verhulst began by assuming that in early stages of growth, a population would increase exponentially until crucial resources, such as food, became limiting. He called the population existing at that moment the “normal” population. The excess was called the “superabundant” population. Reasoning that the growth rate was resisted by some function linearly proportional to the excess population, Verhulst derived the differential equation for a symmetrical sigmoidal growth curve which was denoted as “logistic” (178). However, the argument was incongruent to the mathematics

of his derivation of the curve. The logistic curve does not follow from the assumption that growth varies discontinuously from an exponential rate to a slower one at some critical value. Yet, Verhulst realized that the logistic was only one of many alternatives. (99)

Verhulst never explained his choice of the term “logistique” for his curve. However, in the nineteenth century, the French word was used to indicate the art of calculation distinct from the theory of proportion. The word was generally applied to a type of logarithm for astronomical calculations. It is suggested that Verhulst meant for this term to convey the idea of a calculating device that could determine the saturation level of a population and the time when that value would be reached. (94)

Well before Verhulst, according to Doctorow (57), Bernoulli and Riccati had already noticed together that exponentials played a seminal role in the Bernoulli-Riccati class of differential equations and in the exponential expansion-decay equation and in their applications to mathematical physics and mathematical biology. For reasons unknown, they did not realize it as being a new kind of "information/entropy" which is descriptive of growth-expansion-contraction. The most likely reason for this "non-history" of the exponential in the knowledge base was the fact that the Bernoulli, Riccati, logistic, and exponential growth equations are first-order differential equations. Meanwhile, the exponential function usually solves or simplifies higher order linear differential equations.

Doctorow (57) argues that expansion-contraction-growth equations differ fundamentally from curvilinear motion equations both mathematically and

materially. Curvilinear motion is "in one direction at a time," although the direction can be time-varying. Meanwhile, expansion-contraction-growth can involve infinitely many simultaneous motions in different directions. These myriad motions frequently occur with varying degrees or magnitudes and at times with global control. Thus, the failure to distinguish between two types of "information", logarithmic and exponential, was paralleled by a failure to distinguish between two types of motion, expansion-contraction and curvilinear. Most of contemporary science and engineering has been concerned with the curvilinear motion.

The question to be contemplated is whether expansion-contraction can approximate curvilinear motion when the former is far more rapid in one direction or a small angle than in others. Since the expansion-contraction equations and their solutions are simple, finding theorems for these approximations could simplify the study of curvilinear motion. As a suggested starting point, the Riccati equation $y'=A+By+Cy^2$ where A, B, C are functions of t could be compared with a second order linear differential equation with variable coefficients $A(t)y''+B(t)y'+C(t)y=E(t)$ for E(t) a function of t. (57)

A.3.2 A cursory argument to the sublime

It has been observed that the General Riccati Equation is rather ubiquitous in all areas of science. Its apparent ubiquity has many implications for the understanding the way the Universe is constructed at the most fundamental level. The answers would involve philosophical inquiry as well as scientific experimentation. Extending the earlier parallel of the logistic equation with

Newtonian mechanics, the Riccati equation may be thought of as a principle that belongs to the variational framework of science as established by Lagrange and Hamilton.

Since a special case of the Riccati equation generates the dose-response curves, it is argued from the literature that all therapeutic interventions, regardless of form or modality, are dose-response phenomena. Furthermore, it is at best inappropriate to assume that physiologic processes behave under Newtonian curvilinear constraints since chemical reactions occur omnidirectionally in any given space. Thus, considering and elucidating the fundamental construct of the dose-response relationship in rehabilitation research by extending this powerful equation to different clinical problems and associated models is of great societal importance and urgency. Through that effort, public health and well-being may be better maintained and protected as appropriate and safe doses of any given intervention may be determined.

APPENDIX B: SPINAL CORD INJURY

Spinal cord injury (SCI) due to trauma is an uncommon condition. However, it has a profound effect on personal functional, medical, financial, and psycho- social well-being upon injury. The most common causes of SCI are motor vehicle accidents, falls, violence, and sports injuries. Other causes of SCI include vascular disorders, tumors, infections, spondylosis, iatrogenic injuries from spinal injections and epidural catheter placement, osteoporotic vertebral fractures, and developmental disorders. (43, 44)

The incidence of traumatic SCI in the United States is 30-60 new cases per million population, or 10,000 cases per year in the United States. (43) Estimates of prevalence vary from approximately 183,000 to 230,000 cases in the United States, the equivalent of 700-900 cases per million population. (43) Overall incidence among Caucasians is higher than among African Americans, which is higher than among Hispanics. (43, 45, 105) Current studies indicate Caucasians at 66.4%, African Americans at 21.1%, Hispanics at 8.8%, Asians at 1.6%, Native Americans at 1.1%, and others at 1%. (45, 108) The male-to-female ratio of individuals with SCI in the United States is 4:1. (44, 105) More than 50% of all cases of SCI occur in persons aged 16-30 years. The median age is 26.4 years, while the mean age is 31.8 years and the mode age at injury is 19 years. (44, 105) Traumatic SCI is more common in persons younger than 40 years, while nontraumatic SCI is more common in persons older than 40 years. (45, 104, 105) Greater mortality is reported in the older patients with SCI. (104, 105)

In a recent study on pediatric SCI using information from the Kids' Inpatient Database (KID) and the National Trauma Database (NTDB), significant differences in the yearly incidence rate of pediatric SCI were shown between patient groups stratified by race and sex. (183) African Americans show a significantly higher rate of pediatric SCI (1.53 cases per 100,000 children) than Native Americans (1.0 case per 100,000 children), and Hispanics (0.87 case per 100,000 children). Meanwhile, Asians show a substantially lower incidence than all other racial groups (0.36per 100,000 children). Also, boys (2.79 cases per 100,000 children) are over twice as likely to sustain SCI as girls (1.15 cases per 100,000 children). The aggregate incidence of SCI under the age of 18 in the United States is 1.99 cases per 100,000 children. It is estimated that 1455 children are admitted to US hospitals each year for treatment of SCI.

In the KID/NTDB study (183), the etiology of pediatric SCI was also investigated. The major causal factors were identified to be motor vehicle accident, accidental fall, firearm injury, and sports injury. Of those children injured in a motor vehicle accident, 67.7% were reported as not wearing a seatbelt. Alcohol and drugs was found to be involved in 30% of all pediatric SCI cases. (175)

Other injuries are often associated with traumatic SCI. These include bone fractures, coma, and traumatic brain injury affecting psychoemotional functioning From the perspective of the ASIA classification, injuries statistically occur according to the following pattern: incomplete quadriplegia - 29.5%, complete paraplegia - 27.9%, incomplete paraplegia - 21.3%, and complete

quadriplegia - 18.5% In quadriplegia, the most frequent level of neurologic injury is C5. In paraplegia, T12 is the general level of neurologic injury. (104, 105, 108)

Concomitant injuries are frequent in traumatic spinal cord injury (SCI). Brain injury and pulmonary dysfunction are common causes of the acute deaths in traumatic SCI. This is the reason that complete quadriplegia has a remarkable ratio of early cases to fatalities. However, late deaths in SCI primarily result from complications associated with neurogenic bladder. Upon receiving care in comprehensive spinal cord injury centers, over eighty percent of patients with traumatic SCI will live ten years with an average of almost 18 years. Median post-injury life may be almost 14 years for complete quadriplegia, 17 for complete paraplegia, 19 for incomplete quadriplegia, and 20 for incomplete paraplegia. The prevalence of traumatic SCI is approximately 50 per 100,000 with complete paralysis seen in approximately 20 per 100,000. Nevertheless, eighty percent of survivors of traumatic SCI live independently and obtain gainful employment after rehabilitation. (108)

APPENDIX C: HISTORY OF ELECTRICITY IN MEDICINE

According to DeVahl (42), the earliest known use of electrical stimulation in medicine was described by Hippocrates in about 420 B.C. who prescribed use of the torpedo fish. It is a species which has special organs that produce an electric discharge to shock its prey. Hippocrates recommended that it be boiled and included as part of breakfast for asthmatics. Several hundred years later, the properties of the torpedo fish were used by Scribonius Largus, a Roman physician, in 46 A.D. to treat painful conditions. Placing the fish over the painful body part was recommended for gout and headache.

Nevertheless, the torpedo fish was not a practical way to apply electrical stimulation. It was only when electricity could be reliably generated and stored that this type of treatment could be used on a regular basis. The Leyden jar, invented in 1745, is a glass jar that is coated with metal foil on inner and outer surfaces and is able to consistently generate and store static electricity. The earliest documented therapeutic treatment using this type of machine goes back to 1744 in Germany. C.G. Kratzenstein purported to have restored function to a paralyzed small finger of a female patient by applying electricity for less than fifteen minutes. Subsequent claims include Benjamin Franklin using electricity to cure a young woman suffering from seizures. Nevertheless, in the 18th century, other electrotherapeutic applications included treatment for kidney stones, sciatica, and chest pains. (42, 157)

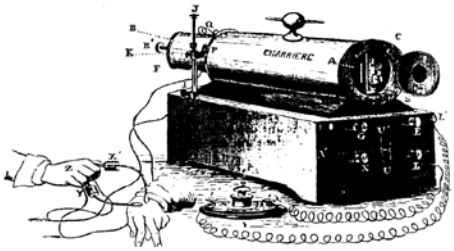

Figure C-1. Duchenne stimulator. (42)

In the late eighteenth century, Luigi Galvani and Alessandro Volta experimented with the effects of electricity on animal muscle and nerve. Galvani theorized that muscle had innate “animal electricity” (1, 42, 157). However, Volta credited the origin of electricity to the metal rod used in the experiment, rather than the muscle of the animal. Progress in electricity-generating technology and animal experimentation carried forward in the nineteenth century. In 1831, Faraday invented a generator that elicited a current when a metal wire was revolved in a magnetic field. This generator was the harbinger of the electric motor. The flow of electrons that was produced in this manner was termed faradic current. By the middle of the 1800s, G.B. Duchenne began to publish his work. Generally referred to as the “father of electrotherapy,” Duchenne was interested in the physiology of electrical stimulation and is known for identification of muscle actions and motor points. In his research, Duchenne preferred biphasic current because it circumvented the electrolytic and heating actions of monophasic current. (42, 152) Nevertheless, the possible benefits of electrostimulation of paralyzed muscle were first documented by Reid and Brown-Sequard. The claim was put forth that daily electrical stimulation of the

paralyzed limbs of various animals produced a gradual, but complete restoration of limb muscle mass. Although stimulated muscle regained its mass, the limb still remained unusable. (38)

In the middle of the twentieth century, electrodiagnostic devices were introduced for clinical use. Researchers reported that paralyzed muscle responded to biphasic but not monophasic current. The propagation of electric current in a muscle was found to be a critical factor in producing a contraction. The terms rheobase and chronaxie were originated by LaPicque in 1909 to define the relationship between magnitude and duration of current needed to excite muscle or nerve. (42) By 1916, the strength-duration curves for human muscle in health and disease demonstrating this relationship were documented by Adrian. (42, 157)

As soon as the induction coil and the battery were invented and easily accessible, the golden age of electrotherapy commenced. Most clinicians employed some form of electrical stimulation in their practices on a routine basis. Although greatly improved since the time of the Leyden jar, electrotherapy machines in the early 1900s were cumbersome. In a typical apparatus, electrodes were comprised of brass and covered with felt or sponge. Water acted as the conductor for the transmission of current. Interventions for peripheral nerve injuries flourished during the Second World War with the development of a clinical stimulator able to generate input waveforms that were able to excite both partially innervated and paralyzed muscles. (42, 157)

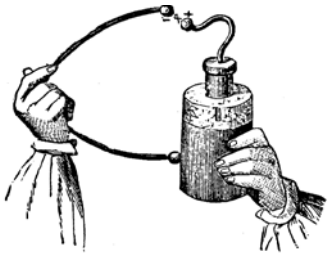

Figure C-2. Leyden jar. (42)

The use of neuromuscular electrical stimulation (NMES) to provide functional use of limbs was demonstrated in the early 1960s. Using a single input channel for stimuli, ankle dorsiflexion was elicited with a foot switch during the swing phase of gait. This corrected foot drop in a patient. The stimulator used was approximately the size of a cigar box and was fastened on patient clothing. Rubber electrodes were attached to the lower limb by straps. In this protocol, a transient carryover of function in the tibialis anterior after peroneal nerve stimulation in hemiplegic patients was additionally reported. (42)

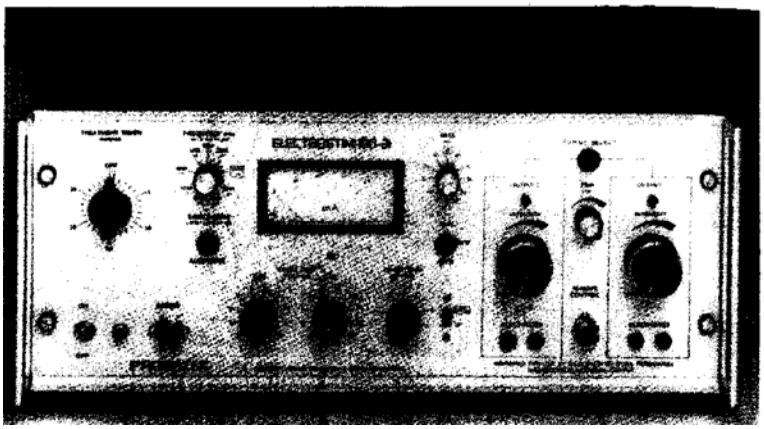

Figure C-3. Neuromuscular electrical stimulation device. (42)

Neuromuscular electrical stimulation (NMES) is a procedure that employs electrical currents to activate nerves that innervate extremities that have been paralyzed due to spinal cord injury (SCI), head injury, stroke or other neurological disorders. This procedure can be used to restore function in those affected. Injuries to the spinal cord interfere with electrical signals between the brain and the muscles. This causes paralysis below the injury level. Restoration of limb function as well as regulation of organ function are the primary applications of NMES. Other applications of NMES involve the use of prostheses that allow paraplegics to stand, restore hand grasp function in quadriplegics, or restore eliminatory and excretory functions. (36, 37, 151-53, 157)

APPENDIX D: BIOCHEMISTRY OF LACTIC ACIDOSIS AND GLYCOLYSIS

The intracellular creatine phosphate reserve provides a nearly spontaneous metabolic mechanism to generate ATP during the initial transient phase of muscle contraction. Creatine phosphate is also thought to modulate the general transfer of cytosolic phosphate groups. By extension, it could be vital for all skeletal muscle metabolism. However, the creatine kinase lytic reaction alkalinizes the cell, since it consumes H^+. The consumed proton replaces the phosphate group of creatine phosphate, yielding the second NH_2 group of creatine. (71, 112, 159)

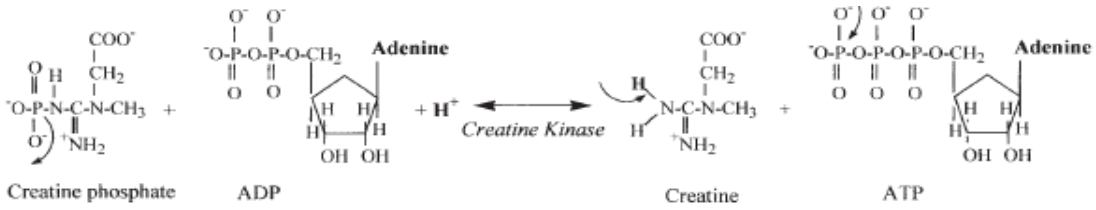

Figure D-1. Phosphagen reaction system. (112, 156)

It has been shown that increasing concentration of P_i during intense stimulation does not come from the creatine kinase reaction. Instead, intramuscular P_i accumulates from conditions in which the ATP demand rate exceeds mitochondrial ATP supplied. In this state, cytosolic ATP turnover reliance increases and generates P_i at a rate that is faster than the rate of

mitochondrial P_i influx. This causes P_i to accumulate and leads to acidosis. (71, 112, 159)

Glycolysis is modulated by glucose-6-phosphate (G6P) production, which comes from either glucose in the blood or muscle glycogen. Although glycogen provides the majority of carbohydrate for muscle glycolysis during intense stimulation, the traditional explanations of glycolysis denote the biochemical pathway starting with glucose and progressing through ten reactions that result in the end product of pyruvate. Using glycogen as the primary substrate is different from glycolysis in that the initial reaction is bypassed but progresses through the remaining nine reactions. This distinction about origin of glycolysis is vital. It has been shown that the release of H^+ from glycolysis differs depending on whether glucose or muscle glycogen is the initial substrate. (112, 131-142, 159)

Table D-1. Summary of reactions in glycolysis. (159)

#	Reaction	Enzyme	H^+ Source: Glu	H^+ Source: Gly
	G6P from glycogen			
	Glycogen-$_n$ + Pi^{2-} → Glycogen-$_{n-1}$ + Glucose 1-phosphate	Phosphorylase		
	Glucose 1-phosphate → Glucose 6-phosphate	Phosphoglucomutase		
	G6P from glucose			
	Glucose + $MgATP^{2-}$ → Glucose 6-phosphate^{2-} + $MgADP^-$ + H^+	Hexokinase	1	
	Glycolysis			
1	Glucose 6-phosphate^{2-} → fructose 6-phosphate^{2-}	Glucose-6-phosphate isomerase		
2	Fructose 6-phosphate^{2-} + $MgATP^{2-}$ → fructose 1,6-bisphosphate^{4-} + $MgADP^-$ + H^+	6-Phosphofructokinase	1	1
3	Fructose 1,6-bisphosphate^{4-} → Dihydroxyacetone phosphate + Glyceraldehyde 3-phosphate^{2-}	Aldolase		
4	Dihydroxyacetone phosphate → Glyceraldehyde 3-phosphate^{2-}	Triose Phosphate Isomerase		
5	2 Glyceraldehyde 3-phosphate^{2-} + 2NAD^+ + 2Pi^{2-} → 2 1,3-bisphosphoglyerate^{4-} + 2 NADH + 2 H^+	Glyceraldehyde-3-Phosphate dehydrogenase	2	2
6	2 1,3-bisphosphoglyerate^{4-} + 2 $MgADP^-$ → 2 3-phosphoglycerate^{3-} + 2 $MgATP^{2-}$	Phosphoglycerate kinase		
7	2 3-phosphoglycerate^{4-} → 2 2-phosphoglycerate^{4-}	Phosphoglycerate mutase		
8	2 2-phosphoglycerate^{3-} → 2 phosphoenolpyruvate^{3-} + 2H_2O	Phosphopyruvate hydratase		
9	2 phosphoenolpyruvate^{3-} + 2 $MgADP^-$ + 2 H^+ → 2 pyruvate$^-$ + 2 $MgATP^{2-}$	Pyruvate kinase	−2	−2
		Net protons per 2 pyruvate	2	1

From the above table, it is seen that release of H^+ from glycolysis comes from ATP hydrolysis in the hexokinase and phosphofructokinase steps, in addition to the glyceraldehyde 3-phosphate dehydrogenase reaction. The chemical structures for these reactions are given in the figures below. (112, 131-142, 159)

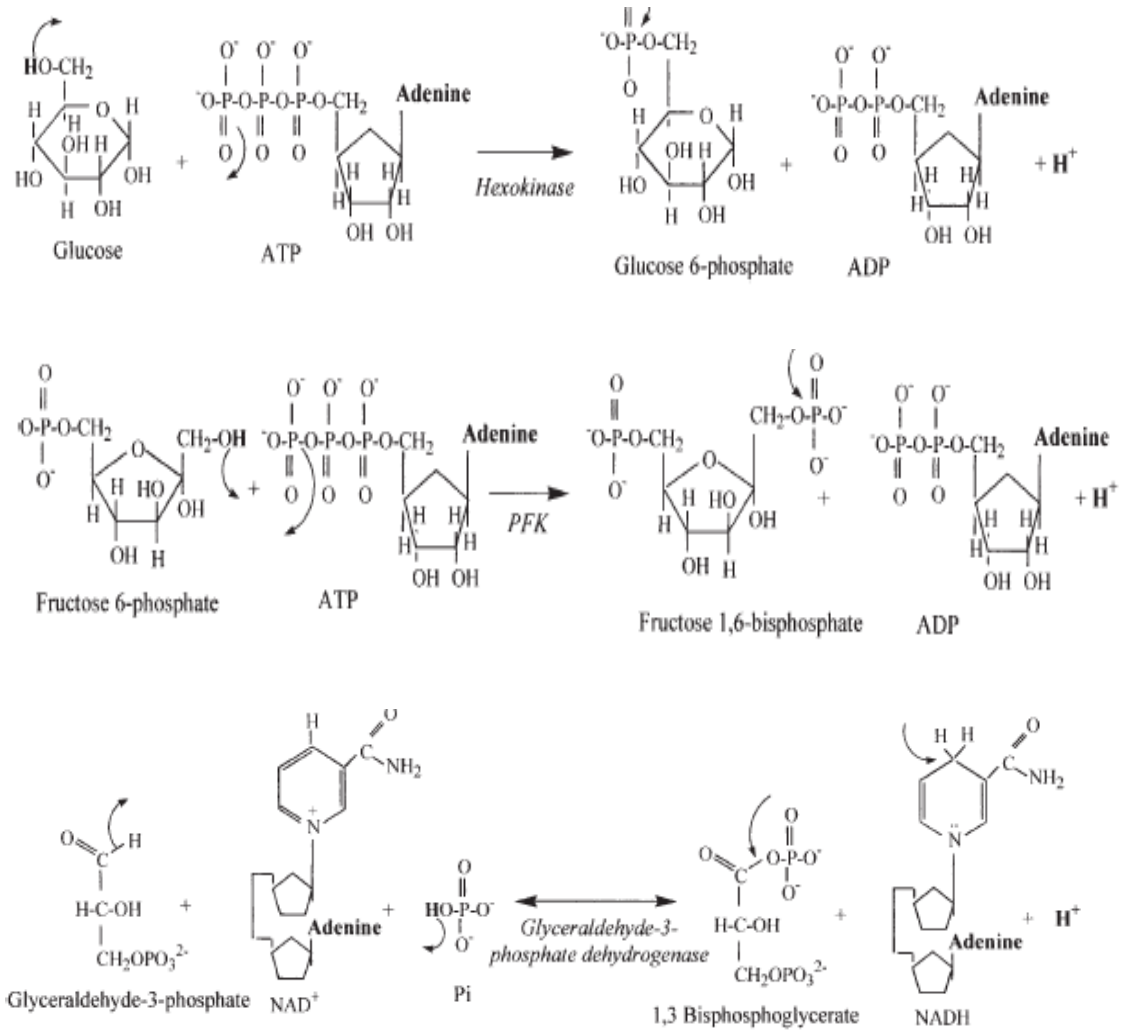

Figure D-2. Hexokinase, phosphofructokinase, and G3P dehydrogenase reaction steps in glycolysis. (112, 156)

A summary of glycolysis metabolism, starting from glucose or glycogen (112, 131-142, 159) follows below:

$$\text{glucose} + 2\ ADP + 2P_i + 2\ NAD^+ \rightarrow \text{pyruvate} + 2\ ATP + 2\ NADH + 2H_2O + 2H^+$$

$$\text{glycogen}_n + 3\ ADP + 3P_i + 2\ NAD^+ \rightarrow \text{glycogen}_{n-1} + 2\ \text{pyruvate} + 3\ ATP + 2\ NADH + 2H_2O + H^+$$

Biochemically, production of lactate in skeletal muscle is advantageous for various reasons. First, the lactate dehydrogenase (LDH) reaction generates cytosplasmic NAD^+. This supports the demand for NAD^+ substrate in the glyceraldehyde 3-phosphate dehydrogenase step. In turn, cytosolic redox potential (NAD^+/NADH) is better maintained, continued substrate flux through the second phase of glycolysis is supported, and thereby allows continued ATP regeneration from glycolysis. Another important function of the LDH reaction is that for every pyruvate molecule catalyzed to lactate and NAD^+, a proton is consumed. Hence, this reaction buffers a muscle cell against the accumulation of protons known as acidosis. (81, 82, 112, 159)

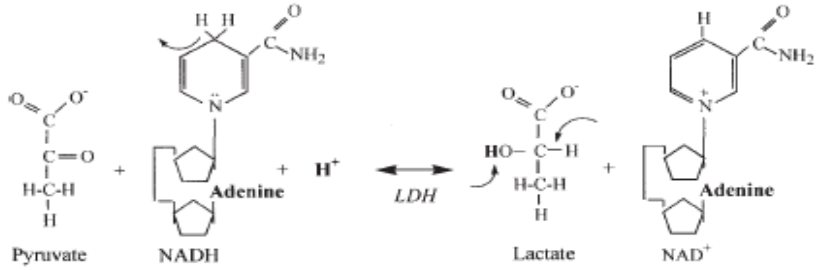

Figure D-3. Lactate dehydrogenase (LDH) reaction. (112, 156)

In the LDH reaction, one proton and two electrons are removed from NADH. Additionally, a proton is gained is exchanged for the two electron and two proton reduction of pyruvate to lactate. As a result, the LDH reaction alka-linizes, not acidifies, the cell according to the lactic acidosis construct. Yet, the organic chemistry of the LDH reaction shows that production of lactate consumes H^+. Therefore, these biochemical facts are correctly interpreted physiologically as lactate production retards metabolic acidosis and aids proton removal from muscle cells. (112, 156)

When glycolytic pyruvate is converted to lactate, protons are not gained with glucose as substrate. Moreover, one proton is lost and an additional ATP is gained with glycogen as substrate.

$$\text{glucose} + 2\,\text{ADP} + 2P_i \rightarrow \text{lactate} + 2\,\text{ATP} + 2H_2O$$

$$\text{glycogen}_n + 3\,\text{ADP} + 3P_i + 1H^+ \rightarrow \text{glycogen}_{n-1} + 2\,\text{lactate} + 3\,\text{ATP} + 2H_2O$$

This coupling is important in many physiological events such as the processes in red blood cells. Red blood cells have no mitochondria and depend on glycolysis for ATP regeneration using glucose substrate. The gain of two protons from glycolysis equilibrates with the loss of two protons from converting two pyruvate to two lactate molecules. Red blood cell cytosolic redox is further maintained by the NAD^+ generated from the LDH reaction. For the red blood cell, production of lactate prevents acidosis and maintains cellular NAD^+ levels. However, in skeletal muscle, mitochondrial presence and the use of glycogen as a substrate for G6P to drive glycolysis changes the stoichiometry between glycolytic H^+ release and lactate/proton consumption. Also the high rate of ATP

hydrolysis and regeneration during contraction presents specific metabolic demands that are not seen in other tissues. Terminal phosphate is removed from ATP to generate ADP and the associated liberation of free energy and P_i and requires water as the substrate. The P_i produced from the ATP hydrolysis can buffer the H^+ that is released. As a result, increases in P_i during intense stimulation quantify the buffering capacity of P_i by the extent of its accumulation when cellular pH goes acidic. (112, 194)

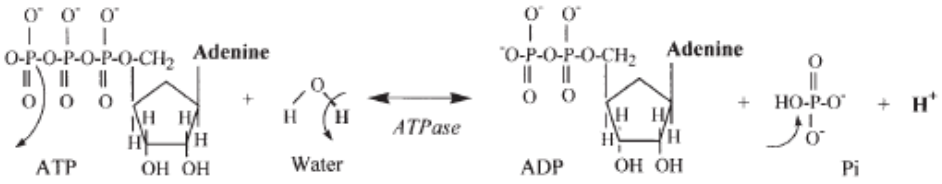

Figure D-4. ATP hydrolysis. (112, 156)

It is not true that the buffering capacity of P_i negates ATP hydrolysis as a vital source of H^+ release that leads to acidosis. Actually, increases in cytosolic P_i are significantly less than the total free phosphate ion released from ATP hydrolysis. During that process, the ADP and P_i both function as substrates for glycolytic production of ATP. This allows free H^+ accumulation once the systems for cellular proton outflow have been overwhelmed. Free phosphate ion also substrates glycogenolysis and is pumped into the mitochondria in oxidative phosphorylation. Hence, the accumulation of phosphate ion does not have a

stoichiometric relationship to ATP turnover. Accumulation only occurs if the rate of cytosolic ATP turnover is greater than the intracellular ATP supply. (112, 156)

The hydrolysis of ATP required to fuel muscle contraction is the crux of cellular proton equilibrium. This is the primary source of H^+ release in contracting skeletal muscle. Once NADH and protons from cytoplasmic reactions are produced at rates greater than mitochondrial capacity, cytosolic redox is assisted by lactate production. It is lactate that accounts for glycolytic H^+ release. As the ATP hydrolysis rate exceeds all other reaction rates, proton release over time becomes greater than metabolic proton buffering by production of lactate and protein breakdown. Furthermore, when cellular proton removal capacity is exceeded, pH decreases. Indeed, the origin of the accumulating P_i in the muscle is the hydrolysis of ATP, not the breakdown of creatine phosphate. This causal belief in creatine phosphate breakdown as the origin of intramuscular P_i is still erroneously held by many physiologists. (112, 156)

A schematic of mitochondrial respiration is show below. Metabolism in mitochondria releases electrons and protons from substrates, produces CO_2, and employs the charged particles to generate ATP. The primary molecules in these processes are acetyl CoA, NAD^+, FAD^+, O_2, ADP, P_i, protons, and electrons. The ADP, phosphate, and H^+ are all actively transported into the mitochondria. The protons are needed to reduce molecular oxygen. ADP and phosphate are needed to regenerate ATP. These mechanisms link cytoplasmic and mitochondrial metabolism, especially for transferring phosphates and H^+ between the cytoplasm and mitochondria. The transport systems for H^+ between the

cytoplasm and the mitochondria reveal the power of mitochondrial respiration in controlling the intracellular proton balance when muscle contraction depends on mitochondrial respiration for ATP. (112, 156)

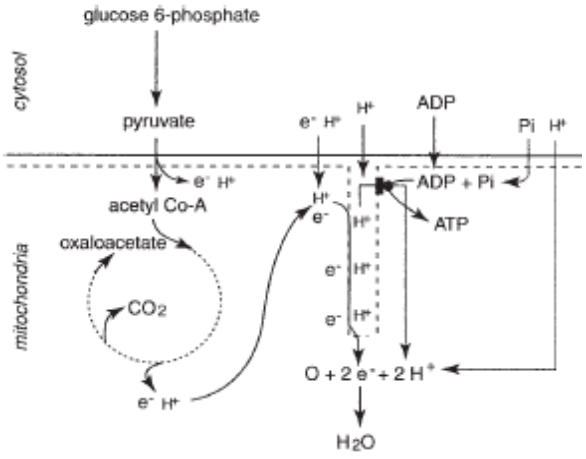

Figure D-5. Schematic representation of mitochondrial respiration and ATP regeneration. (112, 156)

APPENDIX E: PHYSICOCHEMICAL PRINCIPLES UNDERLYING CALCIUM-TROPONIN BINDING

There are many physical and chemical processes in play during a muscle contraction. These processes have not been adequately considered in previous models of muscle force and fatigue. The fundamental principles that underlie these processes are discussed in this section.

E.1 Periodic reactions

In the law of mass-action, according to Lotka (117), every isothermal reaction approaches its equilibrium asymptotically. In systems with several reactions occurring simultaneously, equilibrium or a steady state might be reached by other pathways. Consider below a series of consecutive, irreversible reactions:

1. a → A

2. A → B

3. B → C.

It is assumed that the transformation of a into A is slow as compared with the establishment of equilibrium between A and B. Thus, the differential equations describing the change of the concentrations of A and B are:

$$\frac{dc_A}{dt} = F\text{-}k_1 c_A \qquad \text{(E-1)}$$

$$\frac{dc_B}{dt} = k_1 c_A - k_2 c_B \qquad \text{(E-2)}$$

where H, k_1, and k_2, are constants, and c_A, c_B, denote concentrations. Allow B to influence autocatalytically its own formation rate, so that k_1 can be written as:

$$k_1 = kc_B \qquad \text{(E-3)}$$

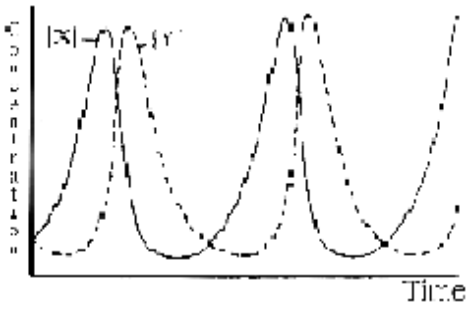

Figure E-1. Periodic reactions with time-varying concentrations of reactants. The dynamics of [Y] lag the dynamics of [X]. (117-119)

The differential equations transform to:

$$\frac{dc_A}{dt} = F - kc_A c_A \qquad \text{(E-4)}$$

$$\frac{dc_B}{dt} = kc_A c_B - k_2 c_B \qquad \text{(E-5)}$$

After a series of numerous transformations of variables, the following equations are obtained:

$$-\frac{dx}{dT} = xy'+ky+Lx \qquad \text{(E-6)}$$

$$\frac{dy}{dT} = xy+Lx\,. \qquad \text{(E-7)}$$

When the reactions equilibrate, x and y become infinitesimal. Hence the xy product terms can be neglected. By elimination of y and x from both equations, the system transforms to ‘‘damped vibration’’ laws:

$$x''+Lx'+KLx=0 \qquad \text{(E-8)}$$

$$y''+Ly'+KLy=0 \qquad \text{(E-9)}$$

The reaction is periodic provided that L < 4K. The solution of the above equations are $y=y_0e^{-pT}\cos qT$ and $x=Me^{-pT}\sin(\varphi+qT)$ where $p=L/2$, $q=½(4KL-L^2)^{1/2}$, $Lz=(p^2+q^2)^{1/2}$, $\sin\varphi=p/(p^2+q^2)^{1/2}$, $\cos\varphi=q/(p^2+q^2)^{1/2}$, and $y_0=y(T=0)$. (112)

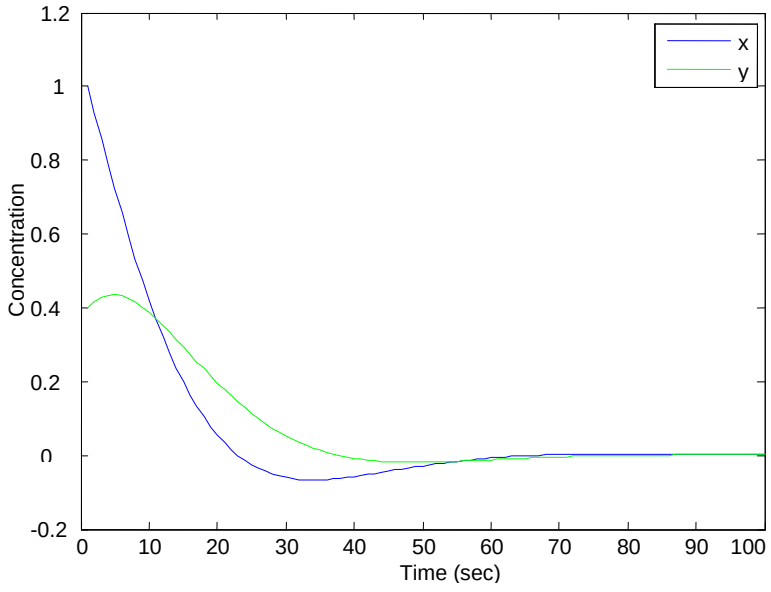

Figure E-2. Example of damped periodic reactions for x and y with y_0=1, M=0.8, φ=π/6, p=0.707, and q=0.707. The dynamics of y are damped and lag the dynamics of x.

Lotka (117) further noted that in a system in which consecutive reactions occur in the presence of a product of autocatalysis, essential conditions exist that allow a “periodic” process to happen. In the case of two consecutive reactions of equal period that behave as “damped vibrations”, one lags behind the other by a phase that depends on certain reaction-specific boundary and initial conditions. This behavior happens regardless of the initial concentrations of the reactants.

E.2 Concepts of equilibrium

Typical definitions for equilibrium connote a stationary state with respect to the kinetics of chemical reactions. It is defined as a state in which certain velocities go to zero. However, it must be noted that there are numerous concepts of equilibrium. From etymology, the word equilibrium is linked to a dynamic idea. *Aequa libra*, the poised balance, connotes a state in which the total forces on a system are balanced to zero. (118, 119)

A third concept of equilibrium is derived from a consideration of energy relationships within a system. A system in dynamic equilibrium is characterized by the attainment of a critical point of certain functions having the units of energy. This is a state in which the virtual work done in any infinitesimal displacement within the constraints goes to zero. For example, a ball in a hemispherical cup is in equilibrium when its potential energy is a minimum that is geometrically admissible. From this perspective, equilibrium is defined as a state in which certain potential functions have a critical point. Metabolic equilibrium, population equilibrium, and the like, are not true equilibria in the strict sense. However, those phenomena are steady states that are maintained only with a constant flux

of energy. One of the basic examples of equilibria in systems of that type comes from a pair of or opposing chemical reactions. This is seen in the reaction of divalent calcium and the proteins of muscle contraction. (118, 119)

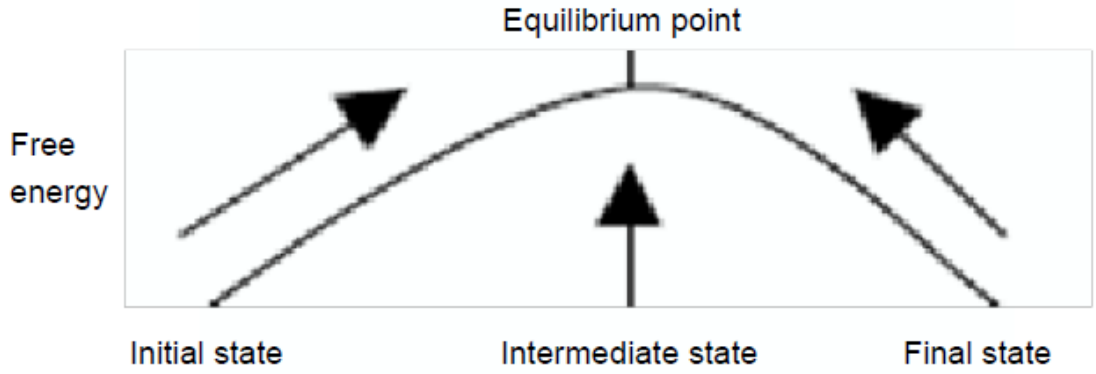

Figure E-3. Dynamic equilibrium of a chemical system. Free energy is required to drive a reaction through the intermediate state and past the equilibrium point in either direction. (116)

The simplest type of balanced chemical reaction at constant volume and temperature is monomolecular in both directions. A substance S_1 transforms into S_2, and S_2 in turn changes into S_1. Only one molecule takes part, in each transformation. Assume x_1 and x_2 are the respective concentrations of S_1 and S_2. This gives isothermally, by the law of mass action, the rate of decomposition of S_1 and S_2 respectively. (118, 119)

$$(Dx_1) = -k_1 x_1 \qquad \text{(E-10)}$$

$$(Dx_2) = -k_2 x_2 \qquad \text{(E-11)}$$

where k_1, k_2 are temperature-dependent coefficients characteristic of the reaction. The rate of increase of the substance S is the excess of its rate of formation divided by its rate of decomposition. This is analogous to birth rates and death rates in a human population. Each molecule of S_1 that "dies" transforms into a molecule of S_2. Every molecule of S_2 that "dies" becomes a molecule of S_1. (116)

All complete reactions consist of three separate stages. Each stage has a characteristic energy change. Generally, molecules in the free state exist in an inert phase. In order to induce any reaction it is necessary to render them into a reactive phase. This is the first stage of the reaction. It dictates that a specific amount of energy be supplied to each molecule. The amount required is the energetic difference between the initial phase and the particular phase necessary for the desired reaction to occur. Meanwhile, the second stage of the reaction is the rearrangement of atoms in which new molecules are produced. It is only this stage that is denoted by the reaction equation. The final stage is the phase change of the newly produced molecules. In this stage, the molecules transform into their inertial phases. The last two stages of reaction are both concurrent with energy dissipation. If the total energy dissipated in the second and third stages is greater than the energy taken in during the first stage, the reaction is exothermic. An endothermic reaction is one in which the energy required to overcome inertia is greater than the total amount dissipated in the second and third stages. As to the agencies that provide the necessary energy to carry a transforming molecule

"over the crest of the hill," there is the thermal and electromagnetic excitation of the molecules and the influence of catalysts which lower the requisite level of energy. From the perspective of energy, the initial and final states remain unchanged and independent of the path of work. Final equilibrium must agree with the second law of thermodynamics, which may be considered as a law of evolution for this type of system. The second law of thermodynamics has a plethora of forms. However, analogous to gravitation, the form in which it serves this discussion is the one which states that the system evolves toward a state in which thermodynamic potentials of the variables defining its condition are at a minimum. Many principles of nature are expressed as minimum or maximum laws. Thus, it is plausible that the law of evolution in physiological systems and processes has a similar form. Like the law of chemical evolution, it should be expressed in terms of the global system. The reason is that the energy of the entire system is what approaches a minimum. (118, 119)

E.3 The Principle of Le Chatelier

However, there is another special case of the general problem of chemical equilibrium which submits relatively easily to analysis. That special case considers only the final state, at equilibrium, of a given total change in a parameter. It ignores all issues regarding the path by which the perturbation of equilibrium occurs. This is possible by the fact that, in certain rate-independent cases, the equilibrium is displaced independently of the path of chemical change. It is dependent entirely on the initial and final values of the parameters whose variation causes or results from the change. Thus, in these physicochemical

state changes, the Principle of Le Chatelier predicts of the direction of the perturbation of equilibrium that results from a change in certain parameters that maintain the equilibrium depends (118, 119)

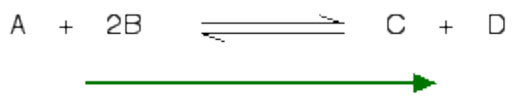

Increasing concentration of A

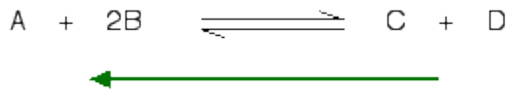

Decreasing concentration of A

Figure E-4. An example of the Principle of Le Chatelier. Changing the concentration of A drives the reaction in its opposing direction towards equilibrium. (8, 193)

From physical chemistry, the Principle of Le Chatelier describes the nature of equilibria in chemical reactions. The broadest definition of the Principle of Le Chatelier is that a system changes in order to minimize an external perturbation (8). That means that every external stimulus on a system produces changes in the direction that elevates the resistance of the system against the external stimulus. If the equilibrium of a system is disturbed, the system adapts itself to the perturbation, in such manner that the perturbation dampens until equilibrium

is reestablished. (121) Yet, the Principle of Le Chatelier only indicates the direction of changes from stresses on a system. It does not, however, in any way indicate if any particular stress will produce an actual change in the system. Furthermore, the Principle makes no indication whatsoever about the conditions needed to produce maximal change. (8)

E.4 Michaelis-Menten kinetics

According to Zumdahl (193), for catalytic reactions which exhibit simple Michaelis-Menten kinetics and in which product formation is governed by the rate-limiting step $k_m \approx k_{-1}/k_1 = k_d$, where k_d is the dissociation constant of the enzyme-substrate (ES) complex. Yet, frequently $k_2 >> k_{-1}$, or k_2 and k_{-1} are similar. Hence the Michaelis constant can be defined as:

$$K_m = \frac{k_{-1} + k_2}{k_1} \qquad \text{(E-12)}$$

The catalytic reaction is assumed to be irreversible, and the product does not bind to the catalyst.

$$E + S \underset{k_{-1}}{\overset{k_1}{\rightleftarrows}} ES \xrightarrow{k_2} E + P \qquad \text{(E-13)}$$

The rate of production of the product, $d[P]/dt$ is define as the reaction rate, V in reaction kinetics. It depends on the catalytic constant, k_2, and [*ES*], the concentration of catalyst bound to substrate. As [*ES*] is usually unmeasurable, it must be expressed in terms of the concentration of catalyst and substrate originally added.

A crucial assumption in the derivation of the Michaelis-Menten equation is that the concentration of the catalyst changes much more slowly than those of the product and substrate. This is known as the quasi steady-state approximation. The derivation of the equation follows below.

$$\frac{d[ES]}{dt} = 0 = k_1[E][S] - [ES](k_{-1} + k_2) \tag{E-14}$$

This can be rearranged to:

$$[ES] = \frac{k_1[E][S]}{k_{-1} + k_2} \tag{E-15}$$

Defining the Michaelis-Menten constant as:

$$K_m = \frac{k_{-1} + k_2}{k_1} \tag{E-16}$$

yields:

$$[ES] = \frac{[E][S]}{K_m} \tag{E-17}$$

The total concentration of catalyst [E_0] is the sum of the free enzyme in solution [E] and that which is bound to the substrate [ES]. This allows the free catalyst concentration to be derived from (E-14):

$$[E_0] = [E] + [ES] \tag{E-18}$$

$$[E] = [E_0] - [ES] \tag{E-19}$$

Using [E], [ES] can now be written:

$$[ES] = \frac{([E_0] - [ES])[S]}{K_m} \tag{E-20}$$

Algebraic manipulation gives:

$$[ES]\frac{K_m}{[S]} = [E_0] - [ES] \tag{E-21}$$

$$[ES]\left(1 + \frac{K_m}{[S]}\right) = [E_0] \tag{E-22}$$

$$[ES] = [E_0]\frac{1}{1 + \frac{K_m}{[S]}} \tag{E-23}$$

The reaction rate is:

$$V = \frac{d[P]}{dt} = k_2[ES] \tag{E-24}$$

Substitution and more algebra gives

$$\frac{d[P]}{d} = \frac{k_2[E_0]}{t}\frac{[S]}{K_m + [S]} = V_{\max}\frac{[S]}{K_m + [S]} \tag{E-25}$$

If the substrate concentration is large compared to K_m, [S]/(K_m+[S]) goes to 1. In that case, the rate of product formation equals $k_2[E_0]$. (193)

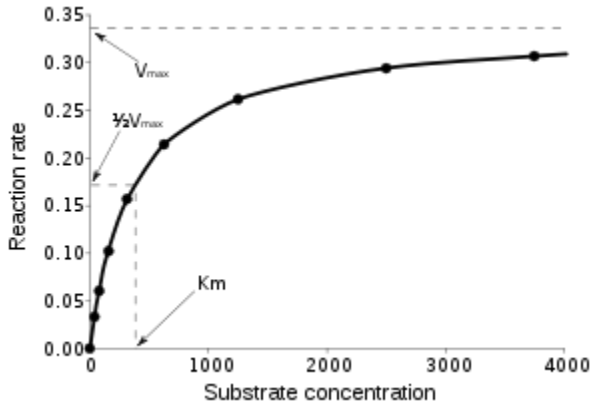

Figure E-5. Traditional Michaelis-Menten kinetics plot. The kinetics are asymptotically bound. (193)

Implicit in traditional chemical kinetics is the assumption that the reaction occurs in homogeneous solutions that are dilute. However, it has been shown by theory, computer simulation, and experiment that traditional chemical kinetics are markedly dissimilar when reactions are constrained or occur on fractal surfaces. In these cases, a standard reaction rate law shows a specific time-varying decrease in the rate constant. This is equivalent to a rate law with a higher kinetic order that does not vary with time. For example, a bimolecular reaction has a kinetic order that is no longer equal to the molecularity of the reaction when it is constrained dimensionally may has a kinetic order that approaches 49. The increased kinetic orders may reflect the fractal dimension of the reaction surface.

As a result, the generalized kinetics are sometimes denoted as fractal kinetics and may arise in reaction-limited states if the surface of potential energy possesses fractal characteristics. (162)

Power-law formalism exhibits at all organizational levels from molecule to organism. (14, 150, 160, 161) This ubiquity of the power law at different organizational levels is similar to fractal phenomena. Both constructs behave in similar ways independent with respect to scale. It has been shown for fractals that this self-similarity is closely connected to power law expressions as a very promising alternative to the traditional Michaelis-Menten construct. (162)

The power law formalism is a mathematical structure consisting of ordinary nonlinear differential equations comprised of multiplicative functions of power laws. The formalism satisfies two crucial specifications for evaluating whether a kinetic representation is appropriate for a complex biological system. The first requirement is the degree of systematic structure of the formalism and is related to mathematical solvability. The second requirement is the degree of system conformity to the formalism. This is associated with accuracy. Power law formalism also includes specific representations such as traditional Michaelis-Menten reaction rate kinetics. (162)

With the more complex mathematics, Savageau (162) applies the power-law formalism to the Michaelis-Menten rate kinetics. This leads to the following mathematical formulation.

$$\frac{d[S]}{dt} = -k_1[S]^{\alpha}[E]^{\beta} + k_{-1}[C] \qquad \text{(E-26)}$$

$$\frac{d[E]}{dt} = -k_1[S]^{\alpha}[E]^{\beta} + (k_{-1} + k_2)[C] \quad \text{(E-27)}$$

$$\frac{d[C]}{dt} = k_1[S]^{\alpha}[E]^{\beta} - (k_{-1} + k_2)[C] \quad \text{(E-28)}$$

$$\frac{d[P]}{dt} = k_2[C] \quad \text{(E-29)}$$

where α and β are the real number kinetic orders of the substrate and catalyst, respectively. The catalyst-substrate complex is assumed to be constant on the basis of monomolecularity.

Fractal-like kinetics and power law formalism can apparently be applied to non-homogeneous reactions, according to Schnell and Turner (163) because they include parameters that depend on environment dimensionality. This suggests that these modifications may be superior for modeling *in vivo* reaction dynamics to the law of mass action. However, they do have drawbacks that need to be discussed. Fractal kinetics presents a fundamental difficulty with singularity at t=0, which diminishes its feasibility at reaction modeling. This raises the question of whether this problem can be worked around by modifying the mathematical form or whether it demonstrates pathology in the approach. Yet, estimation by power law has only been validated using computer simulations for homodimeric reactions. (162) The extension of the approach to more

complex reaction systems has no supporting evidence currently. The inference is made solely on the reason that power laws are considered as intricate constructs of fractal environments. (163) It therefore remains to be seen how the approach compares real physiologic data.

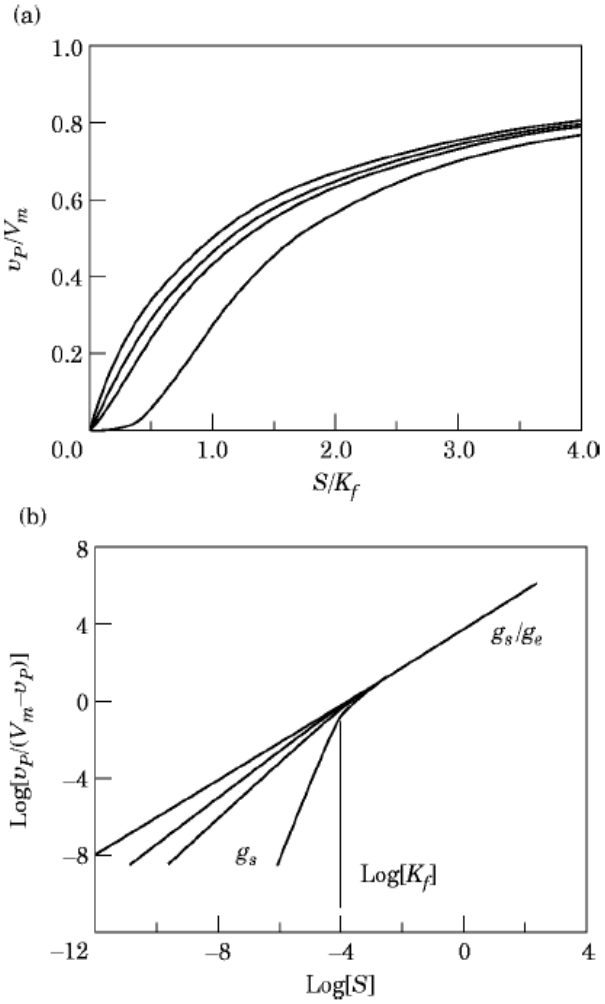

Figure E-6. Fractal rate law plots of reaction velocity as a function of the concentration of substrate: (a) Cartesian plot. Sigmoidal behavior increases with kinetic order (g). Traditional Michaelis-Menten rate law is top curve with g=1. (b) Hill plot. A slope (g_s/g_e) greater than 1 indicates non-hyperbolic cooperativity. The rate law is governed by asymptotic lines. The top asymptote is the traditional Michaelis-Menten law. (162)

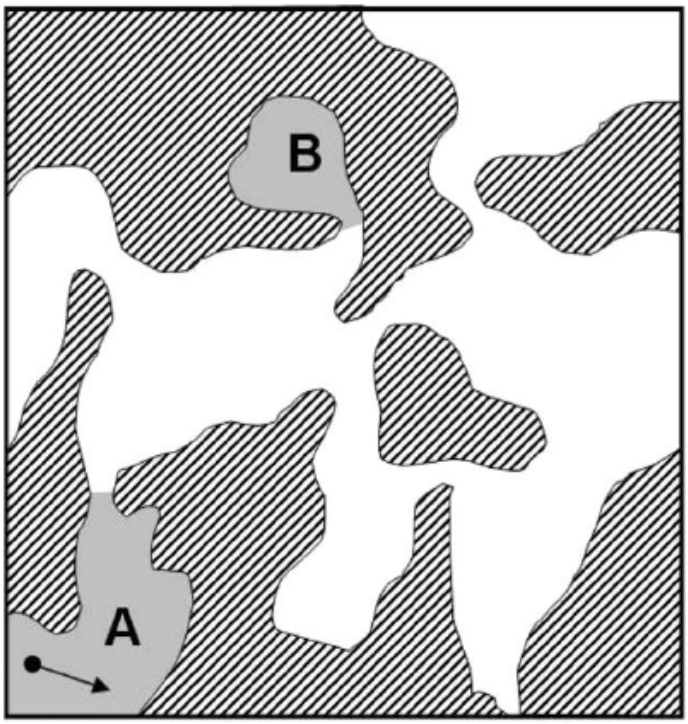

Figure E-7. A hypothetical depiction of macromolecular crowding. (163)

According to Schnell and Turner (163), the kinetics of cytoplasmic reactions follow anomalous rate laws with macromolecular crowding as a major factor. Reactants are constrained in space in crowded environments microscopically by forces such as steric hindrance and electromagnetic interactions which can occur intermolecularly. The reaction volume available for a specific molecule is modulated by number, size and shape of all other molecules in a reaction compartment. Diffusion and mixing are also important as a substance coefficient of is diffusion is dictated by the molecular mean free path. For small solvated molecules, the mean free path between collisions will be mostly a function of the average distance between individual molecules.

Regardless of macromolecular presence in solution, collisions between small molecules and macromolecules will be much less numerous than collisions between small molecules. Hence a macromolecular presence is not likely to have significant effect on the diffusion of small molecules. However, it will affect the degree of mixing of small molecules through the solution by decreasing the probability of their motions throughout the entire reaction volume. Furthermore, high macromolecular density will impact substantially on the average path of each macromolecule. With the assumption that collisions with many small molecules produce no overall effect, the macromolecular mean free path will depend most on the mean separation between macromolecules. Therefore, macromolecular crowding significantly decreases the macromolecular diffusion coefficient.

E.5 Hysteresis

Hysteresis is a term that describes systems in which the effects of a current input to the system are not felt instantaneously. Such systems may exhibit path dependence. Hysteresis phenomena occur in all materials in which a lag occurs between the application and the removal of a force or field and its subsequent effect. Hysteretic systems are also found in economics and biology, where it describes a lagging effect. (103)

In a deterministic system with no hysteresis, it is possible to predict system output at one instant in time, given only its input at that instant. In a system with hysteresis, there is no way to predict the output without knowing the current state of the system. Yet, it is impossible to know the system state without

looking at the input history. Hence, it becomes necessary to know the path that the input followed before it attained a present value. (103)

The word "lag" above should not necessarily be interpreted as a time lag. Even linear systems such as an RC circuit exhibit a time lag between input and output. For most hysteretic systems, there is a very short time scale when its dynamics and associated time dependences are recorded. If observations are carried out over very long periods, creep or slow relaxation toward true equilibrium can be noticed. Without either condition, rate-independent irreversible behavior is the salient characteristic that distinguishes hysteresis from most other dynamic behavior in many systems. (103)

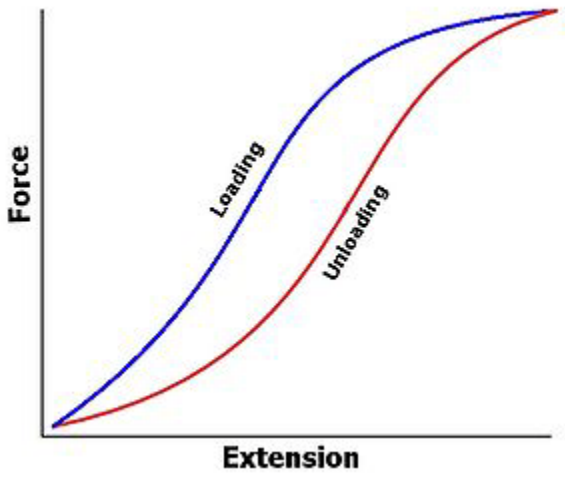

Figure E-8. Idealized elastic hysteresis. The area in the center of the hysteresis loop is the energy dissipated. (103)

If the displacement of a system with hysteresis is plotted on a graph against the applied force, the resulting curve is in the form of a loop. Although the hysteresis loop depends on the physical properties of a given material, there is no complete theoretical description that explains the phenomenon. The family of hysteresis loops, from different inputs, forms a closed three-dimensional space called the hysteroid. (103)

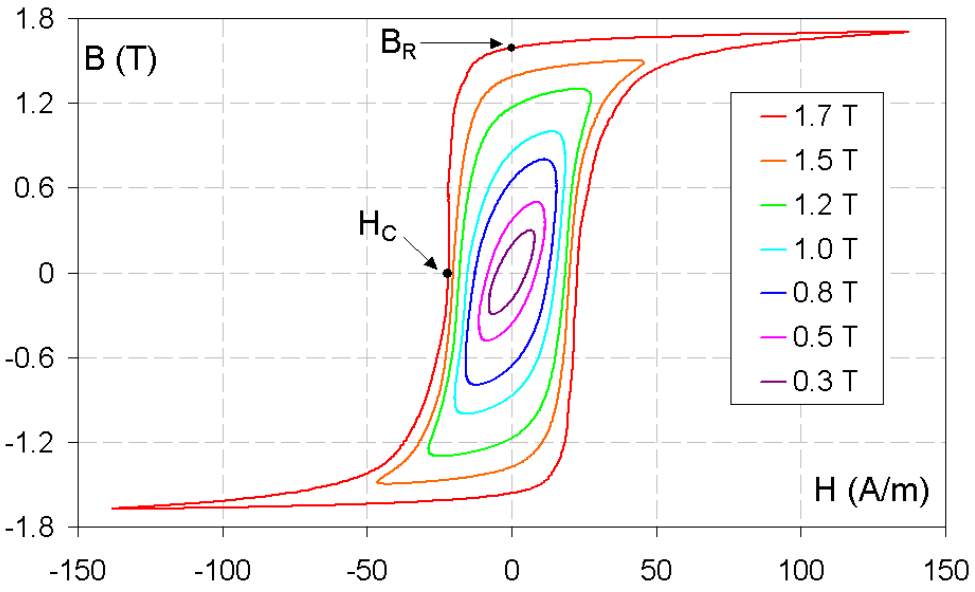

Figure E-9. Hypothetical B vs. H magnetization hysteroid. (103)

Hysteresis represents states. The characteristic curve shape is sometimes denoted as a bistable state. (103) Bistability is the property of a system in which the system can exist in two states and is a chemical version of supercooling, in

which the temperature of a liquid may be decreased below its freezing point without it solidification. (193)

A reaction in which there are two intermediate aggregates X and Y in a reactor is considered as an example. If the concentration of Y is high, and X is added, then the concentration of Y could decrease as shown by the upper line in Figure E-10. However, if X is high, and Y is added, the reaction could slow the increase of Y as indicated by the lower line. However, in each case, a point might be reached at which the concentration will jump between the two curves. These represent the two stable states of the bistable system. Neither is a thermodynamic equilibrium state. Rather, they occur in steady states that are very far from equilibrium. The concentrations of the reactants and products indicate the respective effects of constant flow in to and out of the reactor. (193)

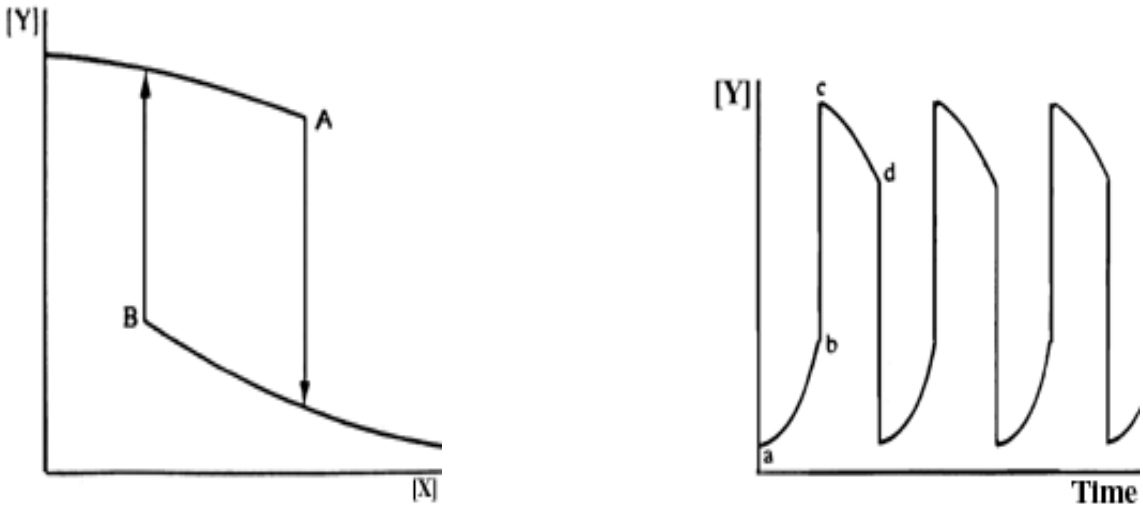

Figure E-10. Chemical system with bistability and oscillating states of concentration surge and depletion. (193)

The hysteresis curve actually contains infinite number of states. An elementary application is to let the threshold regions represent the on and off states respectively. This is seen in the stop transducer state diagram below. Hence, the system can be regarded as bistable. Even if no external input is applied, the position of the hysteresis curve is not necessarily stationary. Thus, the system might require additional energy transfer to be stationary. (103)

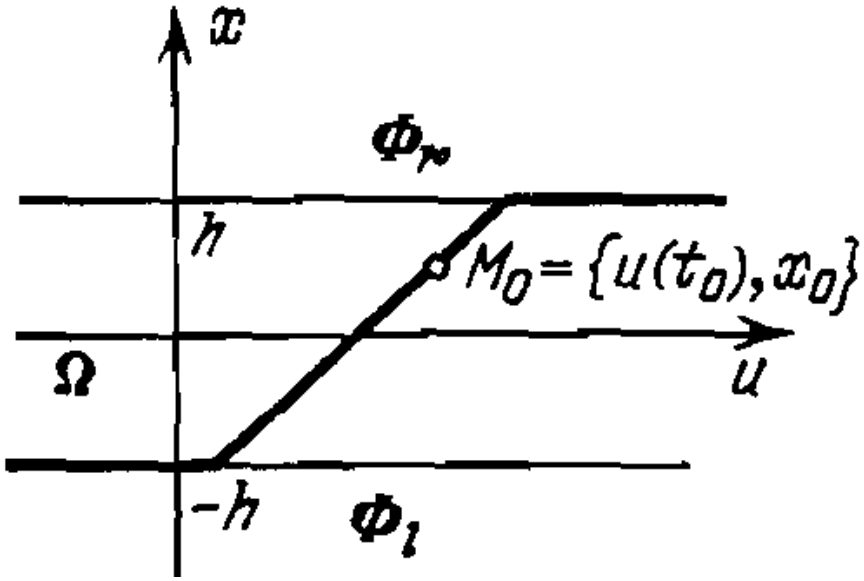

Figure E-11. State diagram of stop transducer. The limits of action are at x=h and x=-h. (103)

According to Krasnosel'skii and Pokrovskii (103), the transducer diagrammed above is denoted as a stop. Most models of electromechanical transducers, such as those of muscle, completely describe the states by values

of the current u and the force x. They can be treated as transducers with variable current as input and with variable force as output.

APPENDIX F: MISCELLANEOUS FREE PARAMETER DATA

Table F-1. Subject 17 trained warmup.

Contraction	k_m	k_m σ	τ_1	τ_1 σ	τ_2	τ_2 σ
1	0.004397	0.000112422	16.6694	0.523345	88.6592	0.659632
2	0.003141	8.19221F-05	17.221	0.55684	69.4121	0.567407
3	0.001341	0.00009494	34.4373	2.3688	50.6807	2.28314

Table F-2. Subject 18 untrained warmup.

Contraction	k_m	k_m σ	τ_1	τ_1 σ	τ_2	τ_2σ
1	0.003077	0.000112171	26.4797	0.638868	136.478	1.61127
2	0.003094	0.000112071	25.3839	0.705112	129.24	1.43776
3	0.002093	0.000063243	28.8787	0.609273	122.266	1.13582

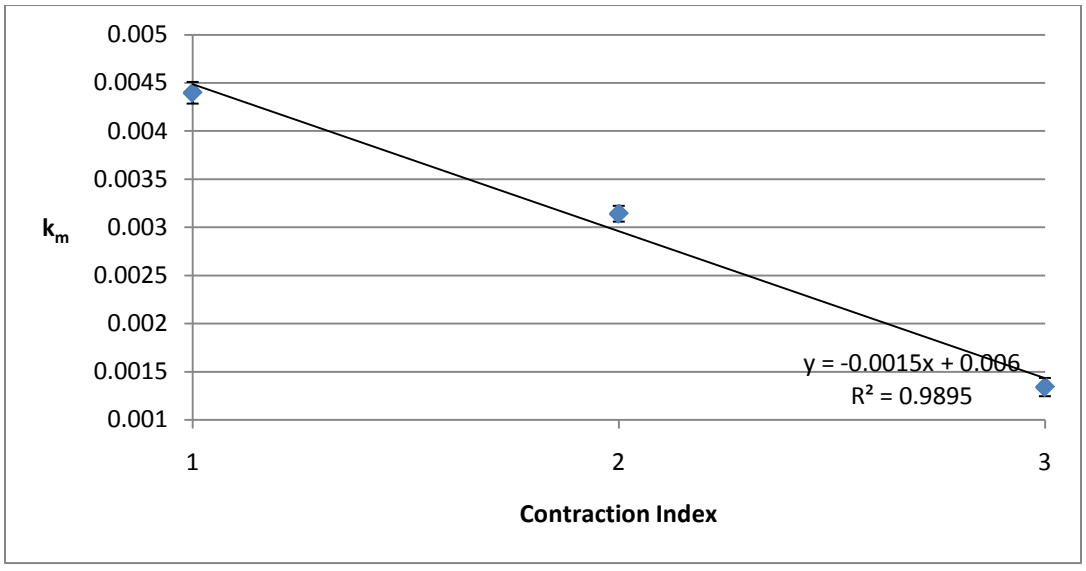

Figure F-1. Behavior of k_m in trained limb of Subject 17 at warm-up.

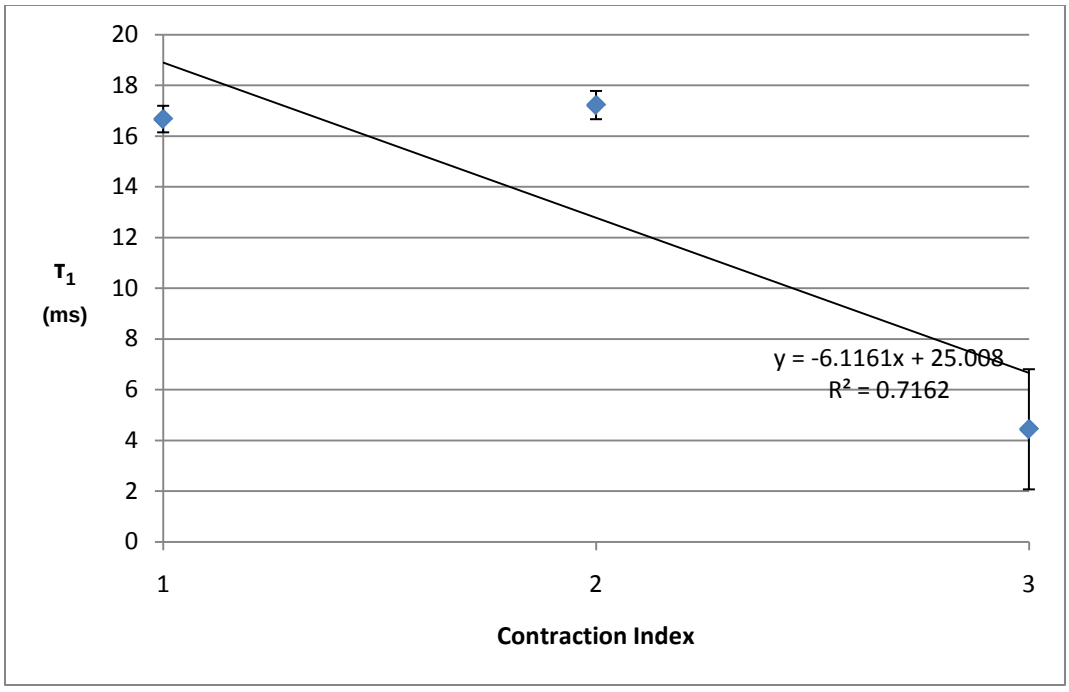

Figure F-2. Behavior of τ_1 in trained limb of Subject 17 at warm-up.

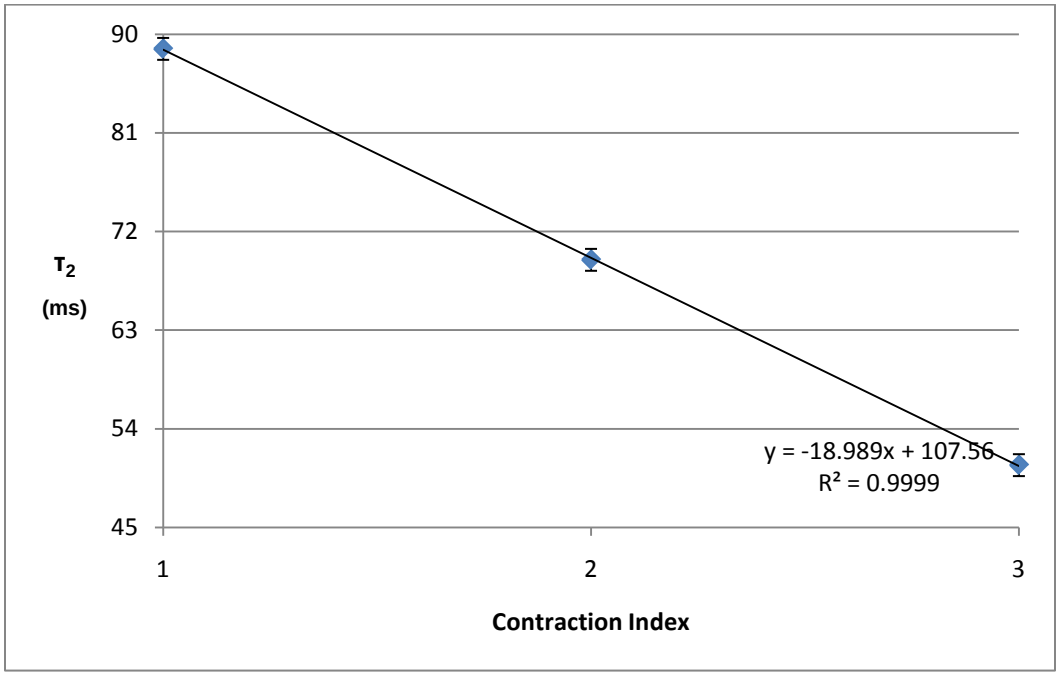

Figure F-3. Behavior of τ_2 in trained limb of Subject 17 at warm-up.

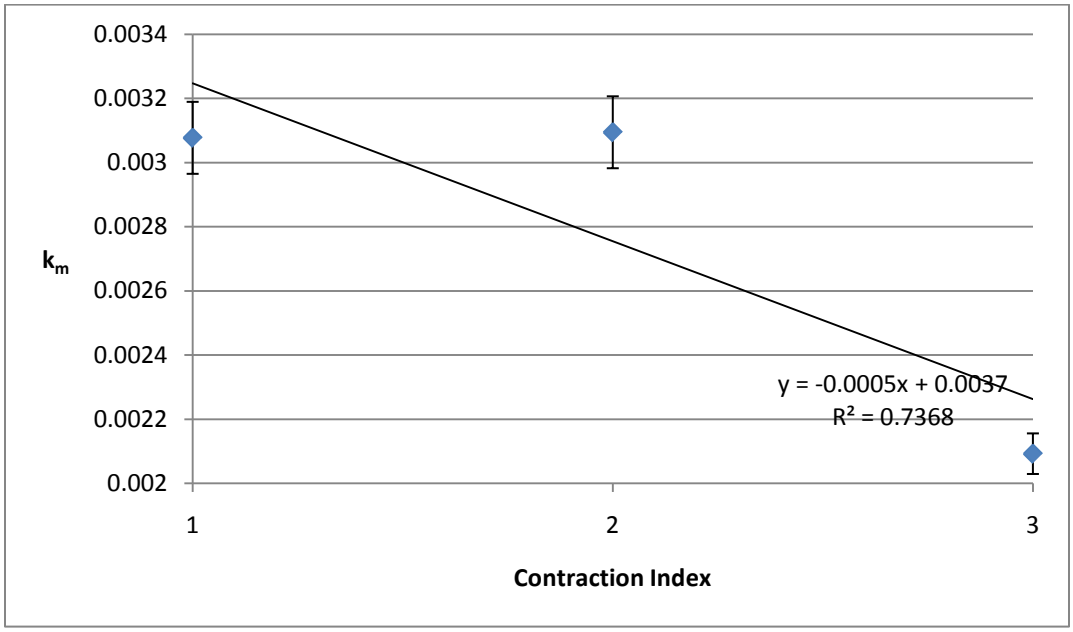

Figure F-4. Behavior of k_m in untrained limb of Subject 18 at warm-up.

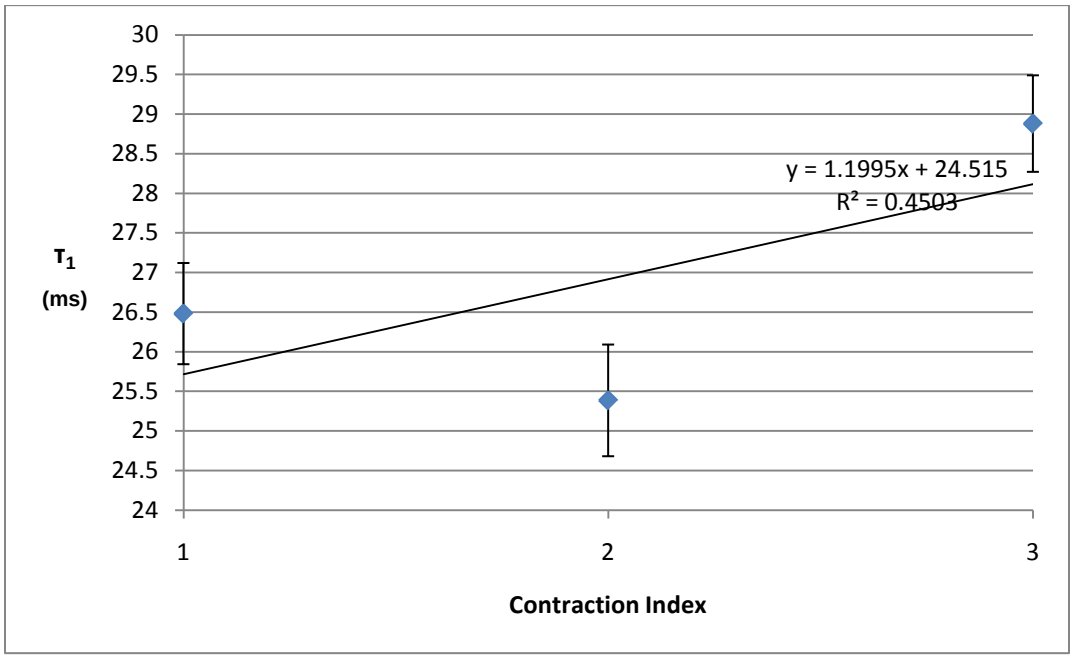

Figure F-5. Behavior of τ_1 in untrained limb of Subject 18 at warm-up.

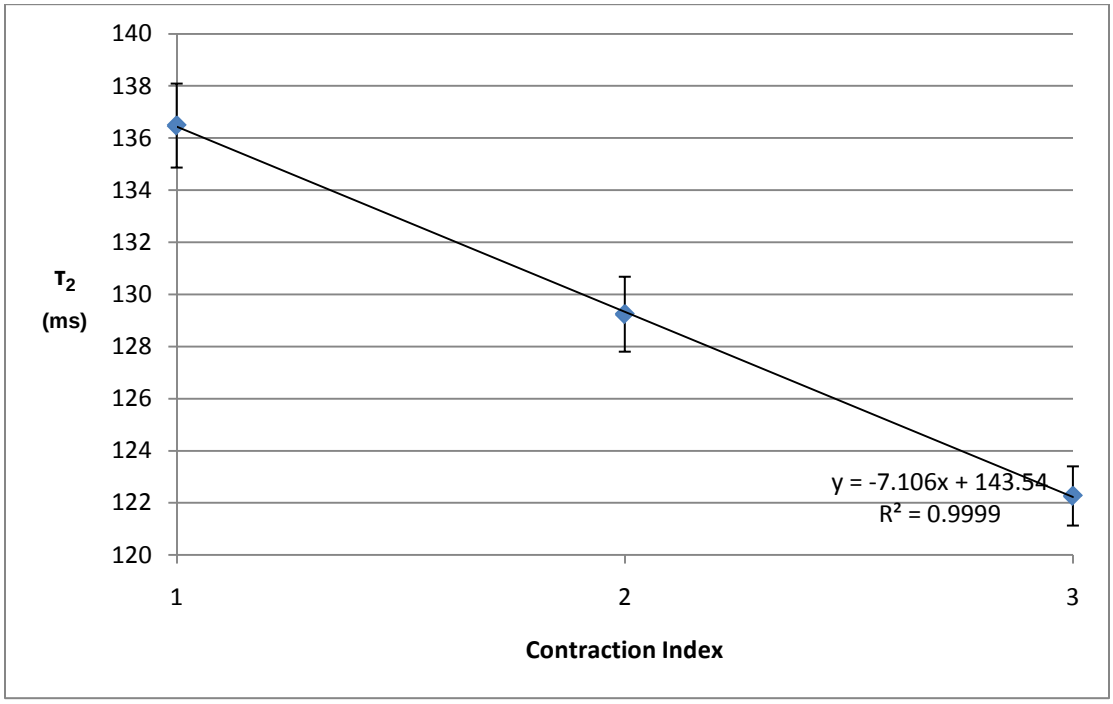

Figure F-6. Behavior of τ_2 in untrained limb of Subject 18 at warm-up.

Table F-3. Behavior of free parameters from doublet ramp inputs in untrained muscle optimized on the set $\{k_m, \tau_1\}$. The parameters do not change much between first and second contractions for all Subjects. There are no discernable trends.

Subject/ contraction number	k_m	k_m σ	τ_1	τ_1 σ
17-1	0.005594	0.000334398	8.02345	1.89011
17-2	0.000969	2.6565F-05	17.2267	0.950537
18-1	0.001446	0.000123907	84.3839	2.76143
18-2	0.001827	0.000139804	86.193	2.46818
27-1	0.001204	9.87511F-05	88.0623	2.64616
27-2	0.001201	9.83593F-05	88.0096	2.64504
28-1	0.000868	6.11702F-05	48.9058	2.18009
28-2	0.000865	0.000060984	48.8702	2.17944

Table F-4. Behavior of free parameters from doublet ramp inputs in untrained muscle optimized on the set {k_m, τ_1}. The parameters do not change much between first and second contractions for all Subjects. There are no discernable trends.

Subject/ contraction number	k_m	k_m σ	τ_1	τ_1 σ
17-1	0.005193	0.000466608	92.0709	2.65564
17-2	0.003543	0.000364893	105.786	3.24478
18-1	0.003591	0.00034845	81.4703	2.80956
18-2	0.005236	0.000471061	92.2338	2.65827
27-1	0.004527	0.000577342	99.8102	3.6713
27-2	0.002972	0.000229781	110.543	2.87731
28-1	0.001061	6.55643F-05	76.1982	2.3745
28-2	0.000116	6.20646F-05	78.5621	2.02025

APPENDIX G: A FATIGUING BOUT IN TRAINED MUSCLE

Table G-1. Parameter values for contraction 1 in the trained limb of Subject 17.

Parameter	Optimized value	Standard deviation	Free or fixed	Range
τ_2	62.7	0	Fixed	[0 ∞]
τ_c	20	0	Fixed	[0 ∞]
a	1	0	Free	[0,50]
b	1.5	0	Free	[0,10]
c	1	0	Free	[0,10]
τ_{1rest}	28.3	0	Fixed	[0,10]
τ_{fat}	82.6344	9.34955	Free	[0,50]
$\alpha_{\tau 1}$	0.678847	0.102152	Free	[0 50]
μ_1	0.38	0	Fixed	[0 ∞]
μ_2	0.5	0	Fixed	[0 ∞]
τ_{leak}	245.676	4.73417	Free	[0, 1000]
A [gain]	0.049609	0.0011162	Free	[0 ∞]

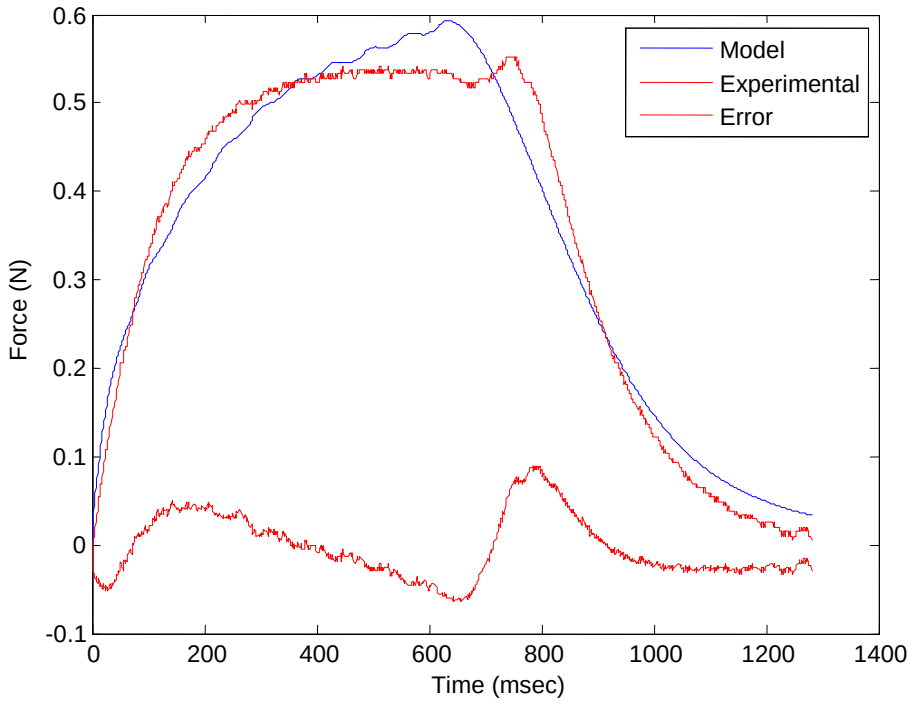

Figure G-1. Contraction 1 of fatiguing bout in the trained limb of Subject 17. The agreement of the Conaway model with the experimental data is 0.98436.

Table G-2. Parameter values for contraction 2 in the trained limb of Subject 17.

Parameter	Optimized value	Standard deviation	Free or fixed	Range
τ_2	62.7	0	Fixed	[0 ∞]
τ_c	20	0	Fixed	[0 ∞]
a	1	0	Free	[0,50]
b	1.5	0	Free	[0,10]
c	1	0	Free	[0,10]
τ_{1rest}	28.3	0	Fixed	[0,10]
τ_{fat}	47.9305	8.932	Free	[0,50]
$\alpha_{\tau 1}$	1.35213	0.320982	Free	[0 50]
μ_1	0.38	0	Fixed	[0 ∞]
μ_2	0.5	0	Fixed	[0 ∞]
τ_{leak}	248.536	5.13729	Free	[0, 1000]
A [gain]	0.0434818	0.001232444	Free	[0 ∞]

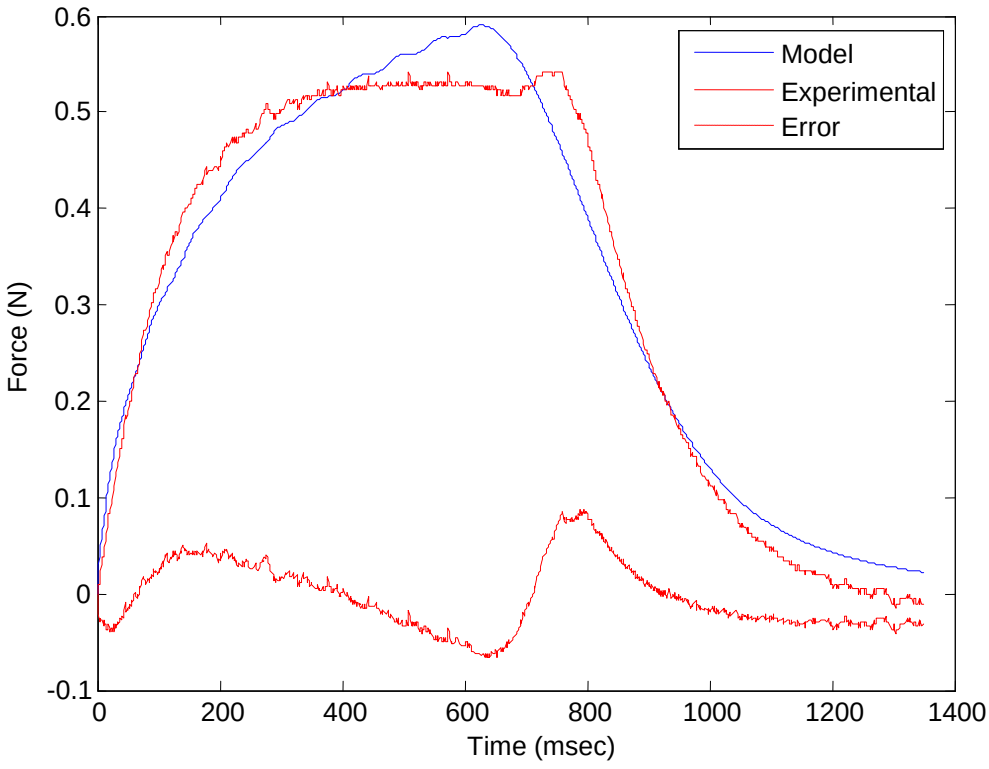

Figure G-2. Contraction 2 of fatiguing bout in the trained limb of Subject 17. The agreement of the Conaway model with the experimental data is 0.985999.

Table G-3. Parameter values for contraction 3 in the trained limb of Subject 17.

Parameter	Optimized value	Standard deviation	Free or fixed	Range
τ_2	62.7	0	Fixed	[0 ∞]
τ_c	20	0	Fixed	[0 ∞]
a	1	0	Free	[0,50]
b	1.5	0	Free	[0,10]
c	1	0	Free	[0,10]
τ_{1rest}	28.3	0	Fixed	[0,10]
τ_{fat}	30.5766	9.27007	Free	[0,50]
$\alpha_{\tau 1}$	2.44676	0.891975	Free	[0 50]
μ_1	0.38	0	Fixed	[0 ∞]
μ_2	0.5	0	Fixed	[0 ∞]
τ_{leak}	258.528	6.38156	Free	[0, 1000]
A [gain]	0.0405142	0.00139022	Free	[0 ∞]

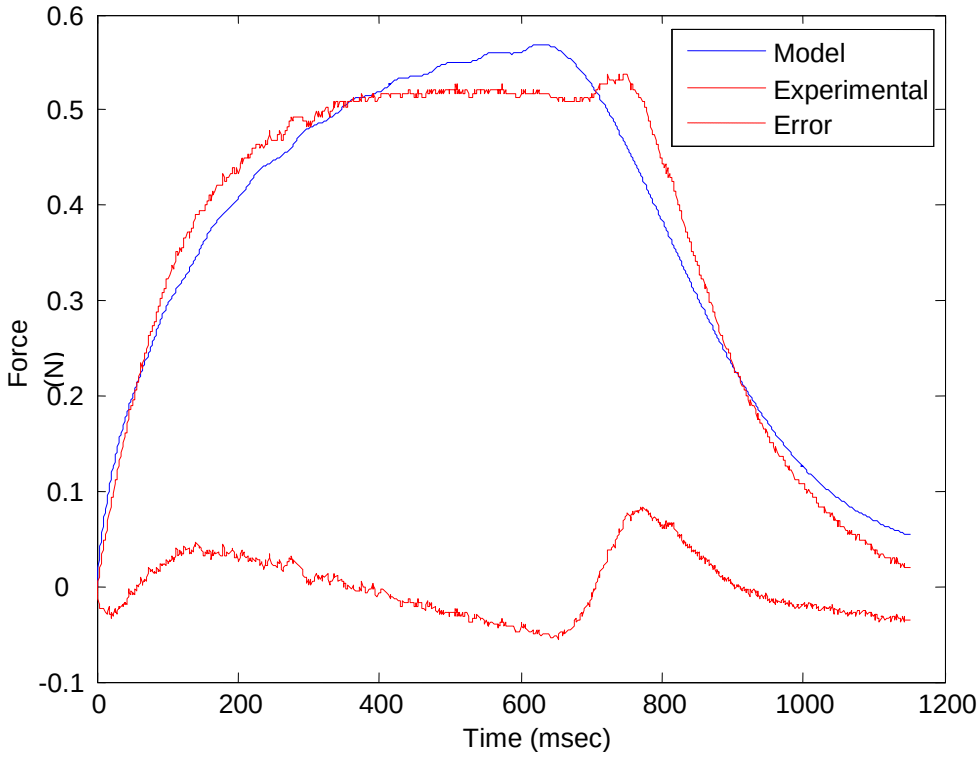

Figure G-3. Contraction 3 of fatiguing bout in the trained limb of Subject 17. The agreement of the Conaway model with the experimental data is 0.982276.

Table G-4. Parameter values for contraction 4 in the trained limb of Subject 17.

Parameter	Optimized value	Standard deviation	Free or fixed	Range
τ_2	62.7	0	Fixed	[0 ∞]
τ_c	20	0	Fixed	[0 ∞]
a	1	0	Free	[0,50]
b	1.5	0	Free	[0,10]
c	1	0	Free	[0,10]
τ_{1rest}	28.3	0	Fixed	[0,10]
τ_{fat}	20.7245	8.35242	Free	[0,50]
$\alpha_{\tau 1}$	3.84758	1.77835	Free	[0 50]
μ_1	0.38	0	Fixed	[0 ∞]
μ_2	0.5	0	Fixed	[0 ∞]
τ_{leak}	265.434	6.22485	Free	[0, 1000]
A [gain]	0.0404436	0.00136347	Free	[0 ∞]

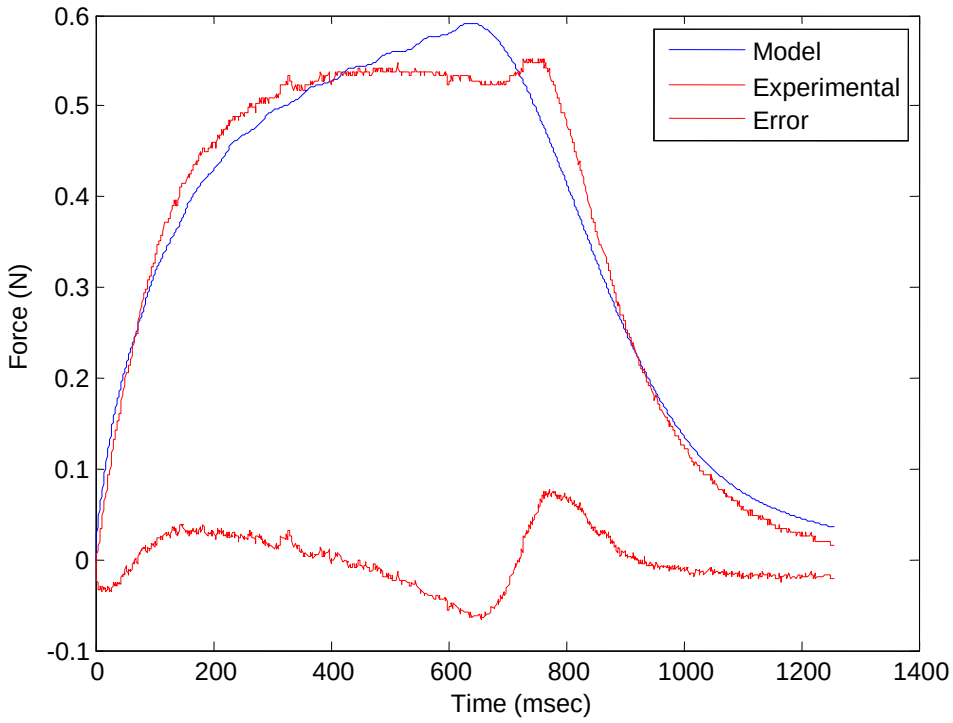

Figure G-4. Contraction 4 of fatiguing bout in the trained limb of Subject 17. The agreement of the Conaway model with the experimental data is 0.9870934.

Table G-5. Parameter values for contraction 5 in the trained limb of Subject 17.

Parameter	Optimized Value	Standard deviation	Free or fixed	Range
τ_2	62.7	0	Fixed	[0 ∞]
τ_c	20	0	Fixed	[0 ∞]
a	1	0	Free	[0,50]
b	1.5	0	Free	[0,10]
c	1	0	Free	[0,10]
τ_{1rest}	28.3	0	Fixed	[0,10]
τ_{fat}	14.6612	10.8726	Free	[0,50]
$\alpha_{\tau 1}$	5.94942	4.86385	Free	[0 50]
μ_1	0.38	0	Fixed	[0 ∞]
μ_2	0.5	0	Fixed	[0 ∞]
τ_{leak}	262.178	8.07727	Free	[0, 1000]
A [gain]	0.0374571	0.00162895	Free	[0 ∞]

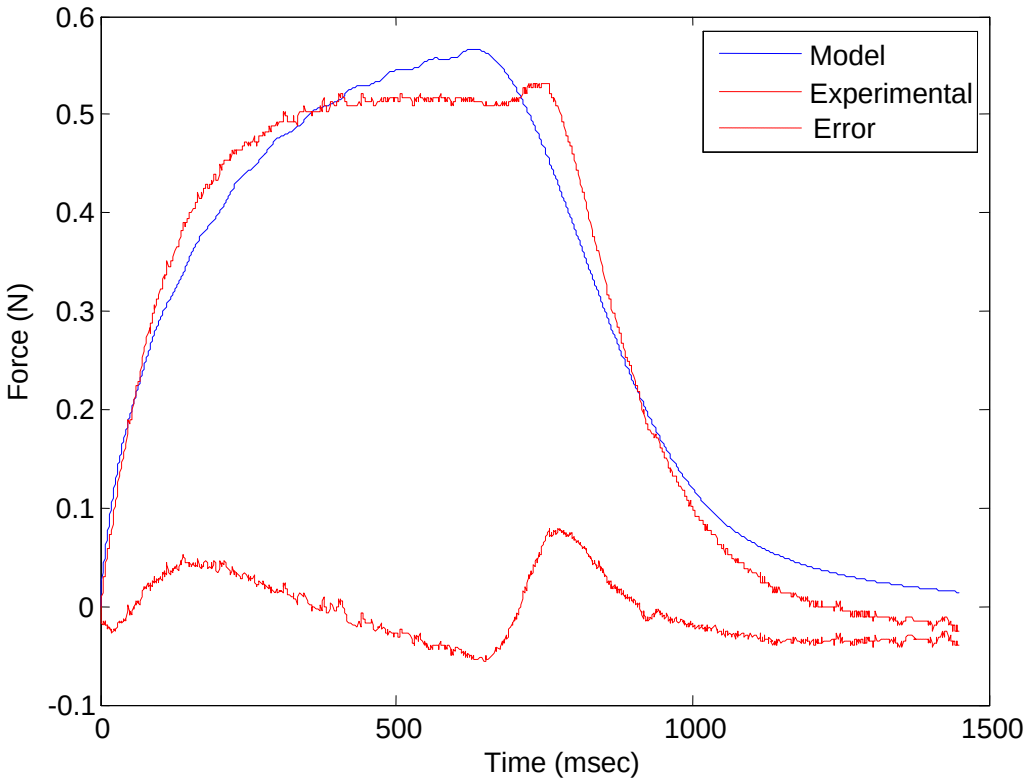

Figure G-5. Contraction 5 of fatiguing bout in the trained limb of Subject 17. The agreement of the Conaway model with the experimental data is 0.989389.

Table G-6. Parameter values for contraction 6 in the trained limb of Subject 17.

Parameter	Optimized value	Standard deviation	Free or fixed	Range
τ_2	62.7	0	Fixed	[0 ∞]
τ_c	20	0	Fixed	[0 ∞]
a	1	0	Free	[0,50]
b	1.5	0	Free	[0,10]
c	1	0	Free	[0,10]
τ_{1rest}	28.3	0	Fixed	[0,10]
τ_{fat}	10.5671	11.3016	Free	[0,50]
$\alpha_{\tau 1}$	8.4335	9.68217	Free	[0 50]
μ_1	0.38	0	Fixed	[0 ∞]
μ_2	0.5	0	Fixed	[0 ∞]
τ_{leak}	282.119	9.69667	Free	[0, 1000]
A [gain]	0.0385665	0.00177335	Free	[0 ∞]

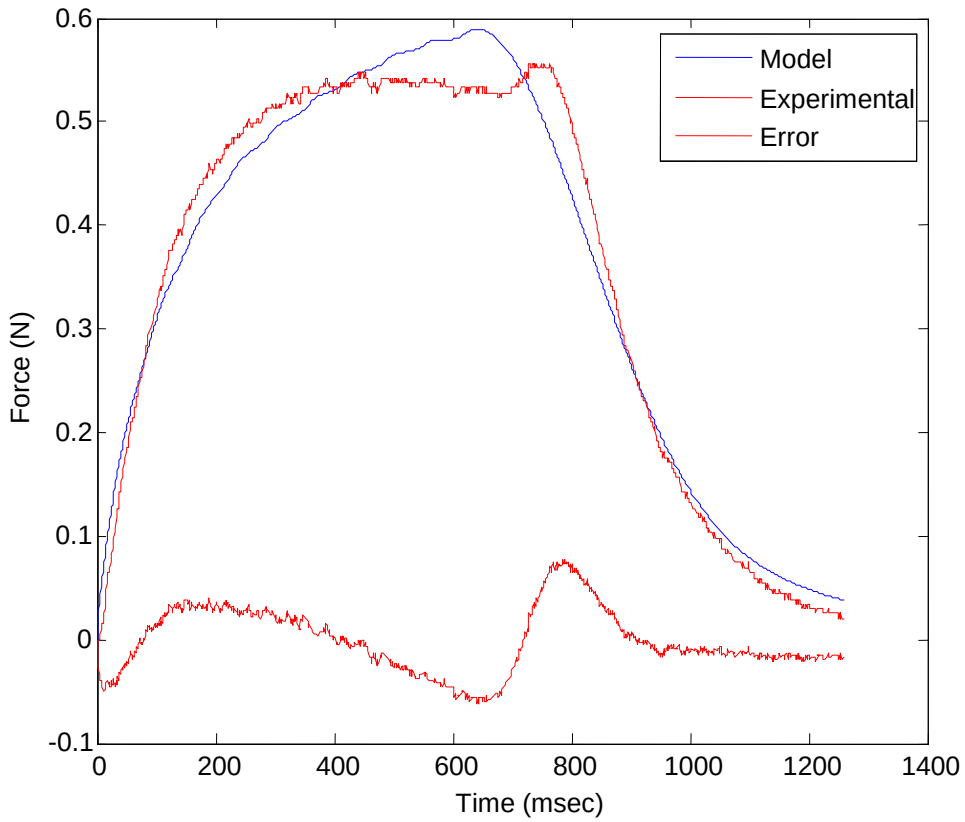

Figure G-6. Contraction 6 of fatiguing bout in the trained limb of Subject 17. The agreement of the Conaway model with the experimental data is 0.987693.

Table G-7. Comparison of error statistics of the Conaway fatigue model for each contraction of the trained limb of Subject 17. The statistics are consistent throughout the fatiguing bout.

Index of contraction	Mean Squared Error	Mean Absolute Error	Correlation Coefficient	95% CI	r^2	p-value
1	0.0357964	0.00292124	0.98436	(0.982525 0.985942	0.96888	<0.001
2	0.0358214	0.00347381	0.985999	(0.984434 0.987408	0.972194	<0.001
3	0.0332351	0.000291189	0.982276	(0.980124 0.984197)	0.964867	<0.001
4	0.0305759	0.000861972	0.9870934	(0.98653 0.98912)	0.976013	<0.001
5	0.0033963	0.00667116	0.989389	(0.988244 0.990422)	0.97889	<0.001
6	0.0309711	0.00133888	0.987693	(0.986265 0.988974)	0.975538	<0.001

Table G-8. Loss functions and Akaike FPEs for each contraction of the trained limb of Subject 17. The functions are consistently low throughout the fatiguing bout.

Index of contraction	1	2	3	4	5	6
Loss Function	0.001281	0.0012831	0.0011045	0.00093488	0.0011534	0.00095920
Akaike final prediction error	0.001295	0.0012964	0.0011180	0.00094530	0.0011646	0.00096985

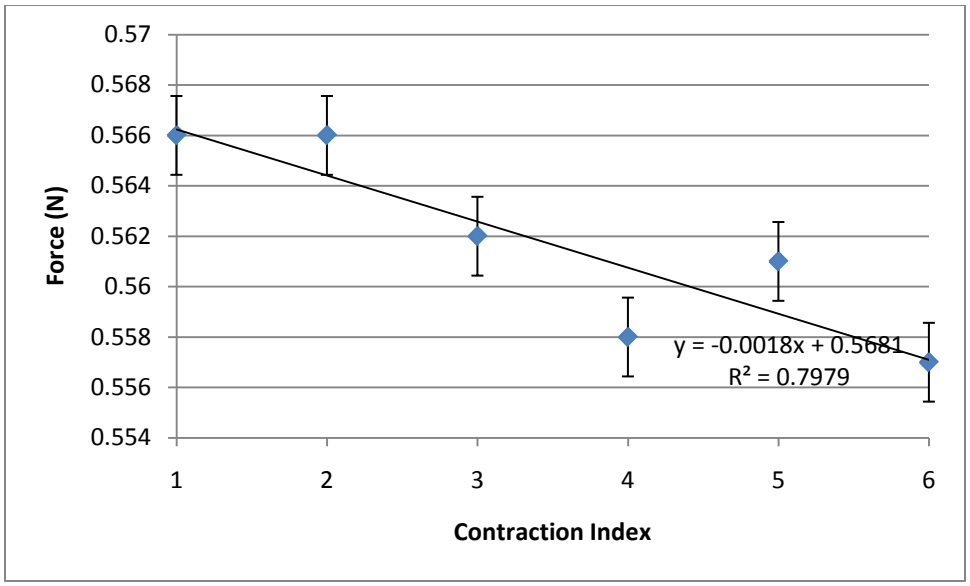

Figure G-7. Peak forces for each contraction in a fatiguing bout n the trained limb of Subject 17. The peak forces generally decay with each contraction. This shows that potentiation occurs in fatiguing paralyzed muscle.

APPENDIX H: A FATIGUING BOUT IN UNTRAINED MUSCLE

Table H-1. Parameter values for contraction 1 in the untrained limb of Subject 18.

Parameter	Optimized value	Standard deviation	Free or fixed	Range
τ_2	62.7	0	Fixed	[0 ∞]
τ_c	20	0	Fixed	[0 ∞]
a	1	0	Free	[0,50]
b	1.5	0	Free	[0,10]
c	1	0	Free	[0,10]
τ_{1rest}	28.3	0	Fixed	[0 ∞]
τ_{fat}	29.8741	6.5412	Free	[0,50]
$\alpha_{\tau 1}$	3.044584	0.459981	Free	[0 50]
μ_1	0.38	0	Fixed	[0 ∞]
μ_2	0.5	0	Fixed	[0 ∞]
τ_{leak}	95.1453	2.73726	Free	[0, 1000]
A [gain]	0.440372	0.0249183	Free	[0 ∞]

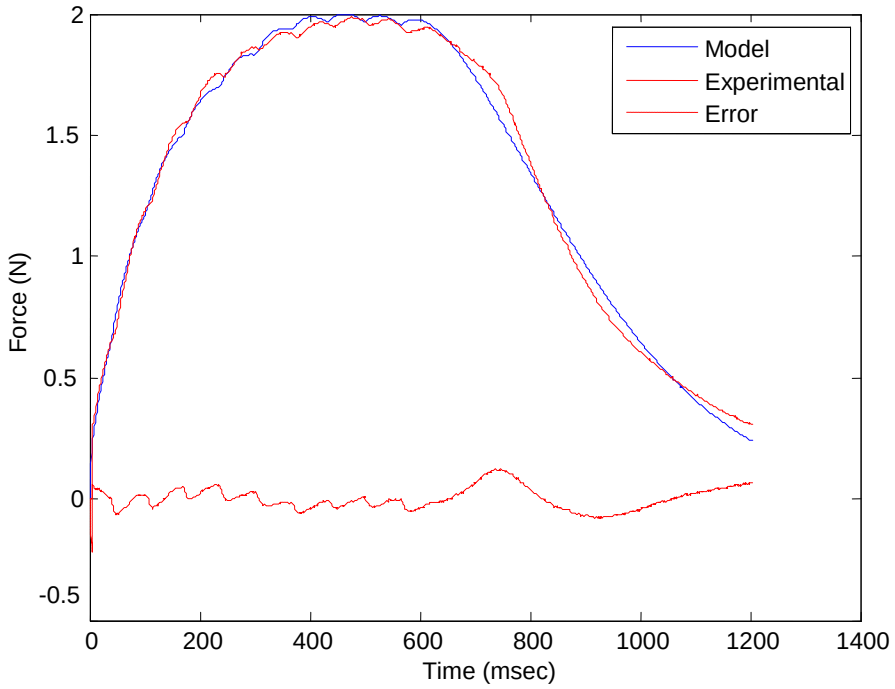

Figure H-1. Contraction 1 of fatiguing bout in the untrained limb of Subject 18. The agreement of the Conaway model with the experimental data is 0.975184.

Table H-2. Parameter values for contraction 2 in the untrained limb of Subject 18.

Parameter	Optimized value	Standard deviation	Free or fixed	Range
τ_2	62.7	0	Fixed	[0 ∞]
τ_c	20	0	Fixed	[0 ∞]
a	1	0	Free	[0,50]
b	1.5	0	Free	[0,10]
c	1	0	Free	[0,10]
τ_{1rest}	28.3	0	Fixed	[0 ∞]
τ_{fat}	31.7369	4.88137	Free	[0,50]
$\alpha_{\tau 1}$	3.909893	0.451615	Free	[0 50]
μ_1	0.38	0	Fixed	[0 ∞]
μ_2	0.5	0	Fixed	[0 ∞]
τ_{leak}	95.1785	2.48151	Free	[0, 1000]
A [gain]	0.560193	0.0356424	Free	[0 ∞]

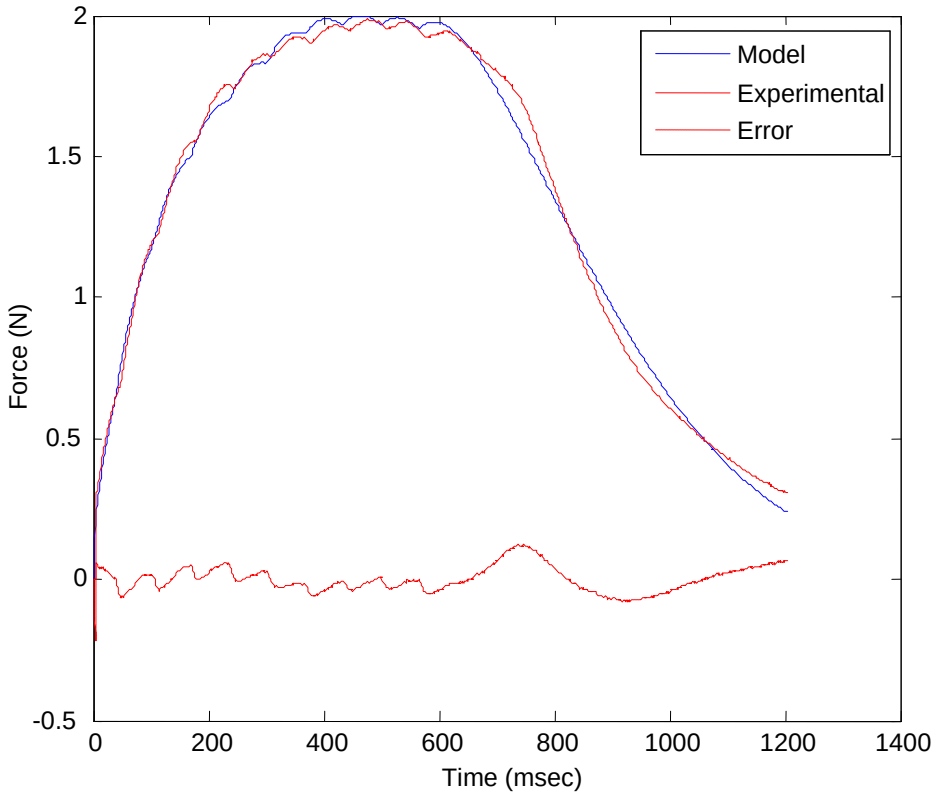

Figure H-2. Contraction 2 of fatiguing bout in the untrained limb of Subject 18. The agreement of the Conaway model with the experimental data is 0.932472.

Table H-3. Parameter values for contraction 3 in the untrained limb of Subject 18.

Parameter	Optimized value	Standard deviation	Free or fixed	Range
τ_2	62.7	0	Fixed	[0 ∞]
τ_c	20	0	Fixed	[0 ∞]
a	1	0	Free	[0,50]
b	1.5	0	Free	[0,10]
c	1	0	Free	[0,10]
τ_{1rest}	28.3	0	Fixed	[0 ∞]
τ_{fat}	35.01743	5.01294	Free	[0,50]
$\alpha_{\tau 1}$	3.003732	0.168069	Free	[0 50]
μ_1	0.38	0	Fixed	[0 ∞]
μ_2	0.5	0	Fixed	[0 ∞]
τ_{leak}	102.3633	3.94424	Free	[0, 1000]
A [gain]	0.517513	0.00993602	Free	[0 ∞]

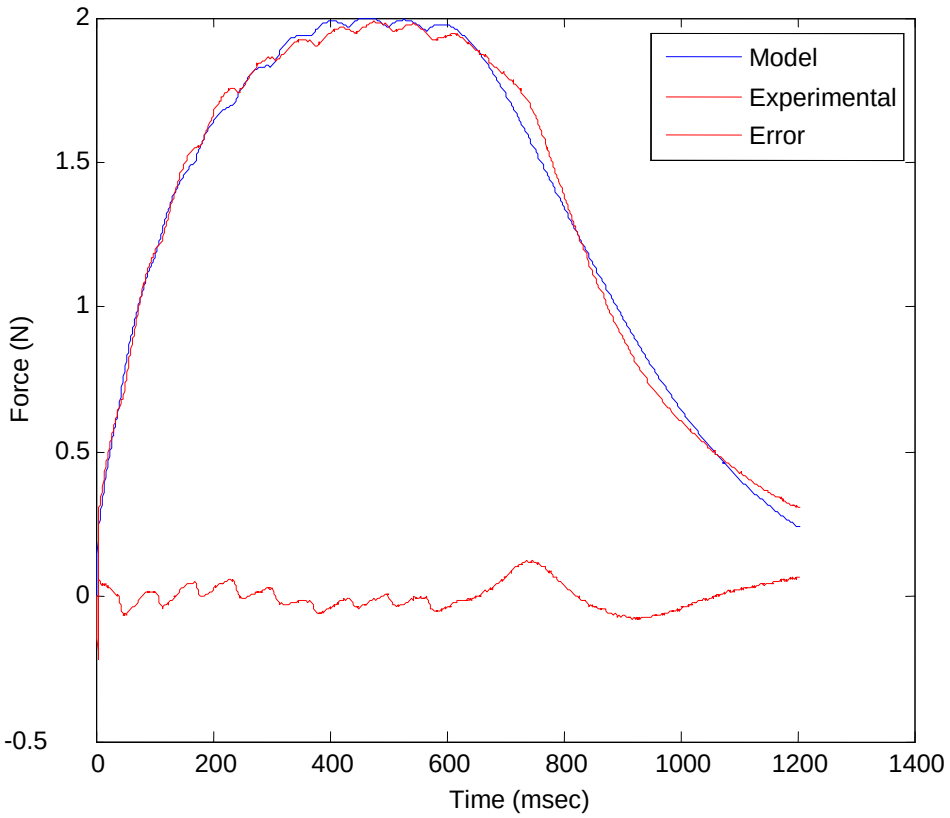

Figure H-3. Contraction 3 of fatiguing bout in the untrained limb of Subject 18. The agreement of the Conaway model with the experimental data is 0.912205.

Table H-4. Comparison of error statistics of the Conaway fatigue model for each contraction in the untrained limb of Subject 18. The statistics are consistent throughout the fatiguing bout.

Index of contraction	Mean Squared Error	Mean Absolute Error:	Correlation Coefficient	95% CI	r^2	p-value
1	0.119603	0.0244814	0.987514	(0.98239 0.99154)	0.975184	<0.001
2	0.223413	0.0465656	0.965646	(0.956317 0.97301)	0.932472	<0.001
3	0.243065	0.0494019	0.955094	(0.9427766 0.964815)	0.912205	<0.001

Table H-5. Loss functions and Akaike FPEs for each contraction of the untrained limb of Subject 18. The functions are consistently low throughout the fatiguing bout.

Index of contraction	1	2	3
Loss Function	0.0143049	0.0499135	0.0590804
Akaike final prediction error	0.0151785	0.0514552	0.0609635

REFERENCES

1. Aidley DJ. The physiology of excitable cells, 4th edition. Cambridge: Cambridge University Press, 1998.

2. Allen DG. Skeletal muscle function: role of ionic changes in fatigue, damage and disease. Clin Exp Pharmacol Physiol. 2004 Aug;31(8):485-93.

3. Allen DG, Lamb GD, Westerblad H. Skeletal muscle fatigue: cellular mechanisms. Physiol Rev. 2008 Jan;88(1):287-332.

4. Allen DG, Lamb GD, Westerblad H. Impaired calcium release during fatigue. J Appl Physiol. 2008 Jan;104(1):296-305. Epub 2007 Oct 25.

5. Anderson RM, May RM. Infectious diseases of humans. Oxford: Oxford University Press, 1992.

6. Balasubramaniam, P. Samath, JA, Kumaresan N, Kumar, AVA. Solution of matrix Riccati differential equation for the linear quadratic singular system using neural networks. Appl Math Comput, 2006; 182(2): 1832-9.

7. Baldwin KM, Roy RR, Sacks RD, Blanco C, and Edgerton VR. Relative independence of metabolic enzymes and neuromuscular activity. 1984; J Appl Physiol 56: 1602-07

8. Bancroft WD. A universal law. J Am Chem Soc. 1911; 33(2): 91-120.

9. Banks RB. Growth and diffusion phenomena: mathematical frameworks and applications. Berlin, New York: Springer-Verlag, 1994.

10. Bass FM. A new product growth model for consumer durables. Mgmt Sci, 1969;15(5):215-227.

11 Bellinger AM, Reiken S, Dura M, Murphy PW, Deng SX, Landry DW, Nieman D, Lehnart SE, Samaru M, LaCampagne A, Marks AR. Remodeling of ryanodine receptor complex causes "leaky" channels: a molecular mechanism for decreased exercise capacity. Proc Natl Acad Sci USA. 2008 Feb 12; 105(6): 2198-2202.

12. Berchtold MW, Brinkmeier H, Müntener M. Calcium ion in skeletal muscle: its crucial role for muscle function, plasticity, and disease. Physiol Rev. 2000 Jul;80(3):1215-65.

13. Bernoulli D. Exercitationes quaedam Mathematicae. Basel: 1724.

14. von Bertalanffy L. Quantitative laws in metabolism and growth. Quart. Rev. Biol., 1957; 32(3): 217-31.

15. Billingham J, Needham DJ. Mathematical modelling of chemical clock reactions. I. Induction, inhibition and the iodate-arsenous-acid reactions. Phil Trans Royal Soc Lond: Physical Sciences and Engineering, 1992; 340:1659; 569-91.

16. Bittanti S. History and prehistory of the Riccati equation. Proceedings of the 35th IEEE Conference on Decision and Control. Kobe, Japan. December 11-13, 1996; 2: 1599-1604.

17. Bobet J and Stein RB. A simple model of force generation by skeletal muscle during dynamic isometric contractions. IEEE Trans Biomed Eng, 1998; 45:1010-16.

18. Bobet J, Gossen ER, Stein RB. A comparison of models of force production during stimulated isometric ankle dorsiflexion in humans. IEEE Trans Neural Sys Rehab Eng, 2005; 13(4):444-51.

19 Boole G. A treatise on differential equations. Cambridge: Macmillan, 1859.

20. Bozzo C, Spolaore B, Toniolo L, Stevens L, Bastide B, Cieniewski-Bernard C, Fontana A, Mounier Y, and Reggiani C. Nerve influence on myosin light chain phosphorylation in slow and fast skeletal muscles. Am J Physiol Cell Physiol. 2005; 272: 571-85.

21. Bozzo C, Stevens L, Toniolo L, Mounier Y, and Reggiani C. Increased phosphorylation of myosin light chain associated with slow-to-fast transition in rat soleus. Am J Physiol Cell Physiol, 2003; 285: C575-83.

22. Bradley DM. Verhulst's logistic curve. The College Mathematics Journal, 2001; 32(2): 94-98.

23. Bryson AE, Ho YC. Applied optimal control. Washington, DC: Hemisphere, 1975.

24. Buis R. On the generalization of the logistic law of growth. Acta Biotheoretica, 1991: 39: 185-95.

25. Cajal SR. Histologie du systeme nerveux de l'homme et des vertebrés. Paris: Maloine, 1909.

26. Capasso V. The mathematical structure of epidemic systems. Berlin: Springer-Verlag, 1993.

27. del Castillo J, Stark L. The effect of calcium ions on the motor end-plate potentials. J. Physiol. (Lond.), 1952 Apr;116(4):507-15.

28. del Castillo J, Katz B. Quantal components of the end-plate potential. J. Physiol. (Lond.), 1954; 124: 560-73.

29. del Castillo J, Katz B. Statistical factors involved in neuromuscular facilitation and depression. J. Physiol. (Lond.), 1954; 124: 574-85.

30. del Castillo J, Katz B. The membrane change produced by the neuromuscular transmitter. J. Physiol. (Lond.), 1954; 125: 546-65.

31. del Castillo J, Katz B. Biophysical aspects of neuromuscular transmission. Prog. Biophys. Biophys. Chem. 1956; 6: 121-70.

32. Catterall WA. Structure and regulation of voltage-gated Ca^{2+} channels. Ann Rev Cell Dev Biol, 2000;16:521–55.

33. Chang YJ and Shields RK. Within-train neuromuscular propagation varies with torque in denervated human muscle. Muscle Nerve, 2002; 26: 673-80.

34. Coleman JS. Introduction to mathematical sociology. Glencoe, CA: The Free Press, 1964.

35. Chua M, Dulhunty AF. Inactivation of excitation-contraction coupling in rat extensor digitorum longus and soleus muscles. J Gen Physiol, 1988 May;91(5):737-57.

36. Crago PE, Mortimer JT, Peckham PH. Closed-loop control of force during electrical stimulation of muscle. IEEE Trans Biomed Eng, 1980;27(6):306-12.

37. Crago PE, Lan N, Veltink PH, Abbas JJ, Kantor CK. New control strategies for neuroprosthetic systems. J Rehab Res Dev, 1996; 33(2); 158-72.

38. Cummings JP. "Electrical stimulation of denervated muscle." Ch. 8 in Gersh MR, editor. Electrotherapy in rehabilitation. Philadelphia: FA Davis; 1992.

39. Davis, HT. Introduction to nonlinear differential and integral equations. New York: Dover Publications, 1962.

40. Delbono O. Calcium current activation and charge movement in denervated mammalian skeletal muscle fibres. J Physiol. (Lond.), 1992; 451: 187-203.

41. Delbono O, Stefani E. Calcium current inactivation in denervated rat skeletal muscle fibres. J Physiol. (Lond.), 1993; 460: 173-83.

42. DeVahI J. "Neuromuscular electrical stimulation (NMES) in rehabilitation." Ch. 7 in Gersh MR (ed.), Electrotherapy in rehabilitation. Philadelphia: FA Davis; 1992.

43. DeVivo MJ. Epidemiology of traumatic spinal cord injury. In: Kirshblum S et al (eds.), Spinal cord medicine, vol 1. Baltimore: Lippincott Williams & Wilkins; 2002: 69-81.

44. DeVivo MJ, Kartus PL, Rutt RD, et al. The influence of age at time of spinal cord injury on rehabilitation outcome. Arch Neurol, 1990; 47: 687-91.

45. DeVivo MJ, Rutt RD, Black KJ, et al. Trends in spinal cord injury demographics and treatment outcomes between 1973 and 1986. Arch Phys Med Rehab, 1992; 73(5): 424-30.

46. DeVivo MJ, Krause MJ, Lammertse DP: Recent trends in mortality and causes of death among persons with spinal cord injury. Arch Phys Med Rehab, 1999; 80(11): 1411-19.

47. Dietz V. Spinal cord lesion: effects of and perspectives for treatment. Neural Plast. 2001; 8(1-2): 83-90.

48. Ding J, Wexler AS, Binder-Macleod SA. A mathematical model that predicts skeletal muscle force. IEEE Trans Biomed Eng, 1997; 44(5): 337-48.

49. Ding J, Binder-Macleod SA, and Wexler AS. Two-step, predictive, isometric force model tested on data from human and rat muscles. J Appl Physiol, 1998; 85: 2176-89.

50. Ding J, Wexler AS, and Binder-Macleod SA. Development of a mathematical model that predicts optimal muscle activation patterns by using brief trains. J Appl Physiol, 2000; 88: 917-25.

51. Ding J, Wexler AS, Binder-Macleod SA. A predictive model of fatigue in human skeletal muscles. J Appl Physiol, 2000; 89:1322-32.

52. Ding J, Wexler AS, Binder-Macleod SA. A predictive fatigue model--I: Predicting the effect of stimulation frequency and pattern on fatigue. IEEE Trans Neural Syst Rehabil Eng. 2002 Mar;10(1):48-58. Erratum in: IEEE Trans Neural Syst Rehabil Eng. 2003 Mar;11(1):86.

53. Ding J, Wexler AS, Binder-Macleod SA. A predictive fatigue model--II: Predicting the effect of resting times on fatigue. IEEE Trans Neural Syst Rehabil Eng. 2002 Mar;10(1):59-67.

54. Ding J, Wexler AS, Binder-Macleod SA. A mathematical model that predicts the force-frequency relationship of human skeletal muscle. Muscle Nerve. 2002 Oct;26(4):477-85.

55. Ding J, Wexler AS, Binder-Macleod SA. Mathematical models for fatigue minimization during functional electrical stimulation. J Electromyogr Kinesiol. 2003 Dec;13(6):575-88.

56. Ding J, Wexler AS, Lee SC, Johnston TE, Scott WB, Binder-Macleod SA. Mathematical model that predicts isometric muscle forces for individuals with spinal cord injuries. Muscle Nerve, 2005 Jun; 31(6): 702-12.

57. Doctorow O. The strange case of the non-history of exponential "information". http://mathforum.org/kb/thread.jspa?threadID=438360&tstart=210. [20 Oct 2003].

58. Duchateau J, Hainaut K. Nonlinear summation of contractions in skeletal muscle. I. Twitch potentiation in human muscle. J Muscle Cell Motil 1986;7:11-17.

59. Dulhunty AF. Activation and inactivation of excitation-contraction coupling in rat soleus muscle. J Physiol, 1991 Aug;439:605-26.

60. Dulhunty AF, Gage PW. Asymmetrical charge movement in slow- and fast-twitch mammalian muscle fibres in normal and paraplegic rats. J Physiol, 1983 Aug;341:213-31.

61. Dulhunty AF, Gage PW. Excitation-contraction coupling and charge emovement in denervated rat extensor digitorum longus and soleus muscles. J Physiol, 1985 Jan;358:75-89.

62. Edwards HT. Human muscle function and fatigue. In Porter R. and Whelan S. (eds.), Human muscle fatigue: physiological mechanisms. London: Pitman Medical, 1981.

63. Enoka RM. Muscle strength and its development: a new perspective. Sports Medicine. 1998;6:146-68.

64. Epstein M, Herzog W. Theoretical models of skeletal muscle. Chichester, England: John Wiley & Sons; 1998.

65. Euler L. Constructio Aequationum quarundam differentialium, que indeterminarium separationem non admittunt. Nova Acta Eruditorum, Aug. 1733;369-72 Translated by Bruce IR at www.17thcenturymaths.com, 2005.

66. Frey-Law LA, Shields RK. Predicting human chronically denervated muscle force: A comparison of three mathematical models. J Appl Physiol, 2006;100: 1027-36.

67. Gail MH. Dose-response. Encyclopedia of biostatistics. New York: Wiley, 2005, p. 56.

68. Gill PE, Murray W. Algorithms for the solution of the nonlinear least-squares problem. SIAM J Numer Anal, 1978; 15(5):977-92.

69. Goldman YE. Huxley AF. Actin compliance: are you pulling my chain? Biophvs J. 1994; 67: 2131-33.

70. Gompertz B. On the nature of the function expressive of the law of human mortality, and on a new mode of determining the value of life contingencies. Phil Trans Royal Soc Lond, 1825; 115: 513-85.

71. Green DM, Swets JA. Signal detection theory and psychophysics. New York: Wiley, 1966.

72. Grimby G, Broberg C, Krotkiewska I, and Krotkiewski M. Muscle fiber composition in patients with traumatic cord lesion. Scand J Rehabil Med 1976; 8: 37-42.

73. Guyton AC, Hall JH. Textbook of medical physiology. 10th edition. Philadelphia: WB Saunders Company; 2000.

74. Harris RL, Bobet J, Sanelli L, Bennett DJ. Tail muscles become slow but fatigable in chronic sacral spinal rats with spasticity. J Neurophysiol. 2006: 95: 1124-33.

75. Hannaford B. A nonlinear model of the phasic dynamics of muscle activation. IEEE Trans Biomed Eng, 1990 Nov;37(11):1067-75.

76. Henneman E, Olson CB. Relations between structure and function in the design of skeletal muscles. J Neurophysiol, 1965;28:581-98.

77. Henneman E. Organization of the spinal cord and its reflexes. In Mountcastle VB editor. Medical physiology, 14th edition. St Louis: CV Mosby,1980.

78. Hernes G. Diffusion and growth-the non-homogeneous case. Scand J. Econ, 1976; 78(3): 427-36.

79. Hidler JM, Harvey RL, Rymer WZ. Frequency response characteristics of ankle plantar flexors in humans following spinal cord injury: relation to degree of spasticity. Ann Biomed Eng, 2002; 30: 969-81.

80. Hill AV. The heat of shortening and the dynamic constants of muscle. Proc. R. Soc. London B, 1938; 126: 136-95.

81. Hill AV, Long CNH, Lupton H. Muscular exercise, lactic acid, and the supply and utilization of oxygen. Proc R Soc Lond B Biol Sci, 1924; 16: 84-137.

82. Hill AV. Croonian lecture. Proc R Soc Lond B Biol Sci, 1926; 100: 87.

83. Hill TL. Eisenberg E. Chen Y. Some self-consistent two-state sliding filament models of muscle contraction. Biophvs J, 1975; 15: 335-72.

84. Hill TL. Free energy transduction in biology. New York: Academic Press, 1977.

85. Huxley AF. Muscle structure and theories of contraction. Prog Biophys Biophys Chem. 1957; 7: 225-318.

86. Huxley.AF, Simmons RM. Proposed mechanism of force generation in striated muscle. Nature, 1971; 233: 533-8.

87. Huxley AF. Muscular contraction. J Physiol. 1974 Nov;243(1):1-43.

88. Huxley AF. Muscular contraction. Ann Rev Physiol, 1988; 50, 1-16.

89. Huxley AF, Tideswell B. Filament compliance and tension transients in muscle. J Musc Res Cell Mat. 1996; 17: 507-11.

90. Ince EL. Ordinary differential equations. New York: Dover Publications, 1956.

91. Irnich W. The chronaxie time and its practical importance. Pacing Clin Electrophysiol, 1980 May;3(3):292-301.

92 Jack JB, Noble, O, and Tsien, RW. Electric current flow in excitable cells. Oxford: Clarendon Press, 1983.

93. Jewett DL, Raymer MD. Basic concepts of neuronal function. Boston; Toronto: Little, Brown & Co, 1984.

94. Jami L, Murthy KS, Petit J, Zytnicki D. After-effects of repetitive stimulation at low frequency on fast-contracting motor units of cat muscle. J Physiol, 1983; 340:129-43.

95. Johnson MA, Sideri G, Weightman D, and Appleton D. A comparison of fibre size, fibre type constitution and spatial fibre type distribution in normal human muscle and in muscle from cases of spinal muscular atrophy and from other neuromuscular disorders. J Neurol Sci, 1973; 20: 345-61.

96. Kalman RE. A new approach to linear filtering and prediction problems. J Basic Engineering, 1960; 82(1): 35-45.

97. Kandel ER, Schwartz JH, Jessell TM, (eds.). Principles of neural science, New York: McGraw-Hill Health Professions Division: 2000.

98. Katz B. The relation between force and speed in muscular contraction. J. Physiol, 1939; 96: 45-64.

99. Kingsland SE. The refractory model: the logistic curve and the history of population ecology. Quart Rev Biol, 1982; 57(1): 29-52.

100. Kingsland SE. Modeling nature. Chicago: University of Chicago Press, 1995.

101. Klaassen CD. Principles of toxicology and treatment of poisoning. Ch. 66 in Brunton LL et al. (eds.), Goodman and Gilman's the pharmacological basis of therapeutics, 11th edition. New York: McGraw-Hill, 2006.

102. Klass M, Guissard N, and Duchateau J. Limiting mechanisms of force production after repetitive dynamic contractions in human triceps surae. J Appl Physiol. 2004; 96: 1516-21.

103. Krasnosel'skii M, Pokrovskii A. Systems with hysteresis, New York: Springer-Verlag, 1989.

104. Krause JS, Sternberg M, Lottes S, et al. Mortality after spinal cord injury: an 11-year prospective study. Arch Phys Med Rehab, 1997; 78: 815-21.

105. Krause JS, Broderick L. Outcomes after spinal cord injury: comparisons as a function of gender and race and ethnicity. Arch Phys Med Rehab, 2004; 85(3): 355-62.

106. Kuffler SW, Nicholls JG. From neuron to brain. Sunderland, MA: Sinauer Associates, Inc., 1976.

107. Kukulka CG. “Principles of neuromuscular excitation“. Ch. 1 in Gersh MR (ed.), Electrotherapy in rehabilitation. Philadelphia: FA Davis; 1992.

108. Kurtzke JF. Epidemiology of spinal cord injury. Neurol Neurocir Psiquiatr, 1977; 18(Suppl 2-3): S157-91.

109. Lamb GD, Recupero E, and Stephenson DG. Effect of myoplasmic pH on excitation-contraction coupling in skeletal muscle fibres of the toad. J Physiol, 1992; 448: 211-24.

110. Lansky P, Pokora O, Rospars JP. Stimulus-response curves in sensory neurons: how to find the stimulus measurable with the highest precision. In: Advances in brain, vision, and artificial intelligence. Berlin: Springer-Verlag, 2007, 338-49.

111. Lee JA, Westerblad H, and Allen DG. Changes in tetanic and resting $[Ca^{2+}]_{[}$ during fatigue and recovery of single muscle fibres from Xenopus laevis. J Physiol, 1991; 433: 307-26.

112. Lehninger AL. Principles of biochemistry, 2nd edition. New York: Worth, 1982.

113. Lekvall P, Wahlbin C. A study of some assumptions underlying innovation diffusion functions. Swed J Econ, 1973; 75(4):362-77.

114. Levenberg K. A method for the solution of certain problems in least squares. Quart Appl Math. 1944; 2:164-8.

115. Lloyd DPC. Neuron patterns controlling transmission of ipsilateral hind limb reflexes in cat. J Neurophysiol, 1943: 6: 293.

116. Lotka AJ. Studies on the mode of growth of material aggregates. Am J Sci, 1907; 24(141): 199-217.

117. Lotka AJ. Contribution to the theory of periodic reactions. J Phys Chem, 1910; 14: 271-4.

118. Lotka AJ. Elements of physical biology. New York: Dover Publications, 1925.

119. Lotka AJ. Elements of mathematical biology. New York: Dover Publications, 1956.

120. Lotta S, Scelsi R, Alfonsi E, Saitta A, Nicolotti D, Epifani P, and Carraro U. Morphometric and neurophysiological analysis of skeletal muscle in paraplegic patients with traumatic cord lesion. Paraplegia, 1991;29:247-52.

121 Löwy J. Kosmos, 1911, p. 331

122. Lu FC. Basic toxicology. New York: CRC Press, 1996.

123. Ma J, Fill M, Knudson CM, Campbell KP, Coronado R. Ryanodine receptor of skeletal muscle is a gap junction-type channel. Science, 1988;242:99-102.

124. Malthus TR. An essay on the principles of population. London: J. Johnson, 1798.

125. Marquardt D. An algorithm for least-squares estimation of nonlinear parameters. SIAM J Appl Math, 1963; 11: 431-41.

126. Martin AR. Quantal nature of synaptic transmission. Physiol Rev, 1966; 46(1): 51-66.

127. May RM. Simple mathematical models with very complicated dynamics. Nature, 1976 Jun 10;261(5560):459-67.

128. McComas AJ, Jorgensen PR, Upton ARM. The neurapraxic lesion: A clinical contribution to the study of trophic mechanisms. Can J Neurol Sci, 1974; 1: 170-9.

129. McComas A, Galea V, Sinhom RW, Hicks AL, and Kuiaek S. The role of the Na, K4-pump in delaying muscle fatigue. In: Sargeant AJ. and Kernell D. (eds.), Neuromuscular fatigue. Amsterdam: North-Holland, 1993.

130. McComas AJ. Skeletal muscle: form and function, 2nd edition. Champaign, IL: Human Kinetics; 1996.

131. Meyerhof O. Über die Atmung der Froschmuskulatur. Pflüg. Arch. ges. Physiol. 1919; 175: 20.

132. Meyerhof O. Zur Verbrennung der Milchsäure in der Erholungsperiode des Muskels. Pflüg. Arch. ges. Physiol. 1919; 175: 88.

133. Meyerhof O. Über die Energieumwandlungen im arbeitenden Muskel. Med. Klinik, Nr. 1920; 17-25.

134. Meyerhof O. Über die Rolle der Milchsäure in der Energetik des Muskels. Naturwissenschaften, 1920; 8, 696-700.

135. Meyerhof O. Die Energieumwandlungen in Muskel. Über die Beziehungen der Milchsäure zur Wärmebildung und Arbeitsleistung des Muskels in der Anaerobiose. Pflüg. Arch. ges. Physiol. 1920; 182: 232-45

136. Meyerhof O. Das Schicksal der Milchsäure in der Erholungsperiode des Muskels. Pflüg. Arch. ges. Physiol. 1920; 182: 284-300.

137. Meyerhof O. Kohlenhydrat und Milchsäureumsatz im Froschmuskel. Pflüg. Arch. ges. Physiol. 1920; 185: 11-20.

138. Meyerhof O. Über das Schicksal der Milchsäiure in der Erholungsperiode des Muskels und die Energetik des Kontraktionsvorganges. Sonderabdruck aus Ber. ges. Physiol. II, 1920; 2-10.

139. Meyerhof O. Über die Milchsäurebildung in der zerschnittenen Muskulatur. Pflüg. Arch. ges. Physiol. 1921; 188: 114-20.

140. Meyerhof O. Die Energieumwandlungen im Muskel. V. Milchsäurebildung und mechanische Arbeit. Pflüg. Arch. ges. Physiol. 1922; 19: 128-35.

141. Meyerhof O. Die Energieumwandlungen im Muskel. VI. Über den Ursprung der Kontraktionswarme. Pflüg. Arch. ges. Physiol. 1922; 195: 22-31.

142. Meyerhof O. Die Verbrennungswarme der Milchsäure. Biochem. Z. 1922; 129: 594-602.

143. Meyerhof O. Über die Energetik des Müskels. Klin. Wschr. 1922; 1: 230-45.

144. Morgan BJT. Quantal response models. Encyclopedia of biostatistics. New York: Wiley, 2005, p. 300

145. Myklebust BM, Kloth L “Electrodiagnostic and electrotherapeutic instrumentation: characteristics of recording and stimulation systems and the principles of safety.” Ch.3 in Gersh MR (ed.), Electrotherapy in rehabilitation. Philadelphia: FA Davis; 1992

146. Nizami L. Estimating auditory neuronal dynamic range using a fitted function. Hearing Res, 2002; 167: 13-27.

147. Norton JA, Bass FM. A diffusion theory model of adoption and substitution for successive generations of high-technology products. Mgmt Sci, 1987; 33(9): 1069-86.

148. Paracelsus T. Die große Wundarzney. Ulm: 1536. In: Verkehrsmedizin: Fahreignung, Fahrsicherheit, Unfallrekonstruktion. Madea B, Mußhoff F, and Berghaus G, (ed.). Cologne: Deutscher Ärzte-Verlag, 2007.

149. Parmiggiani F, Stein RB. Nonlinear summation of contractions in cat muscles. II. Later facilitation and stiffness changes. J Gen Physiol. 1981 Sep;78(3):295-311.

150. Pearl R, Reed LJ. Skew-growth curves. Proc Nat Acad Sci, 1925;11:16-22.

151. Peckham PH, Marsolais EB, Mortimer JT. Restoration of key grip and release in the C6 tetraplegic patient through functional electrical stimulation. J Hand Surg [Am], 1980; 5(5):462-9.

152. Peckham PH, Keith MW, Freehafer AA. Restoration of functional control by electrical stimulation in the upper extremity of the quadriplegic patient. J Bone Joint Surg, 1988; 70-A:144-8.

153. Peckham PH, Keith MW. Motor prostheses for restoration of upper extremity function, In: Stein RB, Peckham PH, Popovic DB, (eds.), Neural prostheses: replacing motor function after disease or disability. 1992.

154. Polyanin AD, Zaitsev VF. Handbook of exact solutions for ordinary differential equations, 2nd ed., Boca Raton, FL.: Chapman & Hall/CRC, 2003.

155. Pharmacokinetics and pharmacodynamics: the dynamics of drug absorption, distribution, action, and elimination. Ch. 1 in Brunton LL et al. (eds.), Goodman and Gilman's the pharmacological basis of therapeutics, 11th edition. New York: McGraw-Hill, 2006.

156. Quetelet AJ. Sur I'homme et le de'veloppement de ses faculte's; ou Essai de physique sociale, vol. 2. Paris: Bachelier; 1835.

157. Ragnarsson KT. The physiologic aspects and clinical application of functional electrical stimulation in rehabilitation. In: Downey JA, et al. (eds.), The physiological basis of rehabilitation medicine. Boston: Butterworth-Heinemann, 1994.

158. Riccati J. Animadversiones in aequationes differentiales secundi gradus. Acta Euroditorum Lipstae, 1724. Translated by Bruce IR at www.17thcenturymaths.com, 2007.

159. Robergs RA, Ghiasvand F, Parker D. Biochemistry of exercise-induced metabolic acidosis. Am J Physiol Regul Integr Comp Physiol. 2004 Sep;287(3):R502-16.

160. Robertson TB. On the normal rate of growth of an individual and its biochemical significance. Arch. für Entwicklungmechanik der Organismen, 1908; 25: 581-614.

161. Robertson TB. The chemical basis of growth and senescence. Philadelphia: Lippincott, 1923.

162. Savageau MA. Michaelis-Menten mechanism reconsidered: Implications of fractal kinetics. J. Theor. Biol. 1995; 176: 115-24.

163. Schnell S, Turner TE. Reaction kinetics in intracellular environments with macromolecular crowding: simulations and rate laws. Prog. Biophys. Mol. Biol. 2004; 85: 235-60.b

164. Shields RK. Fatigability, relaxation properties, and electromyographic responses of the human denervated soleus muscle. J Neurophysiol. 1995; 73(6):2195-2206.

165. Shields RK. Muscular, skeletal, and neural adaptations following spinal cord injury. J Orthop Sports Phys Ther. 2002; 32: 65-74.

166. Shields RK, Frey-Law LA, Reiling B, Sass K, Wilwert J. Effects of electrically induced fatigue on the twitch and tetanus of denervated soleus muscle in humans. J Appl Physiol. 1997; 82:1499-1507.

167. Shields RK, Chang YJ. The effects of fatigue on the torque-frequency curve of the human denervated soleus muscle. J Electromyogr Kinesiol, 1997; 7: 3-13.

168. Shields RK, Chang YJ, Ross M. Neuromuscular propagation after fatiguing contractions of the denervated soleus muscle in humans. Muscle Nerve, 1998; 21:776-87

169 Shields RK, Dudley-Javoroski S. Musculoskeletal plasticity after acute spinal cord injury: effects of long-term neuromuscular electrical stimulation training. J Neurophysiol, 2006; 95: 2380-90

170. Shields RK, Dudley-Javoroski S, Frey Law LA. Electrically-induced muscle contractions influence bone density decline after spinal cord injury. Spine. 2006; Mar 1; 31(5):548-53.

171. Shields RK, Dudley-Javoroski S, Littmann AE. Post-fatigue potentiation of the denervated soleus muscle: evidence for adaptation with long-term electrical stimulation training. J Appl Physiol. 2006 Aug;101(2):556-65.

172. Shields RK. Dudley-Javoroski S, Littmann AE, Iguchi M, Doublet stimulation protocol to minimize musculoskeletal stress during denervated quadriceps muscle testing. J Appl Physiol. 2008 Jun;104(6):1574-82. Epub 2008 Apr 24.

173. Shoshan-Barmatz V, Ashley RH. The structure, function, and cellular regulation of ryanodine-sensitive Ca^{2+} release channels. Int Rev Cytol 1998; 183: 185-270.

174. Standring S, (ed.). Gray's anatomy: the anatomical basis of clinical practice. 39th edition. Edinburgh; New York: Elsevier Churchill Livingstone; 2005.

175. Stein RB, Parmiggiani F. Nonlinear summation of contractions in cat muscles. I. Early depression. J Gen Physiol. 1981 Sep;78(3):277-93.

176. Talmadge RJ, Roy RR, Caiozzo VJ, Edgerton VR. Mechanical properties of rat soleus after long-term spinal cord transection. J Appl Physiol. 2002; 93: 1487-97.

177. Talmadge RJ, Roy RR, Edgerton VR. Persistence of hybrid fibers in rat soleus after spinal cord transection. Anat Rec. 1999; 255: 188-201.

178. Thies RE. Neuromuscular depression and apparent depletion of transmitter in mammalian muscle. J. Neurophysiol. 1965; 28: 427-42.

179. Trefil JS. Cassell's laws of nature-an A-Z of laws and principles governing the workings of our universe. London: Cassell Reference, 2002.

180. Verhulst PF. Notice sur la loi que la population pursuit dans son accroissement. Correspondance mathématique et physique, 1838; 10: 113-21.

181. Verhulst PF. Recherches mathematiques sur la loi d'accroissement de la population. Nouveaux Memoires de l'Academie Royale des Sciences et Belles-Lettres de Bruxelles. 1845; 18(1): 1-45.

182. Vesalius A. De humani corporis fabrica libri septem. Basel : Joannis Oporini, 1543.

183. Vitale MG, Goss JM, Matsumoto H. Epidemiology of pediatric spinal cord injury in the United States: years 1997 and 2000. J Pediatr Orthop, 2006 Nov-Dec; 26(6): 745-9.

184. Waller A. Experiments on the section of the glossopharyngeal and hypoglossal nerves of the frog, and observation on the alteration produced thereby in the structure of their primitive fibres, Phil Trans Royal Soc, London, 1850; 140: 423.

185. Wallinga-de Jonge W, Boom HB, Heijink RJ, van der Vliet GH. Calcium model for mammalian skeletal muscle. Med Biol Eng Comput. 1981;19(6):734-48.

186. Westerblad H, Allen DG. Changes of myoplasmic concentration during fatigue in single mouse muscle fibers. J Gen Physiol, 1991; 98: 615-35.

187. Westerblad H, Duty S, Allen DG. Intracellular calcium concentration during low-frequency fatigue in isolated single fibers of mouse skeletal muscle. J Appl Physiol. 1993; 75: 382-8.

188. Williams PL, Hall SM. Prolonged *in vivo* observations of normal peripheral nerve fibres and their acute reactions to crush and deliberate trauma. J Anat, 1971; 108: 397-408.

189. Williams PL, Hall SM. Chronic Wallerian degeneration-an *in vivo* and ultrastructural study. J Anat, 1971; 109: 487-503.

190. Zahalak GI, Ma SP. Muscle activation and contraction: constitutive relations based directly on cross-bridge kinetics. J Biomech Eng, 1990; 112: 52-62.

191. Zahalak GI. The two-state cross-bridge model of muscle is an asymptotic limit of multi-state models. J Theor Biol, 2000; 204: 67-82.

192. Zhong H, Roy RR, Hodgson JA, Talmadge RJ, Grossman EJ, Edgerton VR. Activity-independent neural influences on cat soleus motor unit phenotypes. Muscle Nerve, 2002; 26: 252-64.

193. Zumdahl SS. Chemistry. Boston: Brooke/Cole, 1989.